UNIVERSIDADE DE SÃO PAULO
INSTITUTO DE GEOCIÊNCIAS

Petrochronology of ultrahigh-temperature migmatites from the Arapiraca Complex, Borborema Province, NE Brazil

LUCAS RAMOS TESSER

Orientador: Prof. Dr. Miguel Angelo Stipp Basei

Dissertação de Mestrado

Nº 868

COMISSÃO JULGADORA

Dr. Miguel Angelo Stipp Basei

Dr. Telmo Manuel Bento dos Santos

Dra. Jailma Santos de Souza de Oliveira

SÃO PAULO
2021

Serviço de Biblioteca e Documentação do IGc/USP
Ficha catalográfica gerada automaticamente com dados fornecidos pelo(a) autor(a)
via programa desenvolvido pela Seção Técnica de Informática do ICMC/USP

Bibliotecários responsáveis pela estrutura de catalogação da publicação:
Sonia Regina Yole Guerra - CRB-8/4208 | Anderson de Santana - CRB-8/6658

Ramos Tesser, Lucas
Petrochronology of ultrahigh-temperature migmatites from the Arapiraca Complex, Borborema Province, NE Brazil / Lucas Ramos Tesser; orientador Miguel Ângelo Stipp Basei. -- São Paulo, 2021.
153 p.

Dissertação (Mestrado - Programa de Pós-Graduação em Mineralogia e Petrologia) -- Instituto de Geociências, Universidade de São Paulo, 2021.

1. Borborema Province. 2. Phase equilibrium modeling. 3. São Francisco Craton. 4. Ultrahigh-temperature metamorphism. 5. Petrochronology. I. Ângelo Stipp Basei, Miguel, orient. II. Título.

ACKNOWLEDGEMENTS

First, my thanks go to my advisors Miguel Basei and Cae Ganade for their guidance, valuable tips, and encouragement over more than two years of work. I'm sure we're going to break a lot of rocks in the future. Thank you! There are numerous other “advisors” who are involved: to Renato Moraes, I’m very grateful for your contribution of knowledge and encouragement to work with these "complicated rocks" that are the granulites and migmatites. To Roberto Weinberg for the inspiration and great teachings in the fieldwork in the Borborema Province. To Laísa for their valuable contribution in the final article. To my "sapphirine partner" Daniela Leal thank you for sharing your experiences and learnings with these amazing rocks. I thank Cassio (Argila) for the fruitful discussions on tectonics and geophysics and many other things. I would like to thank the members of B-09 room and the other regular assiduous: Fofona, Eliane, Biloba, Vanessa, Julio, and several graduate students who have always made the work environment stress-free, thanks for the reception! I also thank the support of the technical staff of the IGc-USP: I’m grateful to Marcus and Leandro from the EMPA laboratory, Vasco from the sample preparation laboratory, Vinicius and José Paulo from the LA-ICP-MS and X-ray fluorescence laboratories as well for the support of the staff and trainees of CPGeo. To CPRM for their technical support during the fieldwork. To my friends from rural including Cassio, Raphael, Wallace, Abílio, Paulinho, and many others, thank you just for being, reminding me that there is a life outside the academy. My greatest thanks go to my family: Renata, Ronaldo, and Pedro, there is no way I could have achieved this without you. Finally, thank you Pamela for your patience, encouragement, and for believing in me the whole way.

"*A ciência, meu rapaz, é feita de erros, mas de erros benéficos, já que conduzem pouco a pouco à verdade*"

Julio Verne (Viagem ao Centro da Terra)

ABSTRACT

This work reports on the first finding of sapphirine-bearing ultrahigh-temperature (UHT) metamorphic rocks within the Borborema Province, in NE Brazil. The investigated UHT diatexites outcrop in the Arapiraca Complex, a high-grade Paleoproterozoic block embedded within the Neoproterozoic metavolcano-sedimentary sequence of the Sergipano fold-and-thrust belt. A sapphirine-bearing diatexite sample preserves two distinct residual mineral associations as inclusions in cordierite poikiloblasts: a volumetrically dominant silica-saturated, garnet-sillimanite-orthopyroxene-quartz domain, and a restricted silica-undersaturated, sapphirine-magnetite-spinel-corundum domain. Phase equilibrium modeling for the whole-rock bulk composition constrained the reactions preserved in the silica-saturated domain, which coupled with re-integrated ternary feldspar thermometry, Al-in-orthopyroxene thermobarometry, indicates peak UHT metamorphism occurred at ~970 ^{o}C/8.5 kbar followed by a clockwise near isobaric cooling stage crossing the H_2O-undersaturated solidus at ~900 ^{o}C/7.7 kbar. The T-M_{SiO2} and *P-T* phase equilibrium modeling reveals that the stabilization of the first magnetite-spinel in the silica-undersaturated domain can be a product of domainal SiO_2-depletion ascribed to inherited compositional banding and progressive melt loss episodes. The appearance of sapphirine as thin coronas around previously formed magnetite-spinel cores requires an increase in silica-activity during retrogression. This was driven by chemical interaction between the silica-undersaturated domain and trapped silica-rich leucosomes. U-Pb dating of zircons coupled with trace elements chemistry allows constraining the timing of melt crystallization between c. 2.03 and 1.96 Ga, following the peak of UHT metamorphism and supporting a protracted, c. 70 My period of melt presence in the crust. The UHT metamorphism in the Arapiraca Complex is related to a contemporaneous UHT event recorded within the São Francisco Craton, and more broadly coincides with high geothermal gradients at c. 2.0 Ga linked to the formation of the Columbia supercontinent. The integration of new petrological and geochronological data indicates that the Arapiraca Complex is a continental ribbon pulled away from the São Francisco-Congo paleocontinent possibly during the early Neoproterozoic Cariris Velho rifting event and opening of the Sergipano basin between c. 0.98-0.75 Ga. During the late Neoproterozoic at c. 0.63-0.57 Ga, the Arapiraca Complex continental ribbon thrusted back onto the northern margin of the São Francisco Craton as an inlier of the Sergipano fold-and-thrust belt.

Keywords: Borborema Province; Phase equilibrium modeling; São Francisco Craton; Ultrahigh-temperature metamorphism; zircon petrochronology.

RESUMO

Este trabalho relata a primeira descrição de rochas metamórficas de temperatura ultra-alta (TUA) portadoras de safirina na Província Borborema, NE do Brasil. Os diatexitos de TUA investigados afloram no Complexo Arapiraca, um bloco Paleoproterozóico de alta-grau embebida na sequência metavolcano-sedimentar Neoproterozóica da Faixa Sergipana. A amostra safirina-diatexito exibe duas distintas associações minerais preservadas como inclusões em poiquiloblastos cordierita: a volumentricamente dominante e saturada em sílica, o domínio granada-silimanita-ortopiroxênio-quartzo, e o restrito domínio insaturado em sílica de safirina-magnetita-espinélio-coríndon. A modelagem de equilíbrio de fases para a composição de rocha total restringiu as reações preservadas no domínio saturado em sílica, que junto com a termometria de feldspato ternário e a termobarometria de Al-no-ortopiroxênio, indicam que pico do metamorfismo TUA ocorreu em condições de ~970 ^{o}C/8,5 kbar seguido por um estágio de resfriamento quase-isobárico em trajetória horária, cruzando a *solidus* insaturada em H_2O em ~900 ^{o}C/7,7 kbar. Os modelos de T-M_{SiO2} e P-T revelaram que a estabilização precoce de magnetita-espinélio no domínio insaturado em sílica pode ser um produto da exaustão local de SiO_2 atribuído a heranças composicionais e eventos progressivos de perda de fundido. O crescimento da safirina como finas coroas em torno dos núcleos previamente formados de magnetita-espinélio requer um aumento da atividade da sílica durante a retrogressão. Esta foi impulsionada pela interação química entre o domínio insaturado em sílica e o fundido aprisionado rico em sílica. A datação U-Pb de zircão combinada a química de elementos-traço indicam que a cristalização do fundido ocorreu entre c. 2,03 e 1,96 Ga, após o pico do metamorfismo UAT, suportando um período prolongado de c. 70 My para a presença de fundido na crosta. O metamorfismo UAT no Complexo Arapiraca está relacionado a um evento UAT contemporâneo registrado dentro do Cráton São Francisco, e mais amplamente coincide com altos gradientes geotérmicos em c. 2.0 Ga ligados à formação do supercontinente Columbia. A integração de novos dados petrológicos e geocronológicos indicam que o Complexo Arapiraca é um *ribbon* continental desprendido do paleocontinente São Francisco-Congo possivelmente durante o evento Neoproterozóico Cariris Velho e a abertura da bacia Sergipana entre c. 0,98-0,75 Ga. Durante o Neoproterozóico tardio à c. 0,63-0,57 Ga, o *ribbon* continental Complexo Arapiraca foi deslocado de volta para a margem norte do Cráton São Francisco como a infraestrutura da faixa Sergipana.

Palavras-Chave: Província Borborema; modelagem de equilíbrio de fases; Cráton São Francisco; metamorfismo de temperatura ultra-alta; petrocronologia de zircão.

SUMMARY

CHAPTER 1. INTRODUCTION

1.1 Presentation and chapter outlines

The present master's dissertation was carried out within the scope of the Postgraduate Program in Mineralogy and Petrology of the Institute of Geosciences, University of São Paulo (IGc-USP). The main text of this dissertation is presented in the form of a scientific article, following the format of other theses and dissertations presented recently in this postgraduate program (*e.g.* Rocha, 2016; Silva, 2017; Motta, 2018; Esteves, 2019). The scientific article/chapter summarizes and presents all results generated in this master's dissertation and has as its central theme the petrology and geochronology of UHT rocks and their implications for São Francisco Craton dispersion in northeastern Brazil. The numbering of figures and tables and references for each chapter will be presented individually and at the end of each section. The chapters were organized as follows:

- CHAPTER 1. Present the dissertation's theme and organization, the nature of the problem, the general geological context, the research aims, and the materials and methods.
- CHAPTER 2. Here is presented a chapter in form of a scientific article submitted to the *Journal of Metamorphic Geology*. The article contains all the results generated by this work and is titled "*Ultrahigh-temperature Paleoproterozoic rocks in the Neoproterozoic Borborema Province, implications for São Francisco Craton dispersion in NE Brazil*".
- CHAPTER 3. Summarizes the major findings of the work presented here, highlight new questions raised as a result of this work, and outline potential future avenues of research.

1.2 The nature of the problem

The ultrahigh-temperature (UHT) metamorphism corresponds to extreme temperature conditions that exceed 900 ºC at mid-crustal levels, providing a very high geothermal gradient commonly greater than 75 ºC/kbar (Kelsey & Hand, 2015; Brown, 2007; Harley, 1998). Recognize UHT metamorphism is problematic because the common diagnostic mineral assemblages are derived and preserved from rare Mg-Al metasedimentary or metasomatic protoliths (Kelsey & Hand, 2015). In this unusual composition, three mineral associations are diagnostic for UHT metamorphism, there are sapphirine + quartz, orthopyroxene + sillimanite + quartz, and garnet + osumilite (Harley, 1998). Additionally, silica-undersaturated, sapphirine- and spinel-bearing mineral associations are reported in several UHT terranes, particularly for low oxygen fugacity systems and in melt-bearing rocks (Harley, 2008; Kelsey & Hand, 2015). The identification and understanding of the *P-T* evolution of UHT rocks until the mid-2000s was mainly based on experimental data that gave rise to the classic univariant reactions grids *i.e.* petrogenetic grids (*e.g.* Hensen, 1971). Our ability to constrain the *P-T* conditions of UHT metamorphism has grown considerably with the refinement of conventional thermobarometry (inverse *P-T* modeling). A great challenge was to find the ideal thermometer/barometer for this task since the calibrations involving Fe-Mg exchange between minerals did not record UHT temperatures due to the high-diffusion of these elements in such extreme conditions (Pattison et al., 2003). The advent of calibrations involving the Al solubility in orthopyroxene gained notoriety due to their fidelity in recording the peak granulite facies and UHT metamorphic conditions (*e.g.* Harley, 1984; Aranovich & Berman, 1997; Pattison & Bégin, 1994; Fitzsimons & Harley, 1994; Pattison et al., 2003). Other thermobarometric calibrations have been successfully applied, such as the re-integration of ternary feldspars (*e.g.* Hokada,

2001) and Fe-Ti oxides (*e.g.* Wang et al., 2019). More recently, the range of inverse *P-T* modeling tools has been extended to include tetravalent cation thermometry, which uses the experimentally calibrated temperature-dependent partitioning of 4+ cations for major and accessory minerals to recover the temperatures of equilibration. The calibrations of Zr-in-rutile, Ti-in-zircon, and Ti-in-quartz stand out for their versatility and the success of their application in UHT rocks (Ferry & Watson, 2007; Tomkins et al., 2007; Watson & Harrison, 2005; Watson et al., 2006; Zack et al., 2004).

Currently, the quantitative method most used to constrain the *P-T* conditions for the UHT metamorphic rocks is the phase equilibrium modeling. The phase equilibrium diagram is a type of phase diagram that shows the fields of stability of different equilibrium mineral assemblages for a single bulk-rock composition over a P-T range (P-T pseudosection), or for a linear range of bulk compositions between two end-member compositions at a fixed pressure or temperature (P-M or T-M pseudosections). The calculations are performed using an internally consistent thermodynamic data set and activity-composition models for solid solution phases (*e.g.* Holland & Powell, 2011; White et al., 2014). This approach assumes equilibrium on the scale of the bulk composition. Although, granulites (and UHT rocks) do not always equilibrate on volumes sufficiently large that the composition of such a volume can be analyzed by XRF, for example. Much is because there are primary features inherited from the protoliths (igneous or sedimentary layering) added to mass transfer effects of melt loss during its prograde evolution producing compositional heterogeneities. Thus, the critical consideration about the equilibrium volume and the utilization of P-M or T-M models priory to P-T pseudosections can be singularly useful to constrain the reaction history of local equilibrium volumes, where the effective bulk composition can vary on a centimeter or smaller scale (Ague, 1994).

Despite recent advances in quantifying P-T conditions of UHT granulites and migmatites, establishing the connection between metamorphic reactions and ages has been one of the most debated tasks by petrologists and geochronologists in recent years (Engi et al., 2017). Access and interpret the significance of radiometric information (*e.g.* U-Pb zircon ages) in response to the *P-T* metamorphic evolution of the rock has gained notoriety in the so-called "petrochronology" approach (Kylander-Clark et al., 2013; Engi et al., 2017). Notably, zircon stands out in the study of UHT rocks mainly for its high Pb closure temperature and its ability to incorporate the HFSE (high-field strength elements) (Cherniak & Watson, 2001; Rubatto, 2002; Hoskin & Schaltegger, 2003). This last characteristic is extremely important since the differential HREE partition between zircon and garnet, for example, can provide us a direct link between the obtained U-Pb ages with a specific reaction or other microstructural feature of the rock (*e.g.* Clark et al., 2018; Harley, 2016; Kelly & Harley, 2005). The application of this modern petrochronological approach allows a more detailed link between zircon crystallization and metamorphic reactions, thereby establishing a more robust *P-T-t* history for the UHT terranes.

A remarkable record of UHT metamorphism during the Paleoproterozoic orogeny (c. 2.1-2.0 Ga) is preserved in the central and northern portion of São Francisco Craton, NE Brazil (Figure 1; Leite et al., 2009; Barbosa et al., 2006, 2017). The UHT metamorphic rocks are exposed within the Itabuna-Salvador-Curaça orogen along the margins of old Archean nuclei, namely, Serrinha, Gavião, and Jequié blocks. All tectonic models proposed for this orogeny involve a final stage of a Himalayan-style continent-continent collision at c. 2.1-2.0 Ga between the aforementioned blocks together with the Congo block (also recognized as Gabon Massif; Ledru et al., 1994; Barbosa & Sabaté, 2004; Oliveira et al., 2010; Barbosa & Barbosa, 2017). The pre-

collisional history is quite complex and points to the long-lived accretion of magmatic and intraoceanic arcs at c. 2.2-2.1 Ga and intense reworking of the Archean crust during the final continental collision (Peucat et al., 2011; Barbosa & Barbosa, 2017). The most prominent deformational structures arise from the final stage of the continental collision and are characterized by transpressional shear zones associated with sub-vertical foliations and less frequently low-angle foliations with top-to-west vergence (Barbosa & Barbosa, 2017). The ductile deformation is coeval with regional granulite facies metamorphism dated at 2.08-2.03 Ga (Carvalho et al., 2017; Miranda et al., 2020; Aguilar et al., 2017).

The São Francisco Craton is bound to the north by the Neoproterozoic Borborema Province. This Province includes several reworked and deformed Archean-Paleoproterozoic blocks among Neoproterozoic sedimentary basins and granitic bodies (Figure 2a; Ganade et al., 2014). These old blocks in Borborema Province share isotopic and geophysical similarities with São Francisco Craton, leading to several authors to propose a direct correlation between them (*e.g.* Neves, 2015; Neves et al., 2015; Cruz et al., 2014; Simões Neto et al., 2014; Oliveira et al., 2010, 2015; Brito Neves and Silva Filho, 2019). However, until today, these correlations are restricted to comparisons of U-Pb ages and still lack an integrated geological-petrological approach in order to integrate the possible cratonic origin of the old terranes dispersed in the Borborema Province. In this crossing point, this research is inserted as the first attempt of petrological connection between Congo-São Francisco Craton and Borborema Province using as an object of study the occurrence of Paleoproterozoic UHT rocks, pioneered described here in the Arapiraca Complex.

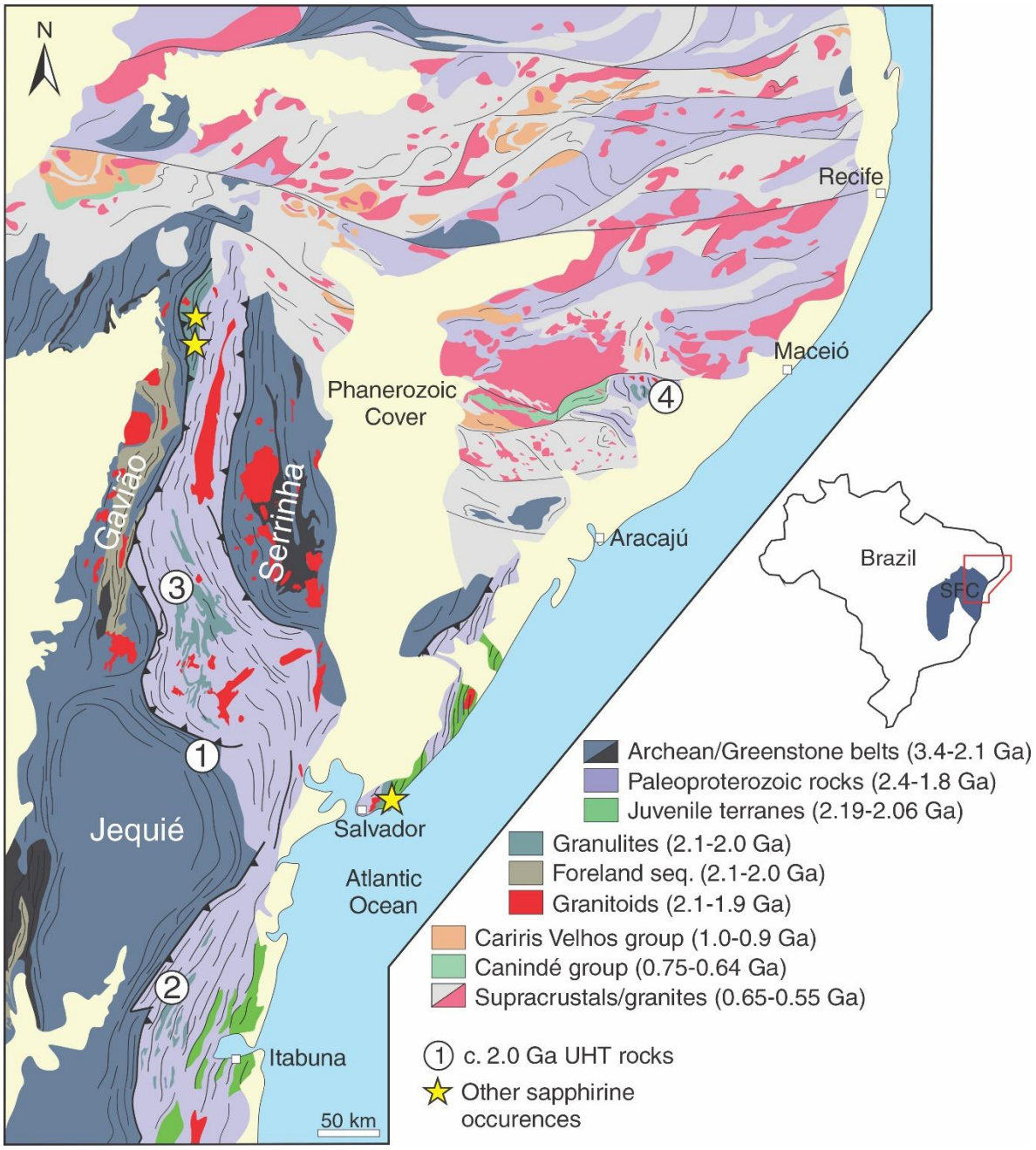

Figure 1. Tectonic map of the northeast of the São Francisco Craton and Borborema Province showing the Archean blocks/nuclei, Paleoproterozoic, and Neoproterozoic rocks. The numbers represent well-studied UHT rocks in the São Francisco Craton: (1) Barbosa et al., 2006; (2) Leite et al., 2009; (3) Barbosa et al., 2017; and within Borborema Province: (4) this dissertation.

Located in the extreme northeast of the Sergipano fold-and-thrust belt the Arapiraca Complex comprises a sequence of quartzofeldspathic gneisses, garnet gneisses, marbles, calc-silicate rocks, banded iron formations, quartzites, basic-ultrabasic dikes and sills, amphibolites, sillimanite-cordierite-bearing diatexites, which

would present characteristics of a rift-type environment, and metamorphism in amphibolite to granulite facies conditions (Figure 2b; Mendes et al., 2009). The recent 1:250,000 scale geological mapping carried out by the Geological Service of Brazil (CPRM) grouped the following field and petrographic criteria all the lithotypes that occur in the region into the Arapiraca Complex (Mendes 2009). More recently, Neves et al. (2016) demonstrated through the zircon provenance study that the migmatites and gneisses that occur along the Palmeira dos Índios Shear Zone (PISZ; see Figure 2b) have a broad population of Paleoproterozoic grains and that they were variably affected by several metamorphic pulses during the Tonian to the Ediacaran times. However, despite recent advances in mapping the mappable units of the Arapiraca Complex, geochronological data are still scarce, especially in the high grade anatectic metamorphic core outcropping near the Arapiraca city (Figure 2b).

In this context, this dissertation will try to bring a new view at various work-scales about the tectonic significance of the ultrahigh temperature metamorphism in the Arapiraca Complex, pioneered described here in the Borborema Province. The petrochronological approach applied in the UHT diatexites from the Arapiraca Complex will be tested as a robust alternative method to trace and recognize fragments with cratonic affinity within the South Borborema Province in northeast Brazil. Additionally, the detailed petrological study of a key-sample of sapphirine-bearing diatexite will be investigated from the point of view of the role of the equilibrium volume in the development of silica-saturated and silica-unsaturated domains and its relationship with the distribution of melt in residue-rich migmatites.

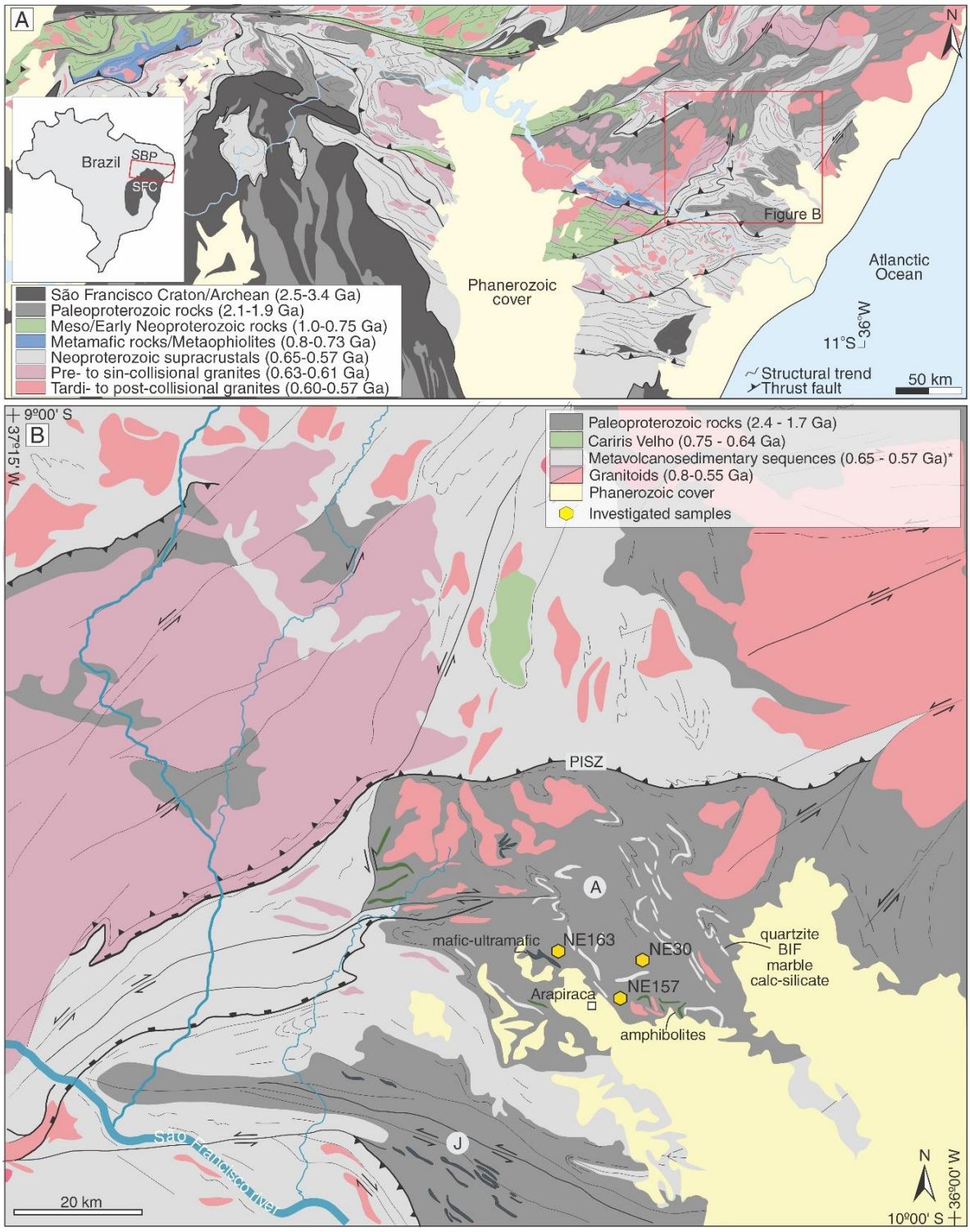

Figure 2. Simplified tectonic map (a) of the northeastern portion of the São Francisco Craton and the Southern Borborema Province; and (b) detail map of the Arapiraca Complex (modified from Mendes et al, 2009).

1.4 Research aims

The central aim of this dissertation is to investigate the time-integrated metamorphic evolution from a suite of ultrahigh-temperature migmatites from the

Arapiraca Complex in order to provide information on the geodynamic significance of high-grade Paleoproterozoic rocks in this area and to establish their possible connections with the São Francisco-Congo paleocontinent. The first approach involved the quantification of the P-T evolution of a single sapphirine-bearing diatexite sample based on conventional thermobarometry and phase equilibrium modeling study. Subsequently, the combination of Th-U-Pb and trace element chemistry in zircon, including rare earth elements (REE), has been used in order to constrain the age and possible length of production and/or crystallization of anatectic melt of the studied migmatites. Finally, the Th-U-Pb ages were linked with the reconstructed P-T path and compared with other UHT rocks with similar ages that occur in the well-preserved nucleus of the São Francisco Craton.

1.5 Methodology

1.5.1 Petrography

The macroscopic description of the samples started in the field, with the identification of the main minerals, textures, and structures. Subsequently, fourteen thin sections were made from three selected samples and described under a conventional optical microscope in order to determine equilibrium assemblages and microstructures. Photomicrographs were acquired using an Olympus BXP-50 coupled with a Camedia C-5050 digital camera at the Petrographic Microscopy Laboratory of the Geoanalítica (NAP) - Institute of Geosciences, University of São Paulo, Brazil (IGc-USP). Four thin sections were investigated using back-scattered electron images (BSE), in order to identify the fine-grained minerals and compositional zoning between the different phases. These images were obtained with a JEOL JXA-FE-8530 equipment at the Electron Microprobe Laboratory of the NAP Geoanalítica of IGc-USP.

1.5.2 Whole-rock geochemistry

The major elements chemistry was obtained by analyzing fused glass discs in X-ray fluorescence equipment from the X-ray Fluorescence Laboratory of the NAP Geoanalítica facilities of IGc-USP. The equipment used was a PANalytical AXIOS MAX spectrometer and the samples were prepared following the laboratory methodologies that were described in Mori et al. (1999). Using the same piece that the thin sections were cut, a ~3kg piece of the most residual and melanocratic portion of the migmatite from the NE30 sample was analyzed.

1.5.3 Mineral Chemistry

The quantitative mineral chemistry was performed using the WDS (wavelength-dispersive spectrometry) with a JEOL JXA-FE-8530 equipment housed at Electron Microprobe Laboratory at the GeoAnalítica facilities in the IGc-USP. The operating conditions were 15 kV of acceleration voltage, 20 nA of probe current, with bean size varying between 5 and 10 µm. Count times were 20 s on peaks and 10s on each background and following synthetic and natural standard reference materials were used: garnet (SiO_2, Al_2O_3), olivine (MgO, FeO, MnO), wollastonite (CaO), albite (Na_2O), orthoclase (K_2O), chromite (Cr_2O_3), strontianite (SrO), and rutile (TiO_2). The data were processed with the online CITZAF routine. Point analyses were carried out in the core and rim of minerals, as well as core-rim-core profiles. The structural formulae were calculated using an Excel spreadsheet written by the author. For sapphirine, orthopyroxene, garnet, and spinel, the amount of Fe^{3+} content was calculated from the ideal mineral stoichiometry (Droop 1987). The complete analytical results are available in **APPENDIX A.**

1.5.4 Inverse P-T modeling

For a precise characterization of P-T conditions of metamorphism, three thermobarometric calibrations were adopted here: (1) Al-in-orthopyroxene thermobarometry corrected for late Fe-Mg exchange (Pattison et al., 2003); (2) reintegration of ternary feldspar thermometry (Kroll et al., 1993; Benisek et al., 2010); and (3) Ti-in-zircon thermometry (Ferry & Watson, 2007).

1.5.4.1 Al-in-orthopyroxene thermobarometry

The solubility of alumina in orthopyroxene coexisting with garnet (Al-in-orthopyroxene thermobarometry) is generally regarded as more robust to retrograde resetting than the Fe-Mg composition of garnet (Aranovich & Berman, 1997). For the sample NE30, the P-T conditions of assuming the equilibrium between garnet-orthopyroxene-plagioclase-quartz were obtained using the Al-in-orthopyroxene corrected for late Fe-Mg exchange thermobarometer of Pattison et al., (2003). Four representative garnet-orthopyroxene-plagioclase compositions were combined and two methods of calculation of aluminum in orthopyroxene *y*(opx) were employed: 1) assuming the ideal Tschermak exchange, where all Fe in orthopyroxene structure is Fe^{2+} (where *y*(opx) = Al/2) considering the stoichiometric distribution of Fe^{3+} in orthopyroxene (where, *y*(opx) = Al-Fe^{3+}-Cr-(2 x Ti)/2).

1.5.4.2 Ternary feldspar thermometry

During the slow cooling from high-temperature conditions, the plagioclase and K-feldspar tend to lose their K- and Ca-contents in order to maintain the equilibrium (Benisek et al., 2004). For example, K-feldspar can be decomposed into plagioclase and K-rich feldspar, forming perthite. In geothermometer calculations, this phenomenon causes divergent temperature estimations for each end-member (Ab, Or, and An). However, the original anorthite content in plagioclase is generally preserved

due to sluggish intracrystalline diffusion of Al-Si (coupled via Ca + Al ↔ (Na, K) + Si) allowing to calculate the temperature of equilibrium by reversing the Na-K contents at constant anorthite value (Kroll et al., 1994; Benisek et al., 2004, 2010).

The composition of ternary feldspar before exsolution was reintegrated from perthite grains and used to calculate the *solvus* temperature through a minimization variance method of Kroll et al. (1995) and Benisek et al. (2010). Following the procedures described in Benisek et al. (2004) were used only homogeneous perthite grains in order to reduce the effects of retrograde compositional resetting. The volume of lamellae/host feldspar was estimated from the areal proportion calculated using high-resolution BSE images treated with ImageJ software (Schneider et al., 2012), and the procedures for calculating the pre-exsolution ternary feldspar composition are those described in Hokada (2001). The volume of lamellae/host feldspar is converted into weight percent using the densities of plagioclase (2.67 g/cm^3) and K-feldspar (2.57 g/cm^3) (Smith, 1974). The re-integrated ternary feldspar compositions were plotted in the Ab-An-Or ternary diagram using the SolvCalc program (Wen & Nevasil, 1994) with different isotherms considering the Margules parameters for feldspar of Benisek et al. (2010), Elkins and Grove (1990), and Fuhrman and Lindsley (1988).

1.5.4.3 Ti-in-zircon thermometry

Ti-in-zircon thermometry using the calibration of Ferry and Watson (2007) was used in order to link the isotopic data with the thermal history. This thermometer involves independence of silica and titania activities, allowing it to apply in rocks without quartz or rutile. The $a\mathrm{SiO_2}$ was set as one for all samples, whereas the $a\mathrm{TiO_2}$ was set as 0.5 for sample NE30 and as one for samples NE163 and NE157.

1.5.5 Thermodynamic modeling

Phase equilibria modeling was undertaken with the software THERIAK-DOMINO (version 04.02.2017; de Capitani & Petrakakis, 2010) and using the dataset version 6 of Holland & Powell (2011) in the model system MnNCKFMASHTO (MnO-NaO-CaO-K_2O-FeO-MgO-Al_2O_3-SiO_2-H_2O-TiO_2-Fe_2O_3) considering the activity models of Holland & Powell (2003) for feldspars, White et al. (2014a, 2014b) for garnet, orthopyroxene, cordierite, biotite, ilmenite-hematite and melt, White et al. (2002a) for spinel and Wheller & Powell (2014) for sapphirine. Corundum, quartz, Al_2SiO_5 isomorphs, rutile, and H_2O are treated as pure end-member phases. All mineral abbreviations are from Holland & Powell (2011) except (sa) for sapphirine and (L) for leucosome/silicate melt. At temperatures greater than 740°C, ilmenite and hematite were modeled as a complete solid-solution (*e.g.* Diener & Powell, 2010; White et al., 2014a) and this phase is referred to as ilmenite (ilm) throughout this contribution. The spinel-hercynite-ülvospinel solid solution was referred to as only spinel (sp) and the end-member magnetite as (mt).

The whole-rock XRF composition of melanosome from the sample NE30 was recalculated to atomic proportion and used in the thermodynamic modeling. The P_2O_5 was removed from the bulk-rock and the equivalent CaO content in apatite was recalculated. The most uncertain compositional variables in the bulk composition are the water content and the oxidation state (Fe_2O_3 vs FeO), commonly requiring that these be constrained with T-M- or P-M-type models (where M refers to the amount of an oxide component) prior to the calculation of the P-T pseudosection. The pressure used for the calculation of T-M models was 7.9 kbar based on results obtained with Al-in-orthopyroxene thermobarometry (see topic 1.5.4.1). For the T-M_O model (where O is oxygen, treated as a proxy for Fe^{3+}), the oxidation state in the bulk composition

varies along the x-axis from very oxidized conditions at the right-hand side (O = 3.57 mol.%) to reduced conditions at the left-hand side (O = 0.001 mol.%). Only for this model the H_2O value was considered as equal to the measured LOI content and the recalculated iron content was considered as FeO* = FeO + 2 x O. For the T-M_{H2O} model, the amount of water varies along the x-axis from 0.001 mol.% at the left-hand side to 2.56 mol.% at the right-hand side. The maximum concentration of H_2O that allows the stability of the inferred peak/near peak equilibrium assemblage close as possible to the *solidus* temperature was used to infer the appropriate water content during the UHT metamorphism (*e.g.* White et al., 2002b). The P-T pseudosection varying between 6.0-9.0 kbar and 850-1050 ˚C using the adjusted H_2O and ferric iron contents was calculated. The diagram was contoured for *y*(opx) (Al on the M1 site in orthopyroxene) and XAn (anorthite in plagioclase) and for selected mineral proportions (vol.%) in order to better constrain the metamorphic P-T evolution.

To investigate the appropriated composition of the silica-undersaturated, sapphirine-bearing domain a T-M_{SiO2} model assuming the previously adjusted values of water and slight lower ferric iron contents was calculated. This approach allows for the assessment of the effect of changing the silica amount on the stability of peak mineral assemblage (*e.g.* Kelsey et al., 2005). Finally, in order to calculate a P-T pseudosection to constrain the reaction history of this compositional domain, the adjusted bulk-silica amount was used.

1.5.6 U-Pb zircon geochronology and trace element chemistry

1.5.6.1 Sample preparation

The zircon separation was carried out in the Laboratory of Sample Preparation of the CPGeo in the IGc-USP. The procedures of mineral separation included: sample comminution using a jaw crusher and an agate disk mill, water table (*Wiffley*), Frantz

magnetic separator, dense liquids (bromoform = 2,89 g/cm3 and methylene iodide = 3,32 g/cm3), allowing the concentration of zircon in the denser and more non-magnetic fraction. The zircons were then hand-picked under a microscope, mounted on epoxy resin, and finally polished to expose the center of the crystals.

1.5.6.2 Zircon imaging

The internal structures of the zircon grains were identified through cathodoluminescence images using a Quanta 250 FEG scanning electron microscope equipped with a Centaurus Mono CL3 + cathodoluminescence spectroscope housed at CPGeo in the IGc-USP. The operation conditions were 15 kV of acceleration voltage, 70 µA of probe current, and 20 mm of the focal distance.

1.5.6.3 Zircon dating

The equipment used to obtain the U-Pb-Th isotopic data corresponds to a MC-LA-ICP-MS system of NEPTUNE - Thermo Scientific coupled with ablation cell (Teledyne) model Excimer 193 (nm) with spot diameter, frequency, and laser fluence of 20 µm at 6 Hz and 6 mJ, respectively. Every ten (10) unknown zircon analyses were included one in the zircon reference material GJ-1 (Jackson et al., 2004) and one blank reading. Elements measured included ^{206}Pb, ^{207}Pb, ^{232}Th, and ^{238}U. The isotopic results were reduced and corrected with an in-house software developed by Siqueira et al. (2014), using an “R” statistical package based on Python programming language. The data of each analysis was filtered considering outliers values of common Pb contents, errors of isotopic ratios, and high percentages of discordance. Finally, the geochronological data was plotted in diagrams using the IsoplotR software (Vermeesch, 2018). Individual uncertainties are presented at the sigma 2 level. The confidence level for the weighted averages is 95 %. The complete analytical results are available in **APPENDIX B**.

1.5.7 Zircon trace element composition

The trace element analyses of zircon were performed with a LA-ICP-MS, model iCAP Q - Thermo Scientific coupled with ablation cell (213 A/F - New Wave), housed at the GeoAnalítica facilities in the IGc-USP. Spots were placed near or comprising one-third of the position of the U-Pb dating spots and in the same CL-domain. The total analysis time was 60s, with the first 25s of ablation time (background) excluded from integration. Conditions for laser fluency, frequency, and spot size were, respectively, 1.13 J/cm2, 20 Hz, and 30 μm. Synthetic glasses (NIST 610 and ZR-91500) were used for external calibration that was analyzed twice for every 10 unknowns, and reference values were taken from Pearce et al. (1997). Each analysis measured masses of ^{7}Li, ^{24}Mg, ^{27}Al, ^{29}Si, ^{31}P, ^{42}Ca, ^{44}Ca, ^{45}Sc, ^{49}Ti, ^{55}Mn, ^{56}Fe, ^{59}Co, ^{85}Rb, ^{88}Sr, ^{89}Y, ^{91}Zr, ^{93}Nb, ^{95}Mo, ^{118}Sn, ^{121}Sb, ^{137}Ba, ^{139}La, ^{140}Ce, ^{141}Pr, ^{146}Nd, ^{147}Sm, ^{151}Eu, ^{153}Eu, ^{157}Gd, ^{159}Tb, ^{163}Dy, ^{165}Ho, ^{166}Er, ^{169}Tm, ^{172}Yb, ^{175}Lu, ^{179}Hf, ^{181}Ta, ^{206}Pb, ^{207}Pb, ^{208}Pb, ^{232}Th, and ^{238}U. Internal standard was stoichiometric Zr content for zircon. The time-resolved data were processed following each session using the Glitter program (Griffin et al., 2008). In the REE plots, the analyzed data are normalized against the chondrite values of McDonough & Sun, 1995. The complete analytical results are presented in **APPENDIX C**.

1.6 References

Ague, J. J. (1994). Mass transfer during Barrovian metamorphism of pelites, south-central Connecticut; I, Evidence for changes in composition and volume. American Journal of Science, 294(8), 989-1057.

Aguilar, C., Alkmim, F. F., Lana, C., & Farina, F. (2017). Palaeoproterozoic assembly of the São Francisco craton, SE Brazil: New insights from U–Pb titanite and monazite dating. Precambrian Research, 289, 95-115.

Aranovich, L. Y., & Berman, R. G. (1997). A new garnet-orthopyroxene thermometer based on reversed Al2O3 solubility in FeO-Al2O3-SiO2 orthopyroxene. American Mineralogist, 82(3-4), 345-353.

Barbosa, J. S. F., & Barbosa, R. G. (2017). The Paleoproterozoic eastern bahia orogenic domain. In São Francisco Craton, Eastern Brazil. 57-69p. Springer, Cham.

Barbosa, J. S. F., & Sabaté, P. (2004). Archean and Paleoproterozoic crust of the São Francisco craton, Bahia, Brazil: geodynamic features. Precambrian Research, 133(1-2), 1-27.

Barbosa, J., Nicollet, C., Leite, C., Kienast, J. R., Fuck, R. A., & Macedo, E. P. (2006). Hercynite-quartz-bearing granulites from Brejões Dome area, Jequié Block, Bahia, Brazil: Influence of charnockite intrusion on granulite facies metamorphism. Lithos, 92(3-4), 537-556.

Bégin, N. J., & Pattison, D. R. M. (1994). Metamorphic evolution of granulites in the Minto Block, northern Québec: extraction of peak P-T conditions taking account of late Fe-Mg exchange. Journal of Metamorphic Geology, 12(4), 411-428.

Benisek, A., Dachs, E., & Kroll, H. (2010). A ternary feldspar-mixing model based on calorimetric data: development and application. Contributions to Mineralogy and Petrology, 160(3), 327-337.

Benisek, A., Kroll, H., & Cemic, L. (2004). New developments in two-feldspar thermometry. American Mineralogist, 89(10), 1496-1504.

Brito Neves, B. B., & Silva Filho, A. F. (2019). Superterreno Pernambuco-Alagoas na Província Borborema: ensaio de regionalização tectônica. Geologia USP. Série Científica, 19(2), 3-28.

Brown, M. (2007). Metamorphism, plate tectonics, and the supercontinent cycle. Earth Science Frontiers, 14(1), 1-18.

Carvalho, B. B., Janasi, V. A., & Sawyer, E. W. (2017). Evidence for Paleoproterozoic anatexis and crustal reworking of Archean crust in the São Francisco Craton, Brazil: a dating and isotopic study of the Kinawa migmatite. Precambrian Research, 291, 98-118.

Cherniak, D. J., & Watson, E. B. (2001). Pb diffusion in zircon. Chemical Geology, 172(1-2), 5-24.

Clark, C., Taylor, R. J., Kylander-Clark, A. R., & Hacker, B. R. (2018). Prolonged (> 100 Ma) ultrahigh temperature metamorphism in the Napier Complex, East Antarctica: A petrochronological investigation of Earth's hottest crust. Journal of Metamorphic Geology, 36(9), 1117-1139.

Cruz, R. F. D., Pimentel, M. M., Accioly, A. C. D. A., & Rodrigues, J. B. (2014). Geological and isotopic characteristics of granites from the Western Pernambuco-Alagoas Domain: implications for the crustal evolution of the Neoproterozoic Borborema Province. Brazilian Journal of Geology, 44(4), 627-652.

de Capitani, C., & Petrakakis, K. (2010). The computation of equilibrium assemblage diagrams with Theriak/Domino software. American Mineralogist, 95(7), 1006-1016.

Diener, J. F. A., & Powell, R. (2010). Influence of ferric iron on the stability of mineral assemblages. Journal of Metamorphic Geology, 28(6), 599-613.

Droop, G. T. R. (1987). A general equation for estimating Fe3+ concentrations in ferromagnesian silicates and oxides from microprobe analyses, using stoichiometric criteria. Mineralogical Magazine, 51(361), 431-435.

Elkins, L. T., & Grove, T. L. (1990). Ternary feldspar experiments and thermodynamic models. American Mineralogist, 75(5-6), 544-559.

Engi, M., Lanari, P., & Kohn, M. J. (2017). Significant ages-An introduction to petrochronology. Reviews in Mineralogy and Geochemistry, 83(1), 1-12.

Esteves, M. C. B. (2018). Thermal history and fluid circulation in deformational structures associated with the Bambuí Group at the fold-and-thrust zone, western margin of the São Francisco Craton (Doctoral dissertation, Universidade de São Paulo).

Ferry, J. M., & Watson, E. B. (2007). New thermodynamic models and revised calibrations for the Ti-in-zircon and Zr-in-rutile thermometers. Contributions to Mineralogy and Petrology, 154(4), 429-437.

Fitzsimons, I. C. W., & Harley, S. L. (1994). The influence of retrograde cation exchange on granulite P-T estimates and a convergence technique for the recovery of peak metamorphic conditions. Journal of Petrology, 35(2), 543-576.

Fuhrman, M. L., & Lindsley, D. H. (1988). Ternary-feldspar modeling and thermometry. American Mineralogist, 73(3-4), 201-215.

Ganade, C. E., Weinberg, R. F., & Cordani, U. G. (2014). Extruding the Borborema Province (NE-Brazil): a two-stage Neoproterozoic collision process. Terra Nova, 26(2), 157-168.

Griffin, W. L. (2008). GLITTER: data reduction software for laser ablation ICP-MS. Laser Ablation ICP-MS in the Earth Sciences: Current practices and outstanding issues, 308-311.

Harley, S. L. (1984). The solubility of alumina in orthopyroxene coexisting with garnet in FeO-MgO-Al2O3-SiO2 and CaO-FeO-MgO-Al2O3-SiO2. Journal of Petrology, 25(3), 665-696.

Harley, S. L. (1998). On the occurrence and characterization of ultrahigh-temperature (UHT) crustal metamorphism. What drives metamorphism and metamorphic reactions? Geological Society of London, Spec. Pub., 138, 75-101.

Harley, S. L. (2008). Refining the P-T records of UHT crustal metamorphism. Journal of Metamorphic Geology, 26, 125-154.

Harley, S. L. (2016). A matter of time: the importance of the duration of UHT metamorphism. Journal of Mineralogical and Petrological Sciences, 111(2), 50-72.

Hensen, B. J. (1971). Theoretical phase relations involving cordierite and garnet in the system MgO-FeO-Al2O3-SiO2. Contributions to Mineralogy and Petrology, 33(3), 191-214.

Hokada, T. (2001). Feldspar thermometry in ultrahigh-temperature metamorphic rocks: Evidence of crustal metamorphism attaining~ 1100 C in the Archean Napier Complex, East Antarctica. American Mineralogist, 86(7-8), 932-938.

Holland, T. J. B., & Powell, R. (2011). An improved and extended internally consistent thermodynamic dataset for phases of petrological interest, involving a new equation of state for solids. Journal of Metamorphic Geology, 29(3), 333-383.

Holland, T., & Powell, R. (2003). Activity-composition relations for phases in petrological calculations; an asymmetric multicomponent formulation. Contributions to Mineralogy and Petrology, 145, 492-501.

Hoskin, P. W., & Schaltegger, U. (2003). The composition of zircon and igneous and metamorphic petrogenesis. Reviews in mineralogy and geochemistry, 53(1), 27-62.

Jackson, S. E., Pearson, N. J., Griffin, W. L., & Belousova, E. A. (2004). The application of laser ablation-inductively coupled plasma-mass spectrometry to in situ U-Pb zircon geochronology. Chemical Geology, 211(1-2), 47-69.

Kelly, N. M., & Harley, S. L. (2005). An integrated microtextural and chemical approach to zircon geochronology: refining the Archaean history of the Napier Complex, east Antarctica. Contributions to Mineralogy and Petrology, 149(1), 57-84.

Kelsey, D. E., & Hand, M. (2015). On ultrahigh temperature crustal metamorphism: phase equilibria, trace element thermometry, bulk composition, heat sources, timescales and tectonic settings. Geoscience Frontiers, 6(3), 311-356.

Kelsey, D. E., White, R. W., & Powell, R. (2005). Calculated phase equilibria in K2O-FeO-MgO-Al2O3-SiO2-H2O for silica-undersaturated sapphirine-bearing mineral assemblages. Journal of Metamorphic Geology, 23(4), 217-239.

Kroll, H., Evangelakakis, C., & Voll, G. (1993). Two-feldspar geothermometry: a review and revision for slowly cooled rocks. Contributions to Mineralogy and petrology, 114(4), 510-518.

Kylander-Clark, A. R., Hacker, B. R., & Cottle, J. M. (2013). Laser-ablation split-stream ICP petrochronology. Chemical Geology, 345, 99-112.

Ledru, P., Johan, V., Milési, J. P., & Tegyey, M. (1994). Markers of the last stages of the Palaeoproterozoic collision: evidence for a 2 Ga continent involving circum-South Atlantic provinces. Precambrian Research, 69(1-4), 169-191.

Leite, C., Barbosa, J. S. F., Goncalves, P., Nicollet, C., & Sabaté, P. (2009). Petrological evolution of silica-undersaturated sapphirine-bearing granulite in the Paleoproterozoic Salvador–Curaçá Belt, Bahia, Brazil. Gondwana Research, 15(1), 49-70.

McDonough, W. F., & Sun, S. S. (1995). The composition of the Earth. Chemical geology, 120(3-4), 223-253.

Mendes, V.A., Brito, M.F.L., Paiva, I.P., 2009. Programa Geologia do Brasil-PGB. Arapiraca. Folha SC.24-X-D. Estado de Alagoas, Pernambuco e Sergipe. In: Mapa Geológico. Escala: 1:250.000, Recife.

Miranda, D. A., Chaves, A. D. O., Dussin, I. A., & Porcher, C. C. (2020). Paleoproterozoic khondalites in Brazil: a case study of metamorphism and anatexis in khondalites from Itapecerica supracrustal succession of the southern São Francisco Craton. International Geology Review, 1-25.

Mori, P. E., Correia, C. T., Reeves, S., & Haukka, M. (1999). Development of a fused glass disc XRF facility and comparison with the pressed powder pellet technique at Instituto de Geociências, São Paulo University, Brazil. Revista Brasileira de Geociências, 29(3), 441-446.

Motta, R. G. D. (2018). Formação, transformação e evolução da crosta continental inferior: Investigando o Orógeno Brasília Meridional (Doctoral dissertation, Universidade de São Paulo).

Neves, S. P. (2015). Constraints from zircon geochronology on the tectonic evolution of the Borborema Province (NE Brazil): widespread intracontinental Neoproterozoic reworking of a Paleoproterozoic accretionary orogen. Journal of South American Earth Sciences, 58, 150-164.

Neves, S. P., Lages, G. A., Brasilino, R. G., & Miranda, A. W. (2015). Paleoproterozoic accretionary and collisional processes and the build-up of the Borborema Province (NE Brazil): Geochronological and geochemical evidence from the Central Domain. Journal of South American Earth Sciences, 58, 165-187.

Neves, S. P., da Silva, J. M. R., & Bruguier, O. (2016). The transition zone between the Pernambuco-Alagoas Domain and the Sergipano Belt (Borborema Province, NE Brazil): Geochronological constraints on the ages of deposition, tectonic setting and metamorphism of metasedimentary rocks. Journal of South American Earth Sciences, 72, 266-278.

Oliveira, E. P., McNaughton, N. J., & Armstrong, R. (2010). Mesoarchaean to Palaeoproterozoic growth of the northern segment of the Itabuna–Salvador–Curaçá

orogen, São Francisco craton, Brazil. Geological Society, London, Special Publications, 338(1), 263-286.

Oliveira, E. P., McNaughton, N. J., Windley, B. F., Carvalho, M. J., & Nascimento, R. S. (2015). Detrital zircon U–Pb geochronology and whole-rock Nd-isotope constraints on sediment provenance in the Neoproterozoic Sergipano orogen, Brazil: From early passive margins to late foreland basins. Tectonophysics, 662, 183-194.

Oliveira, E. P., Windley, B. F., & Araújo, M. N. (2010). The Neoproterozoic Sergipano orogenic belt, NE Brazil: a complete plate tectonic cycle in western Gondwana. Precambrian Research, 181(1-4), 64-84.

Pattison, D. R., Chacko, T., Farquhar, J., & McFarlane, C. R. (2003). Temperatures of granulite-facies metamorphism: constraints from experimental phase equilibria and thermobarometry corrected for retrograde exchange. Journal of Petrology, 44(5), 867-900.

Peucat, J. J., Barbosa, J. S. F., de Araújo Pinho, I. C., Paquette, J. L., Martin, H., Fanning, C. M., ... & Cruz, S. (2011). Geochronology of granulites from the south Itabuna-Salvador-Curaçá Block, São Francisco Craton (Brazil): Nd isotopes and U–Pb zircon ages. Journal of South American Earth Sciences, 31(4), 397-413.

Rocha, B. C. D. (2016). Idade, duração e condições PT do metamorfismo de temperatura ultra-alta, anatexia e cristalização de fundido na nappe Socorro-Guaxupé (Doctoral dissertation, Universidade de São Paulo).

Rubatto, D. (2002). Zircon trace element geochemistry: partitioning with garnet and the link between U–Pb ages and metamorphism. Chemical geology, 184(1-2), 123-138.

Schneider, C. A., Rasband, W. S., & Eliceiri, K. W. (2012). NIH Image to ImageJ: 25 years of image analysis. Nature Methods, 9(7), 671-675.

Silva, M. P. (2017). Modelagem termodinâmica de fusão parcial e metamorfismo em condições de fácies granulito: exemplo do Complexo Itatins, SP (Doctoral dissertation, Universidade de São Paulo).

Simões Neto, F. L., Julià, J., & Schimmel, M. (2019). Upper-mantle structure of the Borborema Province, NE Brazil, from P-wave tomography: implications for rheology and volcanism. Geophysical Journal International, 216(1), 231-250.

Siqueira, R., Hollanda, M. H. B. M., & Basei, M. A. S. (2014). A novel approach to (LA-ICP-MS acquired) U–Th–Pb data processing. In: IX South-American Symposium on Isotope Geology. Chile, 2014. Program and Abstracts, 306.

Tomkins, H. S., Powell, R., & Ellis, D. J. (2007). The pressure dependence of the zirconium-in-rutile thermometer. Journal of metamorphic Geology, 25(6), 703-713.

Vermeesch, P. (2018). IsoplotR: A free and open toolbox for geochronology. Geoscience Frontiers, 9(5), 1479-1493.

Wang, B., Tian, W., Wei, C., & Di, Y. (2019). Ultrahigh metamorphic temperatures over 1050° C recorded by Fe-Ti oxides and implications for Paleoproterozoic magma-induced crustal thermal perturbation in Jining area, North China Craton. Lithos, 348, 105180.

Watson, E. B., & Harrison, T. M. (2005). Zircon thermometer reveals minimum melting conditions on earliest Earth. Science, 308(5723), 841-844.

Watson, E. B., Wark, D. A., & Thomas, J. B. (2006). Crystallization thermometers for zircon and rutile. Contributions to Mineralogy and Petrology, 151(4), 413.

Wen, S., & Nekvasil, H. (1994). SOLVALC: An interactive graphics program package for calculating the ternary feldspar solvus and for two-feldspar geothermometry. Computers and Geosciences, 20(6), 1025-1040.

Wheller, C. J., & Powell, R. (2014). A new thermodynamic model for sapphirine: calculated phase equilibria in K2O-FeO-MgO-Al2O3-SiO2-H2O-TiO2-Fe2O3. Journal of Metamorphic Geology, 32(3), 287-299.

White, R. W., & Powell, R. (2002b). Melt loss and the preservation of granulite facies mineral assemblages. Journal of Metamorphic Geology, 20(7), 621-632.

White, R. W., Powell, R., & Johnson, T. E. (2014). The effect of Mn on mineral stability in metapelites revisited: New a–x relations for manganese-bearing minerals. Journal of Metamorphic Geology, 32(8), 809-828.

White, R. W., Powell, R., & Johnson, T. E. (2014a). The effect of Mn on mineral stability in metapelites revisited: New a–x relations for manganese-bearing minerals. Journal of Metamorphic Geology, 32(8), 809-828.

White, R., Powell, R. & Clarke, G.L. (2002a). The interpretation of reaction textures in Fe-rich metapelitic granulites of the Musgrave Block, central Australia: constraints from mineral equilibrium calculations in the system K2O-FeO-MgO-Al2O3-SiO2-H2O-TiO2-Fe2O3. Journal of Metamorphic Geology, 20, 41-55.

White, R.W., Powell, R., Holland, T.J.B., Johnson, T.E. & Green, E.C.R. (2014b). New mineral activity-composition relations for thermodynamic calculations in metapelitic systems. Journal of Metamorphic Geology, 32, 261-286.

Zack, T., Moraes, R., & Kronz, A. (2004). Temperature dependence of Zr in rutile: empirical calibration of a rutile thermometer. Contributions to Mineralogy and Petrology, 148(4), 471-488.

CHAPTER 2. ULTRAHIGH-TEMPERATURE PALEOPROTEROZOIC ROCKS IN THE NEOPROTEROZOIC BORBOREMA PROVINCE, IMPLICATIONS FOR SÃO FRANCISCO CRATON DISPERSION IN NE BRAZIL*

Lucas R. Tesser[1], Carlos E. Ganade[2], Roberto F. Weinberg[3], Miguel A. S. Basei[1], Renato Moraes[1], Laísa A. Batista[1]

[1]Department of Mineralogy and Geotectonics, São Paulo University, São Paulo, Brazil;

[2]Geological Survey of Brazil, Rio de Janeiro, Brazil;

[3]School of Earth, Atmosphere and Environment, Monash University, Clayton, Australia.

**Under review in the Journal of Metamorphic Geology.*

Abstract

This work reports on the first finding of sapphirine-bearing ultrahigh-temperature (UHT) metamorphic rocks within the Borborema Province, in NE Brazil. The investigated UHT diatexites outcrop in the Arapiraca Complex, a high-grade Paleoproterozoic block embedded within the Neoproterozoic metavolcano-sedimentary sequence of the Sergipano fold-and-thrust belt. A sapphirine-bearing diatexite sample preserves two distinct residual mineral associations as inclusions in cordierite poikiloblasts: a volumetrically dominant silica-saturated, garnet-sillimanite-orthopyroxene-quartz domain, and a restricted silica-undersaturated, sapphirine-magnetite-spinel-corundum domain. Phase equilibrium modeling for the whole-rock bulk composition constrained the reactions preserved in the silica-saturated domain, which coupled with re-integrated ternary feldspar thermometry, Al-in-orthopyroxene thermobarometry, indicates peak UHT metamorphism occurred at ~970 °C/8.5 kbar followed by a clockwise near isobaric cooling stage crossing the H2O-undersaturated solidus at ~900 °C/7.7 kbar. The T-MSiO2 and P-T phase equilibrium modeling reveals that the stabilization of first magnetite-spinel in the silica-undersaturated domain can be a product of domanial SiO2-depletion ascribed to inherited compositional banding and progressive melt loss episodes. The appearance of sapphirine as thin coronas around previously formed magnetite-spinel cores requires an increase in silica-activity during retrogression. This was driven by chemical interaction between the silica-undersaturated domain and trapped silica-rich leucosomes. U-Pb dating of zircons coupled with trace elements behavior records the timing of melt crystallization between c. 2.03 and 1.96 Ga, following the peak of UHT metamorphism and supporting a protracted, c. 70 My period of melt presence in crust. The UHT metamorphism in the Arapiraca Complex is related to a contemporaneous UHT event recorded within the São Francisco Craton, and more broadly coincides with high geothermal gradients at c. 2.0 Ga linked to the formation of the Columbia supercontinent. The integration of new petrological and geochronological data indicates that the Arapiraca Complex is a continental ribbon pulled away from the São Francisco-Congo paleocontinent possibly during the early Neoproterozoic intermittent rifting events and opening of Sergipano oceanic basin between c. 0.98-0.75 Ga. During the late Neoproterozoic at c. 0.63-0.57 Ga, the Arapiraca Complex continental ribbon thrusted back onto the northern margin of the São Francisco Craton as an inlier of the Sergipano fold-and-thrust belt.

Keywords: Borborema Province; Phase equilibrium modeling; São Francisco Craton; Ultrahigh-temperature metamorphism; zircon petrochronology.

2.1. Introduction

Assessment of the *P-T* evolution of middle to deep crustal levels rocks provides crucial inputs to unravel geodynamic processes in ancient and modern orogenic belts (Harley, 1989; Brown & Johnson, 2018). The reconstruction of accurate *P-T* paths coupled with timing (t) of ultrahigh-temperature (UHT) metamorphism is particularly important due to gaps in the understanding of heat sources, duration of metamorphism, preservation of diagnostic mineral phases, and tectonic setting of these metamorphic terranes (Harley & Kelly, 2007; Kelsey & Hand, 2015). Constraining the metamorphic *P-T-t* paths of UHT terranes are also important in geological reconstructions of ancient and polydeformed orogens (*e.g.* Baba, 2002; Tadokoro, Tsunogae, & Santosh, 2008; Dasgputa & Sengupta, 2003; Kelsey et al., 2017). This reconstruction depends on the potential preservation of diagnostic UHT mineral assemblages, which is acknowledged as high in dry and residual Mg-Al-rich rocks, stablishing one of the most reliable tools for the investigation of metamorphic *P-T* paths (Kelsey & Hand, 2015). When these Mg-Al-rich rocks melt under extreme thermal conditions, they produce residual high-temperature minerals, such as sapphirine, aluminous orthopyroxene, garnet, sillimanite, spinel, cordierite, and corundum during metamorphic peak or retrogression (*e.g.* Moraes, Brown, Fuck, Camargo, & Lima, 2002; Kelsey & Hand, 2015). Notably, sapphirine-bearing assemblages are highlighted as a common indicator of UHT metamorphic conditions (Harley, 2008; Kelsey, 2008; Kelsey & Hand, 2015).

There are several occurrences of sapphirine-bearing UHT terranes in South America (see Kelsey & Hand, 2015 for a compilation). Some of them are exposed in the central portion of the São Francisco Craton in NE Brazil (Leite, Barbosa, Goncalves, Nicollet, & Sabaté, 2009; Barbosa et al., 2006; Barbosa et al., 2017; Ackermand, Herd, Reinhardt, & Windley, 1987; Rodrigues, Oliveira, & Moraes, 2020).

The UHT metamorphism in this craton is related to the 2.1-2.0 Ga orogeny which assembled the São Francisco-Congo paleocontinent as part of the Columbia supercontinent formation (Barbosa & Sabaté, 2002; Leite et al., 2009). The São Francisco Craton is now bounded to the north by a large Neoproterozoic continental collision zone extending from northeast Brazil to northwest Africa (Oliveira et al., 2006; Ganade de Araujo, Weinberg, & Cordani, 2014; Caxito et al., 2020). The Brazilian part of this orogenic area is the Borborema Province, which consists of a mosaic of Paleoproterozoic blocks and minor Archean nuclei, partially covered by Neoproterozoic metasedimentary belts, deformed by shear zones and intruded by several syn- to post-tectonic granitoids (Figure 1a-b; Ganade de Araujo et al., 2014; Caxito et al., 2020). It has been noted that the Archean and Paleoproterozoic rocks in the Borborema Province has isotopic (U-Pb ages and Nd isotopic signature) and geophysical similarity to the adjacent São Francisco Craton (e.g. Ganade et al., 2021; Neves, 2020; Cruz, Pimentel, Accioly, & Rodrigues, 2014; Simões Neto, Julià, & Schimmel, 2019;). The present study characterizes sapphirine-bearing UHT diatexites found in the Arapiraca Complex, a Paleoproterozoic inlier within the passive-margin metavolcano sedimentary of the Neoproterozoic Borborema Province. This contribution provides a metamorphic petrochronological backbone to correlations between the Archean-Paleoproterozoic blocks in the Neoproterozoic Borborema Province and the São Francisco Craton.

Results of P-T pseudosection calculation, thermobarometry based on Al-in-orthopyroxene and ternary feldspar are then presented and used to address the metamorphic P-T evolution of a sapphirine-bearing diatexite sample. Additionally, a T-M_{SiO2} models were used to discuss the role of bulk-silica in the formation of sapphirine in silica-undersaturated microdomains. The timing and duration of UHT metamorphism

were assessed by combining zircon U-Pb dating, trace element chemistry, and Ti-in-zircon thermometry from three diatexite samples. The UHT rocks described are interpreted as remnants of the UHT event related to the amalgamation of the Columbia supercontinent and the results provide a robust petrochronological basis for correlating the Archean-Paleoproterozoic blocks in the Neoproterozoic Borborema Province to the São Francisco Craton.

2.2. Geological background

The northern São Francisco Craton comprises three Archean blocks (Gavião, Serrinha and, Jequié) separated by Paleoproterozoic rocks of the Eastern Bahia Orogen, also known as the Itabuna-Salvador-Curaça Orogen (Figure 1a-b; Barbosa & Sabaté, 2004). The interaction between these blocks at 2.1-2.0 Ga in addition to the Gabonese Block of the Congo Craton resulted in a large Paleoproterozoic orogenic system associated with the formation of the Columbia supercontinent (Ledru, Johan, Milési, & Tegyey, 1994; Barbosa & Sabaté, 2004; Oliveira, Windley, McNaughton, Pimentel, & Fletcher, 2004.; Rogers & Santosh, 2009). This ancient orogen, well-preserved in NE Brazil and Central-West Africa, comprises a diversity of high-grade metamorphic rocks, including high-temperature (HT) eclogite facies rocks (e.g. Loose & Schenk, 2018; Weber, Gauthier-Lafaye, Whitechurch, Ulrich, & El Albani, 2016), sapphirine- spinel-(*e.g.* Leite et al., 2009;, 2017; Rodrigues et al., 2020) and spinel-quartz- (Barbosa et al., 2006) bearing UHT granulite facies rocks. In NE Brazil, the timing of continental collision and related UHT metamorphism was constrained to between 2.08 and 2.05 Ga (Leite et al., 2009; Barbosa et al., 2006, 2017). After cratonization at c. 1.9-1.8 Ga, the São Francisco-Congo remained intact and unaffected by large-scale deformation events and major magmatic activity, leading to intracratonic basin development between 1.75 and 1.40 Ga (*e.g.* Pedrosa-Soares &

Alkmim, 2011; Guadagnin et al., 2015). During the Early Neoproterozoic, the craton starts to break-up and becomes the hinterland to passive margin basins and Late Neoproterozoic orogens, such as the Araçuaí and Ribeira Belts in SE Brazil (Degler et al., 2018), the Central African Orogenic Belt in NE Cameroon (Tchakounté et al., 2017), and the Borborema Province in NE Brazil (Teixeira, Misi, Silva, & Brito, 2019; Oliveira et al., 2010).

The northern margin of the São Francisco Craton is overthrust by the south-southwest verging Sergipano fold-and-thrust belt (Figure 1c). The fold belt is bounded to the north by the Paleoproterozoic Pernambuco-Alagoas Massif, interpreted as the hinterland that collided against the craton deforming and inverting the Sergipano oceanic basin formed during early Neoproterozoic extension (e.g. Oliveira et al., 2010). This early extensional event related to the opening of the Sergipano Basin is evidenced by the intrusion of c. 0.98-0.95 Ga granitoids associated with bi-modal metavolcanic rocks (Figure 1c; Davidson & Santos, 1989; Oliveira et al., 2010). These rocks are part of the contemporaneous Cariris Velho event (1.0-0.92 Ga), first recognized in the Central Borborema Province (Guimarães et al., 2012; Davidson & Santos, 1989; Oliveira et al., 2010). In the Sergipano fold-and-thrust belt, the Cariris Velhos rocks comprise a ~200 km E-W trend domain composed of I- to A-type granitoids associated with amphibolites, meta-andesites, meta-dacites, meta-rhyolites, and serpentinites interleaved with immature metasedimentary rocks (Figure 1c; Oliveira et al., 2010). The tectonic significance of the Cariris Velhos event is still debated with interpretations varying from collisional (Oliveira et al., 2010) to an extensional, rift-related event (Guimarães et al., 2015). However, the dominance of bi-modal volcanic rocks, A-type granitoids, and the lack of documented metamorphism related to this event favor an extensional origin (Neves, 2003; Guimarães et al., 2015).

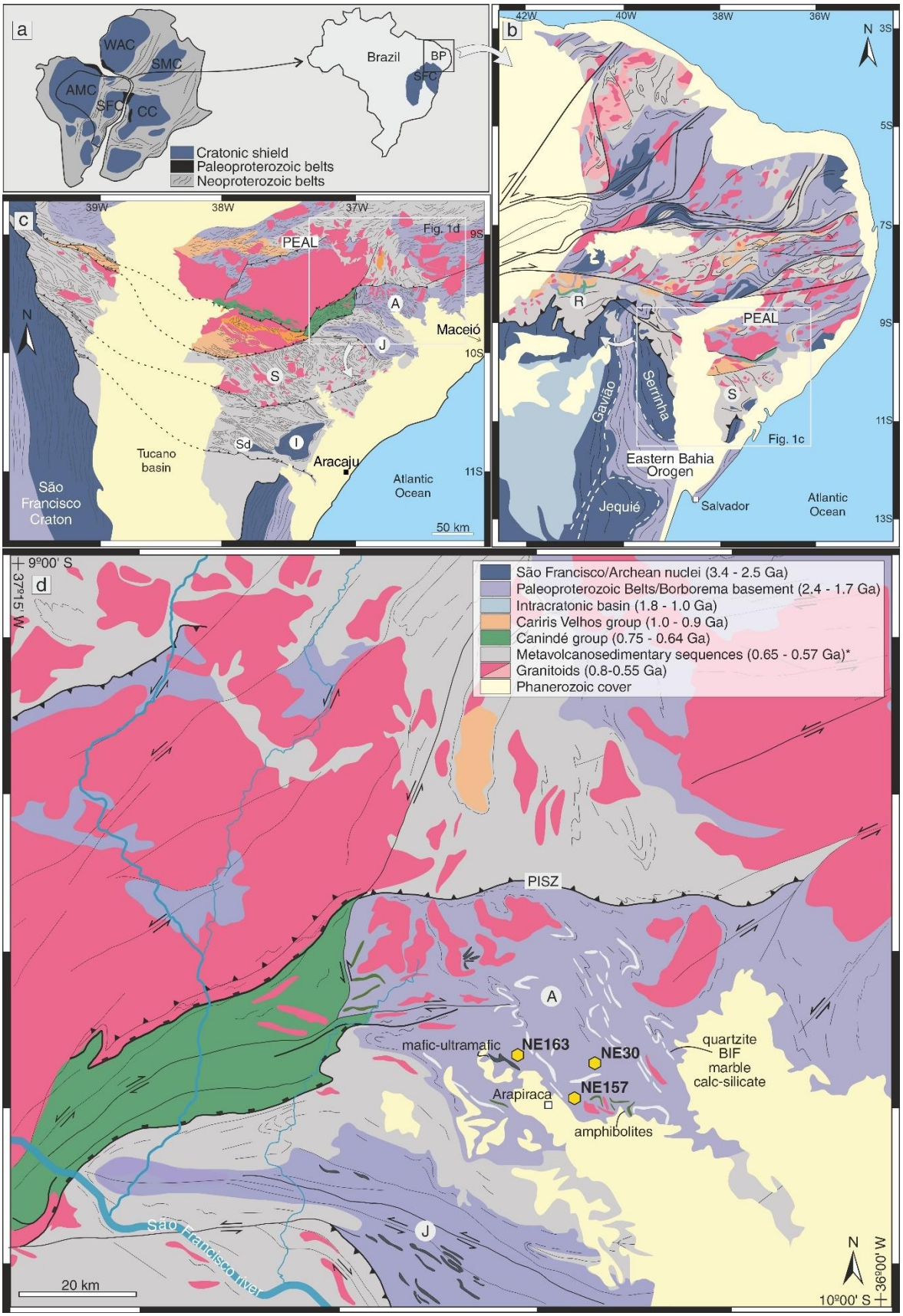

Figure 1. Tectonic and geological maps of the study area. (a) Schematic paleogeographic fit of South America and West Africa depicting cratons, Paleoproterozoic and Neoproterozoic belts (after Zhao et al., 2004); (b) Geological map of the Borborema Province and main tectonic units from the northern part of the

São Francisco Craton; (c) Simplified tectonic map of the Sergipano fold-and-thrust belt (modified from Oliveira et al., 2010); (d) Geological map of the Arapiraca complex region (modified from Mendes et al., 2009). Yellow polygons represent the location of the investigated samples; abbreviations: SFC = São Francisco Craton; CC = Congo Craton; AMC = Amazonian Craton; WAC = West Africa Craton; SMC = Sahara Metacraton; R = Riacho do Pontal fold belt; S = Sergipano fold belt; PEAL = Pernambuco-Alagoas massif; A = Arapiraca Complex; J = Jiraú do Ponciano; I = Itabaiana; Sd = Simão Dias; PISZ = Palmeira dos Índios shear zone. *metamorphic ages.

The tectonic extension within the Sergipano Basin is also recorded at c. 0.71-0.63 Ga by mafic-ultramafic suites, A-type granitoids, and volcano-sedimentary rocks forming the Canindé group (Figure 1b-c; Davidson & Santos, 1989). The major and trace element signatures of the mafic rocks are similar to those of continental basalts and are interpreted to record an extensional intraplate setting (Oliveira et al., 2010; Oliveira & Tarney, 1990). Between 0.60-0.57 Ga, the continental collision of the São Francisco-Congo Craton against the Paleoproterozoic Pernambuco-Alagoas Massif and other continental blocks to the north inverted the the oceanic Sergipano Basin and gave rise to the Sergipano fold-and-thrust belt (Oliveira et al., 2010). Rocks were metamorphosed under greenschist to amphibolite facies conditions (Davison & Santos, 1989; Oliveira et al., 2010).

Within the supracrustal sequence of the Sergipano fold-and-thrust belt, four Archean-Paleoproterozoic blocks are exposed, from south to north these are: the Itabaiana, Simão Dias, Jirau do Ponciano, and Arapiraca complexes (Figure 1c; Davison and Santos, 1989). The first two, close to the São Francisco Craton, are interpreted as uplifts of the cratonic margin (e.g. Rosa, Conceição, Marinho, Pereira, & Conceição, 2020). The Jirau do Ponciano dome, ~200 km north of the São Francisco Craton margin is dominated by high-grade orthogneisses interleaved with amphibolite facies metavolcanic rocks and amphibolites (Mendes, Brito, & Paiva, 2009). Based on geochemistry and zircon dating of metavolcanic rocks, Lima et al (2019) proposed that

the Jirau do Ponciano dome comprises a crustal TTG association related to a 2.1-2.0 Ga magmatic arc.

The Arapiraca Complex, the focus of this work, is to the north of the Jirau do Ponciano dome (Mendes et al., 2009; Figure 1c-d). It comprises metapelitic migmatites and orthogneisses, with local lenses of metamafic rocks, marbles, banded iron formation, quartzites, and igneous mafic-ultramafic layered rocks (Figure 1d; Mendes et al., 2009). It is partially covered by the Neoproterozoic passive-margin metasedimentary sequences of the Sergipano Basin (Figure 1d). In the west, it is separated from the Neoproterozoic supracrustal rocks of the Canindé group by a sinistral N-S strike-slip shear zone (Mendes et al., 2009). Due to scarce geochronological and structural data, the origin of the Arapiraca Complex remains uncertain, leading to different interpretations, such as it being a continuation of the Neoproterozoic sequence (0.71-0.60 Ga; Oliveira et al., 2010; Neves, da Silva, & Bruguier, 2016) or a Paleoproterozoic-Archean basement (Mendes et al., 2009).

2.3. Materials and methods

2.3.1 Sample selection

In order to unravel the nature and timing of metamorphism in the Arapiraca Complex, this study focused on three samples from diatexites outcropping in a region at north of the Arapiraca city, Alagoas, Brazil (Figure 1d). The sapphirine-bearing diatexite (sample NE30) was selected for detailed mineral chemistry and *P-T* modeling, whereas the two other samples (NE163 and NE157), lacking sapphirine and orthopyroxene, were included for zircon trace element and dating. Here, the term residue is used to designate the part of the diatexite neosome constituted by minerals that were in excess in melt reactions, plus retained peritectic phases, with little melt fraction preserved. The term leucosome is applied to the neosome portion segregated from melting sites during anatexis, and resister corresponds to the part of the migmatite

that did not melt (*e.g.* Sawyer, 2008). The mineral and end-members abbreviations used in figures and tables are from Holland and Powell (2011) plus sapphirine (sa) and leucosome (L).

2.3.2 Mineral chemistry

The quantitative mineral chemistry was performed using the wavelength-dispersive spectrometry (WDS) with a JEOL JXA-FE-8530 Electron Microprobe in the NAP-Geoanalítica facilities from the Institute of Geosciences at the University of São Paulo (IGc-USP), Brazil. The operating conditions were 15 kV of acceleration voltage, 20 nA of probe current, with a focused beam varying between 5 and 10 µm. Counting times were 20s on peaks, and 10s on each background, and following synthetic and natural standard reference materials: garnet (SiO2, Al2O3), olivine (MgO, FeO, Mn), wollastonite (CaO), albite (Na2O), orthoclase (K2O), cromite (Cr2O3), strontianite (SrO), and rutile (TiO2). Oxide mass fractions were calculated using the CITZAF routine. For sapphirine, orthopyroxene, garnet, and spinel, the amount of ferric iron content was calculated assuming a perfect mineral stoichiometry, using charge balance (Droop, 1987). No ferric iron calculation was performed for cordierite and biotite. The representative mineral chemistry analysis is provided in Table S1.

2.3.3 Thermobarometry

For sample NE30, we use four combinations of representative compositions of the garnet rim, Al-rich orthopyroxene, and plagioclase from the matrix to calculate the *P-T* conditions using the Al-solubility in orthopyroxene thermobarometry, corrected for late Fe-Mg resetting though the *RCLC* program developed by Pattison, Chacko, Farquhar, and McFarlane (2003). The detailed *P-T* parameters and input compositions are provided in Table S2. The average *P-T* results were reported considering the standard average error equal to $s/\sqrt{n}$ (where, s = standard deviation; n = number of observations).

Re-integrated perthite compositions were used to calculate the *solvus* feldspar temperature using the method of Kroll, Evangelakakis, and Voll (1993) and feldspar activity models of Benisek, Dachs, and Kroll (2010) using the pressure reference of 8.0 kbar. The areal proportion of host and lamellae was calculated using backscattered electron images (BSE) edited with the ImageJ software (Schneider, Rasband, & Eliceiri, 2012). The weight percentage of re-integrated feldspar was obtained correlating proportional volume and densities of plagioclase (2.67 g/cm^3) and alkali feldspar (2.57 g/cm^3) (Hokada, 2001). The re-integrated ternary feldspar compositions were plotted in the Ab-An-Or diagram using the SolvCalc software (Wen & Nekvasil, 1994), and the isotherms were calculated considering the Margules parameters of Benisek et al. (2010), Elkins & Grove (1990), and Fuhrman & Lindsley (1988). The re-integrated compositions and thermometry results are provided in Table S3.

Ti-in-zircon thermometry was applied to all three investigated samples. From each sample, 25 to 30 zircon grains were selected to quantify the content of titanium via LA-ICP-MS (detailed in section 3.5). The Ti-in-zircon temperatures were calculated using the calibration of Ferry & Watson (2007) and different aTiO2 (titania activity) for each sample based on occurrence and/or absence of Ti-bearing phases.

2.3.4 Phase equilibria modeling

The phase equilibria modeling for the sample NE30 was performed using the THERIAK-DOMINO program package (version 11.02.2015; de Capitani & Petrakakis, 2010) modeled in the MnO-NaO-CaO-K_2O-FeO-MgO-Al_2O_3-SiO_2-H_2O-TiO_2-Fe_2O_3 (MnNCKFMASHTO) chemical system considering the internally consistent thermodynamic dataset of Holland & Powell (2011) with activity models of Holland & Powell (2003) for feldspars, White, Powell, and Johnson (2014a) and White, Powell, Holland, Johnson, and Green (2014b) for garnet, orthopyroxene, cordierite, biotite,

ilmenite-hematite and melt, White, Powell, and Clarke (2002a) for spinel, and Wheller & Powell (2014) for sapphirine. The ilmenite-hematite is a complete solid solution at >740 ^{o}C and was referred to as ilmenite (ilm). The spinel-hercynite-ülvospinel solid solution was referred to as spinel (sp) and magnetite as (mt). Corundum, quartz, Al_2SiO_5 polymorphs, rutile, and H_2O were considered as pure phases. The bulk rock major element composition was determined through X-ray fluorescence spectroscopy (XRF) of a ~3kg residue-rich hand sample collected from the same piece from which thin sections were cut. The glass discs were analyzed in a PANalytical AXIOS MAX spectrometer at the GeoAnalitica facility at IGc-USP. The samples were prepared following the laboratory methodologies described in Mori, Correia, Reeves, and Haukka (1999).

In order to evaluate the effects of the oxidation state in the metamorphic assemblages, a *T*-M_O pseudosection (800-1050 ^{o}C at 7.9 kbar) was calculated varying the composition from reduced to oxidized conditions (O_2 = 0.002-4.65 mol.%) considering the amount of H_2O equal to the measured LOI content. The recalculated iron content is FeO* = FeO+2xO, and P_2O_5 was removed from the calculations. The bulk-rock H_2O content was estimated with a *T*-M_{H2O} pseudosection (800-1050 ^{o}C at 7.9 kbar) varying the M_{H2O} value from dry to hydrated composition (H_2O = 0.0-2.56 mol.%). The maximum H_2O value that allows stabilizing the inferred equilibrium assemblage was set as close as possible to the *solidus* curve (*e.g.* White & Powell, 2002b). The pseudosection was calculated in a *P*-*T* window of 6.0-9.0 kbar and 850-1050 ^{o}C considering the adjusted ferric iron and water contents. The diagram was contoured with *y*(opx) (Al^{M1} = Al-[2-Si]) and *X*An (molar (Ca/[Ca+Na+K]) in plagioclase) and selected mineral modes (%volume) isopleths. The appropriated bulk-silica for the sapphirine-bearing domain was constrained using a *T*-M_{SiO2} model varying the SiO_2

content along the x-axis from that in the whole-rock composition in the right-hand side (50.57 wt% SiO_2) to a silica-depleted composition in the left-hand side (41.67 wt% SiO_2). The recalculated composition used for *P-T* phase equilibria modeling is shown in Table 1. *T-*M_O and *T-*M_{H2O} models are provided in Figure S1.

Table 1. Whole-rock major element chemistry and adjusted compositions used in the phase equilibrium modeling for sample NE30.

	Whole-rock (wt%)[1]	Input compositions (%mol)			
obs	-	-	B0	B1	SiO_2-undersaturated
SiO_2	50.57	43.74	38.02	43.74	39.05
TiO_2	1.09	0.71	0.88	0.71	0.85
Al_2O_3	22.78	23.22	28.94	23.22	27.91
Fe_2O_3	13.36	-	-	-	-
FeO*	-	12.85	12.30	12.85	12.40
MnO	0.15	0.11	0.14	0.11	0.13
MgO	3.94	5.30	6.35	5.30	6.17
CaO	1.44	1.34	1.66	1.34	1.61
Na_2O	2.23	3.74	4.66	3.74	4.49
K_2O	3.49	3.85	4.80	3.85	4.62
LOI	0.96	-	-	-	-
H_2O	-	0.47	0.59	0.47	0.57
O	-	4.67	1.65	4.67	2.19
Figure	-	7a		8a	8b

[1]normalized to 100%; O is oxygen.

2.3.5 LA-ICP-MS U-Pb zircon dating and trace element composition

The samples for zircon geochronology/geochemistry were prepared in the Sample Preparation Facility of the Geochronological Research Center (CPGeo, IGc-USP, Brazil). The zircon grains were extracted via sample comminution using a jaw crusher and an agate disk mill, followed by density and magnetic separation using a Wilfley table, Frantz separator (0.5A and 1.0A), and dense liquids (bromoform and methylene iodide). The zircon grains were then hand-picked under a microscope, mounted on epoxy resin, and finally polished to expose the center of the crystals. The

internal structures of selected crystals were identified through cathodoluminescence images on a Quanta 250 FEG scanning electron microscope coupled with a Centaurus Mono CL3+ cathodoluminescence spectroscope at the CPGeo. The operation conditions were 15 kV of acceleration voltage, 70 µA of beam current, and 20 mm of focal distance. The U-Pb-Th isotopic data were collected on a NEPTUNE- Thermo Scientific MC-LA-ICP-MS system coupled with ablation cell (Teledyne) model Excimer 193 (nm) with spot diameter, frequency, and laser fluency of 20 µm at 6 Hz and 6 mJ, respectively. Elements measured were ^{206}Pb, ^{207}Pb, ^{232}Th, and ^{238}U. The reference material GJ-1 (608.5 ± 0.4 Ma - TIMS; Jackson, Pearson, Griffin, & Belousova, 2004) was used for the correction of mass bias, instrument drift, and elemental fractionation (obtained concordia age = 605.2 ± 1.0 Ma). The routine comprises one analysis of the zircon reference material, one blank reading, and 10 unknown zircon analyses. The total acquisition time of each analysis was 60 s: 15 s of background measurement, 40 s of integration time, and 5 s for the washout period. The isotopic results were reduced and corrected with an in-house software developed by Siqueira, Hollanda, & Basei (2014), using an “R” statistical package based on Python programming language. Finally, the geochronological data was plotted in diagrams using the IsoplotR software (Vermeesch, 2018). Only U-Pb zircon analyses with less than ± 2% of discordance were used for age calculation. Individual uncertainties are presented at the 2σ level and the confidence level for the weighted averages is 95 %.

Trace element analyses of zircon were performed on an iCAP Q – Thermo Scientific LA-ICP-MS coupled with ablation cell (213 A/F-New Wave), housed at the GeoAnalítica facilities. Spots were placed near or comprising one-third of previously dated spots and in the same CL-domain. The total analysis time was 60 s, with the first 25 s of ablation (background) excluded from integration. Conditions for laser fluency,

frequency, and spot size were, respectively, 1.13 J/cm^2, 20 Hz, and 30 μm. Synthetic glasses (NIST 610 and ZR-91500) were used for external calibration, analyzed twice for every 10 unknowns, and reference values were taken from Pearce et al. (1997). Each analysis measured masses of ^{7}Li, ^{24}Mg, ^{27}Al, ^{29}Si, ^{31}P, ^{42}Ca, ^{44}Ca, ^{45}Sc, ^{49}Ti, ^{55}Mn, ^{56}Fe, ^{59}Co, ^{85}Rb, ^{88}Sr, ^{89}Y, ^{91}Zr, ^{93}Nb, ^{95}Mo, ^{118}Sn, ^{121}Sb, ^{137}Ba, ^{139}La, ^{140}Ce, ^{141}Pr, ^{146}Nd, ^{147}Sm, ^{151}Eu, ^{153}Eu, ^{157}Gd, ^{159}Tb, ^{163}Dy, ^{165}Ho, ^{166}Er, ^{169}Tm, ^{172}Yb, ^{175}Lu, ^{179}Hf, ^{181}Ta, ^{206}Pb, ^{207}Pb, ^{208}Pb, ^{232}Th, and ^{238}U. The time-resolved data were processed following each session using the Glitter program (Griffin, 2008). Internal standard was stoichiometric Zr content for zircon. In the REE plots, the analyzed data were normalized by the chondrite values of McDonough & Sun, 1995. The complete analytical results of U-Pb geochronology and trace-element geochemistry are available in Table S4.

2.4. Results

2.4.1 Field relationships and petrography

The investigated rocks of the Arapiraca Complex (Figure 1d) are dominated by cordierite-garnet-sillimanite diatexites. The main foliation strikes NNW-SSE and has a dominant flat dip to ENE varying between 05 and 17˚, with associated stretching lineation plunging SE. The flat-lying foliation expresses the metamorphic banding defined by the intercalation of residue and leucosome, as defined in section 2.3.1. The three samples studied have different melt fractions and distribution of leucosome (Table 2).

2.4.1.1 Sapphirine-bearing diatexite (sample NE30)

This sample is a residual garnet-cordierite diatexite and due to the occurrence of sapphirine, it will be referred to as sapphirine-bearing diatexite. In outcrop scale, the migmatite has a flat-lying banding defined by the alternation of leucocratic and melanocratic layers up to 30 cm in thickness (Figure 2a). The leucocratic layer defines

the leucosome, comprising 30 to 40% of the rock volume. It is composed of quartz, feldspar, and biotite, and low amounts of garnet (<5%), oxides (<5%), and cordierite (<1%) (Figure 2b). The melanocratic layer, further designated as residue, represents 60 to 70 % of the rock volume. This residual layer is formed by discontinuous lenses of coarse-grained cordierite aggregates (60-70%) with lengths up to 10 cm, enveloped by a leucocratic matrix (Figure 2a-b).

Table 2. Coordinates, mineralogy and type of approach adopted for each sample. Minerals are presented according to their abundance in the thin section. Leucosome proportion (%vol) estimated in the field and thin section scale. Zircon as inclusion in the residue (R) and leucosome (L).

Sample	Coordinates	Residue	Leucosome	Zircon	Approach
NE30	9°41.92'S/36°35.02'W	cd-g-sill-ksp-pl-mt-sp-opx-q-sa-bi-crn-ru-ilm-hem-zrc-mnz±apt	*30-40 (%vol)* ksp-pl-q-bi-sp-g-cd-zrc-apt±mnz	(R) cd; (L) pl-q-ksp	petrology + zircon (U-Pb; REE+Ti)
NE163	9°40.28'S/36°44.38'W	g-cd-bi-sill-q-mt-ksp-ilm-ru-zrc-mnz	*40-55 (%vol)* pl-q-bi-kfs-g-zrc-apt±mnz	(R) cd-g-bi; (L) q-pl-ksp	zircon (U-Pb; REE+Ti)
NE157	9°43.51'S/36°36.54'W	sill-g-cd-bi-q-ksp-pl-sp-ru-ilm-zrc-apt±mnz	*50-70 (%vol)* pl-q-g-kfs-bi-zrc-apt±mnz	(R) cd-g; (L) pl-q-ksp	zircon (U-Pb; REE+Ti)

At thin section scale, the residue is dominated by aggregates of cordierite poikiloblasts interleaved with a leucocratic matrix composed of K-feldspar (70%), plagioclase (20%), quartz (10%), and minor biotite (~1%) (Figure 2b). Similar to alternating silica-saturated and silica-undersaturated domains described as inclusions domains in poikiloblastic UHT garnets (*e.g.* Dharmapriya et al., 2017), the cordierite aggregates have two distinct mineral assemblages spatially organized as inclusion domains: a garnet-sillimanite-orthopyroxene-quartz domain; and a sapphirine-magnetite-spinel-corundum domain (Figure 3a-b). The first domain is volumetrically dominant, making up ~90% of the area within the cordierite. It includes garnet (up to

0.2 mm in diameter) and sillimanite (up to 0.5 mm in length) surrounded and interleaved with fine-grained (30-80 μm in diameter) orthopyroxene, plus sillimanite, quartz, magnetite, plagioclase, and biotite grains (Figure 3c). Thin prismatic sillimanite grains, quartz, and minor biotite are inclusions in garnet, and magnetite occurs as inclusion in sillimanite. The orthopyroxene grains around the garnet form aggregates of up to 400 μm thick in contact with quartz, magnetite, sillimanite, and plagioclase (Figure 3d). Orthopyroxene + sillimanite symplectites occur locally in garnet-poor domains forming continuous millimetric patches associated with magnetite and minor quartz (Figure 3e).

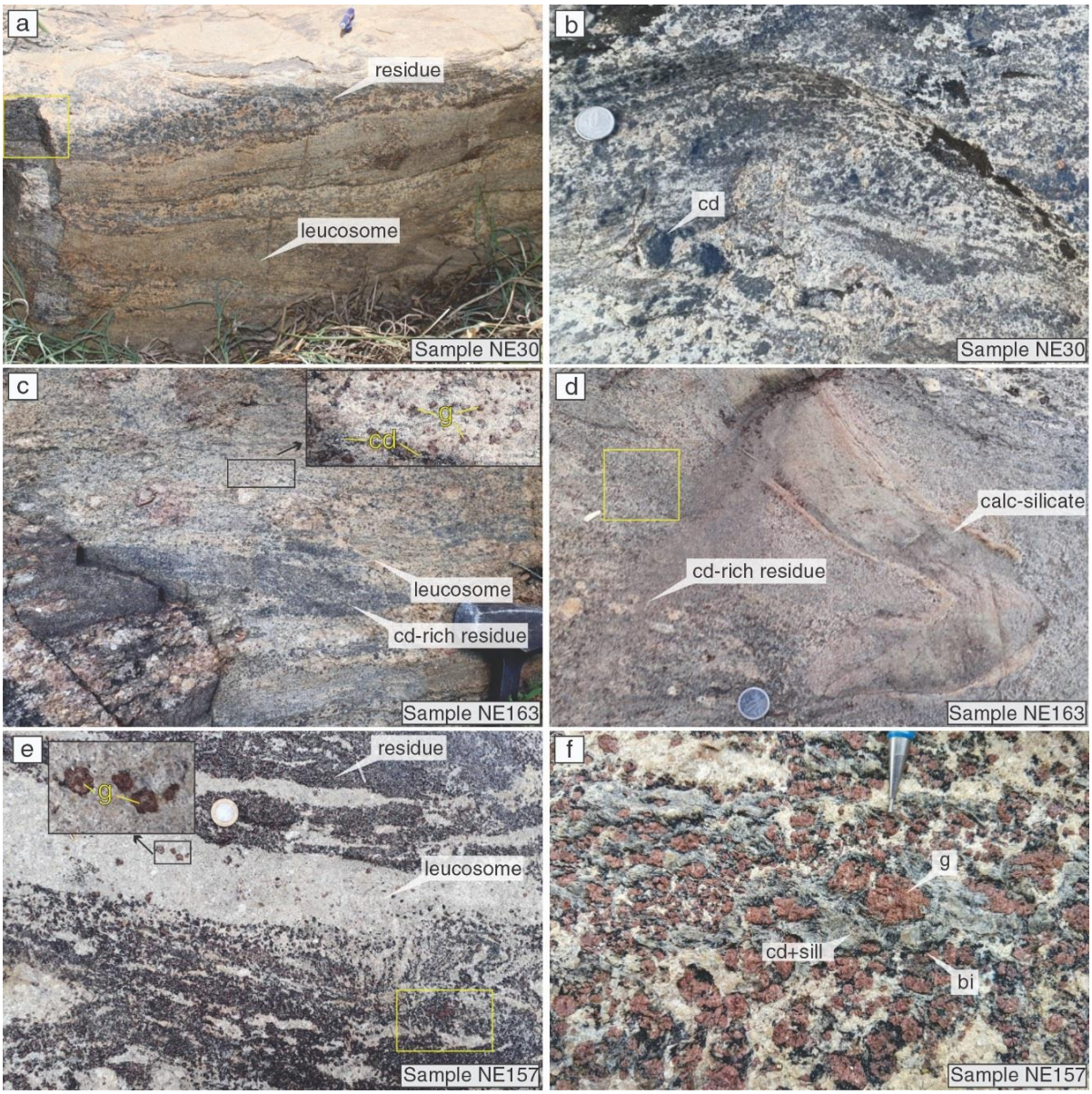

Figure 2. Field relationships of studied samples from the Arapiraca Complex. (a) Sapphirine-bearing diatexite (NE30) exhibiting a flat-lying foliation highlighted by the contrast between the residue and leucosome, note pen above for scale; (b) Interleaving between cordierite-rich lenses residue and leucosome (NE30); (c) Banded diatexite with diffuse transition between cordierite-rich residue and garnet-bearing leucosome (NE163); (d) Mesocratic aspect of the garnet-biotite-cordierite diatexite outcrop with a folded calc-silicate resister surrounded by leucosome accumulation; (e) Segregated garnet-bearing leucosome dikes and patchy distribution of garnet-cordierite-rich residue (NE157); (f) Residual garnet-sillimanite porphyroblasts surrounded by cordierite with biotite selvedge in the transition to leucosome (NE157). Yellow square corresponds to the sampled area for petrographic and petrochronological investigation.

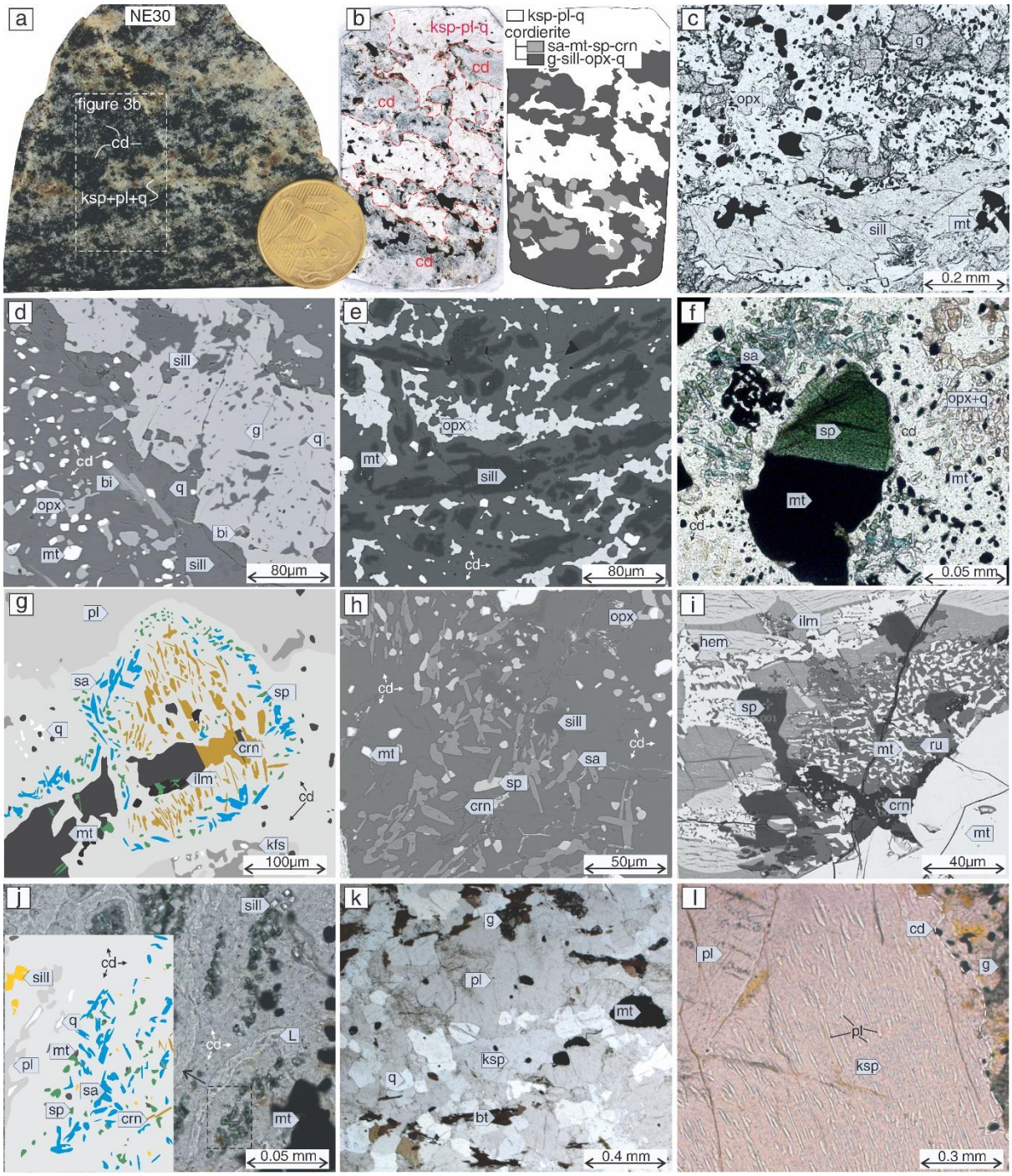

Figure 3. Photomicrographs (parallel-polarized light) and back-scattered electron (BSE) images of sample NE30. (a) A slab of the residual layer in figure 2a comprising a melanocratic portion dominated by cordierite poikiloblasts and a leucocratic portion dominated by K-feldspar, plagioclase, quartz, and biotite; our focus is the mineral assemblage preserved as inclusions in the cordierite grains; (b) Thin section scan and sketch showing the relationship between the cordierite (grey) and the K-feldspar, plagioclase, and quartz (white) in the residue. The cordierite is limited by the dashed red line. The sketch outlines the relationship between the two distinct mineral assemblages recognized as inclusion in the cordierite poikiloblasts: a garnet-sillimanite-orthopyroxene-quartz domain (dark grey) and a sapphirine-magnetite-spinel-corundum domain (light grey); (c-e) Garnet-sillimanite-orthopyroxene-quartz domain included in cordierite poikiloblasts; in (d) Orthopyroxene-quartz-

magnetite±sillimanite±biotite around garnet and all included in cordierite; sillimanite and quartz also occur as inclusion in garnet; (e) Orthopyroxene+sillimanite symplectite included in cordierite poikiloblast; (f-i) Sapphirine-magnetite-spinel-corundum domain within cordierite: (f) Sapphirine-bearing corona around magnetite-spinel grain, note that cordierite layer separates the sapphirine from the orthopyroxene+quartz mineral association; (g) sapphirine and corundum around magnetite-spinel. Quartz grains belonging to the garnet-sillimanite-orthopyroxene-quartz domain is separated from the sapphirine by cordierite (sketch based on BSE image); (h) Sapphirine, sillimanite, spinel, and corundum corona around a spinel-magnetite porphyroblast (left, outside the field of view). All minerals included in cordierite (BSE image); (i) Rutile-magnetite-corundum-spinel symplectite enclosed within a magnetite porphyroblast. Hematite with oriented ilmenite lamellae also occurs inclusion inside the magnetite (BSE image); (j) Quartz-feldspathic films indicated by label [L] (light grey at parallel-polarized light), within sapphirine-magnetite-spinel-corundum domain, all phases hosted by cordierite-rich matrix. Small rectangle marks the position of the inset where plagioclase+quartz is on the left; (k) Garnet, magnetite, and biotite among with feldspars and quartz in the leucosome layer. Very fine-grained cordierite occurs at the edge of garnet grains; (l) Perthite grain in the residue layer. The dashed white line outlines the perthite-cordierite contact.

The second domain, the sapphirine-bearing corona domain is subordinated and occurs as submillimetric (up to 0.3 mm) scattered patches within the cordierite poikiloblasts (Figure 3b). It includes magnetite-spinel grains (up to 0.3 mm in diameter) in the core, surrounded by a corona of thin (10-50 μm) and long sapphirine and corundum laths, associated with minor sillimanite, green-spinel, magnetite, and scarce biotite (Figure 3f-h). The magnetite-spinel cores have concave-convex-type contacts against the host cordierite, which in turn shows straight contacts with the minerals in the sapphirine-bearing corona. In the rims of the magnetite-spinel grains, there are corundum, ilmenite-hematite, and rutile inclusions. Hematite has parallel ilmenite lamellae, and rutile and corundum are euhedral grains or symplectites associated with green-spinel (Figure 3i). The width of these sapphirine-bearing corona around magnetite-spinel grains varies from ~80 to ~400 μm. The transition between the sapphirine-magnetite-spinel-corundum domain and the garnet-sillimanite-orthopyroxene-quartz domains is always separated by cordierite. Less commonly, elongated garnet partially engulfs the sapphirine-magnetite-spinel-corundum domain. Thin cuspate-shaped plagioclase-quartz films, plus minor K-feldspar and biotite occur

widely distributed through cordierite and are interpreted as pseudomorphs after trapped melt (Figure 3j; Holness & Sawyer, 2008).

The coarse-grained leucosome layers are composed of K-feldspar, plagioclase, quartz, and biotite (see Figure 2a), associated with minor garnet and magnetite (Figure 3k). Garnet and magnetite are elongated and anhedral (up to 0.2 mm in length). Local small (10-20 μm) green-spinel grains occur at the edges of the magnetite. The contact between the quartz-feldspathic matrix and garnet and magnetite grains is always separated by a thin (<30-40 μm) and homogeneous cordierite film. The K-feldspar crystals have homogeneous perthite exsolution lamellae (Figure 3l), whereas plagioclase is either exsolution-free or is antiperthite with heterogeneously distributed thin exsolution lamellae.

Zircon, monazite, and apatite are accessory phases in both residue and leucosome. Zircon is widely distributed within cordierite in the residue and within feldspars in the coarse-grained leucosome. Fine, anhedral monazite (<80 μm) occurs at the edges of magnetite-spinel porphyroblasts and rarely within feldspar in the leucosome. Apatite occurs as inclusion in cordierite and in the leucosome.

2.4.1.2 Sillimanite-biotite-cordierite-garnet diatexite (Sample NE163)

In this outcrop, the diffuse transition between leucocratic and melanocratic bands imparts an overall mesocratic aspect to the diatexite (Figure 2c). The leucocratic band, interpreted as leucosome, are dominated by quartz, feldspars, and garnet, comprising up to ~55% of the rock volume. The melanocratic portion of the rock is dominated by cordierite associated with minor garnet, biotite, quartz, and feldspars, defining the residue. There are folded calc-silicate rock lenses up to 1m in length, interpreted as resisters. These lenses are generally surrounded by a thin layer of K-feldspar-rich leucosome (Figure 2d).

At the thin section-scale, lenticular centimetric cordierite aggregates are interleaved with leucocratic material and define the main foliation of the rock. The garnet within the residual band is surrounded by cordierite and is fine- to medium-grained (0.1-0.5 mm) (Figure 4a). Thin prismatic sillimanite, quartz, biotite, and magnetite occur around garnet, all included in cordierite (Figure 4b). Anhedral K-feldspar-quartz-plagioclase-biotite intergrowths occur within cordierite.

The mesoscopic leucosome bands are dominated by plagioclase, K-feldspar, quartz, garnet, and biotite. Garnet is coarse-grained (0.3-1.0 cm in diameter), and contain inclusions of quartz, feldspars, biotite, and sillimanite (Figure 4c). Euhedral biotite associated with magnetite and fine-grained cordierite occur around garnet porphyroblasts (Figure 4c). Plagioclase and K-feldspar are coarse-grained elongated grains interleaved with anhedral quartz patches defining a granoblastic texture in the leucosome.

Zircon, monazite, rutile, and apatite are accessory phases. Zircon is found as inclusion in garnet, cordierite, and feldspars. Monazite as rare inclusions in the garnet and cordierite. Small rutile grains (10-30 μm in length) are found as inclusion in biotite and magnetite grains in the residue.

2.4.1.3 Spinel-biotite-cordierite-garnet-sillimanite diatexite (Sample NE157)

The outcrop of sample NE157 exposes a leucosome-dominated diatexite with leucocratic dykes varying from centimeter-long pods to 2 m-long, laterally continuous dykes, comprising ~60% of rock volume (Figure 2e). Large euhedral garnet porphyroblasts (up to 2 cm in diameter) occur distributed in the leucosome (see detail in Figure 2e). The remaining ~40% of the rock volume comprise melanocratic bands and schollen up to 50 cm in diameter, and is composed of garnet, cordierite, sillimanite, biotite, quartz, and feldspars, interpreted as residue (Figure 2f). Biotite-selvedges

occur at the contacts between residue and leucosome. Garnet porphyroblasts in the residue are surrounded by cordierite and associated with sillimanite, biotite, quartz, ilmenite with minor amounts of green-spinel, feldspars, monazite, zircon, apatite, and rutile (Figure 4d). The garnet porphyroblasts have inclusions of rounded quartz, plagioclase, sillimanite, and biotite. Spinel is scarce (<1%) and occurs in contact with sillimanite and cordierite symplectite in garnet rims (Figure 4e).

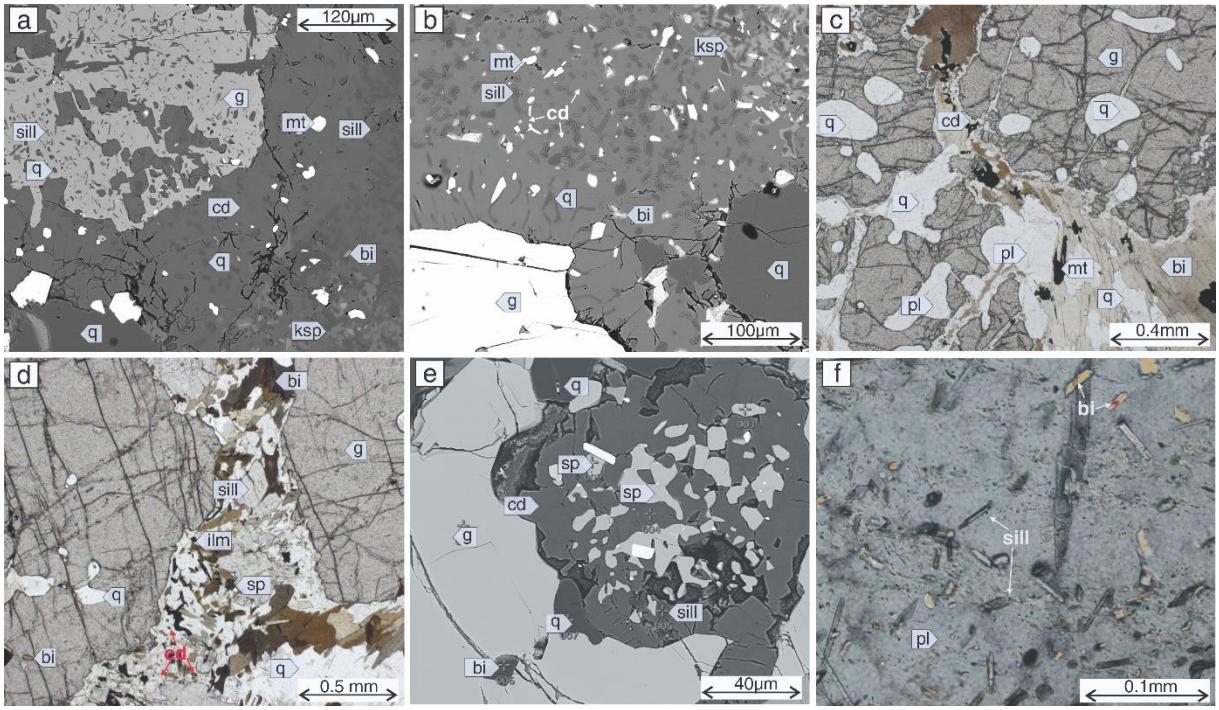

Figure 4. Photomicrographs and back-scattered electron (BSE) images of samples NE163 (a-c) and NE157 (d-e). (a) Resorbed poikilitic garnet and small quartz, sillimanite, K-feldspar, magnetite, and biotite included in cordierite. Sillimanite and quartz also occur as inclusions in garnet; (b) Detail of rim reaction around garnet, composed of quartz, magnetite, sillimanite, and biotite included in cordierite; (c) Coarse-grained garnet porphyroblasts within leucosome associated with cordierite, biotite and magnetite (parallel polarized light); (d) Garnet porphyroblasts surrounded by sillimanite, cordierite, biotite, quartz (parallel-polarized light); (e) spinel-sillimanite included in cordierite in the garnet rim; (f) sillimanite needles and biotite flakes included in plagioclase (cross-polarized light).

The coarse-grained leucosome dykes are dominated by plagioclase, quartz, K-feldspar, garnet, and biotite. The K-feldspar is perthite commonly with exsolution-free rims. Plagioclase has several small prismatic sillimanite and biotite inclusions (Figure

4f) and can also occur as myrmekite and antiperthite. Quartz occurs as interstitial patches between feldspar crystals.

Zircon, monazite, and rutile are accessory phases. Zircon grains occur as inclusions in sillimanite, cordierite, garnet rims, in both residue and leucosome. Fine monazite grains (30-80 µm in diameter) are usually found as inclusions in cordierite or within leucosome. Euhedral rutile grains (50 to 200 µm in length) appear mainly as inclusions in sillimanite and less commonly in biotite or cordierite.

4.2 Mineral chemistry in the sapphirine-bearing diatexite (sample ne30)

2.4.2.1 Garnet

The largest garnet porphyroblasts preserve rimward almandine zoning, increasing from 0.47 to 0.51, whereas pyrope shows the opposite zoning, decreasing from 0.46 to 0.40. Spessartine increases from 0.02 in the core to 0.13, in the rim, with small grossular variation, between 0.02 and 0.04 (Figure 5a-b).

2.4.2.2 Orthopyroxene

Orthopyroxene shows variation in the aluminum content as a function of the distance to garnet porphyroblasts (Figure 5b; Figure 3d). Close to the garnet it has y(opx) varying between 0.05 to 0.12. Further away, these values increase from 0.14 up to 0.17. Orthopyroxene associated with sillimanite needles included in cordierite has intermediate y(opx) contents between 0.13 and 0.15 (e.g. Figure 3e). For all grains, XMg varies between 0.66 to 0.74, and the calculated ferric iron proportion (Fe+3/Fe+2) varies between 0.03 and 0.25.

2.4.2.3 Spinel

Spinel that is part of magnetite-spinel grains (Figure 3i) has low zinc contents, varying between 0.03 and 0.04 apfu, and XMg values varying between 0.34 to 0.43. Small spinel grains that are part of the sapphirine-bearing corona (Figure 3h) show higher zinc contents up to 0.06 apfu and XMg values ranging between 0.36 and 0.44.

2.4.2.4 Sapphirine

All sapphirine analyses have values near the $(Mg, Fe)_7Al_{18}Si_3O_{40}$ end-member composition (7:9:3) (Figure 5c). Ferric iron calculated from ideal stoichiometry is high in all microstructural contexts (Fe^{+3}/Fe^{2+} = 0.14 - 0.59). The X_{Mg} values in the sapphirine grains are relatively homogeneous, ranging from 0.73 to 0.76.

2.4.2.5 Feldspars

The perthite K-feldspar has orthoclase composition $Ab_{0.09-0.35}Or_{0.57-0.90}$ and exsolved plagioclase composition $Ab_{0.61-0.75}An_{0.22-0.29}$. The antiperthite plagioclase has host and lamellae compositions of $Ab_{0.70-0.72}An_{0.25-0.26}$ and $Ab_{4.0}Or_{96}$, respectively. The plagioclase grains of the coarse-grained leucosome have a composition range of $Ab_{0.72-0.73}An_{0.25-0.26}$, whereas inside the residue they are enriched in the anorthite component $Ab_{0.66-0.73}An_{0.26-0.33}$.

2.4.2.6 Cordierite

Poikiloblastic cordierite shows a slight variation in the X_{Mg} content varying between 0.89 and 0.85 close to the sapphirine-spinel-magnetite-corundum domain, and between 0.85 and 0.81 in the garnet-sillimanite-orthopyroxene-quartz domain. The total sum of oxides is around 97-99%, suggesting the presence of $H_2O + CO_2$.

2.4.2.7 Biotite

Biotite grains included in cordierite have low Ti contents <0.05 apfu with X_{Mg} varying from 0.78 to 0.85 and, F from 0.64 to 0.88 apfu. Biotite in leucosome shows high Ti contents of 0.22-0.73 apfu, X_{Mg} varying from 0.72 to 0.85, and F varying between 0.17 to 0.39 apfu.

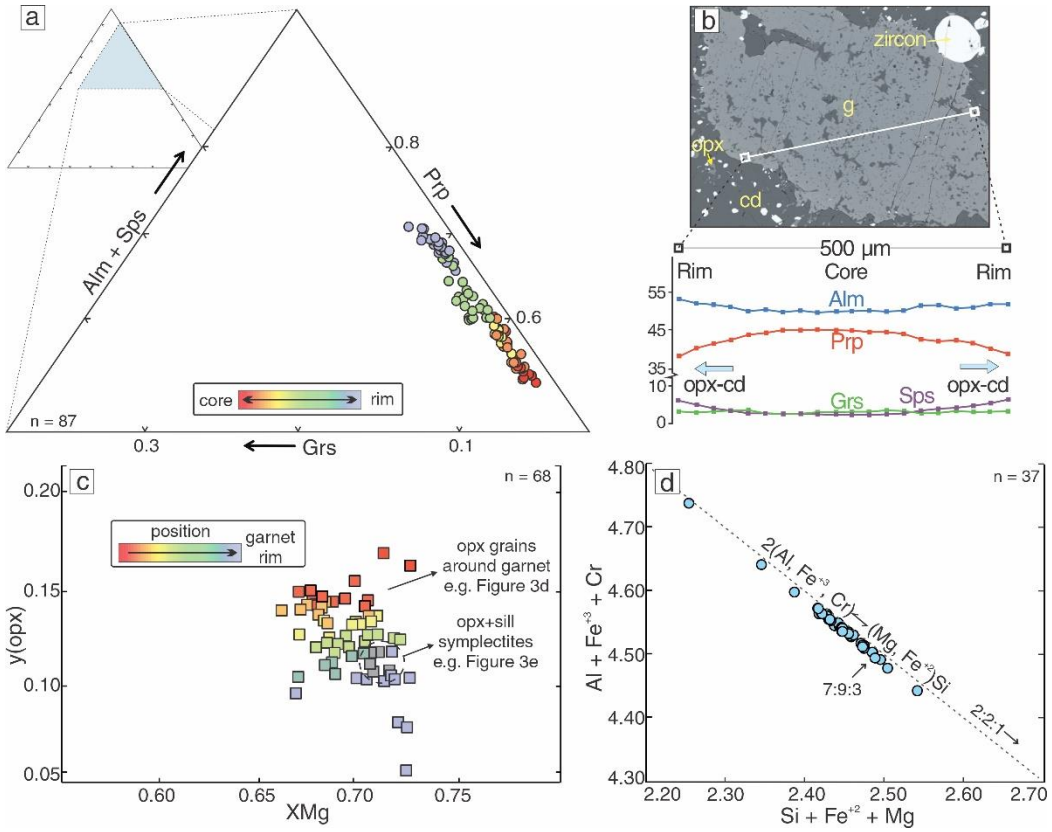

Figure 5. Mineral chemistry. (a) Garnet (Alm+Sps)-Grs-Prp ternary diagram; (b) Rim-core-rim garnet chemical zoning; (c) y(opx) versus XMg diagram showing chemistry variation of orthopyroxene grains in relation to garnet; (d) Sapphirine Al+Fe+3+Cr versus Si+Fe+2+Mg diagram.

2.4.3 Pressure-temperature constraints for the sapphirine-bearing diatexite (sample NE30)

2.4.3.1 Al-in-orthopyroxene thermobarometry

The presence of ilmenite-hematite and the high stoichiometric ferric iron values in the silicates (*e.g.* orthopyroxene and sapphirine; Table S1) indicate a high oxidation state in sample NE30. Considering the Fe^{3+} incorporation in the octahedral site of orthopyroxene (*y*(opx) = Al-Fe^{+3}-Cr-(2xTi)/2), the Al-in-orthopyroxene thermobarometry (Pattison et al., 2003) yields temperatures varying between 892 and 933 ºC and pressures between 7.8 and 8.0 kbar (average of 915 ± 9 ºC and 7.9 ± 0.3 kbar). Calculations assuming ideal Tschermak exchange in orthopyroxene (all Fe as Fe^{2+}; *y*(opx) = Al/2) yield temperature and pressure varying between 1046-1095 ºC and 8.9-9.9 kbar, respectively (average of 1080 ± 12 ºC and 9.6 ± 0.2 kbar).

2.4.3.2 Ternary feldspar thermometry

The re-integrated feldspar compositions of $Ab_{0.21\text{-}0.28}An_{0.36\text{-}0.48}Or_{0.67\text{-}0.74}$ were used in the ternary feldspar thermometry. They yield temperatures between 963 and 980 ºC. Comparatively, the isotherms calculated with Benisek et al., (2010) and Elkins & Grove (1990) feldspar activities showed less than 20 ºC differences (~980-940 ºC), whereas considering the feldspar activity of Fuhrman & Lindsley (1989) the estimated temperatures are ~40 ºC lower (~930 ºC; Figure 6).

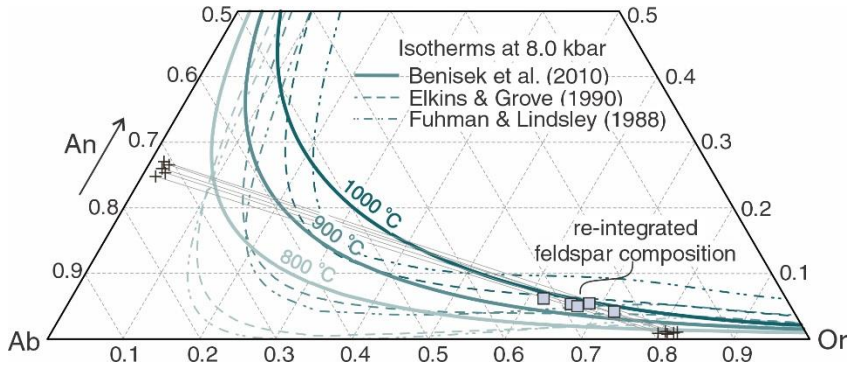

Figure 6. Re-integrated feldspar thermometry. Ab-Or-Na diagram showing re-integrated feldspar composition and isotherms calculated with different interaction parameters for sample NE30. The plus signs represent the measured compositions of the K-feldspar and plagioclase.

2.4.3.3 Phase equilibrium modeling

Two distinct equilibrium assemblages were recognized as relict inclusions forming domains within cordierite poikiloblasts (see section 4.1.1): (i) the garnet-sillimanite-orthopyroxene-quartz; and (ii) sapphirine-magnetite-spinel-corundum domains. The peak assemblage in the first domain is interpreted to be garnet, sillimanite, quartz, magnetite, ilmenite-hematite, K-feldspar, plagioclase, and melt. The rock matrix composed of cordierite, orthopyroxene, and minor biotite is interpreted as being a result of retrogression, concomitant with melt crystallization and cooling. In the second domain, the formation of the sapphirine-bearing cordierite corona is interpreted as a product of reactions between the magnetite-spinel core and melt in a restricted silica-poor compositional domain.

In order to constrain the metamorphic P-T evolution of the silica-saturated residue a P-T pseudosection based on whole-rock composition was calculated and presented in the Figure 7. Before calculating the P-T pseudosection, the effects of the oxidation state in the metamorphic assemblages were investigated using a T-MO phase diagram calculated at 7.9 kbar, varying the composition from reduced to oxidized conditions (O2 = 0.002-4.65 mol.%) and the results are available in Figure S1. From the T-MO model, about of 60% of total Fe were converted to Fe3+ in order to modeling: (i) the orthopyroxene stability at the near peak metamorphic conditions as well as the occurrence of cordierite in low-temperature conditions; and (ii) the presence of minor quartz, magnetite and ilmenite-hematite in the silica-saturated residue (for more details see Figure S1). The scarcity of hydrated minerals, with restricted occurrence of retrogressive biotite along grain boundaries, indicate that the mineral assemblages were essentially dry at the peak metamorphic conditions. We estimate the amount of H2O in the system at near peak metamorphic conditions using a T-MH2O phase diagram calculated at 7.9 kbar, varying the water content from dry to hydrated composition (H2O = 0.0-2.56 mol.%), and the phase diagram is accessible in Figure S1. The maximum H2O value that allows stabilizing the observed mineral assemblage in the silica-saturated domain composed of garnet, sillimanite, orthopyroxene, cordierite, quartz, biotite, feldspars, and melt was set as close as possible to the solidus curve (e.g. White & Powell, 2002b). The pseudosection was calculated in a P-T window of 6.0-9.0 kbar and 850-1050 ºC considering the adjusted ferric iron and water contents. The phase diagram was contoured with y(opx) (AlM1 = Al-[2-Si]) and XAn (molar (Ca/[Ca+Na+K]) in plagioclase) and selected mineral modes (%volume) isopleths.

This P-T pseudosection indicates a broad stability of quartz and the main mineralogy of the garnet-sillimanite-orthopyroxene-quartz domain (Figure 7a). The inferred peak assemblage (garnet, sillimanite, quartz, magnetite, ilmenite-hematite, K-feldspar, plagioclase, and melt) occurs in a wide field at P >8.0 kbar and T >860 oC. The orthopyroxene-cordierite-melt-bearing assemblages occur at lower pressures, and the stability of cordierite leads to an inflection of the H2O-undersaturated solidus to higher temperatures. Orthopyroxene is calculated to have y(opx) values of 0.17 to >0.21 and plagioclase has xAn values of 0.32 to 0.35 in the inferred retrograde fields (Figure 7a). The mode box diagram illustrates the varying abundances of phases modeled in the pseudosection, indicating an increase of orthopyroxene and cordierite modes, and a decrease of garnet, sillimanite, and melt modes along a simplified clockwise P-T path (Figure 7b-f).

In order to evaluate the role of bulk-silica in the formation of the sapphirine-bearing corona within cordierite, two T-MSiO2 phase diagrams spanning from the whole-rock composition to a silica-undersaturated composition were calculated at 7.9 and 7.7 kbar and presented in Figure 8. Both models shows that the sapphirine stability is extremely sensitive to the bulk-silica content: under the silica-saturated side of the diagram (right hand-side in the x-axis), sapphirine is restricted to temperatures >1010 oC, whereas in the quartz-free, silica-undersaturated composition (left hand-side in the x-axis), sapphirine stability is shifted towards lower temperatures (e.g. Kelsey, White, & Powell, 2005). The stability of cordierite and orthopyroxene are favored by an increase of silica content and restricted to the quartz-bearing area. It should be noted that the minor decompression from 7.9 to 7.7 kbar promotes the expansion of the cordierite stability field towards relatively SiO2-depleted compositions (Figure 8).

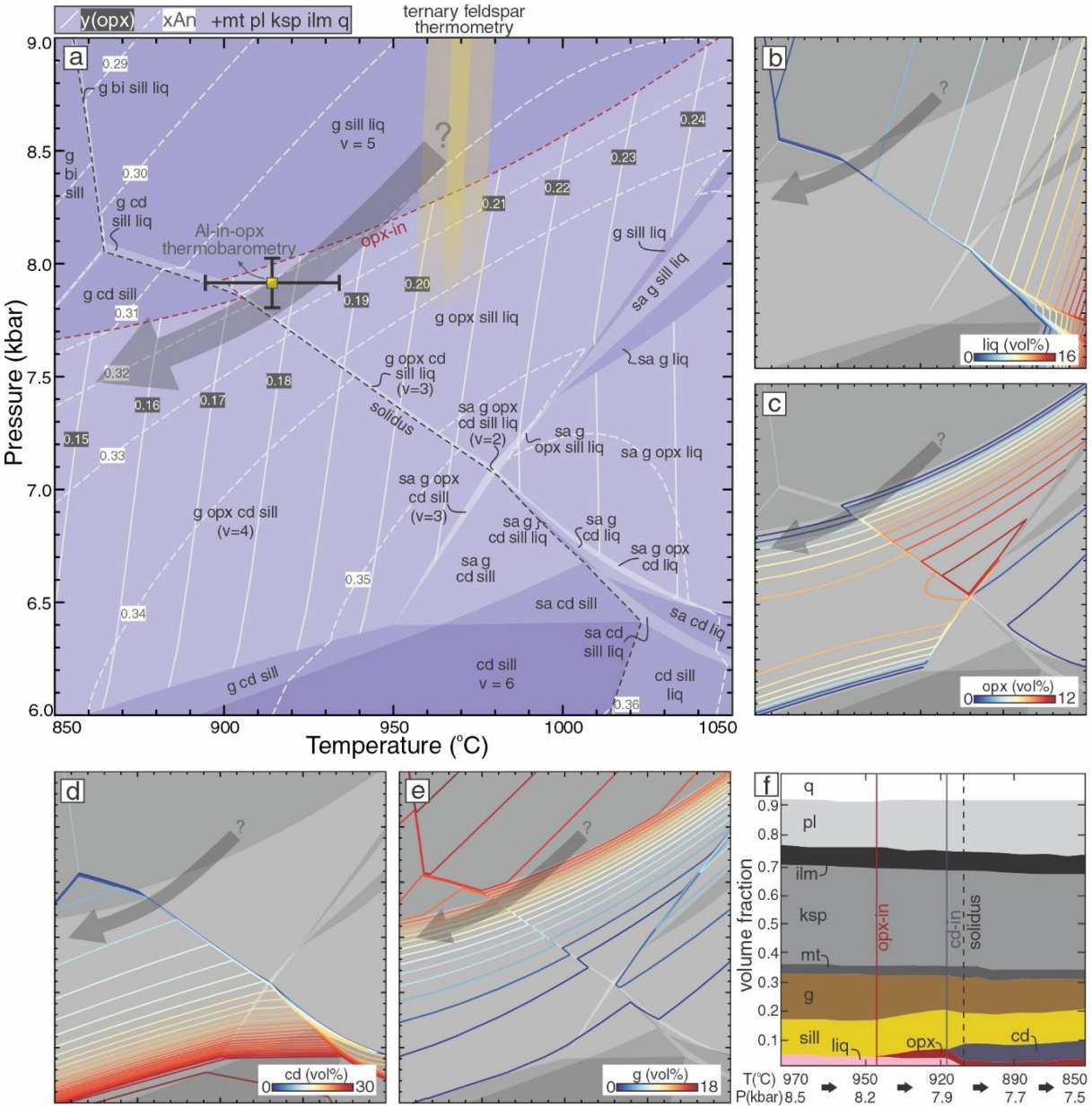

Figure 7. Phase equilibrium modeling. (a) P-T pseudosection (sample NE30) contoured with y(opx) (octahedral Al content in orthopyroxene) and xAn isopleths; grey arrow represents a schematic *P-T* path; yellow square is the Al-in-orthopyroxene thermobarometric results (considering Fe3+ on y(opx) model of Pattison et al., 2003 calibration) and the yellow horizontal field is the thermometric results of the re-integrated ternary feldspar (Kroll et al., 1993; Benisek et al., 2010). (b) to (e) Pseudosection fields as in (a) showing mode (%) isopleths for: (b) Silicate melt; (c) Orthopyroxene; (d) Cordierite; (e) Garnet; (f) Mode box diagram based on schematic P-T path.

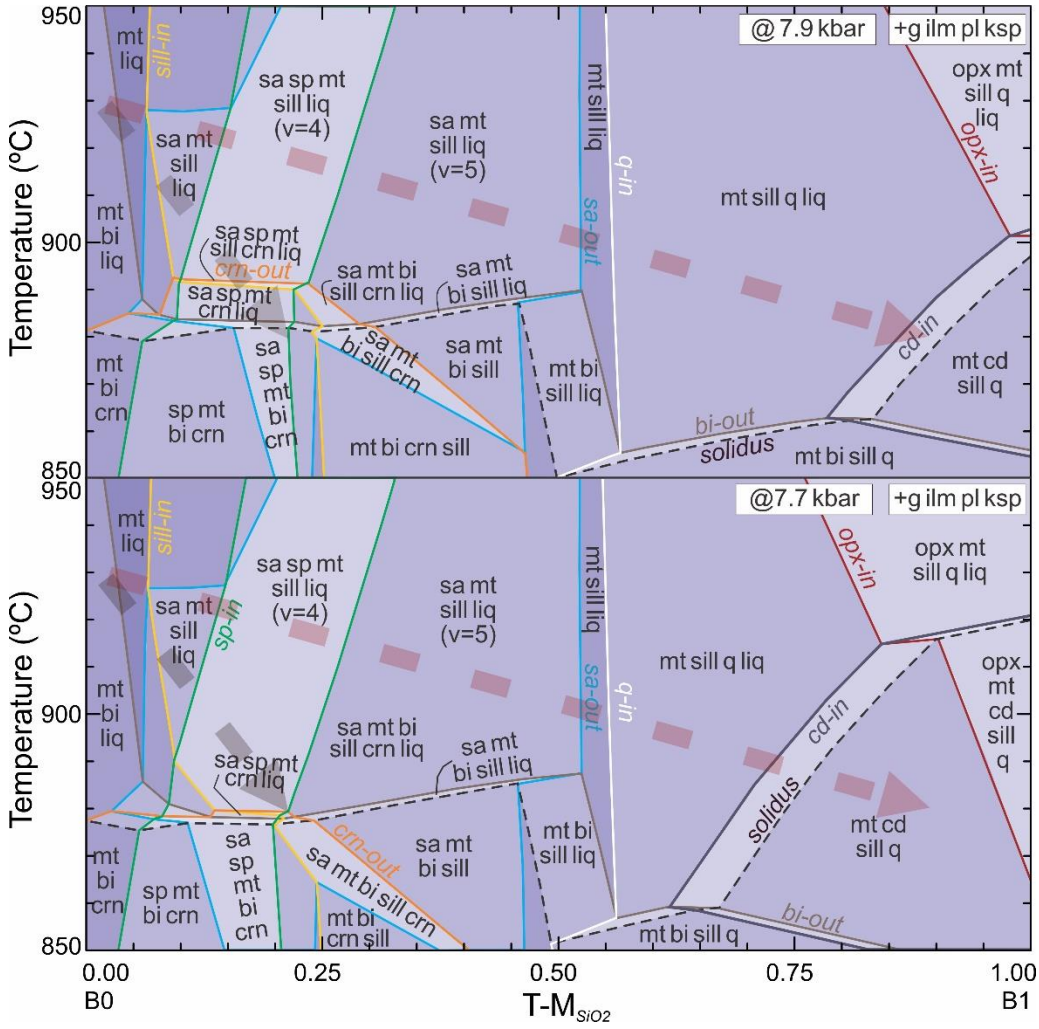

Figure 8. T-MSiO2 models calculated at (a) 7.9 and (b) 7.7 kbar for the sapphirine-bearing domain. The increment of *a*SiO_2 triggered by residue-melt interaction during retrogression leads to the change from the silica-undersaturated stability field (sapphirine, corundum, spinel) to the quartz-present field (orthopyroxene-quartz-cordierite). The combined effect of increment of *a*SiO_2 and decompression promotes the late cordierite growth at the expense silica-undersaturated phases. Intermediate remnants of this process are interpreted as trapped reactions, and therefore are in metastability with the cordierite-rich matrix. The red arrow represents the scenario of low interaction between the silica-undersaturated residue and silicate melt while the black arrow represents considerable interaction and locally increase of silica activity in the diatexite.

The black and red arrows illustrate respectively a low and high SiO2-increment into effective bulk composition with cooling and decompression along a similar P/T slope as defined by the clockwise P-T path in Figure 7. With low-SiO2 increment (black arrow) sapphirine entrance is modelled to occur at the expense of magnetite and then spinel, followed by stabilization of sillimanite and then corundum, concomitant with melt

reduction towards the solidus curve at T<880°C. In this scenario, the corundum stabilization deflects sillimanite entrance towards higher SiO_2 values. Considering an initial silica-undersaturated composition, the red arrow shows that the broad increment of SiO_2 activity during the retrometamorphic P-T path promotes the change of equilibrium mineral assemblages containing sapphirine, spinel, corundum to quartz, sillimanite, and late cordierite (Figure 8).

2.4.4 Zircon age, composition and thermometry

Thirty coupled U-Pb and chemical analyses for each sample were obtained for zircon petrochronology. Figure 9 summarizes selected representative examples of zircon internal texture revealed by cathodoluminescence (CL) investigation prior dating. The integrated results combining zircon internal texture, REE composition, and U-Pb ages are summarized in Figure 10.

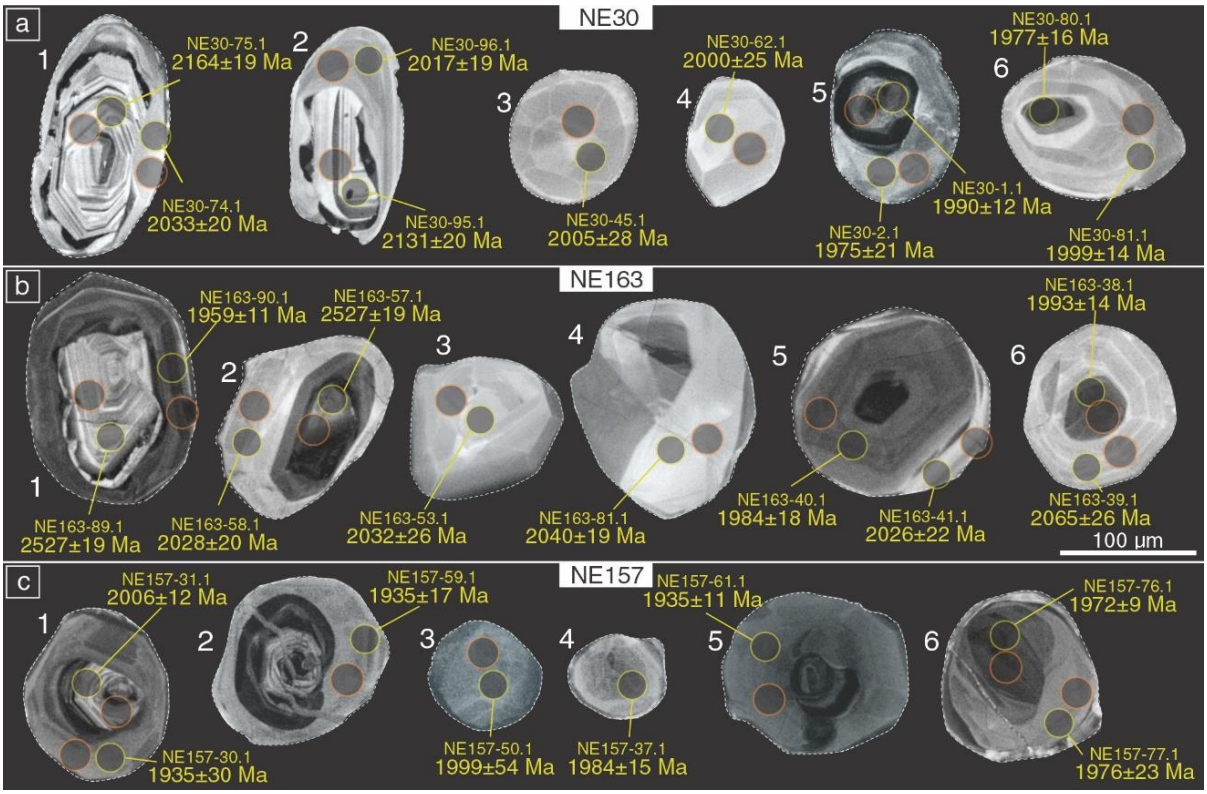

Figure 9. Cathodoluminescence images of representative zircons from the migmatites from the Arapiraca Complex. (a) Sapphirine-bearing diatexite (NE30); (b) Garnet-biotite-cordierite diatexite (NE163); and (c) Spinel-biotite-cordierite-garnet-sillimanite diatexite (NE157). Yellow and orange circles represent spot position for U-

Pb and trace elements analysis, respectively. To best display the internal zoning of each sample the image contrast was edited.

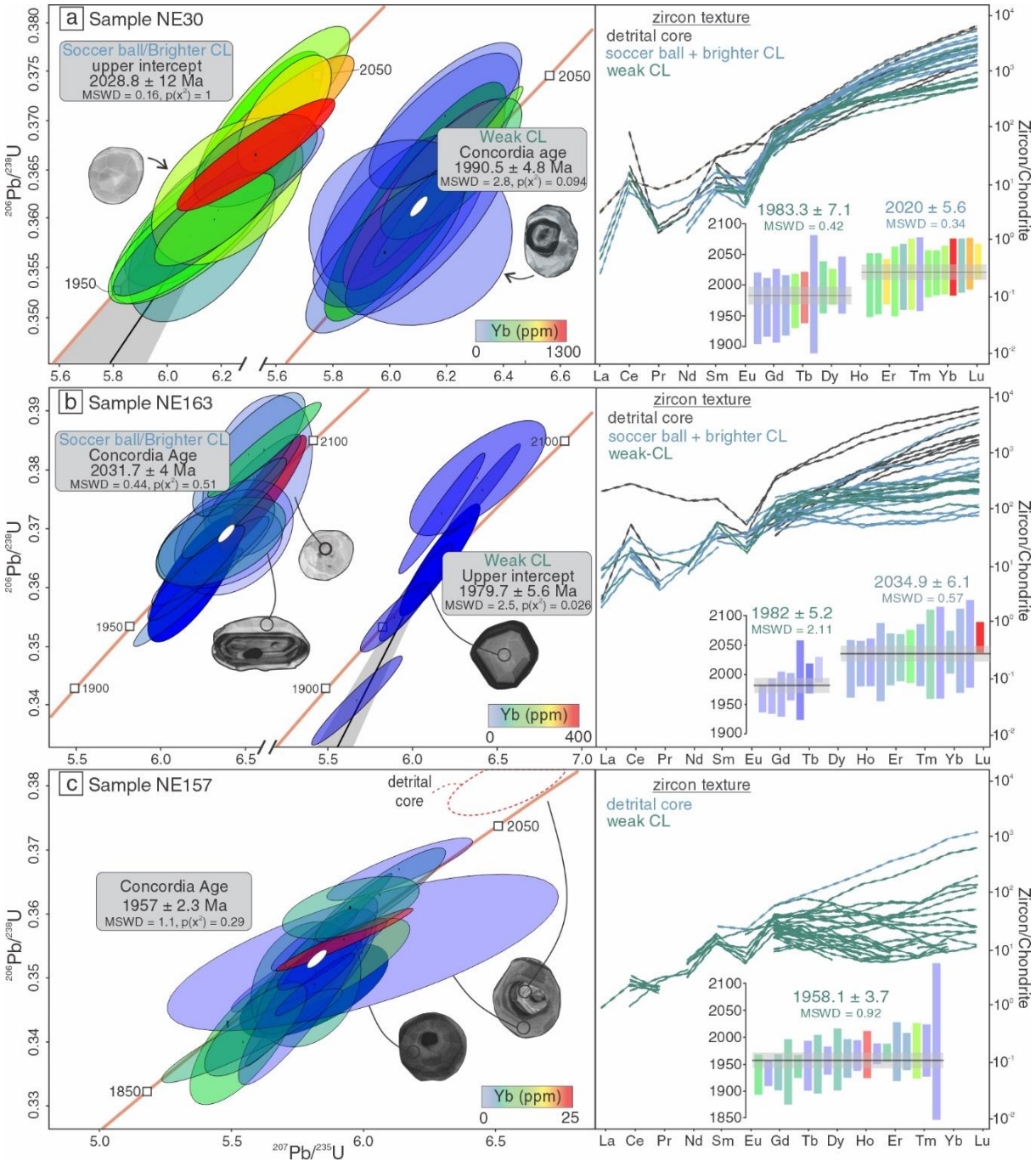

Figure 10. Concordia diagrams of zircon U-Pb LA-ICP-MS data, chondrite-normalized rare earth element diagrams, and weighted mean ages for different chemical and CL zircon groups. (a) Sapphirine-bearing diatexite (NE30). The lower intercept is 1116 ± 485 Ma; (b) Garnet-biotite-cordierite diatexite (NE163). The lower intercept is 178 ± 243 Ma; and (c) Spinel-biotite-cordierite-garnet-sillimanite diatexite (NE157).

The temperature of zircon crystallization was calculated using the revised Ti-in-zircon thermometer of Ferry & Watson (2007). The studied samples are SiO_2 saturated, except for the silica-undersaturated sapphirine-bearing domain in sample NE30. In this sample, rutile is only found as inclusion within magnetite-spinel, whereas ilmenite is the dominant Ti-bearing phase, indicating that the a_{TiO2} would have been low (*e.g.* Figure 3b, h, i). Therefore, the a_{TiO2} equal to 0.5 was set for sample NE30, which represents an approximate average for this rock (Watson & Harrison, 2005). Based on the widespread occurrence of rutile in samples NE163 and NE157, a_{TiO2} was assumed as equal to one for these samples.

2.4.4.1 Sapphirine-bearing diatexite (sample NE30)

The analyzed zircon grains are large (100-150 µm) with rounded to subordinated prismatic (2:1 ratio) habits (Figure 9a). Several grains exhibit corroded cores with an internal fine-scale oscillatory zoning. The transition between detrital cores and neoblastic domains is usually mantled by a thin (<10 µm) dark-CL moat (1-2 in Figure 9a). The neoblastic rims are sector zoned or fir-tree domains with a bright-CL response (grains 1-2 in Figure 9a). Some grains lack core-rim relationships, exhibiting an internal and external form of soccer-ball-type (3-4 in Figure 9a). Another group has core-rim zoning where the cores are dominated by a weak-CL response followed by sector zoned weak-CL overgrowths (grains 5-6 in Figure 9a).

The detrital cores (n=6) are HREE-rich with a slightly negative Eu anomaly with $^{207}Pb/^{206}Pb$ ages varying between 2106 and 2164 Ma. The individual $^{207}Pb/^{206}Pb$ ages for the neoblastic zircon (n=25) vary between 2036 and 1963 Ma, and two distinct groups were recognized: (i) the soccer ball and bright-CL overgrowths form a single Yb-rich group, with steep HREE slope (Gd_N/Yb_N ~ 0.039) and negative Eu anomaly, and yield an upper intercept age of 2029 ± 12 Ma (MSWD = 0.16; p(x^2) = 1; the lower

intercept is 1116 ± 485 Ma) and a weighted mean age of 2020 ± 5 (MSWD = 0.34; p(x^2) = 0.89; figure 10a); (ii) the weakly luminescent zircon grains are relatively Yb-depleted, also with a steep HREE slope (Gd_N/Yb_N ~ 0.095), negative Eu anomaly, and yield a younger concordant age of 1990 ± 5 Ma (MSWD = 2.8; p(x^2) = 0.094) with a weighted mean age of 1983 ± 7Ma (MSWD = 0.42; p(x^2) = 0.92). The youngest group is characterized by inverse age zoning, where cores are younger than rims (grain 6 in Figure 9a). The Ti concentration in the neoblastic zircon ranges from 5.77 to 18.04 ppm, corresponding to temperatures between 760 and 885 °C (upper quartile = 860 °C). Th/U ratios vary between 0.03 to 7.18, without correlation with U-Pb ages or trace elements concentration.

2.4.4.2 Sillimanite-biotite-cordierite-garnet diatexite (sample NE163)

The zircon grains in this sample vary from 80 up to 200 µm in length and exhibit prismatic (2:1 and 3:1) to rounded shapes (Figure 9b). The detrital cores are prismatic with oscillatory zoning and commonly mantled by a thin (<10 µm) dark CL film (grains 1-2 in Figure 9b). The zircon rims are sector zoned or have bright and homogeneous CL. Rounded soccer-ball-type or sector zoned zircon grains are common (grains 3-4 in Figure 9b). Some grains show core-rim zoning with blurred dark CL cores with a diffuse transition towards the sector zoned brighter CL rims (grains 5-6 in Figure 9b).

The detrital cores (n=9) show a positive middle to heavy REE slope (Gd_N/Yb_N ~ 0.07), an intense negative Eu anomaly, and exhibit a range of $^{207}Pb/^{206}Pb$ dates varying between 2119 and 3139 Ma. The neoblastic zircon grains (n=20) have individual $^{207}Pb/^{206}Pb$ ages spanning from 2063 to 1938 Ma forming two distinct age clusters: (i) soccer-ball and bright CL rims with variable Yb contents (4.6 - 345 ppm), negative Eu anomaly and a subtly positive HREE slope (Gd_N/Yb_N ~ 0.4), yield a concordia age of 2032 ± 4 Ma (MSWD = 0.44; p(x^2) = 0.51), and weighted mean age of 2035 ± 6 (MSWD

= 0.57; p(x^2) = 0.88); (ii) blurred dark CL domains are relatively depleted in Yb (18 - 51 ppm), with a flat to subtly positive HREE slope (Gd_N/Yb_N ~ 0.5), and yield an upper intercept age of 1980 ± 6 Ma (MSWD = 2.5; p(x^2) = 0.026; lower intercept date is 178 ± 243 Ma), associated with a weighted mean age of 1982 ± 5 Ma (MSWD = 2.11; p(x^2) = 0.048). The Ti concentration in neoblastic zircon ranges from 7.79 to 53.3 ppm corresponding to temperatures between 725 and 930 °C (upper quartile = 810 °C). One analysis in this sample has a very high TiO_2 concentration of 105.2 ppm, associated with anomalously high Fe, Mg, and Ca contents, and was excluded from consideration. All analyses for have reasonable values of TiO_2 and low Fe, Mg, and Ca contents (Supplementary Material 4). Th/U ratios do not correlate with U-Pb dates or trace elements concentration and vary between 0.01 and 13.22.

2.4.4.3 Spinel-biotite-cordierite-garnet-sillimanite diatexite (sample NE157)

The zircon grains in this sample are typically 70-150 µm in diameter with rounded to ovoid shapes (Figure 9c). The detrital cores in the analyzed zircon population are rare and generally exhibit concentric or sector zoning with a bright CL response. These cores are mantled by a thin (<10 µm) dark CL film (grains 1-2 in Figure 9c). The rims are sector zoned or fir-tree domains with a weak CL response (grains 1-2 in Figure 9c). Small grains exhibit external and internal features of soccer-ball-type zircon grains and other types show fir-tree internal texture with a weak CL response (3-4 in Figure 9c). Numerous grains have core-rim zoning with a blurred dark CL core transitioning to brighter CL rims (grains 5-6 in Figure 9c).

A single core analysis is HREE-rich with a negative Eu anomaly and yields a $^{207}Pb/^{206}Pb$ age of 2006 ± 12 Ma (dashed red ellipse in Figure 10c). The neoblastic zircon exhibits a range of $^{207}Pb/^{206}Pb$ ages varying between 1999 and 1921 Ma with Yb <24.1 ppm, negative Eu anomaly, and a flat middle to heavy REE slope (Gd_N/Yb_N

~ 1.64). The concordant age of 1957 ± 3 Ma (MSWD = 1.1; p(x^2) = 0.29) and a weighted mean age of 1958 ± 4 Ma (MSWD = 0.92; p(x^2) = 0.56) were obtained from nineteen neoblastic zircon. The Ti concentration in these zircon grains varies between 11 to 52 ppm, yielding temperatures between 755 and 930 °C (upper quartile = 830 °C). The Th/U ratios vary between 0.04 and 5.7, with one analysis yielding a very high value of 23.5 and are not correlated with age or trace elements concentration.

2.5. Discussion

2.5.1 Petrological evolution

2.5.1.1 UHT conditions in the Arapiraca Complex

Conventional thermobarometry and pseudosections calculated for the sapphirine-bearing diatexite (sample NE30) provides a framework to address the metamorphic evolution of the Arapiraca Complex. In the phase equilibrium modeling presented in Figure 7, the inferred peak mineral assemblage (garnet, sillimanite, K-feldspar, plagioclase, magnetite, ilmenite, quartz, melt) constrains the peak temperature and pressure to a field above 860 ^{o}C and 8.0 kbar, respectively (Figure 7). The peak temperature of ~970 ^{o}C obtained with re-integrated ternary feldspar thermometry is consistent with the calculated field at pressures >8.3 kbar. However, the maximum pressure conditions could not be constrained, so the peak conditions on the *P-T* path remains as a question mark at ~970 ^{o}C and ~8.5 kbar rather than a precise point in Figure 7a.

The retrograde evolution recorded by the development of orthopyroxene around garnet and sillimanite, and later cordierite (*e.g.* Figure 3c-d), is interpreted as a consequence of decompression and cooling from peak conditions. The measured y(opx) values varies between ~0.10 and 0.17, and the anorthite content in plagioclase xAn between 0.25 and 0.33. Considering these values, the calculated compositional isopleths define a narrow field limited upwards by the orthopyroxene stability at P<8.0

kbar and T<900 ºC (orthopyroxene-in line in Figure 7a), and limited downwards by xAn = 0.33 isopleth at P>7.7 kbar close to the *solidus* line. These constraints match the average *P-T* conditions of 7.9 ± 0.3 kbar and 915 ± 9 ºC calculated with Al-in-orthopyroxene thermobarometer considering the ferric iron calibration of Pattison et al (2003). The rimward *X*Mg depletion in the garnet, and the crystallization of orthopyroxene with *y*(opx)<0.15 preferentially at garnet rims (*e.g.* Figure 5), indicates that the retrograde reactions continued under *subsolidus* conditions (Figure 7). All combined, the metamorphic evolution indicated by the arrow in Figure 7 intersects the H_2O-undersaturated *solidus* at ~900 ºC/7.7 kbar, constraining a point on the retrograde segment of the *P-T* path. The unrealistic average *P-T* conditions of 1080 ºC and 9.6 kbar calculated assuming the ideal Tschermak exchange in the Al-in-orthopyroxene thermobarometry, demonstrates the key role of ferric iron in oxidized UHT metamorphic rocks, and how neglecting it can lead to overestimation of the equilibrium *P-T* conditions (*e.g.* Harley, 2008).

Despite the agreement between modeled and observed equilibrium assemblages and their chemistry, our modeling does not reproduce the mineral proportions observed in the sample. The main disagreement is the low volume of cordierite of ~10% at 7.7 kbar/900 ºC as calculated in Figure 7d, contrasting with the observed volume of cordierite in the residual rock of ~30%, averaging the modal contents in leucocratic and melanocratic sections in the same proportions as found in sample NE30. Furthermore, the melt proportion is underestimated, and the K-feldspar and plagioclase volumes are overestimated. We suggest that the minor amount of leucosome in the residue has contaminated the XRF analysis by adding extra K_2O, CaO, and SiO_2 in which, potentially, were accommodated by the plagioclase and K-feldspar solution models in the modeling. Additionally, CO_2 incorporation into the

cordierite structure and the increase of a_{H2O} resulting from melt crystallization during cooling may have expanded the cordierite stability to higher *P-T* conditions than in H_2O-undersaturated composition as modeled in the pseudosection, favoring the late growth of large poikiloblasts (*e.g.* Harley, 2008; Baldwin, Powell, Brown, Moraes, & Fuck, 2005).

2.5.1.2 The significance of silica-undersaturated domains

The coexistence of silica-saturated and silica-undersaturated compositional domains described in the sapphirine-bearing diatexite (sample NE30) has also been reported in numerous HT/UHT terranes (*e.g.* Leite et al., 2009; Dharmapriya et al., 2015, 2017; Ganguly, Bose, Das, Torimoto, & Ghosh, 2017). Several mechanisms have been proposed to explain their formation, including: (1) quartz depletion in residual solids during progressive biotite-dehydration melting (*e.g.* Kriegsman & Hensen, 1998); (2) inheritance of silica-poor and silica-rich paleo-bedding or laminations from the original sedimentary protoliths (*e.g.* Darmapriya et al., 2017); (3) *P-T* changes leading to entrance into the quartz-stability field during the retrograde path (*e.g.* Kelsey et al., 2005; Ganguly et al., 2017); (4) post-peak domainal retention of quartz, due to sluggish kinetics of SiO_2, leading to the formation of coexistent quartz-bearing and quartz-absent domains (*e.g.* Kelsey et al., 2005); (5) post-peak UHT metamorphism involving metasomatism between silica-rich magma and silica-undersaturated spinel-magnetite bearing rock (e.g. Leite et al., 2009). Given the widespread occurrence of quartz as inclusions in minerals representing the peak- and post-peak assemblages (*i.e.* garnet and cordierite), it is unlikely that quartz grew only in the retrograde path, arguing against mechanisms (3), (4), and (5). Following mechanisms (1) and (2), we envisage that the distinct equilibrium domains in our sample formed before retrogression, probably influenced by compositional

heterogeneities inherited from the original sedimentary protolith (Darmapriaya et al., 2017). We argue that during the progressive biotite-dehydration melting, distinct silica-rich and silica-poor paleo-sequences produced different residual assemblages, allowing the formation of magnetite-spinel solid-solution isolated from the quartz equilibration volume that gave rise to the sapphirine-magnetite-spinel-corundum domain. Analogous to the mechanism of preservation of inclusions domains within UHT garnets from Sri Lanka (Darmapriaya et al., 2017), we suggest that during retrogression, the discrete equilibrium domains were trapped and isolated by cordierite poikiloblasts and the low diffusion of SiO_2 may also allow the preservation of compositional domains even after retrogression and interaction between melt and residue (Figure 8; Kelsey et al., 2005).

Furthermore, the restricted occurrence of sapphirine as a corona around spinel-magnetite grains indicates the persistence of chemical potential gradient and incomplete equilibrium between the reactant magnetite-spinel and quartz-feldspathic leucosome (*e.g.* Leite et al., 2009). So, further phase equilibria modeling using composition derived from electron microprobe X-ray maps and considering chemical potential (*i.e.*μMgO-μSiO_2) are necessary to constrain quantitatively the *P-T-X* evolution of the sapphirine-bearing corona (*e.g.* White, Powell, & Baldwin, 2008; Doukkari, Diener, Ouzegane, & Kienast, 2018).

2.5.2 Zircon petrochronology

The external and internal features of the investigated zircon are characteristic of *suprasolidus* crystallization to post-crystallization features (Taylor, Kirkland, & Clark, 2016). The detritic cores from all three samples yield ages between 2.1-3.1 Ga, and given the predominance of oscillatory zoning, we interpret them as detrital igneous grains found in the sedimentary protolith. The neoblastic and recrystallized zircon rims

yield $^{207}Pb/^{206}Pb$ ages varying from 2.06 to 1.92 Ga, and variable HREE concentrations (Figure 10). In sample NE30, the neoblastic zircons have high HREE concentration, coupled with a slight deflection of the Gd_N/Yb_N ratios with a decrease of U-Pb ages (Figure 10a), indicating that its growth occurred during or after garnet breakdown linked to the near-isobaric cooling retrogression (*e.g.* Figure 7a). This breakdown is supported by garnet that form resorbed grains included in cordierite poikiloblasts (*e.g.* Figure 3c, k). Furthermore, two textural-chemical zircon groups were identified in this sample (Figure 10a). The older group at 2.03 ± 0.12 Ga is HREE-rich and dominated by soccer-ball and brighter-CL rims, interpreted as crystallized from the anatectic melt. The younger zircon group at 1.99 ± 0.05 Ga is typically HREE depleted, has a weak CL response and is frequently characterized by inverse age zoning (*e.g.* grains 5-6 in Figure 9a). Laurent et al (2018) reported a similar inverse age zoning in UHT anatectic zircons from Rogaland (South Norway) and explained it as the product of closed-system post-crystallization disturbance during the UHT metamorphism. Thus, we suggest that at c. 2.03 Ga the anatectic zircons began to crystallize close to the *solidus* temperature and was later disturbed at c. 1.99 Ga under *subsolidus* conditions.

In contrast to zircons from sample NE30, zircons grains from sample NE163 have an overall positive to flat Gd_N/Yb_N slope, associated with a slight decrease of the Gd_N/Yb_N ratios toward younger ages (Figure 10b). This behavior coupled with the widespread occurrence of garnet porphyroblasts within the leucosome suggest that the zircons grew in chemical communication with peritectic garnet during melt crystallization between c. 2.03 and 1.97 Ga (Figure 4c; Figure 10b). It is important to note that seven zircon crystals in this sample have slightly older $^{207}Pb/^{206}Pb$ ages varying between 2.04 and 2.06 Ga which may indicate that some zircons began to grow during the early stages of cooling or even during the peak of UHT metamorphism.

As discussed for sample NE30, the younger zircon group in the sample NE163 is also dominated by inverse age zoning, suggesting the operation of a solid-state recrystallization process during high-temperature metamorphism. Thus, these data combined indicate that the bulk zircons grew close to the *solidus* conditions at c. 2.03 Ga and at c. 1.96 Ga the temperatures remained sufficiently high disturbing the anatectic zircons below the *solidus* temperature.

Sample NE157 yielded the youngest zircon ages of the three samples with only a single age at c. 1.96 Ga with a relatively narrow uncertainty. In contrast to the other samples, the neoblastic zircons have a flat to negative Gd_N/Yb_N slope indicating growth contemporaneous with garnet porphyroblasts, which are present in both leucosome and residue of this rock (Figure 4e-f; Figure 10b). Thus, we interpret the concordia age of c.1.96 Ga as the timing of garnet-bearing leucosome crystallization ~10-30 My later than the other samples. As discussed by Kelsey and Hand (2015), this difference is expected in HT/UHT migmatitic terranes, since heterogeneous melt loss rates will generate residual rocks with different *solidus* temperatures. We suggest that samples NE30 and NE163 may have higher *solidus* temperatures than sample NE157, favoring crystallization of zircon at different *P-T-t* conditions during the exhumation and cooling of the Arapiraca Complex. The long-lived, c. 70 My timing of melt crystallization in the Arapiraca Complex is reinforced by the wide spectrum of Ti-in-zircon temperatures from 720 ^{o}C up to 930 ^{o}C. However, only two zircon crystals with Ti concentration up to 53.3 recorded the near peak temperatures, while most zircons have Ti concentration between 5.77 and 31.66, recording only the retrograde stage of metamorphism (Table S4). Thus, the timing of peak UHT metamorphism in the Arapiraca Complex must have been slightly older than the calculated mean ages of c. 2.03 Ga as interpreted as the onset of zircon crystallization during magma cooling in the retrogressive path.

The anatectic zircons of the Arapiraca Complex diatexites have Th/U ratio between 0.01 and 23.4 with an average of 1.86, considering all samples, which may indicate the absence of Th-rich accessory minerals, notably monazite, during the crystallization of anatectic melt (*e.g.* Harley & Kelly, 2007; Rubatto, 2017). This behavior has been described in many UHT rocks, for example, Yakymchuk et al (2018) reported UHT anatectic zircons with Th/U ratios up to 100. Monazite is rare in our samples, where they are restricted as inclusions in garnet porphyroblasts (samples NE163 and NE157) or at the edges of magnetite-spinel grains (sample NE30) in the residue, and rarely found in the leucosome. These features may indicate that the high Th/U ratios in the anatectic zircons were controlled by the degree of chemical communication between the crystallizing melt and monazite in the residue (Kelsey, Clark, & Hand, 2008). In this scenario, we suggest that during retrogression monazite was partially consumed releasing a large amount of Th into the leucosome prior to the zircon growth (*e.g.* Yakymchuk & Brown, 2014). However, this hypothesis requires further monazite petrochronological studies, which may elucidate part of the prograde and/or peak of metamorphic conditions in the Arapiraca Complex and provide important clues about the monazite stability in melt-bearing UHT rocks (Kelsey et al., 2008).

2.5.3 Regional implications

2.5.3.1 Correlations with UHT rocks from the São Francisco Craton

The Paleoproterozoic UHT metamorphism associated with a clockwise *P-T* path determined here (Figure 7a) has also been determined for different localities in the São Francisco Craton (Figure 11a; Leite et al., 2009; Barbosa et al., 2006, 2017; Ackermand et al., 1987). In these localities, peak of UHT was constrained to between 2.08 and 2.04 Ga (EPMA monazite chemical ages), *P-T* conditions vary from 8.0 to 11.0 kbar and 950 to 1000 ^{o}C, and the metamorphic evolution comprises a clockwise

retrograde *P-T* paths (Figure 11b; Leite et al., 2009; Barbosa et al., 2006, 2017). It has been argued that UHT metamorphic conditions were reached during the collisional event involving the São Francisco and Congo blocks, in the context of the assembly of the Columbia supercontinent (*e.g.* Leite et al., 2009; Barbosa & Sabaté, 2004). Leite et al. (2009) and Barbosa et al. (2006) concluded that syn- to post-tectonic mafic and/or peraluminous magmas provided the heat source for the UHT metamorphism, allowing temperatures to rise from ~850 ºC to >900 ºC at ~8.0 kbar.

The contemporaneity between the UHT event described here with the ages reported for the collision in the São Francisco Craton indicate that the Arapiraca Complex may be a block of rocks that were once part of the construction of the São Francisco-Congo paleocontinent. In contrast to the UHT metamorphism related to continental collision recorded in the central portion of the craton that ended at c. 2.05 Ga, in the Arapiraca Complex the thermal disturbance is further extended for c. 90 My, up to 1.96 Ga. These younger ages for the UHT metamorphism, may indicate that the growth of the São Francisco-Congo paleocontinent was diachronous, probably controlled by lateral accretion of terranes (closure of zipper-shaped basins?) around the Archean blocks.

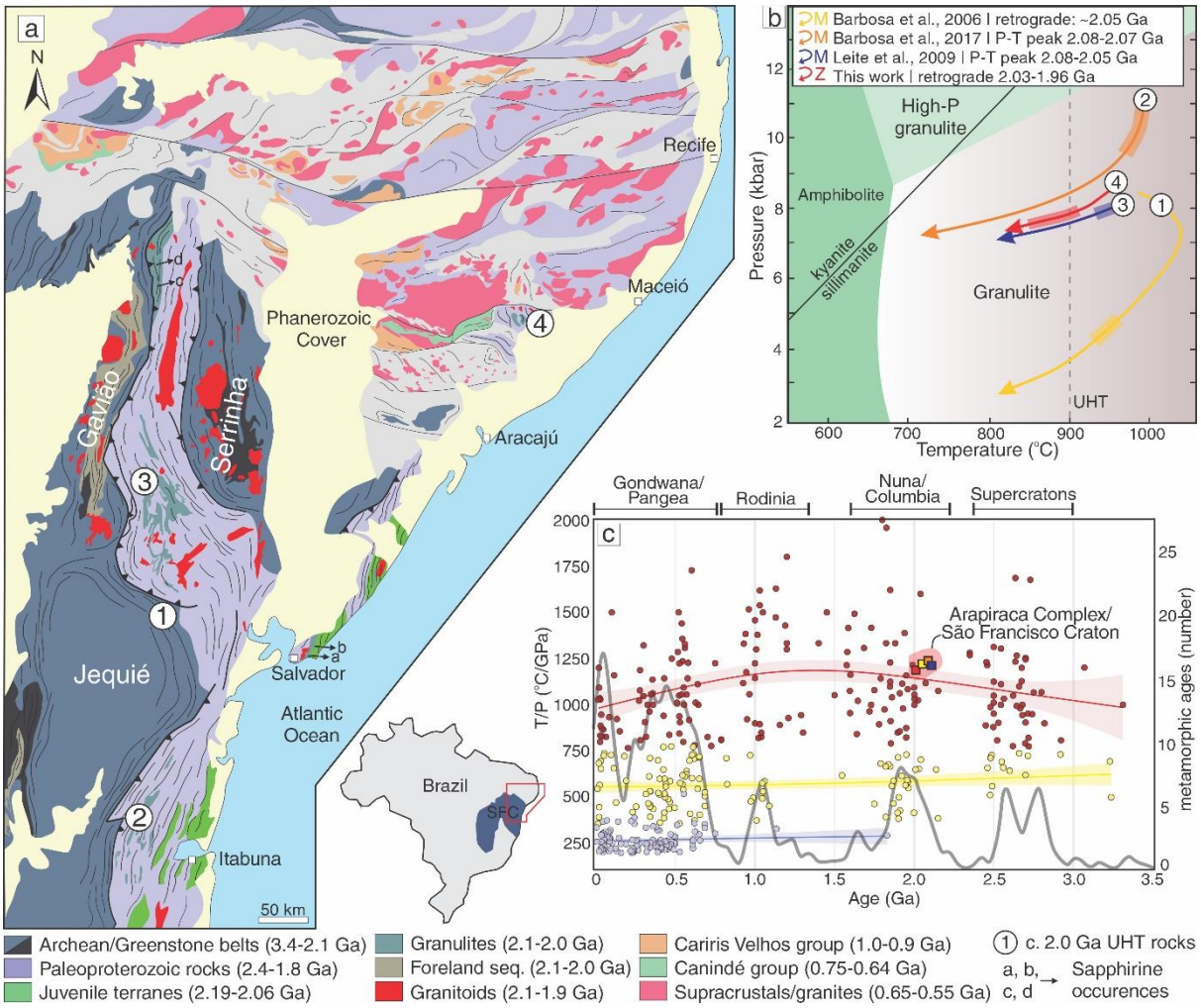

Figure 11. UHT metamorphism in the Arapiraca Complex and São Francisco Craton. (a) Tectonic map of the northeast of the São Francisco Craton and Southern Borborema Province showing the Achaean blocks/nuclei, and Paleoproterozoic and Neoproterozoic rocks. Numbers represent well-studied UHT rocks in the São Francisco Craton (1, 2, and 3) and Arapiraca Complex (4), whereas the letters a, b, c and d are other recognized occurrences of sapphirine-bearing rocks in the São Francisco Craton; (b) P-T metamorphic facies diagram showing the P-T-t paths for the UHT metamorphic rocks in the NE Brazil (same numbers as in (a)); note that all reported UHT rocks define clockwise paths. The thicker segment of the *P-T-t* paths illustrates the timing of the geochronological record (Z = zircon and M = Monazite); (c) Global distribution of metamorphic ages (456 localities from Brown & Johnson, 2018) with Arapiraca Complex/São Francisco UHT rocks (squares corresponding the same color as in (b)). Circles represent metamorphic ages grouped in high (red >775 °C/GPa), intermediate (yellow 775-375 °C/GPa), and low (blue <375 °C/GPa) metamorphic thermal gradients. Colored lines correspond to the linear regression of data and the grey line is the probability curve associated with the distribution of metamorphic ages.

More broadly, the transition from Rhyacian to Orosirian periods (c. 2.08 up to 1.8 Ga) is marked worldwide by orogenies with a high thermal gradient (dT/dP >775 °C/GPa) and occurrences of several UHT terranes, suggesting a close relationship

between the formation and preservation of UHT rocks, and the final stages of supercontinent assembly (Figure 11c; Brown & Johnson, 2018). Thus, further investigations of the Arapiraca Complex may provide clues about the tectonic setting and heat sources involved in UHT metamorphism, and how the São Francisco-Congo continent grew in the context of the Columbia supercontinent amalgamation (Rogers & Santosh, 2009). Additional geochronological investigations at about the age of emplacement of mafic-ultramafic rocks (pyroxenites, gabbos, and anorthosites) interleaved with metapelitic migmatites reported further west of the studied area (see Figure 1d) could provide important information on the heat source and tectonic setting of the Arapiraca Complex.

2.5.3.2 Dispersion of the São Francisco-Congo paleocontinent during the Neoproterozoic Orogeny

The São Francisco-Congo paleocontinent remained intact as a coherent landmass up to the Neoproterozoic era, when it started to break up, acting as a basement for precursor basins that were later inverted as they became involved in orogens (Pedrosa-Soares & Alkmim, 2011). The occurrence of Paleoproterozoic UHT rocks in the Arapiraca Complex converges to the model of São Francisco-Congo decratonization and terrane dispersion during Neoproterozoic as recently proposed by Ganade et al. 2020. Following this model, the Cariris Velhos extensional event at c. 0.98 Ga led to the opening of the Sergipano Basin and pulled away a series of cratonic blocks and ribbons from the São Francisco Craton, including the Arapiraca Complex and the Pernambuco-Alagoas massif (Figure 12a; Ganade et al., 2021). We envisage that during extension, a narrow ocean was formed, and these old continental blocks and ribbons formed highs separating basins (e.g. Péron-Pinvidic & Manatschal, 2010). The passive margin-type sediments were deposited over the extended margin of the São Francisco-Congo in the region that now forms the Southern Borborema Province

all the way north to the Pernambuco-Alagoas Massif. Sediments were derived from the erosion from Cariris Velhos igneous rocks and Paleoproterozoic continental blocks (Figure 12a; Oliveira et al., 2015). Extension was interrupted by the Southern Borborema Orogeny starting at c. 0.63 Ga, causing basin inversion and development of the Sergipano fold-and-thrust belt (Figure 12c). During this orogeny, the old continental basement ribbons and blocks, including the Arapiraca Complex, were folded and thrusted together with the sediments of the São Francisco-Congo paleocontinental margin, generating an inverted metamorphic sequence and collision magmatism between 0.59-0.57 Ga (Figure 12c; Oliveira et al., 2010).

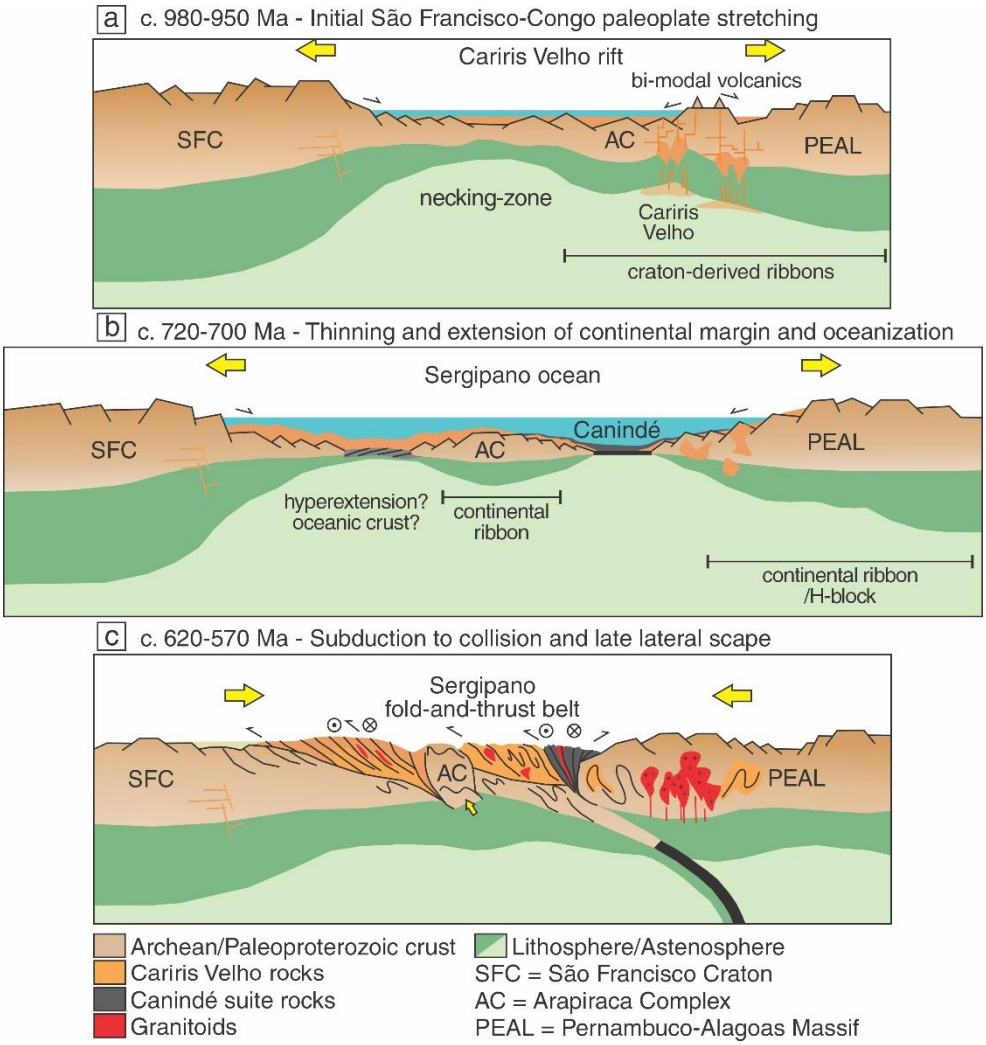

Figure 12. Schematic tectonic model for São Francisco-Congo paleocontinent dispersion in South Borborema Province, NE Brazil. Tonian to Cryogenian tectonic evolution of the continental margin of the São Francisco-Congo paleocontinent,

characterized by extension and mafic magmatism, narrow Sergipano ocean formation, and sedimentation, followed by continental collision. Inversion closed the basins forming the Sergipano fold-and-thrust belt, involving ribbons and blocks of Paleoproterozoic basement, such as the Arapiraca Complex (AC) as well others not shown (Jirau do Ponciano, Itabaiana and Simão Dias domes).

2.6. Conclusions

The diatexites of the Arapiraca Complex, an old structural high in amongst Neoproterozoic metasedimentary sequences, record Paleoproterozoic UHT metamorphism. A thermodynamic investigation of the sapphirine-bearing sample NE30 indicates that peak UHT metamorphism occurred at ~970 ^{o}C and ~8.5 kbar, followed by a near isobaric cooling path crossing the *solidus* at ~900 ^{o}C and 7.7 kbar evidenced by breakdown of garnet and formation of Al-rich orthopyroxene and cordierite. Similar to other UHT rocks worldwide (*e.g.* Dharmapriya et al., 2015, 2017; Ganguly et al., 2017), the investigated diatexite sample preserves distinct silica-saturated and silica-undersaturated domains preserved as inclusions domains within cordierite poikiloblasts, interpreted as result of heterogeneities in protolith composition and open system behavior during UHT metamorphism. Microstructural relationships and phase equilibrium modeling indicate that the sapphirine-bearing corona was formed during retrogression probably driven by chemical interaction between silica-undersaturated, magnetite-spinel cores and silica-rich leucosome. The petrochronological investigation reveals that the neoblastic zircons in the Arapiraca Complex diatexites grew from the crystallizing melt between c. 2.03 and 1.96 Ga, suggesting a protracted geotherm disturbance and slow thermal relaxation after the peak of UHT metamorphism. Rocks recording similar Paleoproterozoic UHT metamorphism have been documented in the São Francisco Craton, indicating that the Arapiraca Complex was part of the São Francisco-Congo paleocontinent, and that the regional UHT metamorphism was diachronous between 2.08 and 2.03 Ga and

related to the amalgamation of the Columbia supercontinent. We propose that during Neoproterozoic extension and formation of the Sergipano Basin, the Arapiraca Complex and other major continental ribbons such as the Pernambuco-Alagoas Massif were pulled away from the São Francisco-Congo paleocontinental margins. During the Late Neoproterozoic between 0.63 and 0.57 Ga, these cratonic fragments, including the Arapiraca Complex, collided against the north of São Francisco-Congo Craton, inverting the passive margin basins and forming the Sergipano fold-and-thrust belt in the Southern Borborema Province.

ACKNOWLEDGEMENTS

This research was supported by Serrapilheira Institute and FAPESP grants 1709-21887 and 2015/03703-7, respectively. Tesser thanks CAPES for their financial support and Geological Survey of Brazil for the logistical support during fieldwork. Thanks to Dr. A. Benisek for assistance with feldspar thermometry calculations.

CONFLICT OF INTEREST

The authors have no conflicts of interest.

2.7 References

Ackermand, D., Herd, R. K., Reinhardt, M., & Windley, B. F. (1987). Sapphirine parageneses from the Caraíba complex, Bahia, Brazil: the influence of Fe2+-Fe3+ distribution on the stability of sapphirine in natural assemblages. Journal of Metamorphic Geology, 5(3), 323-339.

Baba, S. (2002). Tectono-metamorphic events in the North Atlantic region in the Palaeoproterozoic from the view point of high-grade metamorphic rocks in the Lewisian Complex, South Harris, NW Scotland. Gondwana Research, 5(4), 757-770.

Baldwin, J. A., Powell, R., Brown, M., Moraes, R., & Fuck, R. A. (2005). Modelling of mineral equilibria in ultrahigh-temperature metamorphic rocks from the Anápolis-Itauçu Complex, central Brazil. Journal of Metamorphic Geology, 23(7), 511-531.

Barbosa, J. S. F., & Sabaté, P. (2004). Archean and Paleoproterozoic crust of the São Francisco craton, Bahia, Brazil: geodynamic features. Precambrian Research, 133(1-2), 1-27.

Barbosa, J., Nicollet, C., Leite, C., Kienast, J. R., Fuck, R. A., & Macedo, E. P. (2006). Hercynite-quartz-bearing granulites from Brejões Dome area, Jequié Block, Bahia, Brazil: Influence of charnockite intrusion on granulite facies metamorphism. Lithos, 92(3-4), 537-556.

Barbosa, J. S. F., & Barbosa, R. G. (2017). The Paleoproterozoic eastern bahia orogenic domain. In São Francisco Craton, Eastern Brazil. 57-69p. Springer, Cham.

Barbosa, J. S. F., de Menezes Leal, A. B., Fuck, R. A., De Oliveira, J. S. D. S., Gonçalves, P., & Leite, C. D. M. M. (2017). Metamorfismo de temperatura ultra-alta de granulitos com safirina de 2.0 Ga do Bloco Itabuna-Salvador-Curaçá, Bahia, Brasil. Geologia USP. Série Científica, 17(1), 89-108.

Benisek, A., Dachs, E., & Kroll, H. (2010). A ternary feldspar-mixing model based on calorimetric data: development and application. Contributions to Mineralogy and Petrology, 160(3), 327-337.

Brown, M., & Johnson, T. (2018). Secular change in metamorphism and the onset of global plate tectonics. American Mineralogist, 103(2), 181-196.

Bueno, J. F., Oliveira, E. P., McNaughton, N. J., & Laux, J. H. (2009). U-Pb dating of granites in the Neoproterozoic Sergipano Belt, NE-Brazil: implications for the timing

and duration of continental collision and extrusion tectonics in the Borborema Province. Gondwana Research, 15(1), 86-97.

Caxito, F. D. A., Santos, L. C. M. D. L., Ganade, C. E., Bendaoud, A., Fettous, E. H., & Bouyo, M. H. (2020). Toward an integrated model of geological evolution for NE Brazil-NW Africa: The Borborema Province and its connections to the Trans-Saharan (Benino-Nigerian and Tuareg shields) and Central African orogens. Brazilian Journal of Geology, 50(2).

Cruz, R. F. D., Pimentel, M. M., Accioly, A. C. D. A., & Rodrigues, J. B. (2014). Geological and isotopic characteristics of granites from the Western Pernambuco-Alagoas Domain: implications for the crustal evolution of the Neoproterozoic Borborema Province. Brazilian Journal of Geology, 44(4), 627-652.

Dasgupta, S., & Sengupta, P. (2003). Indo-Antarctic correlation: a perspective from the Eastern Ghats granulite belt, India. Geological Society, London, Special Publications, 206(1), 131-143.

Davison, I., & dos Santos, R. A. (1989). Tectonic evolution of the Sergipano fold belt, NE Brazil, during the Brasiliano orogeny. Precambrian Research, 45(4), 319-342.

de Capitani, C., & Petrakakis, K. (2010). The computation of equilibrium assemblage diagrams with Theriak/Domino software. American Mineralogist, 95(7), 1006-1016.

de Oliveira Chaves, A., Ernst, R. E., Söderlund, U., Wang, X., & Naeraa, T. (2019). The 920-900 Ma Bahia-Gangila LIP of the São Francisco and Congo cratons and link with Dashigou-Chulan LIP of North China craton: New insights from U-Pb geochronology and geochemistry. Precambrian Research, 329, 124-137.

Degler, R., Pedrosa-Soares, A., Novo, T., Tedeschi, M., Silva, L. C., Dussin, I., & Lana, C. (2018). Rhyacian-Orosirian isotopic records from the basement of the Araçuaí-

Ribeira orogenic system (SE Brazil): Links in the Congo-São Francisco palaeocontinent. Precambrian Research, 317, 179-195.

Dharmapriya, P.L., Malaviarachchi, S.P.K., Galli, A., Su, Ben-Xun, Subasinghe, N.D., & Dissanayake, C.B. (2015). Rare evidence for formation of garnet + corundum during isobaric cooling of UHT metapelites: new insights for retrograde P-T trajectory of the Highland Complex, Sri Lanka. Lithos, 220, 300-317.

Dharmapriya, P. L., Malaviarachchi, S. P., Kriegsman, L. M., Sajeev, K., Galli, A., Osanai, Y., N. D., Subasinghe & Dissanayake, C. B. (2017). Distinct metamorphic evolution of alternating silica-saturated and silica-deficient microdomains within garnet in ultrahigh-temperature granulites: An example from Sri Lanka. Geoscience Frontiers, 8(5), 1115-1133.

Doukkari, S. A., Diener, J. F., Ouzegane, K., & Kienast, J. R. (2018). Mineral equilibrium modelling and calculated chemical potential relations of reaction textures in the ultrahigh-temperature In Ouzzal terrane (In Hihaou area, Western Hoggar, Algeria). Journal of Metamorphic Geology, 36(9), 1175-1198.

Droop, G. T. R. (1987). A general equation for estimating Fe3+ concentrations in ferromagnesian silicates and oxides from microprobe analyses, using stoichiometric criteria. Mineralogical Magazine, 51(361), 431-435.

Elkins, L. T., & Grove, T. L. (1990). Ternary feldspar experiments and thermodynamic models. American Mineralogist, 75(5-6), 544-559.

Ferry, J. M., & Watson, E. B. (2007). New thermodynamic models and revised calibrations for the Ti-in-zircon and Zr-in-rutile thermometers. Contributions to Mineralogy and Petrology, 154(4), 429-437.

Fuhrman, M. L., & Lindsley, D. H. (1988). Ternary-feldspar modeling and thermometry. American Mineralogist, 73(3-4), 201-215.

Ganade de Araujo, C. E., Weinberg, R. F., & Cordani, U. G. (2014). Extruding the Borborema Province (NE-Brazil): a two-stage Neoproterozoic collision process. Terra Nova, 26(2), 157-168.

Ganguly, P., Bose, S., Das, K., Torimoto, J., & Ghosh, G. (2017). Origin of spinel + quartz assemblage in a Si-undersaturated ultrahigh-temperature aluminous granulite and its implication for the P–T–fluid history of the Phulbani domain, Eastern Ghats belt, India. Journal of Petrology, 58(10), 1941-1974.

Griffin, W. L. (2008). GLITTER: data reduction software for laser ablation ICP-MS. Laser Ablation ICP-MS in the Earth Sciences: Current practices and outstanding issues, 308-311.

Guimarães, I. P., Van Schmus, W. R., de Brito Neves, B. B., Bittar, S. M. B., Silva Filho, A. F., & Armstrong, R. (2012). U-Pb zircon ages of orthogneisses and supracrustal rocks of the Cariris Velhos belt: onset of Neoproterozoic rifting in the Borborema Province, NE Brazil. Precambrian Research, 192, 52-77.

Harley, S. L. (1989). The origins of granulites: a metamorphic perspective. Geological Magazine, 126(3), 215-247.

Harley, S. L. (1998). On the occurrence and characterization of ultrahigh-temperature (UHT) crustal metamorphism. What drives metamorphism and metamorphic reactions? Geological Society of London, Spec. Pub., 138, 75-101.

Harley, S. L. (2008). Refining the P-T records of UHT crustal metamorphism. Journal of Metamorphic Geology, 26, 125–154.

Harley, S. L., & Kelly, N. M. (2007). Zircon tiny but timely. Elements, 3(1), 13-18.

Hokada, T. (2001). Feldspar thermometry in ultrahigh-temperature metamorphic rocks: Evidence of crustal metamorphism attaining~ 1100 C in the Archean Napier Complex, East Antarctica. American Mineralogist, 86(7-8), 932-938.

Holland, T., & Powell, R. (2003). Activity-composition relations for phases in petrological calculations; an asymmetric multicomponent formulation. Contributions to Mineralogy and Petrology, 145, 492-501.

Holland, T. J. B., & Powell, R. (2011). An improved and extended internally consistent thermodynamic dataset for phases of petrological interest, involving a new equation of state for solids. Journal of Metamorphic Geology, 29(3), 333-383.

Holness, M. B., & Sawyer, E. W. (2008). On the pseudomorphing of melt-filled pores during the crystallization of migmatites. Journal of Petrology, 49(7), 1343-1363.

Jackson, S. E., Pearson, N. J., Griffin, W. L., & Belousova, E. A. (2004). The application of laser ablation-inductively coupled plasma-mass spectrometry to in situ U-Pb zircon geochronology. Chemical Geology, 211(1-2), 47-69.

Kelly, N. M., & Harley, S. L. (2005). An integrated microtextural and chemical approach to zircon geochronology: refining the Archaean history of the Napier Complex, east Antarctica. Contributions to Mineralogy and Petrology, 149(1), 57-84.

Kelsey, D. E., White, R. W., & Powell, R. (2005). Calculated phase equilibria in K2O-FeO-MgO-Al2O3-SiO2-H2O for silica-undersaturated sapphirine-bearing mineral assemblages. Journal of Metamorphic Geology, 23(4), 217-239.

Kelsey, D. E. (2008). On ultrahigh-temperature crustal metamorphism. Gondwana Research, 13, 1–29.

Kelsey, D. E., Clark, C., & Hand, M. (2008). Thermobarometric modelling of zircon and monazite growth in melt-bearing systems: Examples using model metapelitic and metapsammitic granulites. Journal of Metamorphic Geology, 26(2), 199-212.

Kelsey, D. E., & Hand, M. (2015). On ultrahigh temperature crustal metamorphism: phase equilibria, trace element thermometry, bulk composition, heat sources, timescales and tectonic settings. Geoscience Frontiers, 6(3), 311-356.

Kelsey, D. E., Morrissey, L. J., Hand, M., Clark, C., Tamblyn, R., Gaehl, A. A., & Marshall, S. (2017). Significance of post-peak metamorphic reaction microstructures in the ultrahigh temperature Eastern Ghats Province, India. Journal of Metamorphic Geology, 35(9), 1081-1109.

Kriegsman, L. M., & Hensen, B. J. (1998). Back reaction between restite and melt: Implications for geothermobarometry and pressure-temperature paths. Geology, 26(12), 1111-1114.

Kroll, H., Evangelakakis, C., & Voll, G. (1993). Two-feldspar geothermometry: a review and revision for slowly cooled rocks. Contributions to Mineralogy and petrology, 114(4), 510-518.

Laurent, A. T., Bingen, B., Duchene, S., Whitehouse, M. J., Seydoux-Guillaume, A. M., & Bosse, V. (2018). Decoding a protracted zircon geochronological record in ultrahigh temperature granulite, and persistence of partial melting in the crust, Rogaland, Norway. Contributions to Mineralogy and Petrology, 173(4), 29.

Ledru, P., Johan, V., Milési, J. P., & Tegyey, M. (1994). Markers of the last stages of the Palaeoproterozoic collision: evidence for a 2 Ga continent involving circum-South Atlantic provinces. Precambrian Research, 69(1-4), 169-191.

Leite, C., Barbosa, J. S. F., Goncalves, P., Nicollet, C., & Sabaté, P. (2009). Petrological evolution of silica-undersaturated sapphirine-bearing granulite in the Paleoproterozoic Salvador–Curaçá Belt, Bahia, Brazil. Gondwana Research, 15(1), 49-70.

Lima, H. M., Pimentel, M. M., de Lira Santos, L. C. M., & Dantas, E. L. (2019). Isotopic and geochemical characterization of the metavolcano-sedimentary rocks of the Jirau do Ponciano dome: A structural window to a Paleoproterozoic continental arc root within the Southern Borborema province, Northeast Brazil. Journal of South American Earth Sciences, 90, 54-69.

Loose, D., & Schenk, V. (2018). 2.09 Ga old eclogites in the Eburnean-Transamazonian orogen of southern Cameroon: Significance for Palaeoproterozoic plate tectonics. Precambrian Research, 304, 1-11.

McDonough, W. F., & Sun, S. S. (1995). The composition of the Earth. Chemical geology, 120(3-4), 223-253.

Mendes, V.A., Brito, M.F.L., & Paiva, I.P. (2009). Programa Geologia do Brasil-PGB. Arapiraca. Folha SC.24-X-D. Estado de Alagoas, Pernambuco e Sergipe. In: Mapa Geológico. Escala: 1:250.000, Recife.

Moraes, R., Brown, M., Fuck, R. A., Camargo, M. A., & Lima, T. M. (2002). Characterization and P-T evolution of melt-bearing ultrahigh-temperature granulites: an example from the Anápolis–Itauçu Complex of the Brasília Fold Belt, Brazil. Journal of Petrology, 43(9), 1673-1705.

Mori, P. E., Correia, C. T., Reeves, S., & Haukka, M. (1999). Development of a fused glass disc XRF facility and comparison with the pressed powder pellet technique at

Instituto de Geociências, São Paulo University, Brazil. Revista Brasileira de Geociências, 29(3), 441-446.

Neves, S. P. (2015). Constraints from zircon geochronology on the tectonic evolution of the Borborema Province (NE Brazil): widespread intracontinental Neoproterozoic reworking of a Paleoproterozoic accretionary orogen. Journal of South American Earth Sciences, 58, 150-164.

Neves, S. P., da Silva, J. M. R., & Bruguier, O. (2016). The transition zone between the Pernambuco-Alagoas Domain and the Sergipano Belt (Borborema Province, NE Brazil): Geochronological constraints on the ages of deposition, tectonic setting and metamorphism of metasedimentary rocks. Journal of South American Earth Sciences, 72, 266-278.

Oliveira, E. P., & Tarney, J. (1990). Petrogenesis of the Canindé de São Francisco Complex: a major Late Proterozoic gabbroic body in the Sergipe Foldbelt, northeastern Brazil. Journal of South American Earth Sciences, 3(2-3), 125-140.

Oliveira, E. P., Windley, B. F., McNaughton, N. J., Pimentel, M., & Fletcher, I. R. (2004). Contrasting copper and chromium metallogenic evolution of terranes in the Palaeoproterozoic Itabuna-Salvador-Curaçá orogen, São Francisco craton, Brazil: new zircon (SHRIMP) and Sm-Nd (model) ages and their significance for orogen-parallel escape tectonics. Precambrian Research, 128(1-2), 143-165.

Oliveira, E. P., Toteu, S. F., Araújo, M. N. C., Carvalho, M. J., Nascimento, R. S., Bueno, J. F., & Basilici, G. (2006). Geologic correlation between the Neoproterozoic Sergipano belt (NE Brazil) and the Yaoundé belt (Cameroon, Africa). Journal of African Earth Sciences, 44(4-5), 470-478.

Oliveira, E. P., Windley, B. F., & Araújo, M. N. (2010). The Neoproterozoic Sergipano orogenic belt, NE Brazil: a complete plate tectonic cycle in western Gondwana. Precambrian Research, 181(1-4), 64-84.

Oliveira, E. P., McNaughton, N. J., Windley, B. F., Carvalho, M. J., & Nascimento, R. S. (2015). Detrital zircon U–Pb geochronology and whole-rock Nd-isotope constraints on sediment provenance in the Neoproterozoic Sergipano orogen, Brazil: From early passive margins to late foreland basins. Tectonophysics, 662, 183-194.

Pattison, D. R., Chacko, T., Farquhar, J., & McFarlane, C. R. (2003). Temperatures of granulite-facies metamorphism: constraints from experimental phase equilibria and thermobarometry corrected for retrograde exchange. Journal of Petrology, 44(5), 867-900.

Pearce, N. J., Perkins, W. T., Westgate, J. A., Gorton, M. P., Jackson, S. E., Neal, C. R., & Chenery, S. P. (1997). A compilation of new and published major and trace element data for NIST SRM 610 and NIST SRM 612 glass reference materials. Geostandards Newsletter, 21(1), 115-144.

Pedrosa-Soares, A. C., & de Alkmim, F. F. (2011). How many rifting events preceded the development of the Araçuaí-West Congo orogen? Geonomos 19(2), 244-251.

Péron-Pinvidic, G., & Manatschal, G. (2010). From microcontinents to extensional allochthons: witnesses of how continents rift and break apart? Petroleum Geoscience, 16(3), 189-197.

Rogers, J. J., & Santosh, M. (2009). Tectonics and surface effects of the supercontinent Columbia. Gondwana Research, 15(3-4), 373-380.

Rosa, M. D. L. D. S., Conceição, J. A. D., Marinho, M. M., Pereira, F. D. S., & Conceição, H. (2020). U-Pb SHRIMP dating of the Itabaiana Dome: a Mesoarchean

basement inlier (2.83 Ga) in the Sergipano Orogenic System, Borborema Province. Brazilian Journal of Geology, 50(2).

Rubatto, D. (2002). Zircon trace element geochemistry: partitioning with garnet and the link between U-Pb ages and metamorphism. Chemical Geology, 184(1-2), 123-138.

Rubatto, D. (2017). Zircon: the metamorphic mineral. Reviews in Mineralogy and Geochemistry, 83(1), 261-295.

Sawyer, E. W. (2008). Atlas of Migmatites. Special Publications of The Canadian Mineralogist, vol. 9, 386 p.

Schneider, C. A., Rasband, W. S., & Eliceiri, K. W. (2012). NIH Image to ImageJ: 25 years of image analysis. Nature Methods, 9(7), 671-675.

Simões Neto, F. L., Julià, J., & Schimmel, M. (2019). Upper-mantle structure of the Borborema Province, NE Brazil, from P-wave tomography: implications for rheology and volcanism. Geophysical Journal International, 216(1), 231-250.

Siqueira, R., Hollanda, M. H. B. M., & Basei, M. A. S. (2014). A novel approach to (LA-ICP-MS acquired) U–Th–Pb data processing. In: IX South-American Symposium on Isotope Geology. Chile, 2014. Program and Abstracts, 306.

Tadokoro, H., Tsunogae, T., & Santosh, M. (2008). Metamorphic *P-T* path of the eastern Trivandrum Granulite Block, southern India: implications for regional correlation of lower crustal fragments. Journal of Mineralogical and Petrological Sciences, 103(4), 279–284.

Taylor, R. J., Kirkland, C. L., & Clark, C. (2016). Accessories after the facts: Constraining the timing, duration and conditions of high-temperature metamorphic processes. Lithos, 264, 239-257.

Tchakounté, J., Eglinger, A., Toteu, S. F., Zeh, A., Nkoumbou, C., Mvondo-Ondoa, J., J., Penaye., M. de Wit & Barbey, P. (2017). The Adamawa-Yadé domain, a piece of Archaean crust in the Neoproterozoic central African orogenic belt (Bafia area, Cameroon). Precambrian Research, 299, 210-229.

Teixeira, J. B. G., Misi, A., Silva, M. D. G. D., & Brito, R. S. C. D. (2019). Reconstruction of Precambrian terranes of Northeastern Brazil along Cambrian strike-slip faults: a new model of geodynamic evolution and gold metallogeny in the State of Bahia. Brazilian Journal of Geology, 49(3).

Vermeesch, P. (2018). IsoplotR: A free and open toolbox for geochronology. Geoscience Frontiers, 9(5), 1479-1493.

Watson, E. B., & Harrison, T. M. (2005). Zircon thermometer reveals minimum melting conditions on earliest Earth. Science 308:841–844

Weber, F., Gauthier-Lafaye, F., Whitechurch, H., Ulrich, M., & El Albani, A. (2016). The 2-Ga Eburnean Orogeny in Gabon and the opening of the Francevillian intracratonic basins: A review. Comptes Rendus Geoscience, 348(8), 572-586.

Wen, S., & Nekvasil, H. (1994). SOLVALC: An interactive graphics program package for calculating the ternary feldspar solvus and for two-feldspar geothermometry. Computers and Geosciences, 20(6), 1025-1040.

Wheller, C. J., & Powell, R. (2014). A new thermodynamic model for sapphirine: calculated phase equilibria in K2O-FeO-MgO-Al2O3-SiO2-H2O-TiO2-Fe2O3. Journal of Metamorphic Geology, 32(3), 287-299.

White, R., Powell, R. & Clarke, G.L. (2002a). The interpretation of reaction textures in Fe-rich metapelitic granulites of the Musgrave Block, central Australia:

constraints from mineral equilibrium calculations in the system K2O-FeO-MgO-Al2O3-SiO2-H2O-TiO2-Fe2O3. Journal of Metamorphic Geology, 20, 41-55.

White, R. W., & Powell, R. (2002b). Melt loss and the preservation of granulite facies mineral assemblages. Journal of Metamorphic Geology, 20(7), 621-632.

White, R. W., Powell, R., & Baldwin, J. A. (2008). Calculated phase equilibria involving chemical potentials to investigate the textural evolution of metamorphic rocks. Journal of Metamorphic Geology, 26(1), 181–198.

White, R. W., Powell, R., & Johnson, T. E. (2014a). The effect of Mn on mineral stability in metapelites revisited: New a–x relations for manganese-bearing minerals. Journal of Metamorphic Geology, 32(8), 809-828.

White, R.W., Powell, R., Holland, T.J.B., Johnson, T.E. & Green, E.C.R. (2014b). New mineral activity-composition relations for thermodynamic calculations in metapelitic systems. Journal of Metamorphic Geology, 32, 261-286.

Yakymchuk, C., & Brown, M. (2014). Behaviour of zircon and monazite during crustal melting. Journal of the Geological Society, 171(4), 465-479.

Yakymchuk, C., Rehm, A., Liao, Z., & Cottle, J. M. (2019). Petrochronology of oxidized granulites from southern Peru. Journal of Metamorphic Geology, 37(6), 839-862.

Zhao, G., Sun, M., Wilde, S. A., & Li, S. (2004). A Paleo-Mesoproterozoic supercontinent: assembly, growth and breakup. Earth-Science Reviews, 67(1-2), 91-123.

2.8 Supplementary Materials

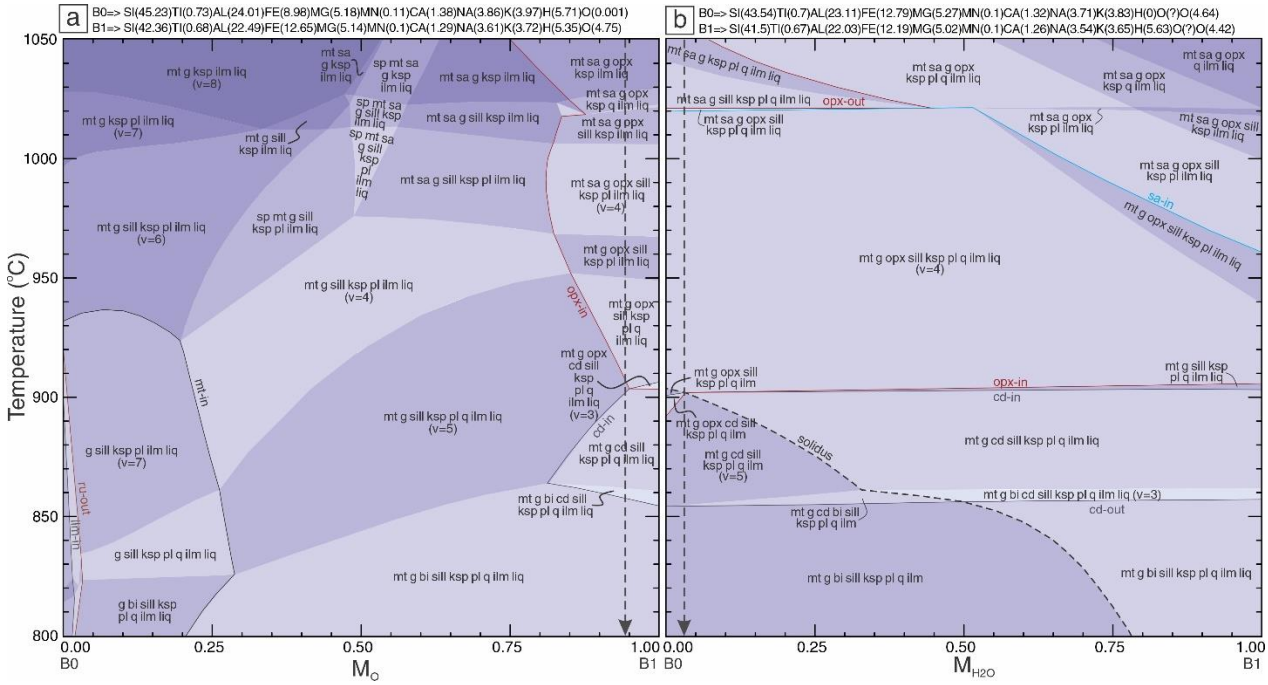

Figure S1. (a) T-MO, and (b) T-MH2O models calculated at 7.9 kbar for sample NE30. The vertical dashed lines depict the composition chosen to adjust the bulk composition and the composition in atomic proportion are provided above each model.

Table S1. Representative EPMA microanalysis results for sample NE30

Mineral	g	g	g	g	g	g	g	g	g	g	g
ID	44	45	33	32	42	43	64	34	30	47	39
Obs.:	core	core	core	core	core	core	core	rim	rim	rim	rim
SiO_2	39.10	39.28	39.50	39.51	39.46	39.89	39.57	39.20	39.48	50.06	38.96
TiO_2	0.01	0.01	0.00	0.00	0.01	0.03	0.02	0.01	0.00	0.00	0.00
Al_2O_3	22.79	23.05	22.60	22.69	23.22	25.34	22.79	22.73	22.84	17.77	22.97
Cr_2O_3	0.01	0.01	0.00	0.00	0.00	0.00	0.01	0.02	0.00	0.01	0.00
FeO*	22.56	22.14	22.67	22.71	22.63	21.61	23.38	23.10	22.39	18.21	23.10
MnO	1.39	1.58	1.47	1.56	1.46	1.22	1.23	2.14	2.89	2.43	2.66
MgO	12.14	11.74	11.99	11.94	11.86	11.27	11.91	11.13	10.65	8.64	10.83
CaO	1.01	1.28	0.99	1.12	1.04	1.18	1.16	1.15	1.16	0.98	0.90
BaO	-	-	-	-	-	-	-	-	-	-	-
Na_2O	-	-	-	-	-	-	-	-	-	-	-
K_2O	-	-	-	-	-	-	-	-	-	-	-
SrO	-	-	-	-	-	-	-	-	-	-	-
ZnO	-	-	-	-	-	-	-	-	-	-	-
Cl	-	-	-	-	-	-	-	-	-	-	-
F	-	-	-	-	-	-	-	-	-	-	-
Total	99.00	99.09	99.22	99.53	99.68	100.54	100.08	99.47	99.41	98.10	99.43
Oxy.	12	12	12	12	12	12	12	12	12	12	12
Si	2.974	2.987	3.002	2.994	2.984	2.984	2.985	2.988	3.017	3.917	2.976
Ti	0.000	0.001	0.000	0.000	0.001	0.002	0.001	0.000	0.000	0.000	0.000
Al	2.043	2.066	2.024	2.027	2.070	2.234	2.026	2.042	2.057	1.639	2.068
Cr	0.000	0.000	0.000	0.000	0.000	0.000	0.001	0.001	0.000	0.001	0.000
Fe^{+3}	0.009	0.000	0.000	0.000	0.000	0.000	0.001	0.000	0.000	0.000	0.000
Fe^{+2}	1.426	1.408	1.441	1.439	1.431	1.352	1.474	1.472	1.431	1.192	1.476
Mn	0.090	0.102	0.095	0.100	0.094	0.078	0.079	0.138	0.187	0.161	0.172
Mg	1.376	1.331	1.358	1.349	1.337	1.257	1.339	1.265	1.213	1.008	1.233
Ca	0.082	0.104	0.081	0.091	0.084	0.094	0.094	0.094	0.095	0.082	0.074
Ba	-	-	-	-	-	-	-	-	-	-	-
Na	-	-	-	-	-	-	-	-	-	-	-
K	-	-	-	-	-	-	-	-	-	-	-
Sr	-	-	-	-	-	-	-	-	-	-	-
Zn	-	-	-	-	-	-	-	-	-	-	-
Cl	-	-	-	-	-	-	-	-	-	-	-
F	-	-	-	-	-	-	-	-	-	-	-
Sum	8.000	8.000	8.000	8.000	8.000	8.000	8.000	8.000	8.000	8.000	8.000
X_{Mg}	0.49	0.49	0.49	0.48	0.48	0.48	0.48	0.46	0.46	0.46	0.46
X_{Prp}	0.46	0.45	0.46	0.45	0.45	0.45	0.45	0.43	0.41	0.41	0.42
y(opx)	-	-	-	-	-	-	-	-	-	-	-
Fe^{+3}/Fe^{2+}	0.01	0.00	0.00	0.00	0.00	0.00	0.00	0.00	0.00	0.00	0.00
X_{An}	-	-	-	-	-	-	-	-	-	-	-
X_{Or}	-	-	-	-	-	-	-	-	-	-	-

XMg = molar (Mg / [Mg + Fe])
XPrp = molar (Mg / [Mg + Fe + Ca + Mn])
y(opx) = molar (Al - [2 - Si])
XAn = molar (Ca / [Ca + Na + K])
XOr = molar (K / [K + Ca + Na])

g 59 rim	g 36 rim	g 70 rim	g 72 rim	g 5 core	g 6 core	g 71 rim	g 4 core	g 73 rim	g 29 rim	opx 68 -	opx 25 -
39.38	39.10	39.49	39.02	40.28	38.59	39.59	38.55	38.87	39.56	48.53	49.86
0.01	0.00	0.00	0.01	0.00	0.00	0.01	0.01	0.03	0.03	0.00	0.00
22.82	22.71	22.67	22.72	21.79	22.54	22.65	22.63	22.83	22.78	7.13	8.20
0.02	0.00	0.01	0.00	0.00	0.01	0.02	0.00	0.01	0.00	0.03	0.00
24.07	23.08	24.33	23.86	22.93	23.86	24.18	23.47	23.99	23.01	20.18	16.99
1.62	2.63	1.67	1.92	2.57	2.60	1.81	2.84	2.13	3.17	1.04	0.86
11.17	10.71	11.22	10.98	10.52	10.93	11.02	10.64	10.80	10.34	22.79	23.61
1.25	0.92	1.08	1.25	1.04	1.10	1.13	1.09	1.18	0.97	0.09	0.09
-	-	-	-	-	-	-	-	-	-	-	-
-	-	-	-	-	-	-	-	-	-	0.01	0.01
-	-	-	-	-	-	-	-	-	-	0.00	0.00
-	-	-	-	-	-	-	-	-	-	-	-
-	-	-	-	-	-	-	-	-	-	-	-
-	-	-	-	-	-	-	-	-	-	-	-
-	-	-	-	-	-	-	-	-	-	-	-
100.34 12	99.15 12	100.47 12	99.76 12	99.13 12	99.63 12	100.41 12	99.22 12	99.85 12	99.86 12	99.80 6	99.63 6
2.978	2.998	2.984	2.970	3.095	2.946	2.996	2.957	2.960	3.020	1.784	1.817
0.001	0.000	0.000	0.001	0.000	0.000	0.001	0.001	0.002	0.002	0.000	0.000
2.034	2.052	2.019	2.038	1.973	2.028	2.020	2.046	2.049	2.049	0.309	0.352
0.001	0.000	0.000	0.000	0.000	0.001	0.001	0.000	0.001	0.000	0.001	0.000
0.008	0.000	0.012	0.020	0.000	0.079	0.000	0.038	0.026	0.000	0.122	0.015
1.514	1.480	1.526	1.499	1.474	1.444	1.531	1.467	1.502	1.469	0.498	0.503
0.104	0.171	0.107	0.124	0.167	0.168	0.116	0.185	0.137	0.205	0.032	0.027
1.259	1.224	1.264	1.246	1.205	1.244	1.243	1.217	1.226	1.177	1.249	1.282
0.101	0.075	0.088	0.102	0.085	0.090	0.091	0.089	0.097	0.079	0.004	0.004
-	-	-	-	-	-	-	-	-	-	-	-
-	-	-	-	-	-	-	-	-	-	0.001	0.001
-	-	-	-	-	-	-	-	-	-	0.000	0.000
-	-	-	-	-	-	-	-	-	-	-	-
-	-	-	-	-	-	-	-	-	-	-	-
-	-	-	-	-	-	-	-	-	-	-	-
-	-	-	-	-	-	-	-	-	-	-	-
8.000	8.000	8.000	8.000	8.000	8.000	8.000	8.000	8.000	8.000	4.000	4.000
0.45	0.45	0.45	0.45	0.45	0.45	0.45	0.45	0.45	0.44	0.67	0.71
0.42	0.41	0.42	0.42	0.41	0.42	0.42	0.41	0.41	0.40	-	-
-	-	-	-	-	-	-	-	-	-	0.09	0.17
0.01	0.00	0.01	0.01	0.00	0.05	0.00	0.03	0.02	0.00	0.24	0.03
-	-	-	-	-	-	-	-	-	-	-	-
-	-	-	-	-	-	-	-	-	-	-	-

opx 1	opx 51	opx 3	opx 9	opx 52	opx 27	opx 17	opx 28	opx 40	opx 61	opx 46	opx 62
-	-	-	-	-	-	-	-	-	-	-	-
49.18	49.24	48.66	48.74	49.59	50.42	49.17	49.52	50.05	50.61	49.38	49.42
0.03	0.00	0.05	0.09	0.04	0.06	0.07	0.04	0.00	0.00	0.09	0.04
6.64	6.29	6.90	6.90	5.51	4.47	7.09	6.02	5.81	4.99	6.95	6.39
0.03	0.08	0.05	0.02	0.04	0.00	0.00	0.02	0.00	0.01	0.06	0.00
19.84	18.60	19.76	19.53	18.17	20.54	19.47	20.34	18.99	17.79	18.03	18.09
0.95	0.87	1.10	1.16	1.11	0.38	1.22	0.37	1.09	0.90	0.74	0.77
22.68	23.97	22.82	22.96	24.07	23.23	22.64	23.19	24.11	25.43	24.13	24.40
0.08	0.14	0.06	0.09	0.09	0.07	0.06	0.07	0.07	0.10	0.07	0.07
-	-	-	-	-	-	-	-	-	-	-	-
0.00	0.02	0.00	0.01	0.01	0.03	0.00	0.00	0.03	0.02	0.02	0.00
0.00	0.03	0.00	0.00	0.00	0.02	0.00	0.01	0.00	0.02	0.00	0.00
-	-	-	-	-	-	-	-	-	-	-	-
-	-	-	-	-	-	-	-	-	-	-	-
-	-	-	-	-	-	-	-	-	-	-	-
-	-	-	-	-	-	-	-	-	-	-	-
99.426	99.246	99.406	99.506	98.636	99.216	99.726	99.576	100.156	99.866	99.466	99.186
1.816	1.808	1.795	1.795	1.832	1.867	1.809	1.823	1.824	1.837	1.804	1.810
0.001	0.000	0.001	0.002	0.001	0.002	0.002	0.001	0.000	0.000	0.003	0.001
0.289	0.272	0.300	0.299	0.240	0.195	0.307	0.261	0.250	0.213	0.299	0.276
0.001	0.002	0.001	0.000	0.001	0.000	0.000	0.000	0.000	0.000	0.002	0.000
0.077	0.113	0.105	0.106	0.094	0.070	0.070	0.090	0.105	0.114	0.086	0.102
0.536	0.458	0.505	0.495	0.467	0.566	0.529	0.537	0.474	0.426	0.465	0.452
0.030	0.027	0.034	0.036	0.035	0.012	0.038	0.012	0.034	0.028	0.023	0.024
1.248	1.312	1.255	1.261	1.325	1.282	1.242	1.273	1.310	1.376	1.314	1.332
0.003	0.005	0.002	0.004	0.004	0.003	0.002	0.003	0.003	0.004	0.003	0.003
-	-	-	-	-	-	-	-	-	-	-	-
0.000	0.001	0.000	0.001	0.001	0.002	0.000	0.000	0.002	0.001	0.001	0.000
0.000	0.001	0.000	0.000	0.000	0.001	0.000	0.000	0.000	0.001	0.000	0.000
-	-	-	-	-	-	-	-	-	-	-	-
-	-	-	-	-	-	-	-	-	-	-	-
-	-	-	-	-	-	-	-	-	-	-	-
-	-	-	-	-	-	-	-	-	-	-	-
4.000	4.000	4.000	4.000	4.000	4.000	4.000	4.000	4.000	4.000	4.000	4.000
0.67	0.70	0.67	0.68	0.70	0.67	0.67	0.67	0.69	0.72	0.70	0.71
-	-	-	-	-	-	-	-	-	-	-	-
0.10	0.08	0.10	0.09	0.07	0.06	0.12	0.08	0.07	0.05	0.10	0.09
0.14	0.25	0.21	0.21	0.20	0.12	0.13	0.17	0.22	0.27	0.19	0.23
-	-	-	-	-	-	-	-	-	-	-	-
-	-	-	-	-	-	-	-	-	-	-	-

opx 5 -	opx 21 -	opx 35 -	opx 22 -	opx 7 -	opx 56 -	opx 13 -	opx 48 -	opx 64 -	opx 49 -	opx 37 -	opx 58 -
49.12	50.14	50.07	49.89	48.73	49.08	49.12	49.87	49.57	49.04	50.79	49.07
0.04	0.04	0.00	0.02	0.02	0.00	0.04	0.04	0.02	0.05	0.00	0.00
6.02	5.44	6.58	5.82	6.92	6.92	6.87	6.38	7.82	6.93	5.97	6.85
0.02	0.03	0.00	0.01	0.04	0.03	0.02	0.03	0.04	0.02	0.00	0.01
19.00	18.38	17.85	19.06	19.57	19.21	18.85	18.41	16.16	18.52	17.18	19.13
1.09	0.97	0.87	0.96	1.08	1.06	1.09	0.70	0.92	0.72	0.86	0.84
24.13	23.67	24.43	23.76	22.83	23.17	23.21	23.93	24.00	23.47	24.88	23.16
0.09	0.16	0.10	0.07	0.06	0.10	0.08	0.10	0.07	0.10	0.10	0.10
-	-	-	-	-	-	-	-	-	-	-	-
0.01	0.01	0.00	0.00	0.01	0.00	0.00	0.00	0.02	0.00	0.00	0.00
0.07	0.02	0.00	0.01	0.01	0.01	0.00	0.00	0.00	0.01	0.01	0.00
-	-	-	-	-	-	-	-	-	-	-	-
-	-	-	-	-	-	-	-	-	-	-	-
-	-	-	-	-	-	-	-	-	-	-	-
-	-	-	-	-	-	-	-	-	-	-	-
99.576	98.856	99.906	99.606	99.266	99.586	99.286	99.466	98.626	98.856	99.796	99.166
1.799	1.852	1.820	1.830	1.799	1.803	1.809	1.826	1.819	1.809	1.845	1.809
0.001	0.001	0.000	0.001	0.000	0.000	0.001	0.001	0.001	0.001	0.000	0.000
0.260	0.237	0.282	0.252	0.301	0.300	0.298	0.275	0.338	0.301	0.256	0.298
0.000	0.001	0.000	0.000	0.001	0.001	0.001	0.001	0.001	0.001	0.000	0.000
0.144	0.058	0.077	0.086	0.099	0.094	0.082	0.069	0.023	0.079	0.055	0.084
0.438	0.510	0.466	0.499	0.505	0.496	0.499	0.495	0.473	0.492	0.466	0.506
0.034	0.030	0.027	0.030	0.034	0.033	0.034	0.022	0.029	0.022	0.026	0.026
1.317	1.303	1.324	1.300	1.257	1.269	1.274	1.306	1.313	1.290	1.347	1.273
0.003	0.006	0.004	0.003	0.002	0.004	0.003	0.004	0.003	0.004	0.004	0.004
-	-	-	-	-	-	-	-	-	-	-	-
0.001	0.001	0.000	0.000	0.000	0.000	0.000	0.000	0.001	0.000	0.000	0.000
0.003	0.001	0.000	0.000	0.000	0.000	0.000	0.000	0.000	0.001	0.000	0.000
-	-	-	-	-	-	-	-	-	-	-	-
-	-	-	-	-	-	-	-	-	-	-	-
-	-	-	-	-	-	-	-	-	-	-	-
-	-	-	-	-	-	-	-	-	-	-	-
4.000	4.000	4.000	4.000	4.000	4.000	4.000	4.000	4.000	4.000	4.000	4.000
0.69	0.70	0.71	0.69	0.68	0.68	0.69	0.70	0.73	0.69	0.72	0.68
-	-	-	-	-	-	-	-	-	-	-	-
0.06	0.09	0.10	0.08	0.10	0.10	0.11	0.10	0.16	0.11	0.10	0.11
0.33	0.11	0.17	0.17	0.20	0.19	0.16	0.14	0.05	0.16	0.12	0.17
-	-	-	-	-	-	-	-	-	-	-	-
-	-	-	-	-	-	-	-	-	-	-	-

opx 50	opx 59	sa 1	sa 2	sa 3	sa 4	sa 5	sa 6	sa 7	sa 8	sa 9	sa 10
-	-	-	-	-	-	-	-	-	-	-	-
51.77	50.31	12.19	11.91	12.02	12.57	12.49	12.35	12.18	11.99	12.05	12.11
0.00	0.01	0.04	0.10	0.07	0.10	0.06	0.00	0.06	0.02	0.02	0.10
3.90	6.02	62.10	62.78	61.76	61.33	61.66	61.81	62.17	62.13	61.84	61.64
0.03	0.01	0.11	0.04	0.29	0.04	0.01	0.13	0.08	0.09	0.04	0.15
17.45	19.48	10.52	9.70	10.15	10.23	10.38	10.00	10.09	10.22	10.51	10.19
0.73	0.90	0.28	0.29	0.23	0.27	0.29	0.29	0.25	0.24	0.27	0.23
25.70	23.80	15.66	15.30	15.70	15.59	15.42	15.44	15.51	15.49	15.48	15.62
0.12	0.08	0.02	0.00	0.00	0.01	0.00	0.00	0.02	0.00	0.01	0.03
-	-	-	-	-	-	-	-	-	-	-	-
0.02	0.01	0.01	0.00	0.01	0.00	0.01	0.00	0.00	0.00	0.00	0.00
0.00	0.02	-	-	-	-	-	-	-	-	-	-
-	-	-	-	-	-	-	-	-	-	-	-
-	-	-	-	-	-	-	-	-	-	-	-
-	-	-	-	-	-	-	-	-	-	-	-
-	-	-	-	-	-	-	-	-	-	-	-
99.726	100.646	100.9310	100.1210	100.2310	100.1410	100.3210	100.0210	100.3610	100.1810	100.2210	100.0710
1.881	1.828	0.724	0.712	0.718	0.752	0.746	0.739	0.727	0.716	0.720	0.725
0.000	0.000	0.002	0.005	0.003	0.004	0.003	0.000	0.003	0.001	0.001	0.004
0.167	0.258	4.345	4.420	4.347	4.325	4.343	4.361	4.371	4.376	4.357	4.347
0.001	0.000	0.005	0.002	0.013	0.002	0.000	0.006	0.004	0.004	0.002	0.007
0.071	0.087	0.200	0.146	0.199	0.161	0.160	0.154	0.167	0.185	0.198	0.188
0.459	0.505	0.322	0.339	0.308	0.351	0.359	0.347	0.336	0.326	0.327	0.322
0.022	0.028	0.014	0.015	0.012	0.014	0.015	0.015	0.013	0.012	0.013	0.012
1.392	1.289	1.386	1.363	1.398	1.391	1.374	1.378	1.379	1.380	1.380	1.393
0.005	0.003	0.001	0.000	0.000	0.001	0.000	0.000	0.001	0.000	0.000	0.002
-	-	-	-	-	-	-	-	-	-	-	-
0.002	0.001	0.001	0.000	0.001	0.000	0.001	0.000	0.000	0.000	0.000	0.000
0.000	0.001	-	-	-	-	-	-	-	-	-	-
-	-	-	-	-	-	-	-	-	-	-	-
-	-	-	-	-	-	-	-	-	-	-	-
-	-	-	-	-	-	-	-	-	-	-	-
-	-	-	-	-	-	-	-	-	-	-	-
4.000	4.000	7.000	7.000	7.000	7.000	7.000	7.000	7.000	7.000	7.000	7.000
0.72	0.69	0.73	0.74	0.73	0.73	0.73	0.73	0.73	0.73	0.72	0.73
-	-	-	-	-	-	-	-	-	-	-	-
0.05	0.09	-	-	-	-	-	-	-	-	-	-
0.16	0.17	0.62	0.43	0.64	0.46	0.45	0.44	0.50	0.57	0.61	0.58
-	-	-	-	-	-	-	-	-	-	-	-
-	-	-	-	-	-	-	-	-	-	-	-

sa 11 -	sa 12 -	sa 13 -	sa 14 -	sa 15 -	sa 16 -	sa 17 -	sa 18 -	sa 19 -	sa 20 -	sa 21 -	sa 22 -
12.35	12.27	12.15	12.14	12.21	12.41	12.01	12.26	12.35	12.01	12.24	13.04
0.04	0.00	0.02	0.00	0.07	0.03	0.03	0.07	0.00	0.00	0.00	0.02
61.71	61.76	61.97	62.78	62.25	61.63	63.20	62.61	62.93	63.78	62.79	62.72
0.06	0.12	0.11	0.11	0.13	0.15	0.05	0.10	0.07	0.01	0.08	0.12
9.85	10.51	10.14	9.78	10.11	10.39	10.26	10.41	10.23	10.07	10.54	9.99
0.30	0.22	0.23	0.28	0.24	0.24	0.24	0.23	0.29	0.24	0.22	0.28
15.58	15.57	15.53	15.65	15.50	15.59	15.00	15.01	15.19	14.91	15.20	15.12
0.00	0.01	0.00	0.01	0.01	0.02	0.03	0.00	0.01	0.01	0.01	0.03
-	-	-	-	-	-	-	-	-	-	-	-
0.00	0.02	0.00	0.00	0.02	0.02	0.00	0.01	0.00	0.00	0.01	0.00
-	-	-	-	-	-	-	-	-	-	-	-
-	-	-	-	-	-	-	-	-	-	-	-
-	-	-	-	-	-	-	-	-	-	-	-
-	-	-	-	-	-	-	-	-	-	-	-
-	-	-	-	-	-	-	-	-	-	-	-
99.89 10	100.48 10	100.16 10	100.75 10	100.54 10	100.47 10	100.82 10	100.70 10	101.07 10	101.03 10	101.10 10	101.32 10
0.740	0.732	0.726	0.720	0.727	0.740	0.714	0.731	0.732	0.712	0.726	0.772
0.002	0.000	0.001	0.000	0.003	0.001	0.001	0.003	0.000	0.000	0.000	0.001
4.356	4.341	4.365	4.390	4.369	4.332	4.429	4.397	4.399	4.457	4.390	4.376
0.003	0.006	0.005	0.005	0.006	0.007	0.002	0.005	0.003	0.001	0.004	0.006
0.158	0.192	0.176	0.164	0.166	0.180	0.138	0.132	0.133	0.118	0.156	0.072
0.335	0.332	0.331	0.321	0.338	0.338	0.372	0.387	0.374	0.382	0.367	0.422
0.015	0.011	0.012	0.014	0.012	0.012	0.012	0.012	0.014	0.012	0.011	0.014
1.391	1.384	1.384	1.384	1.376	1.386	1.330	1.333	1.343	1.318	1.344	1.334
0.000	0.001	0.000	0.000	0.001	0.001	0.002	0.000	0.001	0.000	0.000	0.002
-	-	-	-	-	-	-	-	-	-	-	-
0.000	0.002	0.000	0.000	0.002	0.002	0.000	0.001	0.000	0.000	0.002	0.000
-	-	-	-	-	-	-	-	-	-	-	-
-	-	-	-	-	-	-	-	-	-	-	-
-	-	-	-	-	-	-	-	-	-	-	-
-	-	-	-	-	-	-	-	-	-	-	-
-	-	-	-	-	-	-	-	-	-	-	-
7.000	7.000	7.000	7.000	7.000	7.000	7.000	7.000	7.000	7.000	7.000	7.000
0.74	0.73	0.73	0.74	0.73	0.73	0.72	0.72	0.73	0.73	0.72	0.73
-	-	-	-	-	-	-	-	-	-	-	-
-	-	-	-	-	-	-	-	-	-	-	-
0.47	0.58	0.53	0.51	0.49	0.53	0.37	0.34	0.35	0.31	0.42	0.17
-	-	-	-	-	-	-	-	-	-	-	-
-	-	-	-	-	-	-	-	-	-	-	-

sa 23	sa 24	sa 25	sa 26	sa 27	sa 28	sa 29	sa 30	sa 31	sa 32	sa 33	sa 34
-	-	-	-	-	-	-	-	-	-	-	-
12.32	12.61	10.54	12.56	12.47	12.02	12.36	12.16	12.24	12.13	12.41	11.74
0.00	0.04	0.01	0.02	0.03	0.00	0.02	0.00	0.00	0.10	0.03	0.02
62.48	62.69	61.31	62.56	62.50	62.36	61.86	62.07	62.05	61.86	61.83	63.39
0.08	0.06	0.04	0.02	0.06	0.06	0.07	0.02	0.08	0.05	0.09	0.00
9.90	9.69	12.64	9.03	9.33	10.16	9.81	10.14	9.73	10.13	9.87	10.00
0.19	0.20	0.18	0.19	0.21	0.18	0.18	0.17	0.19	0.15	0.19	0.24
15.68	15.41	15.23	16.02	15.62	15.59	15.79	15.95	15.83	15.96	15.97	14.98
0.01	0.01	0.01	0.01	0.02	0.01	0.03	0.02	0.01	0.00	0.02	0.02
-	-	-	-	-	-	-	-	-	-	-	-
0.00	0.01	0.00	0.02	0.00	0.00	0.01	0.00	0.01	0.01	0.01	0.01
-	-	-	-	-	-	-	-	-	-	-	-
-	-	-	-	-	-	-	-	-	-	-	-
-	-	-	-	-	-	-	-	-	-	-	-
-	-	-	-	-	-	-	-	-	-	-	-
-	-	-	-	-	-	-	-	-	-	-	-
100.65 10	100.72 10	99.94 10	100.42 10	100.25 10	100.38 10	100.13 10	100.54 10	100.14 10	100.39 10	100.41 10	100.41 10
0.732	0.749	0.635	0.745	0.743	0.716	0.738	0.723	0.730	0.722	0.739	0.700
0.000	0.002	0.000	0.001	0.002	0.000	0.001	0.000	0.000	0.004	0.001	0.001
4.374	4.388	4.351	4.375	4.389	4.380	4.351	4.349	4.362	4.341	4.337	4.454
0.004	0.003	0.002	0.001	0.003	0.003	0.003	0.001	0.004	0.002	0.004	0.000
0.158	0.109	0.378	0.134	0.120	0.185	0.170	0.205	0.175	0.204	0.180	0.146
0.333	0.372	0.258	0.314	0.345	0.321	0.320	0.300	0.310	0.301	0.311	0.353
0.010	0.010	0.009	0.010	0.010	0.009	0.009	0.009	0.010	0.008	0.009	0.012
1.389	1.364	1.367	1.417	1.387	1.385	1.405	1.413	1.408	1.417	1.417	1.331
0.000	0.001	0.000	0.001	0.001	0.001	0.002	0.001	0.000	0.000	0.001	0.001
-	-	-	-	-	-	-	-	-	-	-	-
0.000	0.002	0.000	0.002	0.000	0.000	0.002	0.000	0.001	0.001	0.001	0.001
-	-	-	-	-	-	-	-	-	-	-	-
-	-	-	-	-	-	-	-	-	-	-	-
-	-	-	-	-	-	-	-	-	-	-	-
-	-	-	-	-	-	-	-	-	-	-	-
-	-	-	-	-	-	-	-	-	-	-	-
7.000	7.000	7.000	7.000	7.000	7.000	7.000	7.000	7.000	7.000	7.000	7.000
0.74	0.74	0.68	0.76	0.75	0.73	0.74	0.74	0.74	0.74	0.74	0.73
-	-	-	-	-	-	-	-	-	-	-	-
-	-	-	-	-	-	-	-	-	-	-	-
0.48	0.29	1.46	0.43	0.35	0.58	0.53	0.68	0.57	0.68	0.58	0.41
-	-	-	-	-	-	-	-	-	-	-	-
-	-	-	-	-	-	-	-	-	-	-	-

sp 24 corona	sp 25 corona	sp 26 corona	cd 1 -	cd 2 -	cd 3 -	cd 4 -	cd 5 -	cd 6 -	cd 7 -	cd 8 -	cd 9 -
0.09	0.09	0.26	48.96	48.87	49.13	48.83	49.44	48.85	49.55	48.79	48.83
0.01	0.01	0.00	0.08	0.00	0.00	0.02	0.00	0.02	0.00	0.04	0.02
58.62	58.51	59.69	33.59	33.57	33.73	33.57	33.69	33.69	34.02	32.30	33.87
0.04	0.04	0.04	-	-	-	-	-	-	-	-	-
29.21	30.15	29.38	3.43	3.30	3.23	3.31	3.00	3.09	2.72	3.23	2.84
0.42	0.41	0.43	0.22	0.20	0.16	0.20	0.21	0.21	0.20	0.24	0.22
10.87	10.79	10.82	11.56	11.59	11.64	11.65	11.80	11.81	12.01	12.48	11.78
0.00	0.00	0.00	0.03	0.01	0.01	0.02	0.02	0.00	0.01	0.02	0.01
-	-	-	-	-	-	-	-	-	-	-	-
-	-	-	0.02	0.03	0.02	0.03	0.05	0.02	0.02	0.01	0.03
0.01	0.00	0.00	0.00	0.02	0.00	0.00	0.00	0.00	0.01	0.00	0.00
-	-	-	-	-	-	-	-	-	-	-	-
0.42	0.42	0.41	-	-	-	-	-	-	-	-	-
-	-	-	-	-	-	-	-	-	-	-	-
-	-	-	-	-	-	-	-	-	-	-	-
99.694	100.424	101.034	97.8818	97.6018	97.9318	97.6318	98.2118	97.6918	98.5418	97.1118	97.6018
0.002	0.002	0.007	4.958	4.960	4.965	4.955	4.978	4.949	4.965	4.982	4.945
0.000	0.000	0.000	0.006	0.000	0.000	0.002	0.000	0.001	0.000	0.003	0.002
1.875	1.863	1.884	4.009	4.015	4.017	4.014	3.997	4.022	4.018	3.887	4.043
0.001	0.001	0.001	-	-	-	-	-	-	-	-	-
0.119	0.131	0.101	-	-	-	-	-	-	-	-	-
0.544	0.550	0.557	0.290	0.280	0.273	0.281	0.253	0.262	0.228	0.276	0.241
0.010	0.009	0.010	0.019	0.017	0.014	0.017	0.018	0.018	0.017	0.021	0.019
0.440	0.435	0.432	1.745	1.754	1.754	1.762	1.771	1.784	1.794	1.900	1.779
0.000	0.000	0.000	0.003	0.001	0.001	0.002	0.003	0.000	0.001	0.002	0.001
-	-	-	-	-	-	-	-	-	-	-	-
-	-	-	0.004	0.006	0.004	0.005	0.009	0.003	0.004	0.001	0.006
0.000	0.000	0.000	0.000	0.003	0.001	0.000	0.000	0.000	0.001	0.000	0.000
-	-	-	-	-	-	-	-	-	-	-	-
0.008	0.008	0.008	-	-	-	-	-	-	-	-	-
-	-	-	-	-	-	-	-	-	-	-	-
-	-	-	-	-	-	-	-	-	-	-	-
3.000	3.000	3.000	11.034	11.037	11.029	11.039	11.028	11.040	11.028	11.072	11.035
0.40	0.39	0.40	0.86	0.86	0.87	0.86	0.88	0.87	0.89	0.87	0.88
-	-	-	-	-	-	-	-	-	-	-	-
-	-	-	-	-	-	-	-	-	-	-	-
0.22	0.24	0.18	-	-	-	-	-	-	-	-	-
-	-	-	-	-	-	-	-	-	-	-	-
-	-	-	-	-	-	-	-	-	-	-	-

sa 35 -	sa 36 -	sa 37 -	sp 1 core	sp 2 core	sp 3 core	sp 4 core	sp 5 core	sp 6 core	sp 7 core	sp 21 corona	sp 22 corona
12.04	11.96	11.35	0.10	0.02	0.51	0.02	0.04	0.57	0.42	0.88	0.19
0.05	0.03	0.00	0.03	0.01	0.01	0.16	0.27	0.01	0.00	0.00	0.00
62.68	63.07	62.97	58.60	58.68	57.44	58.77	58.62	57.65	59.40	59.33	57.96
0.00	0.04	0.08	0.58	0.59	0.31	0.55	0.46	0.08	0.25	0.01	0.01
10.75	10.28	9.72	30.43	29.49	27.72	29.80	29.32	29.06	29.52	29.66	30.29
0.23	0.22	0.21	0.39	0.38	0.42	0.36	0.32	0.52	0.53	0.47	0.50
15.29	15.15	15.18	9.15	9.93	10.07	9.64	9.82	9.88	9.54	10.33	10.19
0.01	0.00	0.03	0.00	0.00	1.10	0.00	0.00	0.01	0.00	0.00	0.01
-	-	-	-	-	-	-	-	-	-	-	-
0.01	0.00	0.02	-	-	-	-	-	-	-	-	-
-	-	-	0.00	0.00	0.01	0.00	0.00	0.00	0.01	0.00	0.00
-	-	-	-	-	-	-	-	-	-	-	-
-	-	-	1.54	1.51	2.26	1.65	1.60	1.56	1.99	0.82	0.84
-	-	-	-	-	-	-	-	-	-	-	-
-	-	-	-	-	-	-	-	-	-	-	-
101.06 10	100.75 10	99.56 10	100.82 4	100.62 4	99.85 4	100.95 4	100.45 4	99.34 4	101.66 4	101.50 4	99.99 4
0.714	0.711	0.681	0.003	0.001	0.014	0.000	0.001	0.016	0.011	0.024	0.005
0.002	0.001	0.000	0.001	0.000	0.000	0.003	0.006	0.000	0.000	0.000	0.000
4.384	4.420	4.454	1.880	1.877	1.848	1.878	1.879	1.866	1.884	1.873	1.862
0.000	0.002	0.004	0.013	0.013	0.007	0.012	0.010	0.002	0.005	0.000	0.000
0.184	0.153	0.182	0.101	0.109	0.117	0.103	0.098	0.101	0.088	0.080	0.128
0.350	0.358	0.306	0.592	0.560	0.516	0.573	0.569	0.567	0.576	0.584	0.562
0.012	0.011	0.010	0.009	0.009	0.010	0.008	0.007	0.012	0.012	0.011	0.012
1.353	1.343	1.358	0.371	0.402	0.410	0.390	0.398	0.405	0.383	0.412	0.414
0.001	0.000	0.002	0.000	0.000	0.032	0.000	0.000	0.000	0.000	0.000	0.000
-	-	-	-	-	-	-	-	-	-	-	-
0.001	0.000	0.002	-	-	-	-	-	-	-	-	-
-	-	-	0.000	0.000	0.000	0.000	0.000	0.000	0.000	0.000	0.000
-	-	-	-	-	-	-	-	-	-	-	-
-	-	-	0.031	0.030	0.046	0.033	0.032	0.032	0.040	0.016	0.017
-	-	-	-	-	-	-	-	-	-	-	-
-	-	-	-	-	-	-	-	-	-	-	-
7.000	7.000	7.000	3.000	3.000	3.000	3.000	3.000	3.000	3.000	3.000	3.000
0.72	0.72	0.74	0.35	0.38	0.39	0.37	0.37	0.38	0.37	0.38	0.37
-	-	-	-	-	-	-	-	-	-	-	-
-	-	-	-	-	-	-	-	-	-	-	-
0.52	0.43	0.59	0.17	0.19	0.23	0.18	0.17	0.18	0.15	0.14	0.23
-	-	-	-	-	-	-	-	-	-	-	-
-	-	-	-	-	-	-	-	-	-	-	-

cd 10 -	cd 11 -	cd 12 -	cd 13 -	cd 14 -	cd 15 -	pl 3 Antiperthite	pl 35 Antiperthite	pl 85 Leucosome	pl 86 Leucosome	pl 87 Leucosome
48.75	48.89	48.95	48.76	49.36	48.51	62.28	60.29	59.28	59.48	59.72
0.07	0.00	0.00	0.00	0.02	0.00	0.02	0.00	0.07	0.05	0.03
33.49	33.56	33.37	33.41	33.63	33.68	23.83	24.97	26.02	25.56	25.46
-	-	-	-	-	-	-	-	-	-	-
2.96	2.99	3.06	3.30	3.23	2.85	0.07	0.18	0.18	0.19	0.19
0.19	0.20	0.19	0.21	0.15	0.18	0.01	0.00	0.01	0.01	0.01
11.86	11.79	11.73	11.68	11.68	12.10	0.00	0.00	0.00	0.00	0.00
0.01	0.02	0.01	0.02	0.00	0.03	5.44	5.92	6.80	6.38	6.20
-	-	-	-	-	-	0.00	0.04	0.00	0.03	0.02
0.04	0.04	0.02	0.03	0.02	0.02	7.96	7.77	7.46	7.70	7.84
0.00	0.00	0.00	0.00	0.00	0.00	0.46	0.23	0.10	0.08	0.07
-	-	-	-	-	-	0.12	0.09	0.07	0.09	0.11
-	-	-	-	-	-	-	-	-	-	-
-	-	-	-	-	-	-	-	-	-	-
-	-	-	-	-	-	-	-	-	-	-
97.38 18	97.50 18	97.34 18	97.41 18	98.09 18	97.37 18	100.20 8	99.49 8	99.99 8	99.57 8	99.65 8
4.953	4.960	4.974	4.959	4.979	4.928	2.771	2.700	2.645	2.662	2.668
0.005	0.000	0.000	0.000	0.002	0.000	0.001	0.000	0.002	0.002	0.001
4.010	4.013	3.996	4.005	3.997	4.032	1.250	1.318	1.368	1.348	1.340
-	-	-	-	-	-	-	-	-	-	-
-	-	-	-	-	-	-	-	-	-	-
0.251	0.254	0.260	0.281	0.272	0.242	0.002	0.007	0.007	0.007	0.007
0.017	0.017	0.017	0.018	0.013	0.016	0.001	0.000	0.000	0.000	0.001
1.796	1.783	1.777	1.771	1.756	1.833	0.000	0.000	0.000	0.000	0.000
0.001	0.003	0.001	0.002	0.000	0.004	0.259	0.284	0.325	0.306	0.297
-	-	-	-	-	-	0.000	0.001	0.000	0.001	0.000
0.008	0.008	0.004	0.006	0.003	0.003	0.687	0.675	0.645	0.668	0.679
0.000	0.000	0.000	0.000	0.000	0.000	0.026	0.013	0.006	0.004	0.004
-	-	-	-	-	-	0.003	0.002	0.002	0.002	0.003
-	-	-	-	-	-	-	-	-	-	-
-	-	-	-	-	-	-	-	-	-	-
-	-	-	-	-	-	-	-	-	-	-
11.041	11.038	11.030	11.042	11.023	11.058	5.000	5.000	5.000	5.000	5.000
0.88	0.88	0.87	0.86	0.87	0.88					
-	-	-	-	-	-	-	-	-	-	-
-	-	-	-	-	-	-	-	-	-	-
-	-	-	-	-	-	-	-	-	-	-
-	-	-	-	-	-	0.27	0.29	0.33	0.31	0.30
-	-	-	-	-	-	0.03	0.01	0.01	0.00	0.00

pl 88 Leucosome	pl 90 Leucosome	pl 93 Leucosome	pl 44 Leucosome	pl 45 Leucosome	pl 70 Leucosome	ksp 2 Leucosome	ksp 3 Leucosome	ksp 4 Perthite	ksp 1 Perthite	ksp 3 Perthite
59.58	58.78	59.08	60.24	60.43	61.34	64.12	64.21	64.71	65.39	64.54
0.04	0.00	0.00	0.03	0.00	0.02	0.00	0.02	0.04	0.09	0.06
25.65	25.90	25.95	24.43	24.55	24.51	19.25	19.06	18.73	19.28	20.36
-	-	-	-	-	-	-	-	-	-	-
0.17	0.30	0.21	0.22	0.13	0.10	0.11	0.10	0.06	0.02	0.10
0.00	0.00	0.00	0.00	0.02	0.00	0.00	0.00	0.00	0.02	0.00
0.03	0.06	0.00	0.34	0.13	0.00	0.01	0.02	0.03	0.00	0.05
6.47	6.45	6.59	5.34	5.47	5.26	0.05	0.05	0.09	0.58	1.57
0.00	0.00	0.06	0.00	0.09	0.00	0.81	0.81	0.66	0.56	0.44
7.75	7.55	7.70	8.26	8.43	8.49	1.02	1.09	0.97	2.37	3.85
0.10	0.11	0.10	0.15	0.19	0.15	14.31	14.56	14.64	12.24	9.57
0.09	0.06	0.06	0.05	0.06	0.07	0.09	0.10	0.14	0.08	0.11
-	-	-	-	-	-	-	-	-	-	-
-	-	-	-	-	-	-	-	-	-	-
-	-	-	-	-	-	-	-	-	-	-
99.878	99.208	99.768	99.058	99.518	99.938	99.768	100.028	100.098	100.628	100.648
2.656	2.639	2.637	2.697	2.693	2.724	2.981	2.975	2.998	2.991	2.925
0.001	0.000	0.000	0.001	0.000	0.001	0.000	0.001	0.001	0.003	0.002
1.348	1.371	1.365	1.289	1.289	1.283	1.055	1.041	1.023	1.039	1.088
-	-	-	-	-	-	-	-	-	-	-
-	-	-	-	-	-	-	-	-	-	-
0.006	0.011	0.008	0.008	0.005	0.003	0.004	0.004	0.002	0.001	0.004
0.000	0.000	0.000	0.000	0.001	0.000	0.000	0.000	0.000	0.001	0.000
0.002	0.004	0.000	0.022	0.009	0.000	0.000	0.002	0.002	0.000	0.003
0.309	0.310	0.315	0.256	0.261	0.250	0.002	0.003	0.005	0.028	0.076
0.000	0.000	0.001	0.000	0.002	0.000	0.015	0.015	0.012	0.010	0.008
0.670	0.657	0.666	0.717	0.728	0.731	0.092	0.098	0.088	0.210	0.338
0.005	0.006	0.006	0.008	0.011	0.009	0.849	0.860	0.865	0.714	0.553
0.002	0.002	0.002	0.001	0.002	0.002	0.002	0.003	0.004	0.002	0.003
-	-	-	-	-	-	-	-	-	-	-
-	-	-	-	-	-	-	-	-	-	-
-	-	-	-	-	-	-	-	-	-	-
5.000	5.000	5.000	5.000	5.000	5.002	5.000	5.000	5.000	5.000	5.000
-	-	-	-	-	-	-	-	-	-	-
-	-	-	-	-	-	-	-	-	-	-
-	-	-	-	-	-	-	-	-	-	-
0.31	0.32	0.32	0.26	0.26	0.25	0.00	0.00	0.00	0.03	0.08
0.01	0.01	0.01	0.01	0.01	0.01	0.90	0.90	0.90	0.75	0.57

ksp 7 Perthite	ksp 1 Perthite	bi 2 -	bi 4 -	bi 5 -	bi 14 -	bi 16 -	bi 19 -	bi 20 -	bi 21 -	bi 22 -	bi 23 -	bi 24 -	bi 25 -
65.39	63.92	74.10	36.96	36.94	39.90	42.49	35.67	35.60	36.79	35.98	35.35	36.59	35.68
0.00	0.02	1.01	4.16	4.23	0.46	0.44	5.66	6.50	5.71	5.04	5.67	4.37	5.42
18.82	19.46	9.12	16.35	16.37	14.92	14.28	15.78	15.91	16.46	15.24	15.58	15.49	15.62
-	-	-	-	-	-	-	-	-	-	-	-	-	-
0.03	0.06	4.59	11.06	11.44	6.89	7.82	13.34	13.39	12.98	14.30	13.04	11.85	11.05
0.01	0.00	0.02	0.08	0.07	0.05	0.14	0.10	0.09	0.10	0.08	0.07	0.07	0.11
0.00	0.00	7.00	15.78	16.21	22.63	20.45	13.64	13.33	12.70	13.14	13.65	15.60	15.48
0.21	0.15	0.01	0.01	0.00	0.00	0.11	0.07	0.09	0.59	0.07	0.04	0.04	0.08
0.87	0.75	-	-	-	-	-	-	-	-	-	-	-	-
1.48	1.23	0.03	0.06	0.01	0.07	0.03	0.04	0.07	0.23	0.04	0.03	0.02	0.07
13.77	14.35	3.69	9.49	9.67	9.12	7.05	9.51	9.62	8.81	9.46	9.15	9.76	9.45
0.12	0.12	-	-	-	-	-	-	-	-	-	-	-	-
-	-	-	-	-	-	-	-	-	-	-	-	-	-
-	-	0.07	0.10	0.14	0.11	0.11	0.16	0.16	0.14	0.13	0.18	0.17	0.13
-	-	0.21	0.53	0.64	1.94	1.41	0.55	0.46	0.50	0.57	0.54	0.75	0.63
100.708	100.058	99.8522	94.5922	95.7222	96.1022	94.3322	94.5122	95.2322	95.0122	94.0522	93.3022	94.7122	93.7222
3.008	2.956	8.928	5.489	5.444	5.760	6.119	5.388	5.339	5.479	5.483	5.396	5.484	5.383
0.000	0.001	0.092	0.465	0.469	0.050	0.047	0.643	0.733	0.640	0.578	0.651	0.493	0.615
1.020	1.061	1.295	2.862	2.843	2.538	2.424	2.809	2.812	2.889	2.737	2.802	2.736	2.777
-	-	-	-	-	-	-	-	-	-	-	-	-	-
-	-	-	-	-	-	-	-	-	-	-	-	-	-
0.001	0.002	0.462	1.374	1.410	0.832	0.942	1.685	1.679	1.616	1.822	1.664	1.485	1.394
0.000	0.000	0.002	0.010	0.009	0.006	0.018	0.012	0.011	0.013	0.011	0.009	0.009	0.014
0.000	0.000	1.257	3.494	3.562	4.870	4.391	3.072	2.980	2.820	2.985	3.106	3.486	3.482
0.010	0.007	0.002	0.002	0.000	0.001	0.016	0.011	0.015	0.094	0.012	0.006	0.006	0.013
0.016	0.014	-	-	-	-	-	-	-	-	-	-	-	-
0.132	0.110	0.006	0.018	0.003	0.020	0.008	0.011	0.020	0.065	0.012	0.009	0.006	0.021
0.808	0.847	0.567	1.798	1.818	1.679	1.295	1.833	1.840	1.674	1.839	1.781	1.866	1.819
0.003	0.003	-	-	-	-	-	-	-	-	-	-	-	-
-	-	-	-	-	-	-	-	-	-	-	-	-	-
-	-	0.014	0.026	0.035	0.027	0.028	0.042	0.042	0.036	0.032	0.046	0.043	0.033
-	-	0.081	0.250	0.297	0.886	0.642	0.262	0.219	0.235	0.276	0.263	0.356	0.303
5.000	5.000	12.707	15.786	15.890	16.670	15.929	15.769	15.692	15.559	15.787	15.734	15.969	15.852
		0.73	0.72	0.72	0.85	0.82	0.65	0.64	0.64	0.62	0.65	0.70	0.71
-	-	-	-	-	-	-	-	-	-	-	-	-	-
-	-	-	-	-	-	-	-	-	-	-	-	-	-
-	-	-	-	-	-	-	-	-	-	-	-	-	-
0.01	0.01	-	-	-	-	-	-	-	-	-	-	-	-
0.85	0.88	-	-	-	-	-	-	-	-	-	-	-	-

Table S2. Input compositions of garnet, orthopyroxene, cordierite, and plagioclase and P-T results of Al-in-orthopyroxene thermobarometry for sample NE30.

	Elements apfu											y(opx) models	
	Si	Ti	Al	Cr	Fe3	Fe2	Mn	Mg	Ca	Na	K	Al/2	Al-Fe+3-Cr-(2*Ti)/2
G	-	-	-	-	-	1.48	0.17	1.23	0.07	-	-		
Opx	1.78	0	0.31	0	0.12	0.5	0.03	1.25	0	-	-	P-T	P-T
Cd	-	-	-	-	-	0.23	0.01	1.81	-	-	-	1095 ºC	892 ºC
Pl	-	-	-	-	-	-	-	-	0.31	0.66	0.01	9.94 kbar	7.86 kbar
G	-	-	-	-	-	1.51	0.28	1	0.1	-	-		
Opx	1.81	0	0.31	0	0.07	0.53	0.04	1.24	0	-	-	P-T	P-T
Cd	-	-	-	-	-	0.24	0.01	1.81	-	-	-	1046 ºC	933 ºC
Pl	-	-	-	-	-	-	-	-	0.27	0.47	0	8.98 kbar	7.92 kbar
G	-	-	-	-	-	1.52	0.38	0.94	0.11	-	-		
Opx	1.8	0	0.3	0	0.1	0.51	0.03	1.26	0	-	-	P-T	P-T
Cd	-	-	-	-	-	0.26	0.01	1.81	-	-	-	1085 ºC	920 ºC
Pl	-	-	-	-	-	-	-	-	0.33	0.65	0.01	9.46 kbar	7.82 kbar
G	-	-	-	-	-	1.57	0.35	0.91	0.11	-	-		
Opx	1.8	0	0.3	0	0.11	0.51	0.03	1.26	0	-	-	P-T	P-T
Cd	-	-	-	-	-	0.3	0.01	1.75	-	-	-	1093 ºC	913 ºC
Pl	-	-	-	-	-	-	-	-	0.32	0.67	0.01	9.83 kbar	7.96 kbar
									Average P-T			1080 ºC 9.6 kbar	915 ºC 7.9 kbar

Table S3. Compositions of the host and lamellae feldspars, re-integrated single feldspar compositions, and ternary feldspar temperature results in sample NE30. L = lamellae; H = Host.

Feldspar	1		2		3		4		5	
analysis	L	H	L	H	L	H	L	H	L	H
nº analysis	8	6	8	9	9	5	5	13	7	4
SiO_2	61.51	64.03	60.91	64.26	61.14	64.24	61.55	64.05	61.08	64.35
TiO_2	0.01	0.02	0.02	0.02	0.01	0.02	0.05	0.04	0.02	0.03
Al_2O_3	24.40	19.52	24.50	19.32	24.49	19.29	24.46	19.42	24.52	19.47
FeO	0.09	0.03	0.13	0.05	0.10	0.03	0.20	0.04	0.13	0.04
MgO	0.00	0.01	0.12	0.01	0.07	0.02	0.06	0.01	0.20	0.01
CaO	5.19	0.26	5.33	0.11	5.26	0.10	5.18	0.16	5.21	0.17
BaO	0.01	0.58	0.02	0.67	0.02	0.67	0.01	0.79	0.01	0.64
Na_2O	8.45	2.17	8.43	1.54	8.49	1.75	8.41	1.66	8.27	1.90
K_2O	0.23	12.92	0.20	14.00	0.17	13.74	0.18	13.78	0.35	13.46
SrO	0.05	0.11	0.06	0.11	0.06	0.12	0.08	0.12	0.07	0.11
sum	99.9	99.6	99.7	100.1	99.8	100.0	100.2	100.1	99.9	100.2
Structural formula based on 8 oxygens										
Si	2.734	2.952	2.709	2.964	2.716	2.963	2.728	2.955	2.714	2.960
Ti	0.000	0.001	0.001	0.001	0.000	0.001	0.002	0.001	0.001	0.001
Al	1.273	1.060	1.284	1.050	1.282	1.049	1.278	1.056	1.284	1.055
Fe	0.003	0.001	0.005	0.002	0.004	0.001	0.007	0.002	0.005	0.002
Mg	0.000	0.001	0.008	0.001	0.005	0.001	0.004	0.001	0.014	0.001
Ca	0.244	0.013	0.254	0.005	0.250	0.005	0.246	0.008	0.248	0.008
Ba	0.000	0.010	0.000	0.012	0.000	0.012	0.000	0.014	0.000	0.011
Na	0.718	0.194	0.727	0.138	0.731	0.156	0.723	0.149	0.713	0.169
K	0.026	0.759	0.012	0.824	0.010	0.808	0.010	0.811	0.020	0.790
Sr	0.001	0.003	0.002	0.003	0.002	0.003	0.002	0.003	0.002	0.003
X_{An}	0.247	0.013	0.256	0.005	0.250	0.010	0.250	0.008	0.253	0.009
X_{Ab}	0.727	0.201	0.733	0.143	0.740	0.160	0.740	0.153	0.727	0.175
X_{Or}	0.027	0.786	0.012	0.852	0.010	0.830	0.010	0.838	0.020	0.816
vol (%)	13.4	86.6	11.3	88.7	11.6	88.4	12.13	87.87	13.89	86.11
Re-integrated ternary feldspar composition and temperature estimates (at 8.0 kbar)										
X_{An}	0.048		0.036		0.037		0.040		0.045	
X_{Ab}	0.279		0.215		0.234		0.230		0.258	
X_{Or}	0.673		0.748		0.729		0.730		0.697	
T (˚C)	**970**		**974**		**963**		**980**		**977**	

Table S4. LA-ICP-MS zircon U-Pb and trace elements geochemistry.

						U-Pb ratios										Ages (Ma)						
Sample	Spot	Pb ppm	Th ppm	U ppm	Th/U	207/235	1σ	206/238	1σ	coef. c.	238/206	1σ	207/206	1σ	208/206	1σ	206/238	2σ	207/235	2σ	207/206	2σ	Conc. %
NE30	2.1	18.50	90.20	36.40	2.48	6.049	0.133	0.362	0.005	0.870	2.764	0.038	0.121	0.002	0.761	0.064	1991	23.2	1983	19.2	1975	21.8	100
NE30	3.1	26.20	82.90	60.00	1.38	6.066	0.146	0.365	0.005	0.780	2.738	0.035	0.121	0.003	0.994	0.206	2007	22.2	1985	21.0	1963	28.8	101
NE30	6.1	42.50	18.80	118.00	0.16	6.292	0.107	0.367	0.004	0.820	2.724	0.030	0.124	0.002	0.036	0.003	2016	18.9	2017	14.9	2019	18.1	99
NE30	11.1	141.50	225.30	423.10	0.53	6.128	0.092	0.365	0.003	0.990	2.744	0.023	0.122	0.002	0.095	0.004	2003	14.6	1994	13.1	1985	12.0	100
NE30	15.1	33.90	19.00	90.70	0.21	6.176	0.109	0.363	0.003	0.910	2.753	0.024	0.123	0.002	0.067	0.017	1997	15.1	2001	15.4	2005	18.2	99
NE30	19.1	28.10	75.50	69.10	1.09	6.100	0.106	0.359	0.003	0.660	2.783	0.019	0.123	0.002	0.120	0.053	1979	11.9	1990	15.2	2002	24.5	99
NE30	29.1	46.90	101.40	116.50	0.87	7.003	0.110	0.389	0.004	0.840	2.571	0.023	0.131	0.002	0.174	0.012	2118	16.2	2112	13.9	2106	16.6	100
NE30	33.1	17.00	64.50	33.70	1.91	6.079	0.119	0.363	0.004	0.870	2.758	0.030	0.122	0.002	1.113	0.172	1994	18.5	1987	17.1	1980	20.5	100
NE30	35.1	68.80	24.00	186.50	0.13	6.018	0.083	0.359	0.003	0.900	2.783	0.021	0.122	0.002	0.021	0.002	1979	12.3	1979	12.0	1978	14.1	100
NE30	36.1	27.00	2.20	82.60	0.03	6.167	0.110	0.364	0.004	0.980	2.745	0.028	0.123	0.002	0.024	0.007	2003	17.5	2000	15.6	1997	14.4	100
NE30	37.1	24.00	194.90	40.70	4.78	5.993	0.128	0.360	0.004	0.650	2.777	0.028	0.121	0.002	0.572	0.123	1982	17.1	1975	18.5	1967	29.7	100
NE30	38.1	27.80	93.20	63.20	1.47	6.380	0.111	0.371	0.003	0.840	2.693	0.024	0.125	0.002	0.052	0.096	2036	15.5	2029	15.3	2023	19.6	100
NE30	40.1	18.10	109.80	33.90	3.24	6.119	0.108	0.358	0.004	0.530	2.791	0.027	0.124	0.002	0.411	0.113	1974	16.6	1993	15.4	2013	26.6	99
NE30	45.1	26.80	251.20	35.00	7.18	6.125	0.136	0.360	0.004	0.780	2.777	0.027	0.123	0.003	1.032	0.374	1983	16.6	1994	19.3	2005	28.0	99
NE30	51.1	23.50	89.80	53.90	1.67	6.178	0.104	0.365	0.003	0.770	2.739	0.022	0.123	0.002	0.166	0.054	2006	13.7	2001	14.7	1996	21.0	100
NE30	55.1	32.30	19.70	86.60	0.23	6.158	0.112	0.370	0.003	0.750	2.700	0.022	0.121	0.003	0.324	0.135	2031	14.1	1998	15.9	1965	23.7	101
NE30	58.1	21.50	178.20	32.60	5.47	6.032	0.150	0.359	0.004	0.010	2.788	0.030	0.122	0.002	1.089	0.017	1976	18.0	1980	21.6	1985	47.8	99
NE30	62.1	21.40	138.80	38.00	3.65	6.076	0.120	0.358	0.003	0.790	2.790	0.022	0.123	0.002	0.274	0.128	1975	13.3	1987	17.3	2000	25.7	99
NE30	74.1	37.50	18.00	106.20	0.17	6.395	0.111	0.370	0.003	0.870	2.702	0.019	0.125	0.002	0.037	0.004	2030	12.2	2032	15.2	2033	20.8	99
NE30	75.1	28.70	40.50	64.40	0.63	7.439	0.143	0.400	0.004	0.940	2.502	0.022	0.135	0.003	0.148	0.028	2167	16.1	2166	17.2	2164	19.8	100
NE30	76.1	26.50	45.20	68.80	0.66	6.210	0.111	0.363	0.003	0.440	2.756	0.023	0.124	0.002	0.079	0.022	1995	14.2	2006	15.7	2017	28.5	99
NE30	77.1	25.80	184.90	44.00	4.21	6.179	0.155	0.361	0.004	0.910	2.771	0.027	0.124	0.003	0.905	0.239	1987	16.6	2001	22.0	2017	29.8	99
NE30	83.1	55.60	17.20	151.00	0.11	6.416	0.069	0.371	0.002	0.660	2.698	0.017	0.126	0.001	0.070	0.019	2032	11.3	2034	9.5	2036	14.3	99
NE30	84.1	56.90	134.60	131.90	1.02	7.286	0.082	0.400	0.003	0.960	2.503	0.016	0.132	0.001	0.195	0.003	2167	11.5	2147	10.1	2128	9.8	100
NE30	85.1	23.60	188.90	36.00	5.24	6.087	0.119	0.359	0.004	0.810	2.785	0.027	0.123	0.002	0.982	0.154	1978	16.6	1988	17.0	2000	23.0	99
NE30	93.1	42.60	284.50	78.90	3.60	6.312	0.091	0.366	0.002	0.550	2.733	0.014	0.125	0.002	0.218	0.130	2010	9.0	2020	12.6	2030	21.8	99
NE30	95.1	33.10	65.30	83.20	0.78	6.767	0.096	0.371	0.002	0.560	2.699	0.017	0.133	0.002	0.150	0.012	2032	10.8	2081	12.6	2131	20.9	97
NE30	96.1	42.10	17.10	120.20	0.14	6.165	0.089	0.360	0.002	0.790	2.778	0.015	0.124	0.002	0.031	0.002	1982	9.0	1999	12.5	2017	18.9	99
NE30	99.1	45.10	25.30	122.40	0.21	6.313	0.116	0.367	0.002	0.910	2.728	0.017	0.125	0.003	0.035	0.007	2013	10.9	2020	16.1	2028	23.0	99
NE30	100.1	44.50	310.90	69.60	4.47	5.940	0.117	0.357	0.003	0.790	2.803	0.026	0.121	0.003	1.165	0.116	1967	15.7	1967	17.1	1968	24.2	99

Sample NE30 Continuation

		Trace elements concentration (ppm)														
Sample	Spot	La	Ce	Pr	Nd	Sm	Eu	Gd	Tb	Dy	Ho	Er	Tm	Yb	Lu	Sub-population:
NE30	2.1	0.20	12.07	0.26	2.45	*b.d*	0.60	15.57	6.12	92.07	40.29	224.02	55.38	627.06	129.05	Weak-CL
NE30	3.1	*b.d*	17.25	*b.d*	*b.d*	5.61	0.44	25.49	9.46	91.44	32.84	122.26	21.54	173.83	34.94	Weak-CL
NE30	6.1	*b.d*	13.99	*b.d*	3.53	2.34	0.89	17.00	5.55	89.64	41.10	210.74	52.07	531.58	113.18	Soccer ball+Brigth-CL
NE30	11.1	1.37	13.13	1.39	10.39	8.04	5.29	18.72	8.63	122.15	70.40	414.85	111.88	1237.39	295.10	Soccer ball+Brigth-CL
NE30	15.1	*b.d*	7.86	*b.d*	*b.d*	2.06	0.39	17.65	9.85	157.52	71.70	376.23	86.79	843.38	168.06	Soccer ball+Brigth-CL
NE30	19.1	*b.d*	11.25	*b.d*	*b.d*	3.08	*b.d*	25.42	11.27	145.30	56.03	256.40	46.82	439.79	93.70	Soccer ball+Brigth-CL
NE30	29.1	*b.d*	16.88	0.31	*b.d*	3.49	*b.d*	17.47	4.12	51.01	23.40	111.65	25.61	282.30	61.19	Xenocrystic core
NE30	33.1	*b.d*	6.09	*b.d*	*b.d*	2.80	0.87	20.02	12.15	187.38	89.05	499.06	119.41	1271.74	258.17	Weak-CL
NE30	35.1	*b.d*	14.12	*b.d*	*b.d*	2.43	0.74	19.57	9.35	71.39	25.40	91.17	16.66	122.93	24.93	Weak-CL
NE30	36.1	*b.d*	4.49	*b.d*	1.64	*b.d*	*b.d*	11.78	6.07	96.89	49.44	257.93	64.75	649.42	136.21	Weak-CL
NE30	37.1	*b.d*	8.39	*b.d*	*b.d*	*b.d*	0.51	16.84	5.43	54.68	17.59	67.48	13.44	132.86	23.96	Weak-CL
NE30	38.1	*b.d*	5.22	*b.d*	1.56	2.34	0.92	13.80	7.08	117.94	53.12	283.09	66.48	649.30	129.79	Soccer ball+Brigth-CL
NE30	40.1	*b.d*	6.85	*b.d*	1.17	1.91	1.01	18.27	8.20	118.11	48.54	206.34	36.63	328.78	59.61	Soccer ball+Brigth-CL
NE30	45.1	0.11	9.28	*b.d*	*b.d*	3.29	*b.d*	27.34	9.98	139.72	57.19	279.97	58.16	545.95	111.02	Soccer ball+Brigth-CL
NE30	51.1	*b.d*	8.41	*b.d*	*b.d*	2.08	0.72	19.25	9.54	121.19	51.24	228.63	46.25	419.33	85.64	Weak-CL
NE30	55.1	*b.d*	16.69	*b.d*	*b.d*	5.33	*b.d*	30.02	10.29	105.79	32.27	121.86	21.27	167.74	31.87	Weak-CL
NE30	58.1	*b.d*	16.59	*b.d*	*b.d*	6.09	*b.d*	25.30	8.96	90.04	30.12	112.24	20.37	165.20	34.12	Weak-CL
NE30	62.1	*b.d*	10.10	*b.d*	3.47	3.04	*b.d*	26.28	11.48	147.42	59.27	269.35	59.25	507.74	105.32	Soccer ball+Brigth-CL
NE30	74.1	*b.d*	7.35	*b.d*	*b.d*	2.73	0.79	18.28	9.43	141.70	70.83	385.62	89.63	924.59	194.77	Soccer ball+Brigth-CL
NE30	75.1	*b.d*	23.88	0.30	3.28	3.51	1.36	15.79	5.69	66.36	26.60	124.92	30.49	309.33	71.52	Xenocrystic core
NE30	76.1	*b.d*	7.84	0.64	4.79	4.43	1.26	19.20	9.11	134.53	65.73	333.44	73.81	695.95	142.37	Soccer ball+Brigth-CL
NE30	77.1	0.27	18.04	*b.d*	*b.d*	4.93	0.83	30.88	10.51	96.39	32.09	102.62	18.86	170.67	29.78	Soccer ball+Brigth-CL
NE30	83.1	*b.d*	5.65	*b.d*	*b.d*	*b.d*	*b.d*	14.00	10.26	141.67	71.76	390.14	84.54	833.96	171.80	Soccer ball+Brigth-CL
NE30	84.1	*b.d*	95.50	0.23	2.55	8.14	3.94	38.71	14.20	167.18	64.71	305.47	64.43	650.35	126.11	Xenocrystic core
NE30	85.1	*b.d*	18.37	0.29	*b.d*	3.91	*b.d*	30.56	10.33	105.72	31.13	102.25	19.65	154.40	31.87	Weak-CL
NE30	93.1	*b.d*	14.47	*b.d*	*b.d*	*b.d*	*b.d*	29.11	10.06	101.60	42.93	178.95	41.18	342.32	67.40	Soccer ball+Brigth-CL
NE30	95.1	*b.d*	10.36	*b.d*	*b.d*	6.35	0.92	33.42	11.46	139.58	61.83	297.02	57.28	572.68	111.58	Xenocrystic core
NE30	96.1	*b.d*	10.78	*b.d*	*b.d*	2.04	0.68	24.37	10.75	143.32	66.81	319.96	64.19	567.50	112.46	Soccer ball+Brigth-CL
NE30	99.1	*b.d*	6.51	*b.d*	*b.d*	*b.d*	1.56	21.49	12.10	164.20	84.57	468.22	110.97	1126.00	242.69	Soccer ball+Brigth-CL
NE30	100.1	*b.d*	14.84	*b.d*	*b.d*	3.72	*b.d*	26.19	9.06	87.70	30.08	118.93	23.13	207.25	43.37	Weak-CL

Table S4. LA-ICP-MS zircon U-Pb and trace elements geochemistry.

						U-Pb ratios											Ages (Ma)						
Sample	Spot	Pb ppm	Th ppm	U ppm	Th/U	207/235	1σ	206/238	1σ	coef. c.	238/206	1σ	207/206	1σ	208/206	1σ	206/238	2σ	207/235	2σ	207/206	2σ	Conc. %
NE163	4.1	46.00	235.00	83.00	2.83	6.161	0.097	0.365	0.004	0.920	2.743	0.029	0.123	0.002	0.658	0.009	2004	18.4	1999	13.8	1994	12.9	100
NE163	6.1	76.00	70.00	214.00	0.33	6.416	0.090	0.377	0.003	0.970	2.656	0.023	0.124	0.002	0.113	0.048	2060	15.0	2034	12.4	2009	11.0	101
NE163	10.1	9.00	52.00	18.00	2.87	6.201	0.113	0.362	0.004	0.780	2.767	0.033	0.124	0.002	0.337	0.047	1989	20.8	2005	15.9	2020	20.5	99
NE163	12.1	134.00	13.00	323.00	0.04	6.607	0.104	0.376	0.004	0.910	2.659	0.028	0.127	0.002	0.156	0.008	2058	18.7	2060	13.9	2063	13.3	99
NE163	17.1	64.00	425.00	105.00	4.05	6.021	0.088	0.359	0.003	0.940	2.785	0.026	0.122	0.002	0.748	0.016	1978	16.1	1979	12.8	1980	11.8	99
NE163	30.1	116.00	63.00	334.00	0.19	5.896	0.084	0.355	0.002	0.900	2.818	0.019	0.121	0.002	0.016	0.003	1958	11.4	1961	12.3	1964	15.4	99
NE163	31.1	28.00	144.00	53.00	2.72	6.555	0.112	0.379	0.003	0.900	2.642	0.022	0.126	0.002	0.557	0.018	2069	14.5	2053	15.1	2038	18.4	100
NE163	37.1	31.00	144.00	55.00	2.59	6.573	0.133	0.379	0.006	0.350	2.638	0.039	0.126	0.002	0.488	0.018	2072	26.2	2056	17.8	2040	36.1	100
NE163	40.1	55.00	1.00	214.00	0.01	6.298	0.115	0.375	0.004	0.900	2.668	0.025	0.122	0.002	0.029	0.005	2052	16.4	2018	15.9	1984	18.8	101
NE163	41.1	33.00	131.00	67.00	1.97	6.163	0.132	0.358	0.003	0.960	2.791	0.027	0.125	0.003	0.251	0.081	1974	16.1	1999	18.7	2026	22.3	98
NE163	44.1	41.00	235.00	75.00	3.15	6.433	0.143	0.369	0.004	0.330	2.714	0.029	0.127	0.003	0.699	0.042	2022	18.8	2037	19.6	2052	37.6	99
NE163	45.1	59.00	82.00	125.00	0.66	9.127	0.169	0.429	0.004	0.810	2.333	0.022	0.154	0.003	0.117	0.014	2300	17.6	2351	17.0	2395	21.0	97
NE163	50.1	28.00	140.00	53.00	2.65	6.324	0.143	0.369	0.003	0.580	2.713	0.024	0.124	0.003	0.410	0.050	2023	15.5	2022	19.9	2021	33.5	100
NE163	51.1	36.00	189.00	66.00	2.85	6.353	0.150	0.367	0.003	0.320	2.725	0.022	0.126	0.003	0.574	0.015	2015	13.7	2026	20.7	2037	39.5	99
NE163	53.1	43.00	214.00	77.00	2.80	6.295	0.142	0.365	0.003	0.920	2.743	0.024	0.125	0.003	0.793	0.023	2004	14.6	2018	19.7	2032	26.7	99
NE163	54.1	41.00	195.00	78.00	2.49	6.358	0.156	0.368	0.003	0.490	2.719	0.023	0.125	0.003	0.590	0.051	2019	14.6	2026	21.5	2034	38.3	99
NE163	55.1	38.00	198.00	74.00	2.69	6.522	0.136	0.383	0.004	0.780	2.614	0.029	0.124	0.003	0.410	0.031	2088	20.0	2049	18.3	2010	24.7	101
NE163	57.1	97.00	293.00	198.00	1.49	8.768	0.157	0.442	0.004	0.990	2.265	0.019	0.144	0.002	0.258	0.141	2357	16.5	2314	16.3	2276	16.7	101
NE163	58.1	53.00	256.00	100.00	2.57	6.435	0.126	0.374	0.004	0.930	2.677	0.025	0.125	0.002	0.679	0.012	2046	16.4	2037	17.3	2028	20.3	100
NE163	61.1	117.00	45.00	328.00	0.14	5.672	0.110	0.341	0.003	0.960	2.935	0.026	0.121	0.002	0.017	0.001	1890	14.9	1927	16.7	1967	19.4	98
NE163	65.1	25.00	126.00	51.00	2.47	6.386	0.165	0.379	0.004	0.740	2.642	0.028	0.122	0.004	0.396	0.043	2069	18.7	2030	22.6	1991	34.3	101
NE163	66.1	59.00	324.00	107.00	3.01	6.614	0.137	0.383	0.003	0.950	2.608	0.022	0.125	0.003	0.686	0.007	2092	15.4	2061	18.3	2031	22.7	101
NE163	76.1	41.00	219.00	72.00	3.06	6.210	0.117	0.363	0.003	0.920	2.758	0.025	0.124	0.002	0.665	0.033	1994	15.6	2006	16.5	2018	19.6	99
NE163	89.1	52.00	65.00	92.00	0.70	11.007	0.189	0.478	0.005	0.730	2.091	0.024	0.167	0.002	0.169	0.032	2519	23.6	2524	16.0	2527	19.8	99
NE163	90.1	97.00	23.00	366.00	0.06	6.174	0.104	0.373	0.004	0.970	2.684	0.030	0.120	0.002	0.016	0.003	2041	19.7	2001	14.7	1959	11.6	102
NE163	96.1	21.00	4.00	37.00	0.12	10.047	0.149	0.449	0.005	0.960	2.226	0.022	0.162	0.002	0.030	0.010	2392	20.0	2439	13.7	2478	10.0	98
NE163	97.1	9.00	76.00	6.00	13.22	5.952	0.095	0.363	0.003	0.560	2.752	0.025	0.119	0.002	0.219	0.166	1998	15.6	1969	13.9	1938	23.7	101
NE163	98.1	46.00	62.00	106.00	0.58	7.637	0.116	0.411	0.004	0.890	2.433	0.022	0.135	0.002	0.191	0.017	2219	17.4	2189	13.6	2161	14.1	101
NE163	99.1	108.00	55.00	291.00	0.19	5.912	0.089	0.357	0.003	0.900	2.798	0.024	0.120	0.001	0.033	0.017	1970	14.7	1963	13.0	1956	14.5	100
NE163	101	30.00	157.00	67.00	2.33	6.096	0.089	0.363	0.003	0.970	2.753	0.024	0.122	0.002	0.150	0.086	1998	15.1	1990	12.8	1981	11.5	100

						U-Pb ratios										Ages (Ma)						
Sample	Spot	Pb ppm	Th ppm	U ppm	Th/U	207/235	1σ	206/238	1σ	coef. c.	238/206	1σ	207/206	1σ	208/206	1σ	206/238	2σ	207/235	2σ	207/206	2σ	Conc. %
NE157	2.1	57.50	166.70	134.00	1.24	5.813	0.115	0.348	0.003	0.650	2.876	0.027	0.121	0.002	0.228	0.010	1923	15.8	1948	17.1	1975	27.3	98
NE157	4.1	66.60	170.80	157.50	1.08	5.885	0.119	0.352	0.003	0.770	2.840	0.025	0.121	0.002	0.254	0.009	1944	14.8	1959	17.5	1974	25.8	99
NE157	6.1	94.40	113.20	257.70	0.44	5.795	0.121	0.352	0.003	0.940	2.839	0.026	0.119	0.002	0.079	0.002	1945	15.7	1946	18.1	1946	22.3	99
NE157	12.1	193.30	26.90	667.40	0.04	5.421	0.096	0.334	0.007	0.950	2.992	0.066	0.118	0.003	0.006	0.001	1859	35.8	1888	15.2	1921	13.8	98
NE157	17.1	93.30	115.60	261.30	0.44	5.546	0.083	0.340	0.004	0.710	2.940	0.031	0.118	0.001	0.091	0.010	1887	17.3	1908	12.9	1930	18.9	98
NE157	18.1	106.20	99.70	317.20	0.31	5.619	0.080	0.344	0.004	0.890	2.906	0.030	0.118	0.001	0.074	0.005	1906	17.3	1919	12.3	1933	12.4	99
NE157	20.1	29.20	73.00	70.40	1.04	5.773	0.090	0.346	0.004	0.980	2.888	0.031	0.121	0.002	0.160	0.057	1917	17.7	1942	13.5	1969	9.9	98
NE157	21.1	53.60	47.90	140.20	0.34	5.783	0.085	0.349	0.004	0.230	2.870	0.032	0.120	0.002	0.162	0.042	1927	18.2	1944	12.6	1962	28.7	99
NE157	25.1	61.80	217.00	146.90	1.48	5.822	0.093	0.351	0.004	0.770	2.846	0.034	0.120	0.002	0.235	0.011	1941	20.0	1950	13.9	1959	18.3	99
NE157	28.1	13.60	101.30	17.80	5.70	5.612	0.137	0.344	0.003	0.980	2.906	0.022	0.118	0.003	0.087	0.061	1906	12.5	1918	21.1	1931	30.7	99
NE157	30.1	59.30	147.80	144.90	1.02	5.578	0.140	0.341	0.003	0.930	2.932	0.025	0.119	0.003	0.218	0.024	1892	14.4	1913	21.6	1935	30.8	98
NE157	31.1	272.40	5641.00	240.50	23.46	6.458	0.156	0.380	0.003	0.650	2.634	0.019	0.123	0.003	0.777	0.899	2075	12.6	2040	21.2	2006	35.9	101
NE157	45.1	110.00	112.70	306.80	0.37	5.571	0.103	0.341	0.006	0.710	2.935	0.051	0.119	0.002	0.079	0.004	1890	28.4	1912	15.9	1935	24.4	98
NE157	46.1	66.10	227.20	153.00	1.49	5.790	0.108	0.348	0.006	0.900	2.878	0.049	0.121	0.002	0.167	0.077	1923	28.7	1945	16.1	1969	14.5	98
NE157	50.1	64.00	59.50	162.90	0.37	5.998	0.303	0.354	0.005	0.710	2.825	0.040	0.123	0.006	0.264	0.058	1954	23.8	1976	44.0	1999	74.2	98
NE157	51.1	56.50	317.70	122.20	2.60	5.706	0.283	0.343	0.005	0.820	2.913	0.040	0.121	0.006	0.154	0.048	1902	22.6	1932	42.8	1964	69.8	98
NE157	57.1	164.70	46.80	492.70	0.10	5.906	0.083	0.359	0.003	0.980	2.786	0.023	0.119	0.002	0.163	0.071	1977	14.2	1962	12.1	1946	10.8	100
NE157	59.1	65.00	180.70	152.10	1.19	5.592	0.079	0.342	0.003	0.750	2.924	0.024	0.119	0.002	0.190	0.034	1896	13.5	1915	12.1	1935	17.1	99
NE157	61.1	64.30	153.60	170.20	0.90	5.815	0.067	0.356	0.002	0.910	2.813	0.018	0.119	0.001	0.195	0.007	1961	10.9	1949	10.0	1935	11.3	100
NE157	66.1	52.80	131.50	135.70	0.97	5.651	0.066	0.347	0.003	0.320	2.884	0.021	0.118	0.002	0.226	0.006	1919	12.0	1924	10.1	1929	20.8	99
NE157	67.1	53.00	189.60	120.60	1.57	5.842	0.069	0.353	0.002	0.870	2.836	0.020	0.120	0.002	0.257	0.025	1947	11.4	1953	10.3	1959	12.2	99
NE157	68.1	79.60	223.30	201.50	1.11	5.823	0.070	0.355	0.003	0.810	2.821	0.020	0.119	0.002	0.175	0.028	1956	11.9	1950	10.4	1943	13.5	100
NE157	70.1	133.40	80.80	380.90	0.21	6.267	0.070	0.375	0.002	0.970	2.666	0.016	0.121	0.002	0.084	0.016	2053	10.8	2014	9.8	1974	9.8	101
NE157	74.1	116.60	136.40	344.20	0.40	5.870	0.067	0.358	0.002	0.010	2.790	0.017	0.119	0.001	0.080	0.005	1975	10.4	1957	9.9	1938	23.0	100
NE157	76.1	54.30	211.30	121.70	1.74	5.817	0.062	0.349	0.002	0.950	2.869	0.018	0.121	0.002	0.188	0.065	1928	10.5	1949	9.3	1972	9.1	98
NE157	77.1	106.50	129.70	285.30	0.45	6.138	0.113	0.367	0.002	0.880	2.725	0.017	0.121	0.002	0.129	0.014	2015	10.8	1996	16.0	1976	23.4	100
NE157	80.1	102.60	91.60	308.60	0.30	5.687	0.100	0.349	0.002	0.890	2.865	0.018	0.118	0.002	0.033	0.007	1930	10.5	1929	15.2	1929	22.1	100
NE157	81.1	54.30	90.40	152.00	0.60	5.929	0.106	0.356	0.002	0.970	2.812	0.019	0.121	0.002	0.234	0.024	1961	11.4	1966	15.6	1970	20.5	99
NE157	87.1	73.20	220.80	176.50	1.25	6.065	0.101	0.363	0.003	0.900	2.754	0.019	0.121	0.002	0.236	0.009	1997	11.8	1985	14.6	1973	19.5	100
NE157	92.1	61.00	174.00	137.60	1.27	5.952	0.106	0.361	0.002	0.540	2.770	0.019	0.120	0.002	0.284	0.003	1987	11.4	1969	15.5	1950	27.4	100

CHAPTER 3. FINAL CONSIDERATIONS

3.1 Conclusions

The research in this dissertation explores two wide-ranging themes: 1) applying petrochronological techniques for decode the UHT metamorphism in the Arapiraca Complex and reconstructing their P-T-t evolution, and 2) large scale geological correlation using the petrochronology as a tool to unravel the sources of cratonic fragments dispersed within South Borborema Province.

The study results and discussion summarized as a scientific article in Chapter 2 presented an integrated approach using conventional thermobarometry, phase equilibria modeling of a texturally heterogeneous residual diatexite and zircon petrochronology. The sample investigated in detail (sample NE30) is highly heterogeneous in terms of outcropping to microscopic scale. Notably this sample stands out because it is the first described occurrence of sapphirine in the Borborema Province. The detailed petrography of this rock revealed that the mineral assemblages are spatially distributed in domains with distinct initial compositions, representing different equilibrium volumes within residual fraction of the diatexite. The combination of detailed petrography with mineral chemistry and phase equilibrium modeling revealed important information about the possible P-T conditions for the formation of the observed equilibrium and disequilibrium textures, as well as to identify the possible mechanisms for forming compositional domains during metamorphism and partial melting. A series of P-T and T-M models were calculated in order to evaluate the role of equilibrium volume for the sapphirine nucleation and growth in a specific silica-undersaturated domains during the retrogression from UHT metamorphic peak conditions.

I showed that the sapphirine-bearing diatexite from the Arapiraca Complex recorded a near-isobaric cooling P-T path after the UHT metamorphic peak conditions of ~970ºC and ~8.5 kbar. The coexisting silica-undersaturated and silica-saturated domains represent possible compositional heterogeneity inherited form the sedimentary photolith that was intensified by mass transfer effects due to several melt loss episodes during the progression of metamorphism.

The petrochronological investigation revealed that UHT metamorphism occurred during the Rhyacian-Orosirian transition (2.03 - 1.96 Ga) following sluggish melt crystallization rates in the middle crust along the exhumation path of the Arapiraca Complex. Integration of the petrography with the isotopic data demonstrated that the behavior of zircon during the crystallization of the anatectic melt in the diatexites were strongly influenced by the residue-leucosome proportion, where the most residual samples (i.e. NE30 and NE163) with highest *solidus* temperature recorded older ages than the leucosome-rich diatexite (NE157). This behavior described in several granulitic and UHT terranes illustrates the importance of petrochronology as a powerful tool that should be integrated to better understand the crustal metamorphism (e.g. Engi et al., 2017).

Finally the petrochronological data were integrated on a large scale and here it was suggested that the record of Paleoproterozoic UHT metamorphism in the Arapiraca Complex was contemporaneous and genetically linked to the building up of the São Francisco-Congo Paleocontinent. The new view about the connection between the Paleoproterozoic-Archean blocks from the Borborema Province and São Francisco Craton brings important implications about the extension and rifting of the São Francisco-Congo Paleocontinent and the consequent decratonization process

during the early Neoproterozoic (Neves, 2021; Ganade et al., 2021, *in press*). In this sense, the Arapiraca Complex may represent one of several continental blocks and ribbons related to the passive margin of the São Francisco-Congo Paleocontinent or even the Pernambuco-Alagoas Massif continental ribbon if one considers the complete Wilson cycle model during the Brasiliano orogeny (e.g. Oliveira et al., 2010; Caxito et al., 2016).

3.2 Future Research

Answers to the questions and hypotheses raised here will help further elucidate the crustal heating mechanisms during the Paleoproterozoic orogeny in NE Brazil and inform our understanding of Paleoproterozoic geodynamics and HT/UHT metamorphic processes in general. At the time of this writing, other work addressing many of these questions is in progress by myself, my advisor, and other contributors. In this sense two avenues of future investigations should be taken:

Controls on the scale of equilibrium: Phase equilibrium modeling is commonly employed in the study of pressure-temperature evolution of granulite and UHT rocks (Powell & Holland, 2008). However, defining an equilibrium volume for these rocks is not a trivial task, much because of the compositional heterogeneities inherited from the protolith and the open-system nature of migmatites often associated with melt loss and deformation (Ague, 1994, 1997). Despite the high temperatures reached during UHT metamorphism, many rocks exhibit microstructures that reflect centimeter- or millimeter-scale compositional heterogeneities, including simplectites, coronas, and isolated mineral associations. The sample NE30 (sapphirine-bearing diatexite) investigated here in detail, represents an excellent example of how small equilibrium volume can form in the residue of a migmatite due to inherited (primary and/or

secondary) compositional heterogeneities. Different silica-saturated and silica-unsaturated mineral associations occur as inclusions domains within cordierite poikiloblasts and were considered here as not belonging to the same equilibrium volume which was partially equilibrated along chemical potential gradients (White et al., 2008).

Regardless of the presence of small equilibrium volumes in this rock with aSiO2<1 (i.e. sapphirine-bearing domain), we used the measured bulk rock composition as a basis for modeling the textural and mineralogical evolution observed in the quartz-present residue. This simplified approach modeled with a reasonable degree of accuracy the mineral assemblage for the overall equilibrium volume of the residue, in addition to the observed mineral chemistry and zoning, allowing a robust reconstruction of the metamorphic P-T evolution of the diatexite. However, despite these new data, we have made little petrological progress in the quantification of the observed textures considering the solid-state diffusion of isolated silica-undersaturated pockets in the rock. It is suggested here that future studies with the UHT diatexites from the Arapiraca Complex be investigated using calculated chemical potential (μ) diagrams in order to constrain phase relationships based on univariant equilibria (discontinuous reactions) in simplified chemical systems (e.g. Doukkari et al., 2018). Additionally, a local bulk composition for each suggested equilibrium volume could be estimated using quantitative X-ray maps (EPMA), for which the composition at each pixel is integrated with software such as XMapTools (Lanari et al., 2014). This new approach may elucidate new insights into the role of the chemical potential gradient in the development of cm/mm-scale compositional heterogeneities and retrograde reaction microtextures in UHT migmatites, as well as provide clues to the possible

mechanisms of local interaction with the non-segregated melt in the preservation of these textures.

Other possible São Francisco Craton and Borborema Province connections: In northeast Brazil, the northern boundary of the São Francisco Craton is defined by the Late Proterozoic orogenic Borborema Province (BP). This orogenic region has several small Archean to Paleoproterozoic terranes that have been reworked and deformed and are embedded in younger Neoproterozoic metamorphic belts (Ganade et al., 2014). The origin of these ancient fragments is still widely debated in the literature, with models suggesting consanguinity with the São Francisco craton (e.g. Neves, 2003), to models suggesting that they represent unrelated terranes accreted during the Neoproterozoic orogeny (e.g. Brito Neves et al., 2000). In agreement with the cratonic dispersion model recently presented by Ganade et al. (2021), here in this dissertation, we argue that the Paleoproterozoic UHT metamorphism recorded in the Arapiraca Complex diatexites is genetically correlated to the formation of the São Francisco-Congo paleocontinent. Using petrochronology as a tool to constrain the duration and significance of U-Pb ages in zircon, the reconstructed P-T-t paths for the sapphirine-bearing diatexite are very coherent with similar UHT terrains described in the central and northern portion of the São Francisco Craton (e.g. Leite et al., 2009). In this sense, we highlight that during the prolonged interval of rifting and opening of the Sergipano basin which led to the decratonization of the northern margin of the São Francisco-Congo paleocontinent, the Arapiraca Complex was dismembered from the high-grade metamorphic core of the Eastern Bahia Belt and acted as a continental ribbon subsequently involved in the late Neoproterozoic orogeny.

It is suggested here that a new frontier of investigation is opened for the evolution of the knowledge about the geological evolution of the Borborema Province, mainly regarding the use of petrochronology as a tool in the identification of other possible cratonic fragments dispersed in this ancient orogenic region. This kind of approach can also help to establish new connections between the Borborema Province and related units in West-Central Africa (e.g. Oliveira et al., 2006). It is intended to continue the present study by investigating the following topics: (i) identification of other Paleoproterozoic UHT terranes in NE Brazil; (ii) identification of possible Paleoproterozoic age high-pressure metamorphic rocks (HT eclogites) as similarly described in the south of the Oubanguides Belt in Cameroon (Loose & Schenk, 2018).

3.3 References

Ague, J. J. (1994). Mass transfer during Barrovian metamorphism of pelites, south-central Connecticut; I, Evidence for changes in composition and volume. American Journal of Science, 294(8), 989-1057.

Ague, J. J. (1997). Crustal mass transfer and index mineral growth in Barrow's garnet zone, northeast Scotland. Geology, 25(1), 73-76.

Brito Neves, B.B., Santos, E.J. and Van Schmus, W.R., 2000. Tectonic history of the Borborema Province, NW Brazil. In: Tectonic Evolution of South America (U.G. Cordani, E.J. Milani, A. Thomaz-Filho and D.A. Campos, eds), pp. 151–182. 31st International Geological Congress, Rio de Janeiro.

Caxito, F. A., Uhlein, A., Dantas, E. L., Stevenson, R., Salgado, S. S., Dussin, I. A., & da Nóbrega Sial, A. (2016). A complete Wilson Cycle recorded within the Riacho do Pontal Orogen, NE Brazil: Implications for the Neoproterozoic evolution of the Borborema Province at the heart of West Gondwana. Precambrian Research, 282, 97-120.

Doukkari, S. A., Diener, J. F., Ouzegane, K., & Kienast, J. R. (2018). Mineral equilibrium modelling and calculated chemical potential relations of reaction textures in the ultrahigh-temperature In Ouzzal terrane (In Hihaou area, Western Hoggar, Algeria). Journal of Metamorphic Geology, 36(9), 1175-1198.

Ganade de Araujo, C. E., Weinberg, R. F., & Cordani, U. G. (2014). Extruding the Borborema Province (NE-Brazil): a two-stage Neoproterozoic collision process. Terra Nova, 26(2), 157-168.

Ganade, C. E., Weinberg, R. F., Caxito, F. A., Lopes, L. B., Tesser, L. R., & Costa, I. S. (2021). Decratonization by rifting enables orogenic reworking and transcurrent dispersal of old terranes in NE Brazil. Scientific reports, 11(1), 1-13.

Neves, S. P. (2021). Comparative geological evolution of the Borborema Province and São Francisco Craton (eastern Brazil): Decratonization and crustal reworking during West Gondwana assembly and implications for paleogeographic reconstructions. Precambrian Research, 355, 106119.

Lanari P, Vidal O, De Andrade V, Dubacq B, Lewin E, Grosch EG, Schwartz S (2014) XMapTools: A MATLAB©-based program for electron microprobe X-ray image processing and geothermobarometry. Computers and Geosciences. 62:227–240.

Leite, C., Barbosa, J. S. F., Goncalves, P., Nicollet, C., & Sabaté, P. (2009). Petrological evolution of silica-undersaturated sapphirine-bearing granulite in the Paleoproterozoic Salvador-Curaçá Belt, Bahia, Brazil. Gondwana Research, 15(1), 49-70.

Loose, D., & Schenk, V. (2018). 2.09 Ga old eclogites in the Eburnian-Transamazonian orogen of southern Cameroon: significance for Palaeoproterozoic plate tectonics. Precambrian Research, 304, 1-11.

Oliveira, E. P., Windley, B. F., & Araújo, M. N. (2010). The Neoproterozoic Sergipano orogenic belt, NE Brazil: a complete plate tectonic cycle in western Gondwana. Precambrian Research, 181(1-4), 64-84.

Powell, R., & Holland, T. J. B. (2008). On thermobarometry. Journal of Metamorphic Geology, 26(2), 155-179.

White, R. W., Powell, R., & Baldwin, J. A. (2008). Calculated phase equilibria involving chemical potentials to investigate the textural evolution of metamorphic rocks. Journal of Metamorphic Geology, 26(2).

APPENDIX A. ELECTRON MICROPROBE (EPMA) DATA

Chemical composition of garnet (EPMA data)

Sample ID	NE30 1	NE30 2	NE30 3	NE30 4	NE30 5	NE30 6	NE30 7	NE30 8	NE30 9	NE30 10	NE30 11	NE30 12	NE30 13	NE30 14	NE30 15	NE30 16	NE30 17	NE30 18	NE30 19	NE30 20
SiO2	38.54	38.78	38.48	38.55	40.28	38.59	38.71	38.72	38.65	38.63	38.83	38.64	38.81	38.65	38.86	38.55	38.93	38.76	38.56	38.18
TiO2	0.00	0.04	0.02	0.01	0.00	0.00	0.02	0.01	0.02	0.04	0.00	0.04	0.00	0.00	0.00	0.01	0.01	0.00	0.00	0.00
Al2O3	22.23	22.27	22.46	22.63	21.79	22.54	22.51	22.47	22.42	22.25	22.38	22.42	22.57	22.41	22.37	22.44	22.29	22.33	22.19	22.37
Cr2O3	0.00	0.00	0.00	0.00	0.00	0.01	0.01	0.01	0.00	0.00	0.01	0.02	0.01	0.00	0.04	0.00	0.00	0.00	0.00	0.00
FeO	24.25	23.71	23.84	23.47	22.93	23.86	23.53	23.19	24.21	24.70	24.42	24.46	25.14	24.76	24.45	24.02	23.76	24.33	24.20	24.15
MnO	4.18	3.84	3.39	2.84	2.57	2.60	2.88	3.41	2.75	2.87	2.60	2.25	2.23	2.90	2.78	2.72	2.71	3.05	5.12	4.75
MgO	9.39	9.61	10.02	10.64	10.52	10.93	10.55	10.14	10.03	9.74	9.52	10.05	10.26	9.66	9.67	9.97	10.02	9.97	7.83	8.46
CaO	1.21	1.23	1.06	1.09	1.04	1.10	1.14	1.12	1.62	1.58	1.68	1.55	1.04	1.26	1.47	1.69	1.64	1.46	1.28	1.15
Total	99.80	99.48	99.27	99.22	99.13	99.63	99.34	99.07	99.71	99.81	99.44	99.43	100.05	99.64	99.64	99.40	99.36	99.90	99.18	99.06
Oxygens	12	12	12	12	12	12	12	12	12	12	12	12	12	12	12	12	12	12	12	12
Si	2.969	2.989	2.964	2.957	3.095	2.946	2.969	2.984	2.963	2.966	2.992	2.969	2.964	2.974	2.988	2.963	2.993	2.969	3.015	2.977
Ti	0.000	0.002	0.001	0.001	0.000	0.000	0.001	0.001	0.001	0.002	0.000	0.002	0.000	0.000	0.000	0.001	0.001	0.000	0.000	0.000
Al	2.018	2.023	2.039	2.046	1.973	2.028	2.034	2.041	2.026	2.014	2.032	2.030	2.032	2.032	2.027	2.033	2.019	2.016	2.045	2.056
Cr	0.000	0.000	0.000	0.000	0.000	0.001	0.000	0.001	0.000	0.000	0.001	0.001	0.000	0.000	0.002	0.000	0.000	0.000	0.000	0.000
Fe3+	0.044	0.000	0.030	0.038	0.000	0.079	0.026	0.000	0.046	0.049	0.000	0.026	0.039	0.020	0.000	0.039	0.000	0.046	0.000	0.000
Fe2+	1.518	1.528	1.506	1.467	1.474	1.444	1.483	1.495	1.506	1.537	1.574	1.546	1.567	1.573	1.572	1.505	1.527	1.513	1.582	1.575
Mn	0.273	0.251	0.221	0.185	0.167	0.168	0.187	0.223	0.179	0.187	0.170	0.146	0.144	0.189	0.181	0.177	0.176	0.198	0.339	0.314
Mg	1.078	1.104	1.151	1.217	1.205	1.244	1.206	1.165	1.146	1.115	1.093	1.151	1.168	1.108	1.108	1.143	1.148	1.139	0.913	0.983
Ca	0.100	0.102	0.087	0.089	0.085	0.090	0.093	0.092	0.133	0.130	0.139	0.128	0.085	0.104	0.121	0.139	0.135	0.120	0.107	0.096
Sum	8.000	8.000	8.000	8.000	8.000	8.000	8.000	8.000	8.000	8.000	8.000	8.000	8.000	8.000	8.000	8.000	8.000	8.000	8.000	8.000
X(Mg)	0.408	0.419	0.428	0.447	0.450	0.450	0.444	0.438	0.425	0.413	0.410	0.423	0.421	0.410	0.413	0.425	0.429	0.422	0.366	0.384
alm	51.13	51.20	50.79	49.61	50.27	49.03	49.94	50.25	50.82	51.77	52.88	52.03	52.86	52.90	52.71	50.78	51.13	50.95	53.80	53.06
prp	36.32	36.99	38.80	41.14	41.11	42.22	40.62	39.17	38.67	37.56	36.75	38.75	39.41	37.26	37.16	38.55	38.44	38.35	31.03	33.13
grs	3.29	3.41	2.90	2.96	2.91	2.93	3.10	3.10	4.39	4.27	4.66	4.23	2.81	3.45	4.06	4.61	4.52	3.95	3.64	3.24
sps	9.19	8.40	7.46	6.24	5.71	5.71	6.30	7.48	6.02	6.29	5.70	4.93	4.87	6.36	6.07	5.97	5.91	6.67	11.53	10.57
uva	0.00	0.00	0.00	0.00	0.00	0.00	0.00	0.00	0.00	0.00	0.00	0.00	0.00	0.00	0.00	0.00	0.00	0.00	0.00	0.00
adr	0.07	0.00	0.04	0.06	0.00	0.11	0.04	0.00	0.10	0.10	0.00	0.05	0.05	0.03	0.00	0.09	0.00	0.09	0.00	0.00

Chemical composition of garnet (EPMA data)

Sample	NE30	NE30	NE30	NE30	NE30	NE30	NE30	NE30	NE30	NE30	NE30	NE30	NE30	NE30	NE30	NE30	NE30	NE30	NE30	NE30
ID	21	22	23	24	25	26	27	28	29	30	31	32	33	34	35	36	37	38	39	40
SiO2	38.29	38.11	38.18	38.27	38.55	38.20	38.45	39.19	39.56	39.48	39.67	39.51	39.50	39.20	39.42	39.10	39.71	39.49	38.96	39.34
TiO2	0.00	0.02	0.03	0.01	0.04	0.00	0.00	0.02	0.03	0.00	0.00	0.00	0.00	0.01	0.00	0.00	0.00	0.00	0.00	0.02
Al2O3	22.36	22.16	22.31	22.28	22.28	22.36	22.44	22.24	22.78	22.84	22.76	22.69	22.60	22.73	22.64	22.71	22.68	22.61	22.97	22.55
Cr2O3	0.00	0.00	0.00	0.00	0.02	0.03	0.00	0.01	0.00	0.00	0.01	0.00	0.00	0.02	0.00	0.00	0.00	0.01	0.00	0.00
FeO	23.85	23.93	24.01	23.99	23.33	23.35	23.99	24.37	23.01	22.39	22.61	22.71	22.67	23.10	22.57	23.08	23.70	23.34	23.10	23.71
MnO	4.70	4.88	5.30	4.84	4.68	4.62	4.62	4.77	3.17	2.89	2.13	1.56	1.47	2.14	3.36	2.63	1.58	1.79	2.66	2.72
MgO	8.94	8.35	7.79	8.46	8.49	9.03	8.63	8.75	10.34	10.65	11.35	11.94	11.99	11.13	10.10	10.71	11.43	11.55	10.83	10.57
CaO	1.09	1.19	1.32	1.13	1.09	1.18	1.15	1.16	0.97	1.16	1.10	1.12	0.99	1.15	1.11	0.92	1.16	0.91	0.90	0.93
Total	99.23	98.64	98.94	98.98	98.48	98.77	99.28	100.50	99.86	99.41	99.63	99.53	99.22	99.47	99.20	99.15	100.26	99.70	99.43	99.84
Oxygens	12	12	12	12	12	12	12	12	12	12	12	12	12	12	12	12	12	12	12	12
Si	2.972	2.986	2.992	2.986	3.019	2.974	2.987	3.011	3.020	3.017	3.013	2.994	3.002	2.988	3.030	2.998	3.000	2.998	2.976	3.002
Ti	0.000	0.001	0.002	0.000	0.003	0.000	0.000	0.001	0.002	0.000	0.000	0.000	0.000	0.000	0.000	0.000	0.000	0.000	0.000	0.001
Al	2.046	2.046	2.060	2.049	2.056	2.052	2.055	2.014	2.049	2.057	2.038	2.027	2.024	2.042	2.051	2.052	2.020	2.023	2.068	2.028
Cr	0.000	0.000	0.000	0.000	0.001	0.002	0.000	0.000	0.000	0.000	0.001	0.000	0.000	0.001	0.000	0.000	0.000	0.001	0.000	0.000
Fe3+	0.010	0.000	0.000	0.000	0.000	0.000	0.000	0.000	0.000	0.000	0.000	0.000	0.000	0.000	0.000	0.000	0.000	0.000	0.000	0.000
Fe2+	1.538	1.568	1.573	1.566	1.528	1.520	1.559	1.566	1.469	1.431	1.436	1.439	1.441	1.472	1.451	1.480	1.498	1.482	1.476	1.513
Mn	0.309	0.324	0.352	0.320	0.310	0.305	0.304	0.310	0.205	0.187	0.137	0.100	0.095	0.138	0.219	0.171	0.101	0.115	0.172	0.176
Mg	1.034	0.975	0.910	0.984	0.991	1.048	1.000	1.002	1.177	1.213	1.285	1.349	1.358	1.265	1.157	1.224	1.287	1.307	1.233	1.203
Ca	0.091	0.100	0.110	0.094	0.092	0.098	0.096	0.095	0.079	0.095	0.090	0.091	0.081	0.094	0.091	0.075	0.094	0.074	0.074	0.076
Sum	8.000	8.000	8.000	8.000	8.000	8.000	8.000	8.000	8.000	8.000	8.000	8.000	8.000	8.000	8.000	8.000	8.000	8.000	8.000	8.000
X(Mg)	0.401	0.383	0.366	0.386	0.393	0.408	0.391	0.390	0.445	0.459	0.472	0.484	0.485	0.462	0.444	0.453	0.462	0.469	0.455	0.443
alm	53.06	51.75	52.84	53.41	52.82	52.30	51.16	52.69	52.65	50.14	48.90	48.72	48.31	48.43	49.59	49.72	50.16	50.25	49.76	49.94
prp	33.13	34.81	32.87	30.89	33.20	33.93	35.27	33.79	33.70	40.16	41.46	43.59	45.28	45.66	42.60	39.66	41.50	43.20	43.90	41.74
grs	3.24	3.04	3.37	3.75	3.19	3.13	3.31	3.24	3.21	2.70	3.25	3.04	3.05	2.72	3.15	3.13	2.55	3.16	2.47	2.50
sps	10.57	10.40	10.91	11.94	10.79	10.63	10.25	10.28	10.44	7.00	6.39	4.65	3.36	3.18	4.65	7.50	5.79	3.39	3.87	5.82
uva	0.00	0.00	0.00	0.00	0.00	0.00	0.00	0.00	0.00	0.00	0.00	0.00	0.00	0.00	0.00	0.00	0.00	0.00	0.00	0.00
adr	0.00	0.02	0.00	0.00	0.00	0.00	0.00	0.00	0.00	0.00	0.00	0.00	0.00	0.00	0.00	0.00	0.00	0.00	0.00	0.00

Chemical composition of garnet (EPMA data)

Sample	NE30	NE30	NE30	NE30	NE30	NE30	NE30	NE30	NE30	NE30	NE30	NE30	NE30	NE30	NE30	NE30	NE30	NE30	NE30	NE30
ID	41	42	43	44	45	46	47	48	49	50	51	52	53	54	55	56	57	58	59	60
SiO2	39.64	39.46	39.89	39.10	39.28	39.33	50.06	39.44	38.97	38.81	38.24	38.84	38.39	38.63	38.01	39.24	39.21	39.63	39.38	39.34
TiO2	0.00	0.01	0.03	0.01	0.01	0.00	0.00	0.01	0.00	0.00	0.00	0.00	0.00	0.01	0.02	0.01	0.00	0.04	0.01	0.00
Al2O3	23.39	23.22	25.34	22.79	23.05	22.46	17.77	22.61	22.44	22.09	22.01	22.18	22.13	22.47	22.31	22.84	22.71	22.75	22.82	22.87
Cr2O3	0.02	0.00	0.00	0.01	0.01	0.02	0.01	0.02	0.00	0.00	0.00	0.00	0.01	0.00	0.01	0.01	0.00	0.00	0.02	0.02
FeO	22.87	22.63	21.61	22.56	22.14	22.88	18.21	21.51	21.59	24.33	23.91	24.19	25.08	24.61	24.21	24.66	24.77	24.02	24.07	23.68
MnO	1.58	1.46	1.22	1.39	1.58	2.16	2.43	5.48	5.08	4.63	5.03	4.77	4.72	4.35	4.71	2.85	2.37	1.91	1.62	1.39
MgO	11.41	11.86	11.27	12.14	11.74	11.53	8.64	8.86	9.34	8.73	7.95	8.32	8.72	8.85	8.60	9.88	10.51	10.77	11.17	11.50
CaO	1.22	1.04	1.18	1.01	1.28	1.25	0.98	1.50	1.52	1.18	1.53	1.13	1.04	1.15	1.13	1.18	1.12	1.26	1.25	1.31
Total	100.13	99.68	100.54	99.00	99.09	99.63	98.10	99.43	98.94	99.77	98.67	99.43	100.09	100.07	98.99	100.67	100.69	100.38	100.34	100.12
Oxygens	12	12	12	12	12	12	12	12	12	12	12	12	12	12	12	12	12	12	12	12
Si	2.992	2.984	2.984	2.974	2.987	2.988	3.917	3.047	3.017	3.003	3.001	3.021	2.965	2.977	2.964	2.984	2.971	3.003	2.978	2.973
Ti	0.000	0.001	0.002	0.000	0.001	0.000	0.000	0.001	0.000	0.000	0.000	0.000	0.000	0.001	0.001	0.000	0.000	0.002	0.001	0.000
Al	2.080	2.070	2.234	2.043	2.066	2.011	1.639	2.059	2.048	2.014	2.036	2.033	2.015	2.041	2.050	2.047	2.028	2.032	2.034	2.037
Cr	0.001	0.000	0.000	0.000	0.000	0.001	0.001	0.001	0.000	0.000	0.000	0.000	0.000	0.000	0.000	0.001	0.000	0.000	0.001	0.001
Fe3+	0.000	0.000	0.000	0.009	0.000	0.013	0.000	0.000	0.000	0.000	0.000	0.000	0.054	0.004	0.019	0.000	0.029	0.000	0.008	0.014
Fe2+	1.443	1.431	1.352	1.426	1.408	1.441	1.192	1.390	1.398	1.574	1.569	1.573	1.566	1.582	1.560	1.568	1.541	1.522	1.514	1.482
Mn	0.101	0.094	0.078	0.090	0.102	0.139	0.161	0.359	0.333	0.303	0.334	0.314	0.309	0.284	0.311	0.184	0.152	0.123	0.104	0.089
Mg	1.284	1.337	1.257	1.376	1.331	1.306	1.008	1.020	1.078	1.007	0.930	0.965	1.004	1.017	1.000	1.120	1.187	1.217	1.259	1.296
Ca	0.098	0.084	0.094	0.082	0.104	0.102	0.082	0.124	0.126	0.098	0.129	0.094	0.086	0.095	0.094	0.096	0.091	0.102	0.101	0.106
Sum	8.000	8.000	8.000	8.000	8.000	8.000	8.000	8.000	8.000	8.000	8.000	8.000	8.000	8.000	8.000	8.000	8.000	8.000	8.000	8.000
X(Mg)	0.471	0.483	0.482	0.490	0.486	0.473	0.458	0.423	0.435	0.390	0.372	0.380	0.383	0.391	0.388	0.417	0.431	0.444	0.453	0.464
alm	0.53	0.52	0.52	0.51	0.51	0.53	0.54	0.58	0.56	0.61	0.63	0.62	0.62	0.61	0.61	0.58	0.57	0.56	0.55	0.54
prp	49.32	48.58	48.62	47.95	47.81	48.23	48.78	48.04	47.63	52.78	52.97	53.40	52.81	53.14	52.62	52.84	51.87	51.37	50.84	49.85
grs	43.86	45.39	45.20	46.28	45.19	43.70	41.26	35.27	36.73	33.76	31.40	32.74	33.86	34.15	33.72	37.74	39.96	41.06	42.27	43.58
sps	3.36	2.85	3.40	2.75	3.54	3.39	3.36	4.29	4.30	3.28	4.34	3.19	2.84	3.17	3.14	3.23	3.01	3.44	3.39	3.55
uva	3.45	3.17	2.79	3.01	3.46	4.65	6.59	12.40	11.35	10.17	11.29	10.67	10.41	9.54	10.49	6.19	5.12	4.14	3.48	2.99
adr	0.00	0.00	0.00	0.00	0.00	0.00	0.00	0.00	0.00	0.00	0.00	0.00	0.00	0.00	0.00	0.00	0.00	0.00	0.00	0.00

Chemical composition of garnet (EPMA data)

Sample	NE30	NE30	NE30	NE30	NE30	NE30	NE30	NE30	NE30	NE30	NE30	NE30	NE30	NE30	NE30	NE30	NE30	NE30	NE30	NE30
ID	61	62	63	64	65	66	67	68	69	70	71	72	73	74	75	76	77	78	79	80
SiO2	39.65	39.74	39.53	39.57	39.34	39.53	39.37	39.72	39.29	39.49	39.59	39.02	38.87	39.29	39.14	38.67	38.75	38.21	38.61	38.76
TiO2	0.00	0.02	0.00	0.02	0.00	0.01	0.00	0.00	0.05	0.00	0.01	0.01	0.03	0.00	0.01	0.00	0.03	0.00	0.00	0.00
Al2O3	22.77	22.99	23.05	22.79	22.94	23.33	22.90	22.77	22.73	22.67	22.65	22.72	22.83	22.40	22.30	22.40	22.24	22.27	22.27	22.46
Cr2O3	0.00	0.01	0.01	0.01	0.02	0.01	0.01	0.00	0.01	0.01	0.02	0.00	0.01	0.00	0.00	0.00	0.02	0.02	0.01	0.00
FeO	23.60	23.34	23.36	23.38	23.35	23.15	23.69	23.34	23.94	24.33	24.18	23.86	23.99	24.06	24.34	23.74	23.96	23.96	24.15	24.77
MnO	1.28	1.28	1.22	1.23	1.24	1.19	1.24	1.23	1.33	1.67	1.81	1.92	2.13	2.54	2.95	5.41	5.17	5.30	5.35	5.35
MgO	11.62	11.80	11.77	11.91	11.78	11.62	11.68	11.67	11.54	11.22	11.02	10.98	10.80	10.40	10.18	7.94	8.60	8.46	8.57	8.39
CaO	1.19	1.14	1.03	1.16	1.09	1.14	1.22	1.29	1.26	1.08	1.13	1.25	1.18	1.19	1.22	1.42	1.24	1.07	1.11	1.18
Total	100.11	100.32	99.97	100.08	99.76	99.98	100.10	100.02	100.16	100.47	100.41	99.76	99.85	99.88	100.14	99.58	100.00	99.29	100.07	100.91
Oxygens	12	12	12	12	12	12	12	12	12	12	12	12	12	12	12	12	12	12	12	12
Si	2.995	2.992	2.985	2.985	2.978	2.985	2.973	3.001	2.970	2.984	2.996	2.970	2.960	3.001	2.989	3.007	2.993	2.975	2.983	2.974
Ti	0.000	0.001	0.000	0.001	0.000	0.000	0.000	0.000	0.003	0.000	0.001	0.001	0.002	0.000	0.001	0.000	0.002	0.000	0.000	0.000
Al	2.027	2.040	2.052	2.026	2.046	2.076	2.038	2.027	2.025	2.019	2.020	2.038	2.049	2.016	2.007	2.053	2.025	2.043	2.028	2.031
Cr	0.000	0.001	0.000	0.001	0.001	0.000	0.001	0.000	0.001	0.000	0.001	0.000	0.001	0.000	0.000	0.000	0.001	0.001	0.001	0.000
Fe3+	0.000	0.000	0.000	0.001	0.000	0.000	0.015	0.000	0.028	0.012	0.000	0.020	0.026	0.000	0.014	0.000	0.000	0.006	0.006	0.020
Fe2+	1.491	1.469	1.475	1.474	1.478	1.462	1.481	1.475	1.485	1.526	1.531	1.499	1.502	1.537	1.540	1.544	1.548	1.554	1.554	1.570
Mn	0.082	0.082	0.078	0.079	0.080	0.076	0.079	0.078	0.085	0.107	0.116	0.124	0.137	0.164	0.191	0.356	0.338	0.350	0.350	0.348
Mg	1.309	1.324	1.325	1.339	1.329	1.308	1.315	1.314	1.300	1.264	1.243	1.246	1.226	1.184	1.159	0.921	0.990	0.982	0.987	0.960
Ca	0.096	0.092	0.084	0.094	0.088	0.092	0.098	0.105	0.102	0.088	0.091	0.102	0.097	0.098	0.100	0.118	0.103	0.089	0.092	0.097
Sum	8.000	8.000	8.000	8.000	8.000	8.000	8.000	8.000	8.000	8.000	8.000	8.000	8.000	8.000	8.000	8.000	8.000	8.000	8.000	8.000
X(Mg)	0.467	0.474	0.473	0.476	0.473	0.472	0.468	0.471	0.462	0.451	0.448	0.451	0.445	0.435	0.427	0.374	0.390	0.386	0.387	0.376
alm	50.07	49.52	49.80	49.36	49.68	49.75	49.80	49.62	49.95	51.13	51.33	50.46	50.70	51.52	51.51	52.53	51.96	52.25	52.10	52.78
prp	43.95	44.63	44.73	44.85	44.68	44.51	44.23	44.22	43.74	42.36	41.71	41.94	41.40	39.70	38.77	31.32	33.24	33.01	33.09	32.27
grs	3.23	3.09	2.82	3.14	2.97	3.14	3.28	3.52	3.39	2.92	3.07	3.40	3.22	3.27	3.31	4.03	3.44	2.98	3.06	3.23
sps	2.76	2.75	2.64	2.64	2.68	2.59	2.66	2.64	2.86	3.58	3.89	4.17	4.64	5.51	6.38	12.12	11.36	11.75	11.74	11.69
uva	0.00	0.00	0.00	0.00	0.00	0.00	0.00	0.00	0.00	0.00	0.00	0.00	0.00	0.00	0.00	0.00	0.00	0.00	0.00	0.00
adr	0.00	0.00	0.00	0.00	0.00	0.00	0.02	0.00	0.05	0.02	0.00	0.03	0.04	0.00	0.02	0.00	0.00	0.01	0.01	0.03

Chemical composition of garnet (EPMA data)

Sample	NE157	NE157	NE157	NE157	NE157	NE157	NE157	NE157	NE157	NE157	NE157	NE157	NE157	NE157	NE157	NE157	NE157	NE157	NE157	NE157
ID	89	90	91	92	93	94	95	96	97	98	99	100	101	102	103	104	105	106	107	108
SiO2	37.65	38.35	38.74	38.21	38.43	38.03	38.62	38.05	38.00	37.80	37.79	37.45	37.21	38.39	37.84	38.34	38.13	38.10	38.05	38.16
TiO2	0.04	0.04	0.04	0.01	0.05	0.02	0.03	0.00	0.00	0.00	0.05	0.02	0.84	0.03	0.04	0.03	0.00	0.07	0.00	0.04
Al2O3	21.90	22.06	22.23	22.09	22.03	22.15	22.27	22.03	22.26	21.81	22.12	21.54	21.66	22.18	22.09	22.23	22.19	22.18	22.14	22.11
Cr2O3	0.04	0.04	0.03	0.02	0.03	0.01	0.02	0.02	0.00	0.01	0.02	0.02	0.02	0.02	0.02	0.03	0.00	0.00	0.00	0.03
FeO	32.61	29.87	30.36	29.67	30.07	29.57	29.37	30.71	30.53	31.75	30.70	33.50	33.26	31.06	30.10	30.29	30.26	30.34	30.25	30.55
MnO	0.98	0.76	0.75	0.79	0.71	0.75	0.75	0.76	0.82	0.81	0.83	1.13	1.18	0.91	0.86	0.85	0.86	0.77	0.80	0.87
MgO	5.88	7.33	7.84	7.92	7.83	8.07	7.87	7.30	7.47	6.69	7.52	5.13	5.38	7.17	7.87	7.78	7.11	7.71	7.82	7.57
CaO	1.16	1.40	1.16	1.13	0.94	0.99	1.24	1.22	1.22	0.90	0.92	1.09	1.22	0.89	0.91	1.09	1.22	1.06	0.94	0.90
Total	100.26	99.84	101.15	99.84	100.09	99.59	100.17	100.09	100.30	99.78	99.95	99.88	100.76	100.65	99.73	100.63	99.77	100.23	100.01	100.23
Oxygens	12	12	12	12	12	12	12	12	12	12	12	12	12	12	12	12	12	12	12	12
Si	2.964	2.994	2.982	2.975	2.988	2.965	2.995	2.968	2.954	2.974	2.950	2.976	2.932	2.983	2.953	2.966	2.984	2.961	2.961	2.970
Ti	0.002	0.002	0.002	0.001	0.003	0.001	0.002	0.000	0.000	0.000	0.003	0.001	0.049	0.001	0.003	0.001	0.000	0.004	0.000	0.003
Al	2.032	2.030	2.016	2.027	2.019	2.035	2.035	2.026	2.040	2.022	2.035	2.018	2.012	2.031	2.031	2.027	2.047	2.031	2.031	2.028
Cr	0.003	0.002	0.002	0.001	0.002	0.000	0.001	0.001	0.000	0.001	0.001	0.001	0.001	0.001	0.001	0.002	0.000	0.000	0.000	0.002
Fe3+	0.034	0.000	0.014	0.021	0.000	0.032	0.000	0.036	0.052	0.030	0.058	0.026	0.024	0.000	0.057	0.036	0.000	0.040	0.046	0.026
Fe2+	2.113	1.950	1.940	1.910	1.955	1.896	1.905	1.967	1.933	2.059	1.946	2.200	2.168	2.018	1.907	1.924	1.980	1.932	1.922	1.962
Mn	0.065	0.050	0.049	0.052	0.047	0.049	0.049	0.050	0.054	0.054	0.055	0.076	0.079	0.060	0.057	0.056	0.057	0.051	0.053	0.057
Mg	0.690	0.853	0.900	0.919	0.908	0.938	0.910	0.849	0.866	0.785	0.875	0.608	0.632	0.831	0.915	0.897	0.830	0.893	0.907	0.878
Ca	0.098	0.117	0.095	0.094	0.078	0.083	0.103	0.102	0.102	0.076	0.077	0.093	0.103	0.074	0.076	0.090	0.102	0.088	0.079	0.075
Sum	8.000	8.000	8.000	8.000	8.000	8.000	8.000	8.000	8.000	8.000	8.000	8.000	8.000	8.000	8.000	8.000	8.000	8.000	8.000	8.000
X(Mg)	0.243	0.304	0.315	0.322	0.317	0.327	0.323	0.298	0.304	0.273	0.304	0.214	0.224	0.292	0.318	0.314	0.295	0.312	0.315	0.306
alm	71.23	65.65	65.02	64.21	65.44	63.92	64.20	66.27	65.44	69.23	65.90	73.90	72.71	67.67	64.53	64.84	66.70	65.17	64.92	66.01
prp	23.26	28.72	30.15	30.89	30.38	31.62	30.67	28.60	29.31	26.38	29.64	20.41	21.20	27.85	30.98	30.24	27.94	30.13	30.64	29.55
grs	3.25	3.93	3.17	3.12	2.61	2.75	3.48	3.37	3.35	2.52	2.52	3.08	3.33	2.47	2.49	2.98	3.45	2.92	2.60	2.47
sps	2.19	1.68	1.64	1.75	1.57	1.66	1.65	1.70	1.82	1.83	1.87	2.56	2.63	2.01	1.92	1.88	1.91	1.72	1.78	1.93
uva	0.00	0.00	0.00	0.00	0.00	0.00	0.00	0.00	0.00	0.00	0.00	0.00	0.00	0.00	0.00	0.00	0.00	0.00	0.00	0.00
adr	0.05	0.00	0.02	0.03	0.00	0.04	0.00	0.06	0.08	0.04	0.07	0.04	0.04	0.00	0.07	0.05	0.00	0.06	0.06	0.03

Chemical composition of garnet (EPMA data)

Sample	NE157	NE157	NE157	NE157	NE157	NE157	NE157	NE157	NE157	NE157	NE157	NE157	NE157	NE157	NE157	NE157	NE157	NE157	NE157	NE157
ID	109	110	111	112	113	114	115	116	117	118	119	120	121	122	123	124	125	126	127	128
SiO2	37.60	38.38	38.24	38.19	38.59	37.98	38.02	37.87	38.17	38.50	38.07	37.83	37.79	38.20	38.12	38.19	38.04	38.17	37.87	37.48
TiO2	0.00	0.00	0.00	0.02	0.03	0.00	0.01	0.02	0.01	0.03	0.04	0.00	0.02	0.00	0.04	0.01	0.00	0.03	0.03	0.00
Al2O3	21.96	22.01	22.10	22.17	22.08	22.10	22.12	22.13	21.86	21.99	21.85	21.94	21.94	22.09	22.00	22.11	21.95	21.92	21.94	21.75
Cr2O3	0.03	0.05	0.04	0.01	0.03	0.03	0.05	0.03	0.01	0.04	0.04	0.04	0.03	0.06	0.05	0.04	0.04	0.03	0.01	0.04
FeO	31.88	30.91	30.93	30.46	29.64	29.99	30.43	31.06	32.51	34.98	31.48	31.11	30.51	30.61	30.03	30.92	29.95	30.81	33.09	31.43
MnO	1.14	0.89	0.89	0.82	0.85	0.80	0.85	0.92	1.13	1.34	0.96	0.90	0.92	0.90	0.96	0.89	0.86	1.03	1.20	0.97
MgO	5.96	7.04	7.62	7.76	7.89	7.80	7.65	6.92	5.80	3.69	6.47	6.91	7.10	7.14	7.34	7.34	7.19	6.80	5.16	6.64
CaO	1.13	1.41	1.06	0.91	1.02	1.06	1.04	1.05	1.25	1.09	0.98	1.06	1.04	1.23	1.14	1.07	1.29	1.30	1.16	1.25
Total	99.70	100.69	100.88	100.34	100.13	99.76	100.17	100.00	100.73	101.66	99.89	99.79	99.34	100.23	99.68	100.57	99.32	100.08	100.47	99.57
Oxygens	12	12	12	12	12	12	12	12	12	12	12	12	12	12	12	12	12	12	12	12
Si	2.971	2.982	2.958	2.965	2.997	2.962	2.958	2.965	2.992	3.034	2.994	2.969	2.973	2.979	2.984	2.967	2.989	2.987	2.988	2.954
Ti	0.000	0.000	0.000	0.001	0.002	0.000	0.001	0.001	0.001	0.002	0.002	0.000	0.001	0.000	0.002	0.001	0.000	0.002	0.002	0.000
Al	2.045	2.015	2.015	2.028	2.021	2.031	2.028	2.042	2.019	2.042	2.025	2.029	2.035	2.030	2.029	2.024	2.033	2.022	2.040	2.020
Cr	0.002	0.003	0.002	0.001	0.002	0.002	0.003	0.002	0.001	0.003	0.003	0.003	0.002	0.004	0.003	0.003	0.003	0.002	0.001	0.003
Fe3+	0.010	0.018	0.068	0.039	0.000	0.043	0.052	0.025	0.000	0.000	0.000	0.030	0.015	0.010	0.000	0.038	0.000	0.000	0.000	0.068
Fe2+	2.097	1.991	1.933	1.939	1.925	1.914	1.928	2.009	2.131	2.305	2.071	2.011	1.993	1.986	1.966	1.970	1.968	2.017	2.184	2.003
Mn	0.076	0.058	0.058	0.054	0.056	0.053	0.056	0.061	0.075	0.089	0.064	0.060	0.061	0.059	0.063	0.058	0.057	0.068	0.080	0.065
Mg	0.702	0.815	0.879	0.898	0.913	0.907	0.887	0.808	0.678	0.433	0.759	0.808	0.833	0.830	0.856	0.850	0.842	0.793	0.607	0.780
Ca	0.096	0.117	0.088	0.076	0.085	0.089	0.087	0.088	0.105	0.092	0.082	0.089	0.087	0.103	0.096	0.089	0.109	0.109	0.098	0.106
Sum	8.000	8.000	8.000	8.000	8.000	8.000	8.000	8.000	8.000	8.000	8.000	8.000	8.000	8.000	8.000	8.000	8.000	8.000	8.000	8.000
X(Mg)	0.250	0.289	0.305	0.312	0.322	0.317	0.309	0.284	0.241	0.158	0.268	0.284	0.293	0.294	0.303	0.297	0.300	0.282	0.218	0.274
alm	70.58	66.76	65.36	65.36	64.61	64.60	65.17	67.73	71.31	78.95	69.59	67.75	67.00	66.69	65.93	66.40	66.12	67.51	73.55	67.81
prp	23.63	27.34	29.71	30.28	30.66	30.62	29.99	27.23	22.68	14.85	25.49	27.23	28.00	27.86	28.73	28.64	28.30	26.56	20.44	26.41
grs	3.21	3.90	2.87	2.50	2.84	2.92	2.87	2.94	3.50	3.13	2.75	2.95	2.92	3.43	3.20	2.94	3.65	3.65	3.31	3.46
sps	2.56	1.96	1.96	1.82	1.88	1.79	1.90	2.06	2.50	3.06	2.16	2.02	2.06	1.99	2.13	1.96	1.93	2.28	2.70	2.20
uva	0.00	0.01	0.00	0.00	0.00	0.00	0.00	0.00	0.00	0.00	0.00	0.00	0.00	0.01	0.00	0.00	0.00	0.00	0.00	0.00
adr	0.02	0.03	0.10	0.05	0.00	0.06	0.07	0.04	0.00	0.00	0.00	0.04	0.02	0.02	0.00	0.06	0.00	0.00	0.00	0.12

Chemical composition of garnet (EPMA data)

Sample	NE157	NE157	NE157	NE157	NE157	NE157	NE163	NE163	NE163	NE163	NE163	NE163	NE163	NE163	NE163	NE163	NE163	NE163	NE163	NE163
ID	134	135	136	137	138	139	140	141	142	143	144	145	146	147	148	149	150	151	152	153
SiO2	37.95	38.08	37.88	38.66	38.22	37.83	38.07	38.40	38.47	38.60	38.60	38.25	38.25	38.41	38.26	38.10	38.03	37.71	37.63	36.61
TiO2	0.00	0.00	0.03	0.00	0.05	0.00	0.00	0.01	0.03	0.01	0.03	0.00	0.08	0.00	0.03	0.00	0.02	0.04	0.03	0.01
Al2O3	21.84	22.04	22.13	22.21	22.04	21.87	22.05	22.27	22.39	22.49	22.51	22.34	22.38	22.50	22.20	22.21	22.13	22.13	22.31	21.61
Cr2O3	0.03	0.07	0.04	0.04	0.03	0.01	0.02	0.04	0.00	0.00	0.03	0.01	0.04	0.01	0.03	0.00	0.00	0.01	0.01	0.02
FeO	30.35	29.24	29.43	29.54	30.11	30.46	29.38	28.11	26.71	26.90	27.29	27.51	26.77	26.68	27.71	29.30	29.63	29.79	30.46	32.44
MnO	0.80	0.86	0.83	0.86	0.85	0.91	1.98	1.31	1.26	1.44	1.39	1.41	1.36	1.26	1.56	1.39	1.37	1.47	1.40	2.59
MgO	7.62	8.00	7.89	7.95	7.33	6.73	6.58	8.88	9.74	9.50	9.35	9.73	9.90	9.78	8.88	7.12	7.31	6.66	7.06	4.59
CaO	1.18	1.20	1.28	1.30	1.31	1.36	1.31	1.47	1.04	1.28	1.04	1.05	0.99	1.36	1.22	1.86	1.71	2.01	1.86	1.64
Total	99.78	99.49	99.51	100.56	99.94	99.17	99.40	100.49	99.65	100.22	100.24	100.30	99.77	100.00	99.88	99.98	100.20	99.82	100.76	99.51
Oxygens	12	12	12	12	12	12	12	12	12	12	12	12	12	12	12	12	12	12	12	12
Si	2.965	2.972	2.958	2.987	2.983	2.986	2.999	2.951	2.961	2.959	2.963	2.931	2.940	2.945	2.957	2.972	2.960	2.956	2.919	2.928
Ti	0.000	0.000	0.002	0.000	0.003	0.000	0.000	0.000	0.002	0.001	0.002	0.000	0.005	0.000	0.001	0.000	0.001	0.003	0.002	0.001
Al	2.011	2.027	2.036	2.022	2.028	2.035	2.047	2.017	2.031	2.032	2.036	2.017	2.028	2.033	2.022	2.042	2.030	2.044	2.040	2.037
Cr	0.002	0.004	0.003	0.003	0.002	0.001	0.001	0.003	0.000	0.000	0.002	0.001	0.002	0.000	0.002	0.000	0.000	0.000	0.001	0.001
Fe3+	0.058	0.024	0.042	0.001	0.000	0.000	0.000	0.079	0.042	0.049	0.033	0.121	0.080	0.077	0.059	0.015	0.049	0.039	0.118	0.104
Fe2+	1.925	1.884	1.879	1.908	1.966	2.011	1.936	1.727	1.677	1.675	1.719	1.642	1.641	1.633	1.733	1.897	1.880	1.914	1.858	2.066
Mn	0.053	0.057	0.055	0.056	0.056	0.061	0.132	0.085	0.082	0.093	0.090	0.092	0.089	0.082	0.102	0.092	0.090	0.098	0.092	0.175
Mg	0.887	0.931	0.918	0.916	0.853	0.792	0.773	1.017	1.118	1.086	1.070	1.111	1.134	1.118	1.023	0.828	0.848	0.778	0.816	0.547
Ca	0.099	0.100	0.107	0.107	0.109	0.115	0.111	0.121	0.086	0.105	0.086	0.086	0.081	0.112	0.101	0.155	0.143	0.169	0.155	0.141
Sum	8.000	8.000	8.000	8.000	8.000	8.000	8.000	8.000	8.000	8.000	8.000	8.000	8.000	8.000	8.000	8.000	8.000	8.000	8.000	8.000
X(Mg)	0.309	0.328	0.323	0.324	0.303	0.283	0.285	0.360	0.394	0.386	0.379	0.387	0.397	0.395	0.363	0.302	0.305	0.285	0.292	0.201
alm	64.93	63.39	63.51	63.87	65.87	67.51	65.58	58.54	56.60	56.61	57.97	56.03	55.71	55.47	58.56	63.82	63.49	64.69	63.61	70.53
prp	29.93	31.32	31.03	30.65	28.58	26.59	26.18	34.47	37.72	36.68	36.09	37.92	38.52	37.96	34.58	27.86	28.65	26.31	27.95	18.69
grs	3.24	3.33	3.53	3.59	3.65	3.86	3.76	3.94	2.84	3.47	2.84	2.76	2.65	3.66	3.31	5.19	4.70	5.59	5.00	4.56
sps	1.80	1.91	1.85	1.88	1.89	2.04	4.48	2.89	2.78	3.16	3.05	3.12	3.01	2.77	3.45	3.09	3.05	3.30	3.15	5.99
uva	0.00	0.01	0.00	0.00	0.00	0.00	0.00	0.01	0.00	0.00	0.00	0.00	0.00	0.00	0.00	0.00	0.00	0.00	0.00	0.00
adr	0.09	0.04	0.07	0.00	0.00	0.00	0.00	0.15	0.06	0.08	0.05	0.17	0.10	0.14	0.10	0.04	0.11	0.11	0.29	0.23

Chemical composition of orthopyroxene (EPMA data)

Sample	NE30	NE30	NE30	NE30	NE30	NE30	NE30	NE30	NE30	NE30	NE30	NE30	NE30	NE30	NE30	NE30	NE30	NE30	NE30	NE30
ID	1	2	3	4	5	6	7	8	9	10	11	12	13	14	15	16	17	18	19	20
SiO2	49.18	50.04	48.66	49.20	49.12	49.16	48.73	48.99	48.74	49.31	50.32	50.55	49.12	49.85	49.53	49.42	49.17	49.67	49.00	50.41
TiO2	0.03	0.10	0.05	0.02	0.04	0.06	0.02	0.11	0.09	0.05	0.01	0.02	0.04	0.01	0.04	0.03	0.07	0.10	0.00	0.02
Al2O3	6.64	5.74	6.90	6.78	6.02	6.36	6.92	6.80	6.90	6.54	5.29	5.56	6.87	5.78	5.56	6.83	7.09	6.31	6.66	5.80
Cr2O3	0.03	0.01	0.05	0.00	0.02	0.04	0.04	0.01	0.02	0.01	0.03	0.01	0.02	0.00	0.13	0.02	0.00	0.00	0.00	0.02
FeO	19.84	19.94	19.76	19.63	19.00	19.19	19.57	19.38	19.53	19.42	19.01	18.88	18.85	19.31	18.75	19.61	19.47	19.10	19.05	18.96
MnO	0.95	0.95	1.10	1.11	1.09	1.14	1.08	1.08	1.16	1.16	1.20	1.34	1.09	1.14	1.27	1.13	1.22	0.94	0.92	0.92
MgO	22.68	23.61	22.82	22.78	24.13	23.15	22.83	22.94	22.96	23.13	23.36	23.35	23.21	23.56	23.71	23.30	22.64	23.23	22.85	23.63
CaO	0.08	0.06	0.06	0.06	0.09	0.06	0.06	0.06	0.09	0.07	0.09	0.08	0.08	0.07	0.06	0.06	0.06	0.05	0.08	0.05
Na2O	0.00	0.02	0.00	0.03	0.01	0.00	0.01	0.00	0.01	0.00	0.02	0.00	0.00	0.03	0.00	0.01	0.00	0.00	0.00	0.01
K2O	0.00	0.00	0.00	0.00	0.07	0.02	0.01	0.00	0.00	0.02	0.01	0.00	0.00	0.00	0.00	0.00	0.00	0.00	0.01	0.00
Total	99.42	100.47	99.40	99.61	99.57	99.19	99.26	99.37	99.50	99.70	99.33	99.79	99.28	99.75	99.05	100.41	99.72	99.40	98.57	99.82
Oxygens	6	6	6	6	6	6	6	6	6	6	6	6	6	6	6	6	6	6	6	6
Si	1.816	1.825	1.795	1.812	1.799	1.815	1.799	1.806	1.795	1.812	1.856	1.856	1.809	1.829	1.828	1.802	1.809	1.829	1.820	1.846
Al(4)	0.184	0.175	0.205	0.188	0.201	0.185	0.201	0.194	0.205	0.188	0.144	0.144	0.191	0.171	0.172	0.198	0.191	0.171	0.180	0.154
Al(6)	0.105	0.072	0.095	0.106	0.059	0.091	0.100	0.102	0.094	0.095	0.086	0.097	0.107	0.079	0.070	0.096	0.117	0.103	0.111	0.097
Ti	0.001	0.003	0.001	0.001	0.001	0.002	0.000	0.003	0.002	0.001	0.000	0.000	0.001	0.000	0.001	0.001	0.002	0.003	0.000	0.001
Cr	0.001	0.000	0.001	0.000	0.000	0.001	0.001	0.000	0.000	0.000	0.001	0.000	0.001	0.000	0.004	0.001	0.000	0.000	0.000	0.001
Fe+3	0.077	0.098	0.105	0.083	0.144	0.090	0.099	0.085	0.106	0.091	0.058	0.046	0.082	0.093	0.096	0.100	0.070	0.063	0.069	0.055
Fe+2	0.536	0.510	0.505	0.521	0.438	0.502	0.505	0.513	0.495	0.506	0.529	0.533	0.499	0.499	0.483	0.498	0.529	0.525	0.523	0.525
Mn	0.030	0.029	0.034	0.035	0.034	0.036	0.034	0.034	0.036	0.036	0.037	0.042	0.034	0.035	0.040	0.035	0.038	0.029	0.029	0.028
Mg	1.248	1.284	1.255	1.250	1.317	1.274	1.257	1.261	1.261	1.267	1.284	1.278	1.274	1.289	1.305	1.267	1.242	1.275	1.265	1.290
Ca	0.003	0.002	0.002	0.002	0.003	0.003	0.002	0.002	0.004	0.003	0.003	0.003	0.003	0.003	0.002	0.002	0.002	0.002	0.003	0.002
Na	0.000	0.001	0.000	0.002	0.001	0.000	0.000	0.000	0.001	0.000	0.001	0.000	0.000	0.002	0.000	0.000	0.000	0.000	0.000	0.000
K	0.000	0.000	0.000	0.000	0.003	0.001	0.000	0.000	0.000	0.001	0.000	0.000	0.000	0.000	0.000	0.000	0.000	0.000	0.000	0.000
Sum	4.000	4.000	4.000	4.000	4.000	4.000	4.000	4.000	4.000	4.000	4.000	4.000	4.000	4.000	4.000	4.000	4.000	4.000	4.000	4.000
XMg	0.671	0.679	0.673	0.674	0.694	0.683	0.675	0.678	0.677	0.680	0.687	0.688	0.687	0.685	0.693	0.679	0.675	0.684	0.681	0.690
XFe	0.329	0.321	0.327	0.326	0.306	0.317	0.325	0.322	0.323	0.320	0.313	0.312	0.313	0.315	0.307	0.321	0.325	0.316	0.319	0.310
Al p.f.u	0.289	0.247	0.300	0.294	0.260	0.277	0.301	0.296	0.299	0.283	0.230	0.241	0.298	0.250	0.242	0.294	0.307	0.274	0.291	0.250
FeT	0.613	0.608	0.610	0.604	0.582	0.592	0.604	0.598	0.601	0.597	0.586	0.580	0.580	0.592	0.579	0.598	0.599	0.588	0.592	0.581
XWo	0.002	0.001	0.001	0.001	0.002	0.001	0.001	0.001	0.002	0.001	0.002	0.002	0.002	0.001	0.001	0.001	0.001	0.001	0.002	0.001
XEn	0.670	0.678	0.672	0.673	0.692	0.682	0.674	0.678	0.676	0.679	0.685	0.687	0.686	0.684	0.692	0.678	0.674	0.684	0.680	0.689
XFs	0.329	0.321	0.327	0.325	0.306	0.317	0.324	0.321	0.322	0.320	0.313	0.312	0.312	0.315	0.307	0.320	0.325	0.315	0.318	0.310
Fe+3/FeT	0.126	0.162	0.173	0.138	0.248	0.152	0.164	0.142	0.177	0.152	0.098	0.080	0.141	0.158	0.166	0.167	0.117	0.107	0.117	0.095

Chemical composition of orthopyroxene (EPMA data)

Sample	NE30	NE30	NE30	NE30	NE30	NE30	NE30	NE30	NE30	NE30	NE30	NE30	NE30	NE30	NE30	NE30	NE30	NE30	NE30	NE30
ID	21	22	23	24	25	26	27	28	29	30	31	32	33	34	35	36	37	38	39	40
SiO2	50.14	49.89	49.41	51.09	49.86	48.97	50.42	49.52	50.46	50.41	51.42	51.77	52.69	50.26	50.07	51.35	50.79	50.54	50.18	50.05
TiO2	0.04	0.02	0.00	0.01	0.00	0.00	0.06	0.04	0.02	0.03	0.07	0.00	0.00	0.06	0.00	0.01	0.00	0.04	0.00	0.00
Al2O3	5.44	5.82	6.54	5.06	8.20	6.57	4.47	6.02	5.25	4.88	4.94	4.03	3.11	6.01	6.58	5.02	5.97	4.85	5.79	5.81
Cr2O3	0.03	0.01	0.06	0.04	0.00	0.00	0.00	0.02	0.02	0.00	0.01	0.02	0.00	0.03	0.00	0.02	0.00	0.00	0.00	0.00
FeO	18.38	19.06	18.14	17.66	16.99	20.43	20.54	20.34	19.71	20.18	16.84	17.52	17.35	17.52	17.85	17.59	17.18	17.97	18.88	18.99
MnO	0.97	0.96	0.89	0.88	0.86	0.35	0.38	0.37	0.38	0.40	0.95	0.91	0.81	0.84	0.87	0.93	0.86	1.00	1.10	1.09
MgO	23.67	23.76	24.32	25.02	23.61	22.38	23.23	23.19	23.82	22.95	24.97	25.25	25.51	24.98	24.43	24.90	24.88	25.01	24.06	24.11
CaO	0.16	0.07	0.10	0.06	0.09	0.07	0.07	0.07	0.07	0.08	0.09	0.08	0.12	0.10	0.10	0.11	0.10	0.08	0.07	0.07
Na2O	0.01	0.00	0.00	0.01	0.01	0.00	0.03	0.00	0.01	0.05	0.00	0.00	0.01	0.02	0.00	0.00	0.00	0.00	0.01	0.03
K2O	0.02	0.01	0.00	0.01	0.00	0.00	0.02	0.01	0.00	0.02	0.00	0.00	0.01	0.01	0.00	0.02	0.01	0.01	0.03	0.00
Total	98.85	99.60	99.46	99.85	99.63	98.77	99.21	99.57	99.73	98.99	99.29	99.58	99.62	99.83	99.90	99.95	99.79	99.51	100.12	100.15
Oxygens	6	6	6	6	6	6	6	6	6	6	6	6	6	6	6	6	6	6	6	6
Si	1.852	1.830	1.806	1.858	1.817	1.822	1.867	1.823	1.850	1.870	1.878	1.888	1.920	1.825	1.820	1.866	1.845	1.845	1.829	1.824
Al(4)	0.148	0.170	0.194	0.142	0.183	0.178	0.133	0.177	0.150	0.130	0.122	0.112	0.080	0.175	0.180	0.134	0.155	0.155	0.171	0.176
Al(6)	0.089	0.082	0.087	0.075	0.169	0.110	0.062	0.085	0.077	0.084	0.091	0.061	0.054	0.082	0.102	0.081	0.100	0.054	0.078	0.073
Ti	0.001	0.001	0.000	0.000	0.000	0.000	0.002	0.001	0.000	0.001	0.002	0.000	0.000	0.002	0.000	0.000	0.000	0.001	0.000	0.000
Cr	0.001	0.000	0.002	0.001	0.000	0.000	0.000	0.000	0.001	0.000	0.000	0.000	0.000	0.001	0.000	0.001	0.000	0.000	0.000	0.000
Fe+3	0.058	0.086	0.105	0.066	0.015	0.068	0.070	0.090	0.071	0.049	0.027	0.051	0.027	0.091	0.077	0.052	0.055	0.099	0.095	0.105
Fe+2	0.510	0.499	0.449	0.471	0.503	0.567	0.566	0.537	0.533	0.577	0.487	0.484	0.502	0.441	0.466	0.483	0.466	0.450	0.481	0.474
Mn	0.030	0.030	0.028	0.027	0.027	0.011	0.012	0.012	0.012	0.012	0.029	0.028	0.025	0.026	0.027	0.028	0.026	0.031	0.034	0.034
Mg	1.303	1.300	1.325	1.356	1.282	1.241	1.282	1.273	1.302	1.269	1.360	1.373	1.386	1.352	1.324	1.349	1.347	1.361	1.308	1.310
Ca	0.006	0.003	0.004	0.002	0.004	0.003	0.003	0.003	0.003	0.003	0.004	0.003	0.005	0.004	0.004	0.004	0.004	0.003	0.003	0.003
Na	0.001	0.000	0.000	0.001	0.001	0.000	0.002	0.000	0.000	0.003	0.000	0.000	0.001	0.001	0.000	0.000	0.000	0.000	0.001	0.002
K	0.001	0.000	0.000	0.000	0.000	0.000	0.001	0.000	0.000	0.001	0.000	0.000	0.001	0.000	0.000	0.001	0.000	0.001	0.001	0.000
Sum	4.000	4.000	4.000	4.000	4.000	4.000	4.000	4.000	4.000	4.000	4.000	4.000	4.000	4.000	4.000	4.000	4.000	4.000	4.000	4.000
XMg	0.6966	0.6896	0.705	0.7164	0.7124	0.6613	0.6684	0.6702	0.683	0.6697	0.7255	0.7198	0.7238	0.7176	0.7093	0.7162	0.7208	0.7127	0.6943	0.6936
XFe	0.3034	0.3104	0.295	0.2836	0.2876	0.3387	0.3316	0.3298	0.317	0.3303	0.2745	0.2802	0.2762	0.2824	0.2907	0.2838	0.2792	0.2873	0.3057	0.3064
Al p.f.u	0.2368	0.2517	0.2817	0.2169	0.3521	0.288	0.1951	0.2612	0.2269	0.2134	0.2126	0.1732	0.1336	0.2572	0.282	0.215	0.2555	0.2087	0.2488	0.2495
FeT	0.5678	0.5848	0.5544	0.5371	0.5177	0.6355	0.6361	0.6263	0.6045	0.6261	0.5144	0.5343	0.5288	0.532	0.5427	0.5347	0.5218	0.5487	0.5756	0.5787
XWo	0.0033	0.0014	0.0021	0.0013	0.002	0.0014	0.0014	0.0015	0.0015	0.0016	0.002	0.0016	0.0024	0.0021	0.0021	0.0024	0.0022	0.0017	0.0015	0.0015
XEn	0.6943	0.6887	0.7036	0.7154	0.711	0.6604	0.6675	0.6693	0.682	0.6686	0.7241	0.7187	0.7221	0.7161	0.7078	0.7145	0.7192	0.7115	0.6933	0.6925
XFs	0.3024	0.3099	0.2944	0.2833	0.287	0.3382	0.3311	0.3293	0.3166	0.3298	0.2739	0.2797	0.2755	0.2818	0.2901	0.2831	0.2786	0.2868	0.3052	0.306
Fe+3/FeT	0.102	0.1473	0.1898	0.1234	0.0293	0.1077	0.1108	0.1431	0.1179	0.0785	0.0532	0.0949	0.0512	0.1702	0.1421	0.0974	0.1061	0.1806	0.1645	0.1814

Chemical composition of orthopyroxene (EPMA data)

Sample	NE30	NE30	NE30	NE30	NE30	NE30	NE30	NE30	NE30	NE30	NE30	NE30	NE30	NE30	NE30	NE30	NE30	NE30	NE30	NE30
ID	41	42	43	44	45	46	47	48	49	50	51	52	53	54	55	56	57	58	59	60
SiO2	50.19	50.99	50.90	50.19	50.43	49.38	50.25	49.87	49.04	51.77	49.24	49.59	50.99	50.30	50.98	49.08	48.28	49.07	50.31	50.54
TiO2	0.08	0.00	0.07	0.08	0.07	0.09	0.07	0.04	0.05	0.00	0.00	0.04	0.01	0.06	0.06	0.00	0.00	0.00	0.01	0.00
Al2O3	5.89	4.93	5.65	5.61	6.09	6.95	5.58	6.38	6.93	3.90	6.29	5.51	4.89	5.06	5.15	6.92	6.66	6.85	6.02	5.01
Cr2O3	0.04	0.01	0.05	0.02	0.02	0.06	0.01	0.03	0.02	0.03	0.08	0.04	0.00	0.03	0.01	0.03	0.01	0.01	0.01	0.00
FeO	18.23	18.59	17.55	17.99	18.35	18.03	18.08	18.41	18.52	17.45	18.60	18.17	18.24	17.93	17.89	19.21	17.78	19.13	19.48	19.23
MnO	1.07	1.13	0.79	0.78	0.79	0.74	0.75	0.70	0.72	0.73	0.87	1.11	1.16	1.16	1.11	1.06	0.98	0.84	0.90	0.92
MgO	24.22	24.21	24.90	24.72	24.40	24.13	24.47	23.93	23.47	25.70	23.97	24.07	24.33	24.30	24.14	23.17	23.63	23.16	23.80	23.81
CaO	0.08	0.09	0.07	0.08	0.08	0.07	0.06	0.10	0.10	0.12	0.14	0.09	0.10	0.08	0.09	0.10	0.11	0.10	0.08	0.08
Na2O	0.00	0.00	0.00	0.00	0.00	0.02	0.00	0.00	0.00	0.02	0.02	0.01	0.00	0.00	0.01	0.00	0.02	0.00	0.01	0.00
K2O	0.02	0.00	0.01	0.00	0.00	0.00	0.00	0.00	0.01	0.00	0.03	0.00	0.00	0.04	0.00	0.01	0.02	0.00	0.02	0.00
Total	99.82	99.95	100.00	99.47	100.23	99.46	99.28	99.46	98.85	99.72	99.24	98.63	99.71	98.95	99.45	99.58	97.48	99.16	100.64	99.60
Oxygens	6	6	6	6	6	6	6	6	6	6	6	6	6	6	6	6	6	6	6	6
Si	1.832	1.863	1.847	1.833	1.831	1.804	1.841	1.826	1.809	1.881	1.808	1.832	1.865	1.852	1.869	1.803	1.801	1.809	1.828	1.856
Al(4)	0.168	0.137	0.153	0.167	0.169	0.196	0.159	0.174	0.191	0.119	0.192	0.168	0.135	0.148	0.131	0.197	0.199	0.191	0.172	0.144
Al(6)	0.085	0.075	0.089	0.075	0.092	0.104	0.082	0.102	0.110	0.048	0.080	0.072	0.076	0.071	0.091	0.103	0.094	0.107	0.086	0.073
Ti	0.002	0.000	0.002	0.002	0.002	0.003	0.002	0.001	0.001	0.000	0.000	0.001	0.000	0.002	0.002	0.000	0.000	0.000	0.000	0.000
Cr	0.001	0.000	0.002	0.001	0.001	0.002	0.000	0.001	0.001	0.001	0.002	0.001	0.000	0.001	0.000	0.001	0.000	0.000	0.000	0.000
Fe+3	0.078	0.062	0.059	0.087	0.073	0.086	0.074	0.069	0.079	0.071	0.113	0.094	0.059	0.075	0.036	0.094	0.108	0.084	0.087	0.071
Fe+2	0.478	0.506	0.473	0.462	0.485	0.465	0.480	0.495	0.492	0.459	0.458	0.467	0.499	0.477	0.512	0.496	0.447	0.506	0.505	0.520
Mn	0.033	0.035	0.024	0.024	0.024	0.023	0.023	0.022	0.022	0.022	0.027	0.035	0.036	0.036	0.035	0.033	0.031	0.026	0.028	0.029
Mg	1.318	1.318	1.347	1.346	1.321	1.314	1.336	1.306	1.290	1.392	1.312	1.325	1.327	1.333	1.319	1.269	1.314	1.273	1.289	1.304
Ca	0.003	0.003	0.003	0.003	0.003	0.003	0.002	0.004	0.004	0.005	0.005	0.004	0.004	0.003	0.003	0.004	0.004	0.004	0.003	0.003
Na	0.000	0.000	0.000	0.000	0.000	0.001	0.000	0.000	0.000	0.002	0.001	0.001	0.000	0.000	0.001	0.000	0.002	0.000	0.001	0.000
K	0.001	0.000	0.001	0.000	0.000	0.000	0.000	0.000	0.001	0.000	0.001	0.000	0.000	0.002	0.000	0.000	0.001	0.000	0.001	0.000
Sum	4.000	4.000	4.000	4.000	4.000	4.000	4.000	4.000	4.000	4.000	4.000	4.000	4.000	4.000	4.000	4.000	4.000	4.000	4.000	4.000
XMg	0.703	0.699	0.717	0.710	0.703	0.705	0.707	0.699	0.693	0.724	0.697	0.703	0.704	0.707	0.706	0.683	0.703	0.683	0.685	0.688
XFe	0.297	0.301	0.283	0.290	0.297	0.295	0.293	0.301	0.307	0.276	0.303	0.297	0.296	0.293	0.294	0.317	0.297	0.317	0.315	0.312
Al p.f.u	0.253	0.212	0.242	0.241	0.261	0.299	0.241	0.275	0.301	0.167	0.272	0.240	0.211	0.220	0.223	0.300	0.293	0.298	0.258	0.217
FeT	0.556	0.568	0.533	0.549	0.557	0.551	0.554	0.564	0.571	0.530	0.571	0.561	0.558	0.552	0.548	0.590	0.555	0.590	0.592	0.591
XWo	0.002	0.002	0.002	0.002	0.002	0.001	0.001	0.002	0.002	0.002	0.003	0.002	0.002	0.002	0.002	0.002	0.002	0.002	0.002	0.002
XEn	0.702	0.698	0.716	0.709	0.702	0.704	0.706	0.697	0.692	0.722	0.695	0.701	0.703	0.706	0.705	0.681	0.702	0.682	0.684	0.687
XFs	0.296	0.301	0.283	0.289	0.296	0.295	0.293	0.301	0.306	0.275	0.302	0.297	0.295	0.292	0.293	0.317	0.296	0.316	0.314	0.311
Fe+3/FeT	0.140	0.109	0.112	0.159	0.130	0.157	0.133	0.123	0.139	0.134	0.198	0.168	0.106	0.136	0.066	0.159	0.194	0.142	0.148	0.119

Chemical composition of sapphirine (EPMA data)

Sample	NE30	NE30	NE30	NE30	NE30	NE30	NE30	NE30	NE30	NE30	NE30	NE30	NE30	NE30	NE30	NE30	NE30	NE30	NE30	NE30
ID	1	2	3	4	5	6	7	8	9	10	11	12	13	14	15	16	17	18	19	20
SiO2	12.19	11.91	12.02	12.57	12.49	12.35	12.18	11.99	12.05	12.11	12.35	12.27	12.15	12.14	12.21	12.41	12.01	12.26	12.35	12.01
TiO2	0.04	0.10	0.07	0.10	0.06	0.00	0.06	0.02	0.02	0.10	0.04	0.00	0.02	0.00	0.07	0.03	0.03	0.07	0.00	0.00
Al2O3	62.10	62.78	61.76	61.33	61.66	61.81	62.17	62.13	61.84	61.64	61.71	61.76	61.97	62.78	62.25	61.63	63.20	62.61	62.93	63.78
Cr2O3	0.11	0.04	0.29	0.04	0.01	0.13	0.08	0.09	0.04	0.15	0.06	0.12	0.11	0.11	0.13	0.15	0.05	0.10	0.07	0.01
FeO	10.52	9.70	10.15	10.23	10.38	10.00	10.09	10.22	10.51	10.19	9.85	10.51	10.14	9.78	10.11	10.39	10.26	10.41	10.23	10.07
MnO	0.28	0.29	0.23	0.27	0.29	0.29	0.25	0.24	0.27	0.23	0.30	0.22	0.23	0.28	0.24	0.24	0.24	0.23	0.29	0.24
MgO	15.66	15.30	15.70	15.59	15.42	15.44	15.51	15.49	15.48	15.62	15.58	15.57	15.53	15.65	15.50	15.59	15.00	15.01	15.19	14.91
CaO	0.02	0.00	0.00	0.01	0.00	0.00	0.02	0.00	0.01	0.03	0.00	0.01	0.00	0.01	0.01	0.02	0.03	0.00	0.01	0.01
Na2O	0.01	0.00	0.01	0.00	0.01	0.00	0.00	0.00	0.00	0.00	0.00	0.02	0.00	0.00	0.02	0.02	0.00	0.01	0.00	0.00
Total	100.93	100.12	100.23	100.14	100.32	100.02	100.36	100.18	100.22	100.07	99.89	100.48	100.16	100.75	100.54	100.47	100.82	100.70	101.07	101.03
Oxygens	10	10	10	10	10	10	10	10	10	10	10	10	10	10	10	10	10	10	10	10
Si	0.724	0.712	0.718	0.752	0.746	0.739	0.727	0.716	0.720	0.725	0.740	0.732	0.726	0.720	0.727	0.740	0.714	0.731	0.732	0.712
Ti	0.002	0.005	0.003	0.004	0.003	0.000	0.003	0.001	0.001	0.004	0.002	0.000	0.001	0.000	0.003	0.001	0.001	0.003	0.000	0.000
Al	4.345	4.420	4.347	4.325	4.343	4.361	4.371	4.376	4.357	4.347	4.356	4.341	4.365	4.390	4.369	4.332	4.429	4.397	4.399	4.457
Cr	0.005	0.002	0.013	0.002	0.000	0.006	0.004	0.004	0.002	0.007	0.003	0.006	0.005	0.005	0.006	0.007	0.002	0.005	0.003	0.001
Fe+3	0.200	0.146	0.199	0.161	0.160	0.154	0.167	0.185	0.198	0.188	0.158	0.192	0.176	0.164	0.166	0.180	0.138	0.132	0.133	0.118
Fe+2	0.322	0.339	0.308	0.351	0.359	0.347	0.336	0.326	0.327	0.322	0.335	0.332	0.331	0.321	0.338	0.338	0.372	0.387	0.374	0.382
Mn	0.014	0.015	0.012	0.014	0.015	0.015	0.013	0.012	0.013	0.012	0.015	0.011	0.012	0.014	0.012	0.012	0.012	0.012	0.014	0.012
Mg	1.386	1.363	1.398	1.391	1.374	1.378	1.379	1.380	1.380	1.393	1.391	1.384	1.384	1.384	1.376	1.386	1.330	1.333	1.343	1.318
Ca	0.001	0.000	0.000	0.001	0.000	0.000	0.001	0.000	0.000	0.002	0.000	0.001	0.000	0.000	0.001	0.001	0.002	0.000	0.001	0.000
Na	0.001	0.000	0.001	0.000	0.001	0.000	0.000	0.000	0.000	0.000	0.000	0.002	0.000	0.000	0.002	0.002	0.000	0.001	0.000	0.000
Sum	7.000	7.000	7.000	7.000	7.000	7.000	7.000	7.000	7.000	7.000	7.000	7.000	7.000	7.000	7.000	7.000	7.000	7.000	7.000	7.000
XMg	0.726	0.738	0.734	0.731	0.726	0.733	0.733	0.730	0.724	0.732	0.738	0.725	0.732	0.740	0.732	0.728	0.723	0.720	0.726	0.725
Fe+3/FeT	0.384	0.301	0.392	0.314	0.308	0.308	0.332	0.362	0.377	0.369	0.320	0.366	0.347	0.338	0.330	0.347	0.271	0.254	0.262	0.236

Chemical composition of sapphirine (EPMA data)

Sample	NE30	NE30	NE30	NE30	NE30	NE30	NE30	NE30	NE30	NE30	NE30	NE30	NE30	NE30	NE30	NE30	NE30
ID	21	22	23	24	25	26	27	28	29	30	31	32	33	34	35	36	37
SiO2	12.24	13.04	12.32	12.61	10.54	12.56	12.47	12.02	12.36	12.16	12.24	12.13	12.41	11.74	12.04	11.96	11.35
TiO2	0.00	0.02	0.00	0.04	0.01	0.02	0.03	0.00	0.02	0.00	0.00	0.10	0.03	0.02	0.05	0.03	0.00
Al2O3	62.79	62.72	62.48	62.69	61.31	62.56	62.50	62.36	61.86	62.07	62.05	61.86	61.83	63.39	62.68	63.07	62.97
Cr2O3	0.08	0.12	0.08	0.06	0.04	0.02	0.06	0.06	0.07	0.02	0.08	0.05	0.09	0.00	0.00	0.04	0.08
FeO	10.54	9.99	9.90	9.69	12.64	9.03	9.33	10.16	9.81	10.14	9.73	10.13	9.87	10.00	10.75	10.28	9.72
MnO	0.22	0.28	0.19	0.20	0.18	0.19	0.21	0.18	0.18	0.17	0.19	0.15	0.19	0.24	0.23	0.22	0.21
MgO	15.20	15.12	15.68	15.41	15.23	16.02	15.62	15.59	15.79	15.95	15.83	15.96	15.97	14.98	15.29	15.15	15.18
CaO	0.01	0.03	0.01	0.01	0.01	0.01	0.02	0.01	0.03	0.02	0.01	0.00	0.02	0.02	0.01	0.00	0.03
Na2O	0.01	0.00	0.00	0.01	0.00	0.02	0.00	0.00	0.01	0.00	0.01	0.01	0.01	0.01	0.01	0.00	0.02
Total	101.10	101.32	100.65	100.72	99.94	100.42	100.25	100.38	100.13	100.54	100.14	100.39	100.41	100.41	101.06	100.75	99.56
Oxygens	10	10	10	10	10	10	10	10	10	10	10	10	10	10	10	10	10
Si	0.726	0.772	0.732	0.749	0.635	0.745	0.743	0.716	0.738	0.723	0.730	0.722	0.739	0.700	0.714	0.711	0.681
Ti	0.000	0.001	0.000	0.002	0.000	0.001	0.002	0.000	0.001	0.000	0.000	0.004	0.001	0.001	0.002	0.001	0.000
Al	4.390	4.376	4.374	4.388	4.351	4.375	4.389	4.380	4.351	4.349	4.362	4.341	4.337	4.454	4.384	4.420	4.454
Cr	0.004	0.006	0.004	0.003	0.002	0.001	0.003	0.003	0.003	0.001	0.004	0.002	0.004	0.000	0.000	0.002	0.004
Fe+3	0.156	0.072	0.158	0.109	0.378	0.134	0.120	0.185	0.170	0.205	0.175	0.204	0.180	0.146	0.184	0.153	0.182
Fe+2	0.367	0.422	0.333	0.372	0.258	0.314	0.345	0.321	0.320	0.300	0.310	0.301	0.311	0.353	0.350	0.358	0.306
Mn	0.011	0.014	0.010	0.010	0.009	0.010	0.010	0.009	0.009	0.009	0.010	0.008	0.009	0.012	0.012	0.011	0.010
Mg	1.344	1.334	1.389	1.364	1.367	1.417	1.387	1.385	1.405	1.413	1.408	1.417	1.417	1.331	1.353	1.343	1.358
Ca	0.000	0.002	0.000	0.001	0.000	0.001	0.001	0.001	0.002	0.001	0.000	0.000	0.001	0.001	0.001	0.000	0.002
Na	0.002	0.000	0.000	0.002	0.000	0.002	0.000	0.000	0.002	0.000	0.001	0.001	0.001	0.001	0.001	0.000	0.002
Sum	7.000	7.000	7.000	7.000	7.000	7.000	7.000	7.000	7.000	7.000	7.000	7.000	7.000	7.000	7.000	7.000	7.000
XMg	0.720	0.730	0.738	0.739	0.682	0.760	0.749	0.732	0.742	0.737	0.744	0.737	0.743	0.728	0.717	0.724	0.736
Fe+3/FeT	0.298	0.146	0.322	0.227	0.594	0.299	0.257	0.366	0.347	0.406	0.361	0.404	0.367	0.292	0.344	0.300	0.373

Chemical composition of cordierite (EPMA data)

Sample	NE30	NE30	NE30	NE30	NE30	NE30	NE30	NE30	NE30	NE30	NE30	NE30	NE30	NE30	NE30	NE30	NE30	NE30	NE30	NE30
ID	1	2	3	4	5	6	7	8	9	10	11	12	13	14	15	16	17	18	19	20
SiO2	48.96	48.87	49.13	48.83	49.44	48.85	49.55	48.79	48.83	48.75	48.89	48.95	48.76	49.36	48.51	48.79	48.51	48.74	48.75	48.95
TiO2	0.08	0.00	0.00	0.02	0.00	0.02	0.00	0.04	0.02	0.07	0.00	0.00	0.00	0.02	0.00	0.00	0.01	0.00	0.05	0.00
Al2O3	33.59	33.57	33.73	33.57	33.69	33.69	34.02	32.30	33.87	33.49	33.56	33.37	33.41	33.63	33.68	33.80	33.70	33.38	33.79	33.81
FeO	3.43	3.30	3.23	3.31	3.00	3.09	2.72	3.23	2.84	2.96	2.99	3.06	3.30	3.23	2.85	2.87	3.10	3.48	3.07	2.65
MnO	0.22	0.20	0.16	0.20	0.21	0.21	0.20	0.24	0.22	0.19	0.20	0.19	0.21	0.15	0.18	0.21	0.19	0.16	0.14	0.17
MgO	11.56	11.59	11.64	11.65	11.80	11.81	12.01	12.48	11.78	11.86	11.79	11.73	11.68	11.68	12.10	11.82	11.86	11.67	11.96	11.92
CaO	0.03	0.01	0.01	0.02	0.02	0.00	0.01	0.02	0.01	0.01	0.02	0.01	0.02	0.00	0.03	0.00	0.02	0.03	0.04	0.00
Na2O	0.02	0.03	0.02	0.03	0.05	0.02	0.02	0.01	0.03	0.04	0.04	0.02	0.03	0.02	0.02	0.00	0.03	0.02	0.03	0.02
K2O	0.00	0.02	0.00	0.00	0.00	0.00	0.01	0.00	0.00	0.00	0.00	0.00	0.00	0.00	0.00	0.02	0.04	0.00	0.02	0.00
Total	97.88	97.60	97.93	97.63	98.21	97.69	98.54	97.11	97.60	97.38	97.50	97.34	97.41	98.09	97.37	97.51	97.46	97.48	97.85	97.53
Oxygens	18	18	18	18	18	18	18	18	18	18	18	18	18	18	18	18	18	18	18	18
Si	4.958	4.960	4.965	4.955	4.978	4.949	4.965	4.982	4.945	4.953	4.960	4.974	4.959	4.979	4.928	4.947	4.930	4.957	4.932	4.955
Ti	0.006	0.000	0.000	0.002	0.000	0.001	0.000	0.003	0.002	0.005	0.000	0.000	0.000	0.002	0.000	0.000	0.001	0.000	0.003	0.000
Al	4.009	4.015	4.017	4.014	3.997	4.022	4.018	3.887	4.043	4.010	4.013	3.996	4.005	3.997	4.032	4.039	4.036	4.001	4.029	4.033
Fe	0.290	0.280	0.273	0.281	0.253	0.262	0.228	0.276	0.241	0.251	0.254	0.260	0.281	0.272	0.242	0.243	0.263	0.296	0.260	0.224
Mn	0.019	0.017	0.014	0.017	0.018	0.018	0.017	0.021	0.019	0.017	0.017	0.017	0.018	0.013	0.016	0.018	0.016	0.013	0.012	0.015
Mg	1.745	1.754	1.754	1.762	1.771	1.784	1.794	1.900	1.779	1.796	1.783	1.777	1.771	1.756	1.833	1.787	1.797	1.769	1.804	1.799
Ca	0.003	0.001	0.001	0.002	0.003	0.000	0.001	0.002	0.001	0.001	0.003	0.001	0.002	0.000	0.004	0.000	0.002	0.003	0.005	0.000
Na	0.004	0.006	0.004	0.005	0.009	0.003	0.004	0.001	0.006	0.008	0.008	0.004	0.006	0.003	0.003	0.001	0.006	0.004	0.006	0.005
K	0.000	0.003	0.001	0.000	0.000	0.000	0.001	0.000	0.000	0.000	0.000	0.000	0.000	0.000	0.000	0.002	0.005	0.000	0.003	0.000
Sum	11.034	11.037	11.029	11.039	11.028	11.040	11.028	11.072	11.035	11.041	11.038	11.030	11.042	11.023	11.058	11.036	11.057	11.044	11.054	11.031
XMg	0.857	0.862	0.865	0.863	0.875	0.872	0.887	0.873	0.881	0.877	0.875	0.872	0.863	0.866	0.883	0.880	0.872	0.857	0.874	0.889

Chemical composition of cordierite (EPMA data)

Sample	NE30	NE30	NE30	NE30	NE30	NE30	NE30	NE30	NE30	NE30	NE30	NE30	NE30	NE30	NE30	NE30	NE30	NE30	NE30	NE30
ID	21	22	23	24	25	26	27	28	29	30	31	32	33	34	35	36	37	38	39	40
SiO2	48.22	48.31	48.72	48.67	48.58	49.04	48.65	48.87	49.02	49.20	48.93	49.31	49.41	49.18	49.25	49.13	49.12	49.36	48.69	48.55
TiO2	0.01	0.00	0.00	0.05	0.05	0.05	0.00	0.00	0.00	0.02	0.00	0.04	0.09	0.09	0.02	0.04	0.05	0.01	0.01	0.00
Al2O3	33.59	33.50	33.69	33.79	33.63	33.90	33.58	33.61	33.62	33.55	33.53	33.76	33.50	33.81	33.35	33.75	33.61	33.77	33.42	33.75
FeO	2.96	3.05	3.14	2.89	2.85	2.63	2.52	2.55	2.69	2.72	2.82	2.98	2.75	2.49	2.76	2.63	2.87	2.89	2.78	2.70
MnO	0.16	0.15	0.14	0.16	0.17	0.12	0.15	0.12	0.17	0.15	0.12	0.14	0.16	0.15	0.11	0.14	0.09	0.11	0.11	0.11
MgO	11.84	11.91	11.83	11.87	11.84	12.14	12.03	12.17	12.06	12.10	11.89	12.14	12.08	12.33	12.19	12.16	12.00	12.00	12.16	12.19
CaO	0.00	0.02	0.03	0.01	0.01	0.05	0.00	0.03	0.02	0.03	0.00	0.01	0.04	0.01	0.03	0.03	0.04	0.00	0.02	0.00
Na2O	0.00	0.00	0.02	0.01	0.02	0.03	0.02	0.02	0.02	0.03	0.02	0.04	0.02	0.01	0.03	0.03	0.03	0.03	0.00	0.04
K2O	0.01	0.02	0.00	0.00	0.00	0.00	0.01	0.00	0.01	0.02	0.01	0.01	0.01	0.00	0.02	0.00	0.00	0.00	0.01	0.00
Total	96.79	96.96	97.57	97.45	97.15	97.96	96.96	97.37	97.60	97.81	97.33	98.43	98.06	98.07	97.77	97.90	97.81	98.17	97.21	97.35
Oxygens	18	18	18	18	18	18	18	18	18	18	18	18	18	18	18	18	18	18	18	18
Si	4.929	4.932	4.943	4.938	4.943	4.944	4.951	4.954	4.960	4.968	4.966	4.955	4.977	4.949	4.976	4.955	4.963	4.967	4.950	4.928
Ti	0.001	0.000	0.000	0.004	0.004	0.004	0.000	0.000	0.000	0.001	0.000	0.003	0.006	0.007	0.001	0.003	0.004	0.001	0.001	0.000
Al	4.046	4.031	4.028	4.040	4.033	4.027	4.028	4.015	4.009	3.993	4.010	3.998	3.977	4.010	3.971	4.011	4.002	4.005	4.004	4.037
Fe	0.253	0.260	0.266	0.245	0.242	0.222	0.214	0.216	0.228	0.230	0.239	0.250	0.232	0.210	0.233	0.222	0.242	0.243	0.236	0.229
Mn	0.014	0.013	0.012	0.014	0.015	0.010	0.013	0.011	0.015	0.012	0.010	0.012	0.014	0.013	0.010	0.012	0.008	0.009	0.010	0.009
Mg	1.804	1.813	1.789	1.795	1.796	1.824	1.825	1.839	1.819	1.822	1.799	1.819	1.814	1.850	1.836	1.828	1.807	1.800	1.843	1.845
Ca	0.000	0.002	0.003	0.001	0.001	0.005	0.000	0.003	0.002	0.003	0.000	0.002	0.005	0.001	0.004	0.003	0.004	0.000	0.002	0.001
Na	0.000	0.000	0.005	0.002	0.004	0.005	0.005	0.003	0.003	0.006	0.005	0.008	0.004	0.003	0.007	0.006	0.005	0.006	0.001	0.009
K	0.001	0.003	0.000	0.000	0.000	0.000	0.001	0.000	0.001	0.002	0.001	0.001	0.001	0.000	0.002	0.000	0.000	0.000	0.001	0.000
Sum	11.048	11.054	11.046	11.039	11.039	11.042	11.038	11.041	11.037	11.038	11.032	11.048	11.030	11.041	11.041	11.039	11.035	11.032	11.048	11.058
XMg	0.877	0.874	0.870	0.880	0.881	0.892	0.895	0.895	0.889	0.888	0.883	0.879	0.887	0.898	0.887	0.892	0.882	0.881	0.886	0.889

Chemical composition of cordierite (EPMA data)

Sample	NE30	NE30	NE30	NE30	NE30	NE30	NE30	NE30	NE30	NE30	NE157	NE157	NE157	NE157	NE157	NE157	NE157	NE157	NE157	NE157
ID	41	42	43	44	45	46	47	48	49	50	51	52	53	54	55	56	57	58	59	60
SiO2	48.36	48.24	48.44	48.55	48.34	48.29	48.40	48.59	49.55	49.14	48.30	48.03	48.10	47.98	47.60	48.13	47.80	47.80	47.92	48.13
TiO2	0.03	0.04	0.00	0.00	0.00	0.01	0.00	0.00	0.00	0.04	0.02	0.00	0.00	0.01	0.02	0.03	0.03	0.02	0.04	0.05
Al2O3	32.88	33.39	33.23	33.32	33.43	33.28	33.41	33.60	33.11	33.89	33.20	33.11	33.25	33.19	33.01	33.30	33.12	33.04	33.10	33.28
FeO	4.81	3.20	3.05	3.04	3.23	3.27	3.55	3.54	3.51	3.37	5.74	6.34	6.71	6.76	6.74	6.94	6.88	6.82	6.73	6.53
MnO	0.37	0.08	0.05	0.08	0.05	0.09	0.09	0.10	0.09	0.10	0.09	0.07	0.06	0.06	0.11	0.06	0.08	0.08	0.07	0.07
MgO	12.06	11.70	11.71	11.89	11.58	11.57	11.50	11.65	10.91	11.69	10.16	9.82	9.46	9.39	9.48	9.43	9.48	9.43	9.43	9.84
CaO	0.24	0.02	0.03	0.03	0.03	0.00	0.00	0.02	0.34	0.01	0.02	0.03	0.02	0.01	0.00	0.00	0.00	0.00	0.04	0.00
Na2O	0.02	0.04	0.05	0.03	0.04	0.02	0.03	0.04	0.31	0.00	0.01	0.04	0.04	0.04	0.03	0.04	0.04	0.03	0.05	0.03
K2O	0.02	0.00	0.01	0.01	0.00	0.01	0.03	0.01	0.00	0.02	0.00	0.02	0.01	0.02	0.00	0.01	0.00	0.03	0.02	0.00
Total	98.79	96.72	96.57	96.95	96.70	96.54	97.00	97.55	97.83	98.26	97.54	97.45	97.65	97.45	96.99	97.94	97.43	97.25	97.39	97.92
Oxygens	18	18	18	18	18	18	18	18	18	18	18	18	18	18	18	18	18	18	18	18
Si	4.904	4.939	4.961	4.954	4.948	4.953	4.947	4.940	5.023	4.952	4.957	4.950	4.953	4.952	4.939	4.947	4.940	4.947	4.950	4.940
Ti	0.002	0.003	0.000	0.000	0.000	0.001	0.000	0.000	0.000	0.003	0.002	0.000	0.000	0.001	0.001	0.003	0.002	0.001	0.003	0.004
Al	3.930	4.029	4.011	4.007	4.033	4.022	4.025	4.026	3.955	4.025	4.016	4.021	4.035	4.037	4.037	4.033	4.034	4.030	4.029	4.025
Fe	0.408	0.274	0.261	0.259	0.276	0.280	0.303	0.301	0.298	0.284	0.493	0.546	0.578	0.583	0.585	0.596	0.595	0.590	0.581	0.560
Mn	0.032	0.007	0.004	0.007	0.004	0.007	0.008	0.009	0.008	0.009	0.008	0.006	0.005	0.005	0.010	0.005	0.007	0.007	0.006	0.006
Mg	1.823	1.786	1.788	1.809	1.767	1.769	1.753	1.766	1.649	1.756	1.555	1.509	1.452	1.445	1.466	1.445	1.461	1.455	1.452	1.506
Ca	0.026	0.002	0.004	0.003	0.003	0.000	0.000	0.002	0.037	0.001	0.002	0.003	0.003	0.001	0.000	0.000	0.000	0.000	0.004	0.000
Na	0.005	0.009	0.010	0.006	0.008	0.004	0.005	0.007	0.061	0.000	0.003	0.008	0.009	0.008	0.005	0.007	0.009	0.006	0.010	0.005
K	0.002	0.000	0.002	0.002	0.000	0.001	0.003	0.001	0.000	0.002	0.000	0.002	0.001	0.002	0.000	0.001	0.000	0.003	0.002	0.000
Sum	11.132	11.048	11.040	11.046	11.040	11.038	11.044	11.052	11.030	11.033	11.035	11.045	11.034	11.034	11.044	11.038	11.046	11.041	11.038	11.047
XMg	0.817	0.867	0.873	0.875	0.865	0.863	0.852	0.854	0.847	0.861	0.759	0.734	0.715	0.712	0.715	0.708	0.711	0.711	0.714	0.729

Chemical composition of cordierite (EPMA data)

Sample	NE157	NE157	NE157	NE157	NE157	NE157	NE157	NE157	NE163	NE163	NE163	NE163	NE163	NE163	NE163	NE163	NE163
ID	61	62	63	64	65	66	67	68	69	70	71	72	73	74	75	76	77
SiO2	48.53	47.86	48.10	48.33	48.47	48.00	48.22	48.92	49.19	48.92	48.66	48.60	48.49	48.65	49.53	49.49	49.02
TiO2	0.05	0.00	0.05	0.00	0.00	0.08	0.00	0.00	0.00	0.04	0.04	0.02	0.03	0.03	0.05	0.03	0.03
Al2O3	32.87	32.86	32.93	33.20	33.14	33.01	32.82	34.30	34.49	34.22	34.10	33.87	33.97	34.26	34.59	34.53	34.30
FeO	6.53	6.60	6.81	6.74	6.73	6.82	7.02	5.44	5.33	5.50	5.60	5.19	5.42	5.23	5.17	5.17	5.38
MnO	0.09	0.07	0.09	0.05	0.06	0.06	0.09	0.07	0.07	0.06	0.06	0.07	0.07	0.06	0.07	0.09	0.06
MgO	9.31	9.53	9.47	9.40	9.51	9.47	9.39	10.47	10.44	10.33	10.47	10.62	10.99	10.82	10.67	10.73	10.83
CaO	0.02	0.00	0.00	0.01	0.01	0.02	0.03	0.02	0.06	0.02	0.00	0.02	0.02	0.06	0.00	0.02	0.04
Na2O	0.04	0.03	0.00	0.03	0.04	0.03	0.06	0.05	0.04	0.06	0.06	0.07	0.05	0.08	0.06	0.07	0.06
K2O	0.16	0.00	0.00	0.00	0.00	0.01	0.06	0.00	0.00	0.01	0.00	0.02	0.00	0.00	0.03	0.02	0.00
Total	97.59	96.94	97.44	97.75	97.96	97.50	97.69	99.27	99.62	99.15	99.00	98.48	99.05	99.20	100.18	100.14	99.72
Oxygens	18	18	18	18	18	18	18	18	18	18	18	18	18	18	18	18	18
Si	4.997	4.962	4.965	4.969	4.973	4.954	4.973	4.926	4.932	4.932	4.919	4.930	4.900	4.903	4.935	4.934	4.915
Ti	0.003	0.000	0.004	0.000	0.000	0.006	0.000	0.000	0.000	0.003	0.003	0.001	0.003	0.002	0.004	0.002	0.002
Al	3.989	4.015	4.006	4.023	4.007	4.015	3.989	4.070	4.075	4.066	4.062	4.049	4.045	4.069	4.062	4.057	4.053
Fe	0.562	0.572	0.588	0.579	0.577	0.589	0.605	0.458	0.447	0.464	0.473	0.440	0.458	0.441	0.431	0.431	0.451
Mn	0.008	0.006	0.008	0.004	0.005	0.006	0.008	0.006	0.006	0.005	0.005	0.006	0.006	0.005	0.006	0.008	0.005
Mg	1.429	1.473	1.457	1.441	1.455	1.457	1.444	1.572	1.560	1.553	1.578	1.606	1.656	1.626	1.585	1.595	1.619
Ca	0.002	0.000	0.000	0.001	0.001	0.002	0.003	0.003	0.007	0.002	0.000	0.002	0.002	0.006	0.000	0.002	0.004
Na	0.008	0.006	0.000	0.005	0.009	0.005	0.012	0.010	0.009	0.012	0.012	0.014	0.010	0.017	0.012	0.014	0.012
K	0.021	0.000	0.000	0.000	0.000	0.001	0.008	0.000	0.000	0.001	0.001	0.003	0.000	0.000	0.004	0.002	0.000
Sum	11.019	11.033	11.028	11.022	11.027	11.035	11.042	11.044	11.035	11.038	11.053	11.052	11.080	11.069	11.038	11.044	11.062
XMg	0.718	0.720	0.713	0.713	0.716	0.712	0.705	0.774	0.777	0.770	0.769	0.785	0.783	0.787	0.786	0.787	0.782

Chemical composition of feldspars (EPMA data)

Sample	NE30	NE30	NE30	NE30	NE30	NE30	NE30	NE30	NE30	NE30	NE30	NE30	NE30	NE30	NE30	NE30	NE30	NE30	NE30	NE30
ID	1	2	3	4	5	6	7	8	9	10	11	12	13	14	15	16	17	18	19	20
SiO2	62.78	62.67	62.28	64.71	65.39	62.51	64.54	62.44	63.01	65.39	62.97	65.16	62.74	62.57	62.80	61.45	62.18	61.44	62.46	61.77
TiO2	0.01	0.02	0.02	0.04	0.09	0.00	0.06	0.03	0.03	0.00	0.01	0.00	0.00	0.00	0.00	0.05	0.01	0.03	0.04	0.07
Al2O3	23.82	23.65	23.83	18.73	19.28	23.73	20.36	24.25	23.73	18.82	23.76	18.72	23.74	24.00	23.71	24.53	23.51	24.60	23.46	24.40
FeO	0.07	0.06	0.07	0.06	0.02	0.15	0.10	0.02	0.11	0.03	0.13	0.05	0.12	0.09	0.12	0.17	0.18	0.11	0.17	0.40
MnO	0.00	0.00	0.01	0.00	0.02	0.01	0.00	0.00	0.00	0.01	0.00	0.00	0.00	0.02	0.00	0.00	0.00	0.00	0.00	0.00
MgO	0.00	0.00	0.00	0.03	0.00	0.03	0.05	0.00	0.05	0.00	0.00	0.00	0.00	0.00	0.00	0.08	0.33	0.15	0.13	0.00
CaO	5.26	5.17	5.44	0.09	0.58	5.22	1.57	5.51	5.04	0.21	5.02	0.06	5.15	5.49	5.19	5.30	5.13	5.26	4.96	5.12
BaO	0.04	0.03	0.00	0.66	0.56	0.00	0.44	0.02	0.00	0.87	0.04	0.73	0.05	0.03	0.06	0.00	0.00	0.00	0.02	0.01
Na2O	8.12	8.11	7.96	0.97	2.37	8.22	3.85	8.25	8.30	1.48	8.29	0.44	7.85	8.13	8.25	8.25	8.20	8.28	7.87	8.55
K2O	0.38	0.45	0.46	14.64	12.24	0.18	9.57	0.08	0.14	13.77	0.19	15.68	0.54	0.46	0.43	0.15	0.32	0.20	1.08	0.20
SrO	0.10	0.10	0.12	0.14	0.08	0.01	0.11	0.07	0.02	0.12	0.04	0.10	0.10	0.08	0.10	0.07	0.05	0.09	0.02	0.11
Total	100.58	100.27	100.20	100.09	100.62	100.05	100.64	100.67	100.42	100.70	100.45	100.94	100.30	100.87	100.66	100.04	99.92	100.16	100.21	100.63
Oxygens	8	8	8	8	8	8	8	8	8	8	8	8	8	8	8	8	8	8	8	8
Si	2.781	2.785	2.771	2.998	2.991	2.780	2.925	2.760	2.792	3.008	2.791	3.002	2.793	2.763	2.778	2.730	2.767	2.724	2.777	2.726
Ti	0.000	0.001	0.001	0.001	0.003	0.000	0.002	0.001	0.001	0.000	0.000	0.000	0.000	0.000	0.000	0.002	0.000	0.001	0.001	0.002
Al	1.244	1.239	1.250	1.023	1.039	1.244	1.088	1.263	1.239	1.020	1.241	1.016	1.245	1.249	1.236	1.284	1.233	1.286	1.229	1.269
Fe+3	0.000	0.000	0.000	0.000	0.000	0.000	0.000	0.000	0.000	0.000	0.000	0.000	0.000	0.000	0.000	0.000	0.000	0.000	0.000	0.015
Fe+2	0.003	0.002	0.002	0.002	0.001	0.005	0.004	0.001	0.004	0.001	0.005	0.002	0.004	0.003	0.004	0.006	0.007	0.004	0.006	0.000
Mn	0.000	0.000	0.001	0.000	0.001	0.000	0.000	0.000	0.000	0.000	0.000	0.000	0.000	0.001	0.000	0.000	0.000	0.000	0.000	0.000
Mg	0.000	0.000	0.000	0.002	0.000	0.002	0.003	0.000	0.003	0.000	0.000	0.000	0.000	0.000	0.000	0.005	0.022	0.010	0.008	0.000
Ca	0.250	0.246	0.259	0.005	0.028	0.249	0.076	0.261	0.239	0.010	0.238	0.003	0.246	0.260	0.246	0.252	0.245	0.250	0.236	0.242
Ba	0.001	0.001	0.000	0.012	0.010	0.000	0.008	0.000	0.000	0.016	0.001	0.013	0.001	0.000	0.001	0.000	0.000	0.000	0.000	0.000
Na	0.698	0.699	0.687	0.088	0.210	0.709	0.338	0.707	0.713	0.132	0.712	0.040	0.677	0.696	0.708	0.711	0.707	0.712	0.679	0.732
K	0.021	0.026	0.026	0.865	0.714	0.010	0.553	0.005	0.008	0.808	0.011	0.922	0.031	0.026	0.024	0.008	0.018	0.011	0.061	0.011
Sr	0.003	0.003	0.003	0.004	0.002	0.000	0.003	0.002	0.000	0.003	0.001	0.003	0.003	0.002	0.003	0.002	0.001	0.002	0.001	0.003
Sum	5.000	5.000	5.000	5.000	5.000	5.000	5.000	5.000	5.000	5.000	5.000	5.000	5.000	5.000	5.000	5.000	5.000	5.000	5.000	5.000
An	0.258	0.254	0.267	0.005	0.030	0.257	0.079	0.268	0.249	0.011	0.248	0.003	0.257	0.265	0.252	0.260	0.252	0.257	0.242	0.246
Ab	0.720	0.720	0.706	0.091	0.221	0.732	0.350	0.727	0.743	0.139	0.741	0.041	0.710	0.709	0.724	0.732	0.729	0.732	0.695	0.743
Or	0.022	0.026	0.027	0.904	0.750	0.011	0.572	0.005	0.008	0.850	0.011	0.956	0.032	0.026	0.025	0.009	0.019	0.011	0.063	0.012

Chemical composition of feldspars (EPMA data)

Sample	NE30	NE30	NE30	NE30	NE30	NE30	NE30	NE30	NE30	NE30	NE30	NE30	NE30	NE30	NE30	NE30	NE30	NE30	NE30	NE30
ID	21	22	23	24	25	26	27	28	29	30	31	32	33	34	35	36	37	38	39	40
SiO2	62.61	62.97	61.12	62.61	64.33	63.99	65.59	64.35	63.46	65.54	64.52	65.48	64.46	65.60	62.79	64.27	64.14	65.01	62.60	63.72
TiO2	0.03	0.00	0.01	0.08	0.02	0.06	0.04	0.06	0.10	0.03	0.03	0.06	0.04	0.02	0.00	0.07	0.00	0.03	0.04	0.04
Al2O3	23.28	23.87	25.44	23.10	19.50	19.27	18.88	19.52	19.28	19.00	19.49	18.89	19.53	18.89	24.30	19.62	19.46	18.95	23.78	19.20
FeO	0.11	0.08	0.23	0.14	0.03	0.03	0.02	0.08	0.04	0.02	0.04	0.02	0.06	0.00	0.06	0.02	0.00	0.09	0.09	0.02
MnO	0.01	0.01	0.00	0.00	0.00	0.00	0.00	0.00	0.00	0.01	0.01	0.00	0.00	0.00	0.00	0.00	0.00	0.01	0.00	0.01
MgO	0.10	0.00	0.00	0.28	0.00	0.02	0.00	0.02	0.01	0.00	0.00	0.01	0.00	0.00	0.00	0.01	0.00	0.21	0.00	0.01
CaO	4.81	5.11	6.14	4.64	0.14	0.17	0.19	0.11	0.12	0.29	0.17	0.13	0.17	0.12	5.63	0.17	0.19	0.18	5.12	0.15
BaO	0.05	0.01	0.03	0.07	0.90	0.79	0.54	0.87	0.87	0.61	0.84	0.68	0.74	0.68	0.00	0.76	0.78	0.71	0.05	0.75
Na2O	7.52	8.60	7.96	7.41	1.44	1.36	2.19	1.65	1.79	2.16	1.79	1.78	1.88	1.43	8.09	2.25	1.93	2.36	8.29	1.64
K2O	1.51	0.20	0.12	1.87	13.96	14.28	12.88	13.57	13.69	13.27	13.54	13.56	13.38	14.10	0.33	13.05	13.30	12.70	0.35	13.82
SrO	0.05	0.07	0.05	0.04	0.07	0.11	0.14	0.11	0.13	0.12	0.11	0.14	0.16	0.15	0.03	0.14	0.11	0.12	0.08	0.12
Total	100.07	100.92	101.10	100.23	100.39	100.08	100.47	100.33	99.49	101.05	100.54	100.76	100.42	100.99	101.23	100.37	99.92	100.36	100.41	99.49
Oxygens	8	8	8	8	8	8	8	8	8	8	8	8	8	8	8	8	8	8	8	8
Si	2.795	2.771	2.692	2.790	2.965	2.957	3.007	2.965	2.944	2.987	2.963	3.002	2.961	3.006	2.763	2.947	2.960	2.980	2.775	2.956
Ti	0.001	0.000	0.000	0.003	0.001	0.002	0.001	0.002	0.004	0.001	0.001	0.002	0.002	0.001	0.000	0.002	0.000	0.001	0.001	0.001
Al	1.225	1.238	1.321	1.213	1.059	1.049	1.020	1.060	1.054	1.020	1.055	1.021	1.057	1.020	1.260	1.060	1.058	1.024	1.242	1.050
Fe+3	0.000	0.000	0.000	0.000	0.000	0.000	0.000	0.000	0.002	0.000	0.000	0.000	0.000	0.000	0.000	0.001	0.000	0.000	0.000	0.000
Fe+2	0.004	0.003	0.008	0.005	0.001	0.001	0.001	0.003	0.000	0.001	0.002	0.001	0.002	0.000	0.002	0.000	0.000	0.003	0.003	0.001
Mn	0.000	0.000	0.000	0.000	0.000	0.000	0.000	0.000	0.000	0.000	0.001	0.000	0.000	0.000	0.000	0.000	0.000	0.000	0.000	0.000
Mg	0.006	0.000	0.000	0.019	0.000	0.001	0.000	0.001	0.000	0.000	0.000	0.001	0.000	0.000	0.000	0.001	0.000	0.014	0.000	0.001
Ca	0.230	0.241	0.290	0.222	0.007	0.008	0.009	0.006	0.006	0.014	0.008	0.007	0.008	0.006	0.265	0.008	0.009	0.009	0.243	0.007
Ba	0.001	0.000	0.001	0.001	0.016	0.014	0.010	0.016	0.016	0.011	0.015	0.012	0.013	0.012	0.000	0.014	0.014	0.013	0.001	0.014
Na	0.651	0.734	0.680	0.640	0.129	0.122	0.195	0.147	0.161	0.191	0.159	0.158	0.167	0.127	0.690	0.200	0.173	0.210	0.712	0.148
K	0.086	0.011	0.007	0.106	0.821	0.842	0.753	0.798	0.810	0.771	0.793	0.793	0.784	0.824	0.019	0.763	0.783	0.743	0.020	0.818
Sr	0.001	0.002	0.001	0.001	0.002	0.003	0.004	0.003	0.003	0.003	0.003	0.004	0.004	0.004	0.001	0.004	0.003	0.003	0.002	0.003
Sum	5.000	5.000	5.000	5.000	5.000	5.000	5.000	5.000	5.000	5.000	5.000	5.000	5.000	5.000	5.000	5.000	5.000	5.000	5.000	5.000
An	0.238	0.244	0.297	0.229	0.007	0.009	0.010	0.006	0.006	0.014	0.009	0.007	0.009	0.006	0.272	0.009	0.009	0.009	0.249	0.008
Ab	0.673	0.744	0.696	0.661	0.135	0.125	0.203	0.155	0.165	0.195	0.166	0.165	0.174	0.133	0.709	0.206	0.179	0.218	0.731	0.152
Or	0.089	0.011	0.007	0.110	0.858	0.866	0.787	0.839	0.829	0.790	0.825	0.828	0.817	0.861	0.019	0.786	0.812	0.773	0.020	0.841

Chemical composition of feldspars (EPMA data)

Sample	NE157	NE157	NE157	NE157	NE157	NE157	NE157	NE157	NE157	NE163	NE163	NE163	NE163	NE163	NE163	NE163	NE163	NE163	NE163	NE163
ID	41	42	43	44	45	46	47	48	49	50	51	52	53	54	55	56	57	58	59	60
SiO2	64.17	63.67	63.61	64.15	64.35	62.97	61.04	61.79	61.55	60.67	60.21	60.89	59.78	59.76	59.92	60.99	65.77	62.93	60.70	61.85
TiO2	0.02	0.05	0.06	0.10	0.04	0.02	0.02	0.04	0.00	0.03	0.00	0.00	0.00	0.05	0.01	0.00	0.00	0.00	0.08	0.07
Al2O3	19.02	19.01	19.15	19.37	18.58	23.70	24.61	24.16	24.82	25.13	25.46	24.96	25.62	25.68	25.73	24.70	18.60	23.58	24.99	24.50
FeO	0.22	0.26	0.15	0.30	0.19	0.03	0.03	0.07	0.02	0.05	0.04	0.00	0.00	0.03	0.03	0.39	0.06	0.05	0.13	0.08
MnO	0.00	0.00	0.01	0.02	0.00	0.00	0.00	0.02	0.01	0.00	0.01	0.00	0.00	0.01	0.00	0.00	0.00	0.00	0.01	0.00
MgO	0.00	0.00	0.00	0.00	0.00	0.00	0.00	0.00	0.00	0.00	0.00	0.00	0.00	0.00	0.00	0.13	0.02	0.00	0.06	0.00
CaO	0.03	0.00	0.02	0.00	0.01	5.10	6.09	5.25	6.34	5.86	6.28	5.81	6.50	6.52	6.53	5.30	0.06	4.94	6.46	5.69
BaO	0.54	0.71	0.45	0.52	0.57	0.02	0.03	0.04	0.03	0.00	0.00	0.00	0.06	0.00	0.00	0.00	0.43	0.06	0.02	0.06
Na2O	1.02	0.94	0.96	0.99	0.79	8.32	7.79	8.10	7.81	8.14	7.77	8.08	7.56	7.66	7.81	8.38	1.75	8.61	7.75	8.18
K2O	14.71	14.91	15.01	14.89	14.67	0.35	0.25	0.24	0.17	0.24	0.37	0.32	0.38	0.38	0.27	0.18	13.92	0.16	0.15	0.16
SrO	0.08	0.10	0.08	0.05	0.05	0.08	0.14	0.08	0.14	0.05	0.01	0.05	0.09	0.08	0.09	0.03	0.10	0.13	0.04	0.08
Total	99.81	99.66	99.49	100.39	99.23	100.59	100.00	99.80	100.90	100.17	100.16	100.11	99.99	100.17	100.39	100.09	100.70	100.48	100.39	100.67
Oxygens	8	8	8	8	8	8	8	8	8	8	8	8	8	8	8	8	8	8	8	8
Si	2.976	2.961	2.956	2.957	3.009	2.785	2.722	2.757	2.722	2.690	2.675	2.703	2.665	2.657	2.656	2.704	3.011	2.783	2.695	2.735
Ti	0.001	0.002	0.002	0.003	0.001	0.001	0.001	0.001	0.000	0.001	0.000	0.000	0.000	0.002	0.000	0.000	0.000	0.000	0.003	0.002
Al	1.039	1.042	1.049	1.052	1.024	1.235	1.293	1.270	1.293	1.313	1.333	1.306	1.346	1.346	1.344	1.290	1.004	1.229	1.308	1.277
Fe+3	0.000	0.001	0.006	0.000	0.000	0.000	0.000	0.000	0.000	0.002	0.002	0.000	0.000	0.001	0.001	0.014	0.000	0.000	0.000	0.000
Fe+2	0.009	0.009	0.000	0.012	0.007	0.001	0.001	0.003	0.001	0.000	0.000	0.000	0.000	0.000	0.000	0.000	0.002	0.002	0.005	0.003
Mn	0.000	0.000	0.000	0.001	0.000	0.000	0.000	0.001	0.000	0.000	0.001	0.000	0.000	0.000	0.000	0.000	0.000	0.000	0.000	0.000
Mg	0.000	0.000	0.000	0.000	0.000	0.000	0.000	0.000	0.000	0.000	0.000	0.000	0.000	0.000	0.000	0.009	0.001	0.000	0.004	0.000
Ca	0.001	0.000	0.001	0.000	0.000	0.242	0.291	0.251	0.300	0.278	0.299	0.276	0.310	0.311	0.310	0.252	0.003	0.234	0.307	0.270
Ba	0.010	0.013	0.008	0.009	0.010	0.000	0.001	0.001	0.001	0.000	0.000	0.000	0.001	0.000	0.000	0.000	0.008	0.001	0.000	0.001
Na	0.092	0.085	0.087	0.088	0.071	0.714	0.674	0.701	0.670	0.700	0.669	0.695	0.653	0.660	0.671	0.720	0.155	0.738	0.667	0.701
K	0.870	0.885	0.890	0.876	0.875	0.020	0.014	0.014	0.010	0.014	0.021	0.018	0.022	0.021	0.015	0.010	0.813	0.009	0.009	0.009
Sr	0.002	0.003	0.002	0.001	0.001	0.002	0.004	0.002	0.004	0.001	0.000	0.001	0.002	0.002	0.002	0.001	0.003	0.003	0.001	0.002
Sum	5.000	5.000	5.000	5.000	5.000	5.000	5.000	5.000	5.000	5.000	5.000	5.000	5.000	5.000	5.000	5.000	5.000	5.000	5.000	5.000
An	0.000	0.000	0.000	0.000	0.000	0.248	0.297	0.260	0.307	0.280	0.300	0.279	0.320	0.310	0.310	0.256	0.003	0.238	0.313	0.275
Ab	0.100	0.090	0.090	0.090	0.080	0.732	0.688	0.726	0.683	0.710	0.680	0.702	0.660	0.670	0.670	0.733	0.160	0.752	0.679	0.716
Or	0.900	0.910	0.910	0.910	0.920	0.020	0.014	0.014	0.010	0.010	0.020	0.019	0.020	0.020	0.020	0.010	0.837	0.009	0.009	0.009

Chemical composition of feldspars (EPMA data)

Sample	NE157	NE157	NE157	NE157	NE157	NE157	NE157	NE157	NE157	NE163	NE163	NE163	NE163	NE163	NE163	NE163	NE163	NE163	NE163	NE163
ID	61	62	63	64	65	66	67	68	69	70	71	72	73	74	75	76	77	78	79	80
SiO2	64.17	63.67	63.61	64.15	64.35	62.97	61.04	61.79	61.55	60.67	60.21	60.89	59.78	59.76	59.92	60.99	65.77	62.93	60.70	61.85
TiO2	0.02	0.05	0.06	0.10	0.04	0.02	0.02	0.04	0.00	0.03	0.00	0.00	0.00	0.05	0.01	0.00	0.00	0.00	0.08	0.07
Al2O3	19.02	19.01	19.15	19.37	18.58	23.70	24.61	24.16	24.82	25.13	25.46	24.96	25.62	25.68	25.73	24.70	18.60	23.58	24.99	24.50
FeO	0.22	0.26	0.15	0.30	0.19	0.03	0.03	0.07	0.02	0.05	0.04	0.00	0.00	0.03	0.03	0.39	0.06	0.05	0.13	0.08
MnO	0.00	0.00	0.01	0.02	0.00	0.00	0.00	0.02	0.01	0.00	0.01	0.00	0.00	0.01	0.00	0.00	0.00	0.00	0.01	0.00
MgO	0.00	0.00	0.00	0.00	0.00	0.00	0.00	0.00	0.00	0.00	0.00	0.00	0.00	0.00	0.00	0.13	0.02	0.00	0.06	0.00
CaO	0.03	0.00	0.02	0.00	0.01	5.10	6.09	5.25	6.34	5.86	6.28	5.81	6.50	6.52	6.53	5.30	0.06	4.94	6.46	5.69
BaO	0.54	0.71	0.45	0.52	0.57	0.02	0.03	0.04	0.03	0.00	0.00	0.00	0.06	0.00	0.00	0.00	0.43	0.06	0.02	0.06
Na2O	1.02	0.94	0.96	0.99	0.79	8.32	7.79	8.10	7.81	8.14	7.77	8.08	7.56	7.66	7.81	8.38	1.75	8.61	7.75	8.18
K2O	14.71	14.91	15.01	14.89	14.67	0.35	0.25	0.24	0.17	0.24	0.37	0.32	0.38	0.38	0.27	0.18	13.92	0.16	0.15	0.16
SrO	0.08	0.10	0.08	0.05	0.05	0.08	0.14	0.08	0.14	0.05	0.01	0.05	0.09	0.08	0.09	0.03	0.10	0.13	0.04	0.08
Total	99.81	99.66	99.49	100.39	99.23	100.59	100.00	99.80	100.90	100.17	100.16	100.11	99.99	100.17	100.39	100.09	100.70	100.48	100.39	100.67
Oxygens	8	8	8	8	8	8	8	8	8	8	8	8	8	8	8	8	8	8	8	8
Si	2.976	2.961	2.956	2.957	3.009	2.785	2.722	2.757	2.722	2.690	2.675	2.703	2.665	2.657	2.656	2.704	3.011	2.783	2.695	2.735
Ti	0.001	0.002	0.002	0.003	0.001	0.001	0.001	0.001	0.000	0.001	0.000	0.000	0.000	0.002	0.000	0.000	0.000	0.000	0.003	0.002
Al	1.039	1.042	1.049	1.052	1.024	1.235	1.293	1.270	1.293	1.313	1.333	1.306	1.346	1.346	1.344	1.290	1.004	1.229	1.308	1.277
Fe+3	0.000	0.001	0.006	0.000	0.000	0.000	0.000	0.000	0.000	0.002	0.002	0.000	0.000	0.001	0.001	0.014	0.000	0.000	0.000	0.000
Fe+2	0.009	0.009	0.000	0.012	0.007	0.001	0.001	0.003	0.001	0.000	0.000	0.000	0.000	0.000	0.000	0.000	0.002	0.002	0.005	0.003
Mn	0.000	0.000	0.000	0.001	0.000	0.000	0.000	0.001	0.000	0.000	0.001	0.000	0.000	0.000	0.000	0.000	0.000	0.000	0.000	0.000
Mg	0.000	0.000	0.000	0.000	0.000	0.000	0.000	0.000	0.000	0.000	0.000	0.000	0.000	0.000	0.000	0.009	0.001	0.000	0.004	0.000
Ca	0.001	0.000	0.001	0.000	0.000	0.242	0.291	0.251	0.300	0.278	0.299	0.276	0.310	0.311	0.310	0.252	0.003	0.234	0.307	0.270
Ba	0.010	0.013	0.008	0.009	0.010	0.000	0.001	0.001	0.001	0.000	0.000	0.000	0.001	0.000	0.000	0.000	0.008	0.001	0.000	0.001
Na	0.092	0.085	0.087	0.088	0.071	0.714	0.674	0.701	0.670	0.700	0.669	0.695	0.653	0.660	0.671	0.720	0.155	0.738	0.667	0.701
K	0.870	0.885	0.890	0.876	0.875	0.020	0.014	0.014	0.010	0.014	0.021	0.018	0.022	0.021	0.015	0.010	0.813	0.009	0.009	0.009
Sr	0.002	0.003	0.002	0.001	0.001	0.002	0.004	0.002	0.004	0.001	0.000	0.001	0.002	0.002	0.002	0.001	0.003	0.003	0.001	0.002
Sum	5.000	5.000	5.000	5.000	5.000	5.000	5.000	5.000	5.000	5.000	5.000	5.000	5.000	5.000	5.000	5.000	5.000	5.000	5.000	5.000
An	0.000	0.000	0.000	0.000	0.000	0.248	0.297	0.260	0.307	0.280	0.300	0.279	0.320	0.310	0.310	0.256	0.003	0.238	0.313	0.275
Ab	0.100	0.090	0.090	0.090	0.080	0.732	0.688	0.726	0.683	0.710	0.680	0.702	0.660	0.670	0.670	0.733	0.160	0.752	0.679	0.716
Or	0.900	0.910	0.910	0.910	0.920	0.020	0.014	0.014	0.010	0.010	0.020	0.019	0.020	0.020	0.020	0.010	0.837	0.009	0.009	0.009

Chemical composition of spinel (EPMA data)

Sample	NE30	NE30	NE30	NE30	NE30	NE30	NE30	NE30	NE30	NE30	NE30	NE30	NE30	NE30	NE30	NE30	NE30	NE30	NE30	NE30
ID	1	2	3	4	5	6	7	8	9	10	11	12	13	14	15	16	17	18	19	20
SiO2	0.10	0.02	0.51	0.02	0.04	0.57	0.42	0.02	0.07	0.15	0.13	0.09	0.08	0.03	0.03	0.01	0.08	0.08	0.09	0.10
TiO2	0.03	0.01	0.01	0.16	0.27	0.01	0.00	0.04	0.04	0.07	0.06	0.02	0.00	0.01	0.00	0.26	0.00	0.00	0.01	0.00
Al2O3	58.60	58.68	57.44	58.77	58.62	57.65	59.40	58.84	58.14	59.35	58.87	59.92	58.11	59.89	59.17	59.35	58.33	58.70	58.25	58.64
Cr2O3	0.58	0.59	0.31	0.55	0.46	0.08	0.25	0.58	0.51	0.16	0.22	0.21	0.22	0.39	0.50	0.55	0.01	0.00	0.03	0.04
FeO	30.43	29.49	27.72	29.80	29.32	29.06	29.52	28.48	28.43	26.48	26.39	28.09	29.56	27.30	26.94	28.19	30.82	29.38	29.45	28.71
MnO	0.39	0.38	0.42	0.36	0.32	0.52	0.53	0.43	0.47	0.59	0.40	0.26	0.38	0.38	0.32	0.34	0.48	0.53	0.49	0.46
MgO	9.15	9.93	10.07	9.64	9.82	9.88	9.54	10.45	10.01	10.77	11.62	9.03	9.41	10.93	11.47	10.52	10.15	10.32	10.24	10.83
CaO	0.00	0.00	1.10	0.00	0.00	0.01	0.00	0.00	0.00	0.00	0.01	0.02	0.01	0.00	0.01	0.00	0.00	0.00	0.01	0.01
K2O	0.00	0.00	0.01	0.00	0.00	0.00	0.01	0.00	0.02	0.00	0.00	0.00	0.00	0.00	0.00	0.01	0.00	0.00	0.00	0.01
ZnO	1.54	1.51	2.26	1.65	1.60	1.56	1.99	1.76	1.74	2.24	2.06	2.79	2.21	1.85	1.81	1.68	0.78	0.84	0.78	0.78
Total	100.82	100.62	99.85	100.95	100.45	99.34	101.66	100.61	99.43	99.82	99.76	100.44	99.98	100.78	100.25	100.90	100.65	99.85	99.35	99.57
Oxygens	4	4	4	4	4	4	4	4	4	4	4	4	4	4	4	4	4	4	4	4
Si	0.003	0.001	0.014	0.000	0.001	0.016	0.011	0.001	0.002	0.004	0.004	0.002	0.002	0.001	0.001	0.000	0.002	0.002	0.003	0.003
Ti	0.001	0.000	0.000	0.003	0.006	0.000	0.000	0.001	0.001	0.001	0.001	0.000	0.000	0.000	0.000	0.005	0.000	0.000	0.000	0.000
Al	1.880	1.877	1.848	1.878	1.879	1.866	1.884	1.876	1.879	1.897	1.875	1.923	1.877	1.895	1.878	1.884	1.863	1.882	1.878	1.878
Cr	0.013	0.013	0.007	0.012	0.010	0.002	0.005	0.012	0.011	0.003	0.005	0.005	0.005	0.008	0.011	0.012	0.000	0.000	0.001	0.001
Fe3+	0.101	0.109	0.117	0.103	0.098	0.101	0.088	0.109	0.105	0.089	0.110	0.066	0.114	0.095	0.110	0.094	0.133	0.114	0.116	0.116
Fe2+	0.592	0.560	0.516	0.573	0.569	0.567	0.576	0.535	0.547	0.512	0.486	0.573	0.564	0.518	0.497	0.541	0.566	0.555	0.558	0.537
Mn	0.009	0.009	0.010	0.008	0.007	0.012	0.012	0.010	0.011	0.014	0.009	0.006	0.009	0.009	0.007	0.008	0.011	0.012	0.011	0.011
Mg	0.371	0.402	0.410	0.390	0.398	0.405	0.383	0.421	0.409	0.435	0.468	0.367	0.385	0.437	0.460	0.422	0.410	0.418	0.418	0.439
Zn	0.031	0.030	0.046	0.033	0.032	0.032	0.040	0.035	0.035	0.045	0.041	0.056	0.045	0.037	0.036	0.033	0.016	0.017	0.016	0.016
Ca	0.000	0.000	0.032	0.000	0.000	0.000	0.000	0.000	0.000	0.000	0.000	0.001	0.000	0.000	0.000	0.000	0.000	0.000	0.000	0.000
K	0.000	0.000	0.000	0.000	0.000	0.000	0.000	0.000	0.001	0.000	0.000	0.000	0.000	0.000	0.000	0.000	0.000	0.000	0.000	0.000
Sum	3.000	3.000	3.000	3.000	3.000	3.000	3.000	3.000	3.000	3.000	3.000	3.000	3.000	3.000	3.000	3.000	3.000	3.000	3.000	3.000
XMg	0.349	0.375	0.393	0.366	0.374	0.377	0.366	0.395	0.386	0.420	0.440	0.364	0.362	0.416	0.431	0.399	0.370	0.385	0.383	0.402

Chemical composition of spinel (EPMA data)

Sample	NE30	NE30	NE30	NE30	NE30	NE30	NE30	NE30	NE30	NE157	NE157	NE157	NE157	NE157	NE157	NE157	NE157	NE157	NE157
ID	21	22	23	24	25	26	27	28	29	30	31	32	33	34	35	36	37	38	39
SiO2	0.88	0.19	1.61	0.09	0.09	0.26	0.12	0.09	1.33	0.09	0.07	0.07	0.09	0.04	0.08	0.08	0.26	0.05	0.08
TiO2	0.00	0.00	0.00	0.01	0.01	0.00	0.04	0.00	0.03	0.06	0.00	0.02	0.01	0.05	0.03	0.03	0.02	0.02	0.00
Al2O3	59.33	57.96	58.95	58.62	58.51	59.69	58.95	58.54	57.77	55.68	54.43	54.31	54.75	55.27	54.60	55.33	54.94	55.14	54.99
Cr2O3	0.01	0.01	0.03	0.04	0.04	0.04	0.04	0.02	0.01	0.22	0.20	0.11	0.19	0.31	0.21	0.19	0.24	0.15	0.22
FeO	29.66	30.29	28.97	29.21	30.15	29.38	30.02	29.47	29.92	38.61	39.52	40.20	38.90	35.14	35.63	34.99	34.78	34.45	35.11
MnO	0.47	0.50	0.43	0.42	0.41	0.43	0.41	0.42	0.44	0.09	0.08	0.10	0.10	0.06	0.07	0.06	0.07	0.06	0.05
MgO	10.33	10.19	10.76	10.87	10.79	10.82	10.69	10.70	10.70	4.77	4.57	4.34	4.70	5.37	5.29	5.31	5.46	5.50	5.33
CaO	0.00	0.01	0.00	0.00	0.00	0.00	0.01	0.01	0.01	0.01	0.00	0.00	0.01	0.00	0.00	0.00	0.00	0.01	0.00
K2O	0.00	0.00	0.00	0.01	0.00	0.00	0.02	0.00	0.00	0.01	0.01	0.01	0.01	0.00	0.00	0.01	0.00	0.00	0.00
ZnO	0.82	0.84	0.41	0.42	0.42	0.41	0.56	0.54	0.45	1.70	1.60	1.64	1.58	4.92	4.82	4.80	4.86	4.93	4.88
Total	101.50	99.99	101.16	99.69	100.42	101.03	100.84	99.80	100.65	101.24	100.48	100.80	100.35	101.16	100.73	100.81	100.63	100.31	100.66
Oxygens	4	4	4	4	4	4	4	4	4	4	4	4	4	4	4	4	4	4	4
Si	0.024	0.005	0.043	0.002	0.002	0.007	0.003	0.003	0.036	0.003	0.002	0.002	0.003	0.001	0.002	0.002	0.007	0.002	0.002
Ti	0.000	0.000	0.000	0.000	0.000	0.000	0.001	0.000	0.001	0.001	0.000	0.000	0.000	0.001	0.001	0.001	0.000	0.000	0.000
Al	1.873	1.862	1.860	1.875	1.863	1.884	1.870	1.874	1.838	1.845	1.824	1.819	1.833	1.834	1.823	1.841	1.831	1.841	1.834
Cr	0.000	0.000	0.001	0.001	0.001	0.001	0.001	0.000	0.000	0.005	0.005	0.002	0.004	0.007	0.005	0.004	0.005	0.003	0.005
Fe3+	0.080	0.128	0.053	0.119	0.131	0.101	0.123	0.121	0.089	0.143	0.168	0.175	0.157	0.155	0.167	0.149	0.148	0.151	0.157
Fe2+	0.584	0.562	0.595	0.544	0.550	0.557	0.553	0.549	0.587	0.765	0.772	0.781	0.767	0.673	0.677	0.677	0.674	0.665	0.674
Mn	0.011	0.012	0.010	0.010	0.009	0.010	0.009	0.010	0.010	0.002	0.002	0.002	0.002	0.001	0.002	0.002	0.002	0.001	0.001
Mg	0.412	0.414	0.429	0.440	0.435	0.432	0.429	0.433	0.431	0.200	0.194	0.184	0.199	0.225	0.223	0.223	0.230	0.232	0.225
Zn	0.016	0.017	0.008	0.008	0.008	0.008	0.011	0.011	0.009	0.035	0.034	0.034	0.033	0.102	0.101	0.100	0.101	0.103	0.102
Ca	0.000	0.000	0.000	0.000	0.000	0.000	0.000	0.000	0.000	0.000	0.000	0.000	0.000	0.000	0.000	0.000	0.000	0.000	0.000
K	0.000	0.000	0.000	0.000	0.000	0.000	0.001	0.000	0.000	0.001	0.000	0.001	0.000	0.000	0.000	0.000	0.000	0.000	0.000
Sum	3.000	3.000	3.000	3.000	3.000	3.000	3.000	3.000	3.000	3.000	3.000	3.000	3.000	3.000	3.000	3.000	3.000	3.000	3.000
XMg	0.383	0.375	0.398	0.399	0.389	0.396	0.388	0.393	0.389	0.180	0.171	0.161	0.177	0.214	0.209	0.213	0.219	0.222	0.213

Chemical composition of biotite (EPMA data)

Sample	NE30	NE30	NE30	NE30	NE30	NE30	NE30	NE30	NE30	NE30	NE30	NE30	NE30	NE157	NE157	NE157	NE157	NE163	NE163	NE163
ID	1	2	3	4	5	6	7	8	9	10	11	12	13	33	34	35	36	18	19	20
SiO2	38.25	74.10	37.63	36.96	36.94	36.88	39.19	36.70	36.54	36.95	36.98	37.47	37.35	34.00	33.74	34.77	34.21	35.99	35.76	33.27
TiO2	1.73	1.01	3.67	4.16	4.23	3.52	2.05	3.59	4.11	2.79	3.19	3.27	3.59	4.62	4.12	4.19	4.84	4.48	4.22	4.16
Al2O3	16.44	9.12	16.32	16.35	16.37	15.82	22.31	15.43	15.44	16.55	16.83	16.80	16.76	16.34	17.18	17.39	16.73	17.82	17.98	15.93
FeO	9.99	4.59	9.06	11.06	11.44	11.40	8.55	11.02	11.52	9.20	9.57	9.53	10.47	19.72	19.24	18.07	19.28	16.79	17.25	16.76
MnO	0.10	0.02	0.15	0.08	0.07	0.08	0.10	0.11	0.09	0.06	0.06	0.08	0.08	0.03	0.04	0.00	0.01	0.02	0.02	0.04
MgO	18.37	7.00	17.34	15.78	16.21	16.18	12.77	16.10	15.56	18.19	17.78	17.81	16.87	9.76	9.86	10.50	9.76	11.46	11.06	12.26
CaO	0.10	0.01	0.10	0.01	0.00	0.03	0.17	0.14	0.02	0.03	0.00	0.00	0.04	0.03	0.00	0.01	0.00	0.00	0.01	0.10
Na2O	0.02	0.03	0.11	0.06	0.01	0.06	0.07	0.01	0.04	0.04	0.09	0.09	0.06	0.02	0.06	0.07	0.07	0.10	0.06	0.10
K2O	9.64	3.69	9.52	9.49	9.67	9.36	5.90	9.57	9.24	9.49	9.42	9.59	9.33	9.57	9.47	9.59	9.57	9.33	9.32	9.24
Cl	0.18	0.07	0.17	0.10	0.14	0.14	0.13	0.14	0.13	0.12	0.13	0.15	0.13	0.06	0.08	0.08	0.09	0.33	0.36	0.34
F	0.94	0.21	0.75	0.53	0.64	0.67	0.39	0.83	0.66	0.73	0.72	0.82	0.61	0.02	0.01	0.04	0.02	0.30	0.24	0.34
Total	95.76	99.85	94.82	94.59	95.72	94.13	91.64	93.64	93.35	94.16	94.78	95.61	95.29	94.17	93.81	94.71	94.58	96.62	96.28	92.55
Oxygens	22	22	22	22	22	22	22	22	22	22	22	22	22	22	22	22	22	22	22	22
Si	5.594	8.928	5.533	5.489	5.444	5.523	5.698	5.539	5.524	5.476	5.450	5.478	5.483	5.301	5.263	5.327	5.293	5.361	5.355	5.241
Ti	0.190	0.092	0.406	0.465	0.469	0.396	0.224	0.408	0.467	0.311	0.354	0.360	0.396	0.542	0.483	0.483	0.563	0.502	0.475	0.493
Al	2.834	1.295	2.828	2.862	2.843	2.792	3.823	2.744	2.751	2.890	2.923	2.895	2.900	3.002	3.158	3.140	3.050	3.128	3.173	2.957
Fe	1.222	0.462	1.114	1.374	1.410	1.428	1.040	1.391	1.456	1.140	1.179	1.165	1.285	2.571	2.510	2.315	2.494	2.091	2.160	2.207
Mn	0.012	0.002	0.019	0.010	0.009	0.010	0.013	0.015	0.011	0.008	0.008	0.009	0.010	0.003	0.005	0.000	0.002	0.003	0.003	0.005
Mg	4.005	1.257	3.801	3.494	3.562	3.612	2.768	3.623	3.507	4.019	3.906	3.882	3.692	2.269	2.293	2.398	2.251	2.545	2.469	2.879
Ca	0.016	0.002	0.016	0.002	0.000	0.004	0.027	0.023	0.004	0.005	0.000	0.000	0.006	0.005	0.000	0.001	0.000	0.000	0.002	0.017
Na	0.007	0.006	0.030	0.018	0.003	0.016	0.021	0.002	0.013	0.013	0.025	0.026	0.017	0.007	0.018	0.021	0.020	0.029	0.017	0.031
K	1.798	0.567	1.786	1.798	1.818	1.788	1.094	1.842	1.782	1.794	1.771	1.788	1.747	1.903	1.884	1.874	1.889	1.773	1.780	1.857
Cl2	0.044	0.014	0.042	0.026	0.035	0.034	0.032	0.036	0.033	0.031	0.033	0.038	0.032	0.015	0.022	0.020	0.023	0.083	0.091	0.091
F3	0.435	0.081	0.350	0.250	0.297	0.317	0.179	0.395	0.313	0.344	0.337	0.380	0.285	0.010	0.007	0.020	0.009	0.141	0.114	0.169
Sum	16.158	12.707	15.925	15.786	15.890	15.921	14.919	16.016	15.861	16.030	15.986	16.021	15.854	15.629	15.644	15.598	15.594	15.657	15.641	15.946
XMg	0.766	0.731	0.773	0.718	0.716	0.717	0.727	0.723	0.707	0.779	0.768	0.769	0.742	0.469	0.477	0.509	0.474	0.549	0.533	0.566

APPENDIX B. LA-ICP-MS ISOTOPIC ANALYSIS OF ZIRCON

U-Pb LA-ICP-MS analyses of zircon

Sample	Spot	Group	U ppm	Th ppm	%^{206}Pbc	^{206}Pb*	*Isotopic Ratios*									*Age (Ma)*						
							Th/U	^{207}Pb/^{235}U	1σ (%)	^{206}Pb/^{238}U	1σ (%)	^{238}U/^{206}Pb	1σ (%)	^{207}Pb/^{206}Pb	1σ (%)	^{206}Pb/^{238}U	±2σ	^{207}Pb/^{235}U	±2σ	^{207}Pb/^{206}Pb	±2σ	Conc.%
NE30	2	R1	36.4	90.2	0.6	18.5	2.48	6.049	0.133	0.362	0.005	2.764	0.038	0.121	0.002	1991	23	1983	19	1975	22	100
NE30	3	R1	60.0	82.9	0.5	26.2	1.38	6.066	0.146	0.365	0.005	2.738	0.035	0.121	0.003	2007	22	1985	21	1963	29	101
NE30	6	R2	118.0	18.8	0.7	42.5	0.16	6.292	0.107	0.367	0.004	2.724	0.030	0.124	0.002	2016	19	2017	15	2019	18	99
NE30	11	R0	423.1	225.3	0.0	141.5	0.53	6.128	0.092	0.365	0.003	2.744	0.023	0.122	0.002	2003	15	1994	13	1985	12	100
NE30	15	R2	90.7	19	0.0	33.9	0.21	6.176	0.109	0.363	0.003	2.753	0.024	0.123	0.002	1997	15	2001	15	2005	18	99
NE30	19	R2	69.1	75.5	3.6	28.1	1.09	6.100	0.106	0.359	0.003	2.783	0.019	0.123	0.002	1979	12	1990	15	2002	25	99
NE30	29	RC	116.5	101.4	0.1	46.9	0.87	7.003	0.110	0.389	0.004	2.571	0.023	0.131	0.002	2118	16	2112	14	2106	17	100
NE30	33	R1	33.7	64.5	1.7	17.0	1.91	6.079	0.119	0.363	0.004	2.758	0.030	0.122	0.002	1994	19	1987	17	1980	21	100
NE30	35	R0	186.5	24	0.0	68.8	0.13	6.018	0.083	0.359	0.003	2.783	0.021	0.122	0.002	1979	12	1979	12	1978	14	100
NE30	36	R1	82.6	2.2	0.0	27.0	0.03	6.167	0.110	0.364	0.004	2.745	0.028	0.123	0.002	2003	18	2000	16	1997	14	100
NE30	37	R1	40.7	194.9	1.2	24.0	4.79	5.993	0.128	0.360	0.004	2.777	0.028	0.121	0.002	1982	17	1975	19	1967	30	100
NE30	38	R2	63.2	93.2	0.7	27.8	1.47	6.380	0.111	0.371	0.003	2.693	0.024	0.125	0.002	2036	16	2029	15	2023	20	100
NE30	40	R2	33.9	109.8	0.0	18.1	3.24	6.119	0.108	0.358	0.004	2.791	0.027	0.124	0.002	1974	17	1993	15	2013	27	99
NE30	45	R2	35.0	251.2	0.5	26.8	7.18	6.125	0.136	0.360	0.004	2.777	0.027	0.123	0.003	1983	17	1994	19	2005	28	99
NE30	51	R1	53.9	89.8	0.3	23.5	1.67	6.178	0.104	0.365	0.003	2.739	0.022	0.123	0.002	2006	14	2001	15	1996	21	100
NE30	55	R1	86.6	19.7	0.1	32.3	0.23	6.158	0.112	0.370	0.003	2.700	0.022	0.121	0.003	2031	14	1998	16	1965	24	101
NE30	58	R1	32.6	178.2	1.0	21.5	5.47	6.032	0.150	0.359	0.004	2.788	0.030	0.122	0.002	1976	18	1980	22	1985	48	99
NE30	62	R2	38.0	138.8	0.6	21.4	3.65	6.076	0.120	0.358	0.003	2.790	0.022	0.123	0.002	1975	13	1987	17	2000	26	99
NE30	74	R2	106.2	18	0.3	37.5	0.17	6.395	0.111	0.370	0.003	2.702	0.019	0.125	0.002	2030	12	2032	15	2033	21	99
NE30	75	RC	64.4	40.5	0.2	28.7	0.63	7.439	0.143	0.400	0.004	2.502	0.022	0.135	0.003	2167	16	2166	17	2164	20	100
NE30	76	R2	68.8	45.2	0.0	26.5	0.66	6.210	0.111	0.363	0.003	2.756	0.023	0.124	0.002	1995	14	2006	16	2017	29	99
NE30	77	R2	44.0	184.9	0.6	25.8	4.20	6.179	0.155	0.361	0.004	2.771	0.027	0.124	0.003	1987	17	2001	22	2017	30	99
NE30	83	R2	151.0	17.2	0.2	55.6	0.11	6.416	0.069	0.371	0.002	2.698	0.017	0.126	0.001	2032	11	2034	9	2036	14	99
NE30	84	RC	131.9	134.6	0.0	56.9	1.02	7.286	0.082	0.400	0.003	2.503	0.016	0.132	0.001	2167	12	2147	10	2128	10	100
NE30	85	R1	36.0	188.9	0.4	23.6	5.25	6.087	0.119	0.359	0.004	2.785	0.027	0.123	0.002	1978	17	1988	17	2000	23	99
NE30	93	R2	78.9	284.5	0.8	42.6	3.61	6.312	0.091	0.366	0.002	2.733	0.014	0.125	0.002	2010	9	2020	13	2030	22	99
NE30	95	RC	83.2	65.3	0.5	33.1	0.78	6.767	0.096	0.371	0.002	2.699	0.017	0.133	0.002	2032	11	2081	13	2131	21	97
NE30	96	R2	120.2	17.1	0.0	42.1	0.14	6.165	0.089	0.360	0.002	2.778	0.015	0.124	0.002	1982	9	1999	13	2017	19	99
NE30	99	R2	122.4	25.3	0.2	45.1	0.21	6.313	0.116	0.367	0.002	2.728	0.017	0.125	0.003	2013	11	2020	16	2028	23	99
NE30	100	R1	69.6	310.9	0.4	44.5	4.47	5.940	0.117	0.357	0.003	2.803	0.026	0.121	0.003	1967	16	1967	17	1968	24	99

U-Pb LA-ICP-MS analyses of zircon

Sample	Spot	Group	U ppm	Th ppm	%^{206}Pbc	^{206}Pb*	*Isotopic Ratios*									*Age (Ma)*						
							Th/U	^{207}Pb/^{235}U	1σ (%)	^{206}Pb/^{238}U	1σ (%)	^{238}U/^{206}Pb	1σ (%)	^{207}Pb/^{206}Pb	1σ (%)	^{206}Pb/^{238}U	±2σ	^{207}Pb/^{235}U	±2σ	^{207}Pb/^{206}Pb	±2σ	Conc.%
NE157	2	R0	134	166.7	0.5	57.5	1.24	5.813	0.115	0.348	0.003	2.876	0.027	0.121	0.002	1923	16	1948	17	1975	27	98
NE157	4	R1	157.5	170.8	0.0	66.6	1.08	5.885	0.119	0.352	0.003	2.840	0.025	0.121	0.002	1944	15	1959	18	1974	26	99
NE157	6	R0	257.7	113.2	0.1	94.4	0.44	5.795	0.121	0.352	0.003	2.839	0.026	0.119	0.002	1945	16	1946	18	1946	22	99
NE157	12	R1	667.4	26.9	0.1	193.3	0.04	5.421	0.096	0.334	0.007	2.992	0.066	0.118	0.003	1859	36	1888	15	1921	14	98
NE157	17	R0	261.3	115.6	0.2	93.3	0.44	5.546	0.083	0.340	0.004	2.940	0.031	0.118	0.001	1887	17	1908	13	1930	19	98
NE157	18	R0	317.2	99.7	0.2	106.2	0.31	5.619	0.080	0.344	0.004	2.906	0.030	0.118	0.001	1906	17	1919	12	1933	12	99
NE157	20	R0	70.4	73	0.4	29.2	1.04	5.773	0.090	0.346	0.004	2.888	0.031	0.121	0.002	1917	18	1942	14	1969	10	98
NE157	21	R1	140.2	47.9	0.2	53.6	0.34	5.783	0.085	0.349	0.004	2.870	0.032	0.120	0.002	1927	18	1944	13	1962	29	99
NE157	25	R1	146.9	217	0.2	61.8	1.48	5.822	0.093	0.351	0.004	2.846	0.034	0.120	0.002	1941	20	1950	14	1959	18	99
NE157	28	R1	17.8	101.3	0.0	13.6	5.69	5.612	0.137	0.344	0.003	2.906	0.022	0.118	0.003	1906	13	1918	21	1931	31	99
NE157	30	R1	144.9	147.8	1.7	59.3	1.02	5.578	0.140	0.341	0.003	2.932	0.025	0.119	0.003	1892	14	1913	22	1935	31	98
NE157	31	R1	240.5	5641	0.1	272.4	23.46	6.458	0.156	0.380	0.003	2.634	0.019	0.123	0.003	2075	13	2040	21	2006	36	101
NE157	45	R1	306.8	112.7	0.2	110.0	0.37	5.571	0.103	0.341	0.006	2.935	0.051	0.119	0.002	1890	28	1912	16	1935	24	98
NE157	46	R1	153	227.2	0.4	66.1	1.48	5.790	0.108	0.348	0.006	2.878	0.049	0.121	0.002	1923	29	1945	16	1969	15	98
NE157	50	R1	162.9	59.5	0.4	64.0	0.37	5.998	0.303	0.354	0.005	2.825	0.040	0.123	0.006	1954	24	1976	44	1999	74	98
NE157	51	R1	122.2	317.7	0.0	56.5	2.60	5.706	0.283	0.343	0.005	2.913	0.040	0.121	0.006	1902	23	1932	43	1964	70	98
NE157	57	R1	492.7	46.8	0.0	164.7	0.09	5.906	0.083	0.359	0.003	2.786	0.023	0.119	0.002	1977	14	1962	12	1946	11	100
NE157	59	R1	152.1	180.7	0.6	65.0	1.19	5.592	0.079	0.342	0.003	2.924	0.024	0.119	0.002	1896	14	1915	12	1935	17	99
NE157	61	R0	170.2	153.6	0.2	64.3	0.90	5.815	0.067	0.356	0.002	2.813	0.018	0.119	0.001	1961	11	1949	10	1935	11	100
NE157	66	R1	135.7	131.5	0.7	52.8	0.97	5.651	0.066	0.347	0.003	2.884	0.021	0.118	0.002	1919	12	1924	10	1929	21	99
NE157	67	R1	120.6	189.6	0.1	53.0	1.57	5.842	0.069	0.353	0.002	2.836	0.020	0.120	0.002	1947	11	1953	10	1959	12	99
NE157	68	R2	201.5	223.3	0.0	79.6	1.11	5.823	0.070	0.355	0.003	2.821	0.020	0.119	0.002	1956	12	1950	10	1943	14	100
NE157	70	R1	380.9	80.8	0.0	133.4	0.21	6.267	0.070	0.375	0.002	2.666	0.016	0.121	0.002	2053	11	2014	10	1974	10	101
NE157	74	R1	344.2	136.4	0.2	116.6	0.40	5.870	0.067	0.358	0.002	2.790	0.017	0.119	0.001	1975	10	1957	10	1938	23	100
NE157	76	R1	121.7	211.3	2.2	54.3	1.74	5.817	0.062	0.349	0.002	2.869	0.018	0.121	0.002	1928	11	1949	9	1972	9	98
NE157	77	R1	285.3	129.7	0.2	106.5	0.45	6.138	0.113	0.367	0.002	2.725	0.017	0.121	0.002	2015	11	1996	16	1976	23	100
NE157	80	R1	308.6	91.6	0.3	102.6	0.30	5.687	0.100	0.349	0.002	2.865	0.018	0.118	0.002	1930	11	1929	15	1929	22	100
NE157	81	R0	152	90.4	0.8	54.3	0.59	5.929	0.106	0.356	0.002	2.812	0.019	0.121	0.002	1961	11	1966	16	1970	21	99
NE157	87	R0	176.5	220.8	0.3	73.2	1.25	6.065	0.101	0.363	0.003	2.754	0.019	0.121	0.002	1997	12	1985	15	1973	20	100
NE157	92	R1	137.6	174	0.0	61.0	1.26	5.952	0.106	0.361	0.002	2.770	0.019	0.120	0.002	1987	11	1969	16	1950	27	100

U-Pb LA-ICP-MS analyses of zircon

Sample	Spot	Group	U ppm	Th ppm	%^{206}Pbc	^{206}Pb*	*Isotopic Ratios*									*Age (Ma)*						
							Th/U	^{207}Pb/^{235}U	1σ (%)	^{206}Pb/^{238}U	1σ (%)	^{238}U/^{206}Pb	1σ (%)	^{207}Pb/^{206}Pb	1σ (%)	^{206}Pb/^{238}U	±2σ	^{207}Pb/^{235}U	±2σ	^{207}Pb/^{206}Pb	±2σ	Conc.%
NE163	4	R1	83	235	0.1	46.0	2.83	6.161	0.097	0.365	0.004	2.743	0.029	0.123	0.002	2004	18	1999	14	1994	13	100
NE163	6	R1	214	70	1.3	76.0	0.33	6.416	0.090	0.377	0.003	2.656	0.023	0.124	0.002	2060	15	2034	12	2009	11	101
NE163	10	R2	18	52	5.3	9.0	2.89	6.201	0.113	0.362	0.004	2.767	0.033	0.124	0.002	1989	21	2005	16	2020	21	99
NE163	12	R2	323	13	0.1	134.0	0.04	6.607	0.104	0.376	0.004	2.659	0.028	0.127	0.002	2058	19	2060	14	2063	13	99
NE163	17	R1	105	425	0.0	64.0	4.05	6.021	0.088	0.359	0.003	2.785	0.026	0.122	0.002	1978	16	1979	13	1980	12	99
NE163	30	R1	334	63	0.5	116.0	0.19	5.896	0.084	0.355	0.002	2.818	0.019	0.121	0.002	1958	11	1961	12	1964	15	99
NE163	31	R2	53	144	0.9	28.0	2.72	6.555	0.112	0.379	0.003	2.642	0.022	0.126	0.002	2069	15	2053	15	2038	18	100
NE163	37	R2	55	144	4.9	31.0	2.62	6.573	0.133	0.379	0.006	2.638	0.039	0.126	0.002	2072	26	2056	18	2040	36	100
NE163	40	R0	214	1	0.5	55.0	0.00	6.298	0.115	0.375	0.004	2.668	0.025	0.122	0.002	2052	16	2018	16	1984	19	101
NE163	41	R2	67	131	0.6	33.0	1.96	6.163	0.132	0.358	0.003	2.791	0.027	0.125	0.003	1974	16	1999	19	2026	22	98
NE163	44	R2	75	235	0.0	41.0	3.13	6.433	0.143	0.369	0.004	2.714	0.029	0.127	0.003	2022	19	2037	20	2052	38	99
NE163	45	RC	125	82	0.0	59.0	0.66	9.127	0.169	0.429	0.004	2.333	0.022	0.154	0.003	2300	18	2351	17	2395	21	97
NE163	50	R2	53	140	0.9	28.0	2.64	6.324	0.143	0.369	0.003	2.713	0.024	0.124	0.003	2023	16	2022	20	2021	34	100
NE163	51	R2	66	189	0.3	36.0	2.86	6.353	0.150	0.367	0.003	2.725	0.022	0.126	0.003	2015	14	2026	21	2037	40	99
NE163	53	R2	77	214	0.2	43.0	2.78	6.295	0.142	0.365	0.003	2.743	0.024	0.125	0.003	2004	15	2018	20	2032	27	99
NE163	54	R2	78	195	0.3	41.0	2.50	6.358	0.156	0.368	0.003	2.719	0.023	0.125	0.003	2019	15	2026	22	2034	38	99
NE163	55	R2	74	198	1.0	38.0	2.68	6.522	0.136	0.383	0.004	2.614	0.029	0.124	0.003	2088	20	2049	18	2010	25	101
NE163	57	RC	198	293	1.1	97.0	1.48	8.768	0.157	0.442	0.004	2.265	0.019	0.144	0.002	2357	17	2314	16	2276	17	101
NE163	58	R2	100	256	0.3	53.0	2.56	6.435	0.126	0.374	0.004	2.677	0.025	0.125	0.002	2046	16	2037	17	2028	20	100
NE163	61	R1	328	45	0.5	117.0	0.14	5.672	0.110	0.341	0.003	2.935	0.026	0.121	0.002	1890	15	1927	17	1967	19	98
NE163	65	R1	51	126	1.7	25.0	2.47	6.386	0.165	0.379	0.004	2.642	0.028	0.122	0.004	2069	19	2030	23	1991	34	101
NE163	66	R2	107	324	1.0	59.0	3.03	6.614	0.137	0.383	0.003	2.608	0.022	0.125	0.003	2092	15	2061	18	2031	23	101
NE163	76	R2	72	219	2.0	41.0	3.04	6.210	0.117	0.363	0.003	2.758	0.025	0.124	0.002	1994	16	2006	17	2018	20	99
NE163	89	RC	92	65	8.5	52.0	0.71	11.007	0.189	0.478	0.005	2.091	0.024	0.167	0.002	2519	24	2524	16	2527	20	99
NE163	90	R1	366	23	0.0	97.0	0.06	6.174	0.104	0.373	0.004	2.684	0.030	0.120	0.002	2041	20	2001	15	1959	12	102
NE163	96	RC	37	4	2.6	21.0	0.11	10.047	0.149	0.449	0.005	2.226	0.022	0.162	0.002	2392	20	2439	14	2478	10	98
NE163	97	R0	6	76	1.3	9.0	12.67	5.952	0.095	0.363	0.003	2.752	0.025	0.119	0.002	1998	16	1969	14	1938	24	101
NE163	98	RC	106	62	0.1	46.0	0.58	7.637	0.116	0.411	0.004	2.433	0.022	0.135	0.002	2219	17	2189	14	2161	14	101
NE163	99	R0	291	55	0.0	108.0	0.19	5.912	0.089	0.357	0.003	2.798	0.024	0.120	0.001	1970	15	1963	13	1956	15	100
NE163	101	R0	67	157	3.2	30.0	2.34	6.096	0.089	0.363	0.003	2.753	0.024	0.122	0.002	1998	15	1990	13	1981	12	100

APPENDIX C. LA-ICP-MS TRACE ELEMENTS ANALYSIS OF ZIRCON

LA-ICP-MS REE (chondrite normalized), Ti (ppm) and thermometric data for zircon

Sample	Spot	Group	La	Ce	Pr	Nd	Sm	Eu	Gd	Tb	Dy	Ho	Er	Tm	Yb	Lu	Ce/Ce*	Eu/Eu*	Gd/Yb	Ti (ppm)	T(ºC)[a]
NE30	2	R1	0.8	19.7	2.8	5.4		10.7	78.2	169.5	374.3	737.9	1400.1	2242.1	3894.8	5245.9	36.13		0.02	6.52	754
NE30	3	R1		28.1			37.9	7.8	128.1	262.0	371.7	601.5	764.1	872.1	1079.7	1420.3		0.01	0.12	12.68	821
NE30	6	R2		22.8		7.7	15.8	15.8	85.4	153.7	364.4	752.7	1317.1	2108.1	3301.7	4600.8		0.05	0.03	13.40	827
NE30	11	R0	5.8	21.4	15.0	22.7	54.3	94.0	94.1	239.1	496.5	1289.4	2592.8	4529.6	7685.7	11995.9	222.32	0.07	0.01	6.67	756
NE30	15	R2		12.8			13.9	6.9	88.7	272.9	640.3	1313.2	2351.4	3513.8	5238.4	6831.7		0.02	0.02	13.93	832
NE30	19	R2		18.4			20.8		127.7	312.2	590.7	1026.2	1602.5	1895.5	2731.6	3808.9		0.00	0.05	14.59	837
NE30	29	RC		27.5	3.3		23.6		87.8	114.1	207.4	428.6	697.8	1036.8	1753.4	2487.4	45.99	0.00	0.05	15.54	844
NE30	33	R1		23.0			16.4	13.1	98.3	259.0	290.2	465.2	569.8	674.5	763.5	1013.4		0.03	0.13	8.43	779
NE30	35	R0		9.9			18.9	15.5	100.6	336.6	761.7	1631.0	3119.1	4834.4	7899.0	10494.7		0.03	0.01	10.88	805
NE30	36	R1		7.3		3.6			59.2	168.1	393.9	905.5	1612.1	2621.5	4033.7	5537.0			0.01	7.12	762
NE30	37	R1		13.7				9.1	84.6	150.4	222.3	322.2	421.8	544.1	825.2	974.0			0.10	5.77	742
NE30	38	R2		8.5		3.4	15.8	16.3	69.3	196.1	479.4	972.9	1769.3	2691.5	4032.9	5276.0		0.06	0.02	7.85	772
NE30	40	R2		11.2		2.6	12.9	17.9	91.8	227.1	480.1	889.0	1289.6	1483.0	2042.1	2423.2		0.06	0.04	6.63	755
NE30	45	R2	0.5	15.1			22.2		137.4	276.5	568.0	1047.4	1749.8	2354.7	3391.0	4513.0	3.48		0.04	9.43	790
NE30	51	R1		13.7			14.1	12.8	96.7	264.3	492.6	938.5	1428.9	1872.5	2604.5	3481.3		0.04	0.04	8.70	782
NE30	55	R1		27.2			36.0		150.9	285.0	430.0	591.0	761.6	861.1	1041.9	1295.5		0.00	0.14	7.22	764
NE30	58	R1		27.1			41.1		127.1	248.2	366.0	551.6	701.5	824.7	1026.1	1387.0		0.00	0.12	14.56	837
NE30	62	R2		16.5		7.6	20.5		132.1	318.0	599.3	1085.5	1683.4	2398.8	3153.7	4281.3		0.00	0.04	18.04	861
NE30	74	R2		12.0			18.4	14.0	91.9	261.2	576.0	1297.3	2410.1	3628.7	5742.8	7917.5		0.03	0.02	11.82	814
NE30	75	RC		39.0	3.2	7.2	23.7	24.2	79.3	157.6	269.8	487.2	780.8	1234.4	1921.3	2907.3	62.97	0.05	0.04	21.69	883
NE30	76	R2		12.8	6.9	10.5	29.9	22.4	96.5	252.4	546.9	1203.8	2084.0	2988.3	4322.7	5787.4	44.10	0.03	0.02	11.05	807
NE30	77	R2	1.1	29.4			33.3	14.7	155.2	291.1	391.8	587.7	641.4	763.6	1060.1	1210.6	16.76	0.01	0.15	9.73	793
NE30	83	R2		9.2					70.4	284.2	575.9	1314.3	2438.4	3422.7	5179.9	6983.7			0.01	15.18	841
NE30	84	RC		155.8	2.5	5.6	55.0	70.0	194.5	393.4	679.6	1185.2	1909.2	2608.5	4039.4	5126.4	193.06	0.03	0.05	15.59	844
NE30	85	R1		30.0	3.1		26.4		153.6	286.1	429.8	570.1	639.1	795.5	959.0	1295.5	46.82		0.16	18.04	861
NE30	93	R2		23.6					146.3	278.7	413.0	786.3	1118.4	1667.2	2126.2	2739.8			0.07	17.18	855
NE30	95	RC		16.9			42.9	16.3	167.9	317.5	567.4	1132.4	1856.4	2319.0	3557.0	4535.8		0.01	0.05	6.35	751
NE30	96	R2		17.6			13.8	12.1	122.5	297.8	582.6	1223.6	1999.8	2598.8	3524.8	4571.5		0.03	0.03	14.16	833
NE30	99	R2		10.6				27.7	108.0	335.2	667.5	1548.9	2926.4	4492.7	6993.8	9865.4			0.02	14.30	835
NE30	100	R1		24.2			25.1		131.6	251.0	356.5	550.9	743.3	936.4	1287.3	1763.0			0.10	17.87	860

[a]Temperature calculated with Ferry & Watson (2007) calibration with *a* SiO2 = 1 and *a* TiO2 = 0.6. Empty values indicates that analysis was below detection limits of LA-ICP-MS.

LA-ICP-MS REE (chondrite normalized), Ti (ppm) and thermometric data for zircon

Sample	Spot	Group	La	Ce	Pr	Nd	Sm	Eu	Gd	Tb	Dy	Ho	Er	Tm	Yb	Lu	Ce/Ce*	Eu/Eu*	Gd/Yb	Ti (ppm)	T(ºC)[a]
NE157	2	R0		1.0					78.4	89.2	181.7	320.7	424.9	674.5	1142.2	1443.9			0.07	10.68	807
NE157	4	R1		3.5	6.0	7.3	33.3		31.3	52.6	23.9	20.7	13.6			28.5	10.58			19.94	801
NE157	6	R0		12.9			54.7		52.3	89.5	130.0	52.0	77.9	93.5		115.0				26.20	772
NE157	12	R1		9.2			49.1		61.1	61.8	36.1	31.0	21.4	28.7	17.0				3.60	18.42	882
NE157	17	R0		1.2			24.6	21.1	73.9	85.6	97.6	133.9	137.1	138.9	267.8	295.5		0.05	0.28	35.82	826
NE157	18	R0		1.7			36.4	11.7	83.5	80.9	76.0	84.4	64.2	53.8	55.7	50.0		0.02	1.50	20.37	817
NE157	20	R0		3.3			28.2	17.1	54.7	41.3	32.7	35.9	20.7	15.4	22.5			0.04	2.43	10.92	815
NE157	21	R1		6.4		10.9	29.9	43.7	54.1	35.2		17.6		21.1	24.9			0.11	2.17	20.14	824
NE157	25	R1		3.5		11.3			47.2	33.8	51.5	50.9	70.7	131.2	206.3	263.0			0.23	51.69	808
NE157	28	R1		4.4			43.0		85.3	78.1	61.9	58.4	57.1	32.4	41.9	40.2			2.04	21.99	784
NE157	30	R1	1.7	4.6	4.2			36.2	74.4	99.2	98.6	89.6	49.1	40.5	33.6	43.9	13.55		2.21	19.92	752
NE157	31	R1		5.8					38.6	23.3		10.4			28.7				1.34	16.21	809
NE157	45	R1		5.4		11.4	35.8		56.2	36.3	34.7	24.9	17.3		29.0				1.94	21.73	845
NE157	46	R1		5.6	3.2				20.0	25.2	16.5	12.5	14.6				9.12			14.32	795
NE157	50	R1		5.7			31.8		47.9	29.9	35.9	19.8	28.1	30.8	17.8	22.0			2.69	22.01	813
NE157	51	R1		3.6			29.5		70.4	38.5	43.5	21.6	12.4			26.4				16.80	928
NE157	57	R1		5.6		12.6	38.1		45.5	45.4	20.4	33.7	17.8	33.2						16.53	758
NE157	59	R1		7.4		11.5	25.3		33.5	19.1	28.1	15.8			20.0				1.67	18.70	816
NE157	61	R0		6.7	3.8				37.4	35.5	21.5	17.2	11.9	14.2	19.9		12.58		1.88	14.78	797
NE157	66	R1		5.5			25.7	14.4	81.7	74.2	66.7	39.0	56.6	53.4	76.3	51.6		0.03	1.07	17.40	754
NE157	67	R1		12.3		7.9			45.1	34.9		18.7			34.6				1.30	11.34	781
NE157	68	R2		53.0			51.7	46.0	125.2	191.7	294.0	459.9	777.9	1104.0	1999.8	2604.9		0.03	0.06	18.77	751
NE157	70	R1		3.0			54.2		17.9	23.5	13.0									10.78	752
NE157	74	R1		4.4	3.6		23.8		33.7	28.3	22.5	13.4	14.9	15.0	31.4	24.0	7.80		1.07	10.70	798
NE157	76	R1		1.9			24.2		121.1	167.9	136.2	91.2	73.4	78.9	93.4	104.5			1.30	10.69	815
NE157	77	R1		1.9	5.2	8.7			53.5	52.4	46.5	55.9	82.3	98.4	149.7	219.5	4.81		0.36	21.56	753
NE157	80	R1		5.5			23.2		60.8	37.1	28.6	25.6	19.3	25.9						13.09	752
NE157	81	R0		5.3	4.2				48.1	63.7	74.8	96.9	145.4	136.4	274.6	426.0	11.14		0.18	10.61	824
NE157	87	R0		7.7			23.2		41.2	33.8	22.4	12.1	11.8							16.97	826
NE157	92	R1		7.9		6.3	26.3	11.2	39.1	19.7	21.7	16.8		23.9		23.6		0.04		19.61	793

[a]Temperature calculated with Ferry & Watson (2007) calibration with *a* SiO2 = 1 and *a* TiO2 = 1. Empty values indicates that analysis was below detection limits of LA-ICP-MS.

LA-ICP-MS REE (chondrite normalized), Ti (ppm) and thermometric data for zircon

Sample	Spot	Group	La	Ce	Pr	Nd	Sm	Eu	Gd	Tb	Dy	Ho	Er	Tm	Yb	Lu	Ce/Ce*	Eu/Eu*	Gd/Yb	Ti (ppm)	T(ºC)[a]
NE163	4	R1		13.1			53.2		56.2	110.2	148.9	152.9	179.7	189.1	317.6	267.9			0.18	13.24	795
NE163	6	R1	7.8	16.4	12.4	9.7	55.3	18.3	123.7	188.1	138.3	108.1	79.8	81.8	111.2	99.2	166.08	0.01	1.11	12.08	786
NE163	10	R2		13.4	4.0		25.0	20.2	53.1	62.3	52.6	48.9	50.4	50.6	73.0	69.1	26.70	0.06	0.73	105.20	1063
NE163	12	R2		11.6					42.6	134.9	221.1	423.6	801.6	1406.1	2325.3	3322.8			0.02	13.14	795
NE163	17	R1		14.3			45.6	16.0	79.9	123.8	120.3	126.4	143.8	144.9	173.2	198.4		0.02	0.46	13.74	799
NE163	30	R1		6.7					93.3	134.3	119.8	136.6	126.6	122.7	163.5	187.8			0.57	13.72	799
NE163	31	R2	8.3	28.8				56.8	106.9	146.8	193.3	237.7	260.1	316.6	296.6	372.4	119.80		0.36	19.15	835
NE163	37	R2		15.4	5.2	11.0	30.3	34.6	73.3	86.7	124.7	144.3	143.8	161.5	168.8	170.7	39.74	0.06	0.43	16.58	819
NE163	40	R0		23.1				24.2	48.1	76.7	210.8	404.6	653.2	1325.5	2013.9	2888.2			0.02	9.08	805
NE163	41	R2	1.8	8.3	4.4			22.2	87.2	163.2	202.3	186.6	173.4	237.7	286.6	286.6	25.72		0.30	7.79	743
NE163	44	R2		13.7	4.1		25.9		65.4	64.3	52.2	71.4	77.1	74.9	77.4	111.0	28.09		0.85	17.94	828
NE163	45	RC	2.4	49.5	8.0		27.8	36.4	53.5	85.3	117.6	248.0	385.8	532.8	843.7	1222.0	258.07	0.10	0.06	10.02	816
NE163	50	R2		13.4		7.4	19.7		74.2	73.7	63.7	104.0	106.9	134.0	183.4	169.5			0.40	12.40	789
NE163	51	R2		10.6					40.0	48.8	67.2	44.0	56.4	55.9	58.4	82.5			0.69	31.66	894
NE163	53	R2		11.8		8.3			59.9	74.5	95.2	114.3	132.6	155.9	182.6	184.6			0.33	15.69	813
NE163	54	R2		8.9		7.0	38.7		66.1	90.6	110.7	135.5	176.4	288.3	431.4	617.5			0.15	18.37	830
NE163	55	R2	2.2	17.2	12.2			33.7	107.4	81.7	120.6	257.5	217.8	340.1	289.4	462.2	123.42		0.37	53.30	962
NE163	57	RC	186.0	253.5	174.7	126.3	136.1	49.2	302.5	534.9	758.8	1324.0	1783.6	2440.1	3330.1	4369.1	45715.5	0.00	0.09	24.11	919
NE163	58	R2		13.2					92.7	119.4	147.9	264.7	257.6	308.9	371.8	419.5			0.25	21.64	849
NE163	61	R1	2.8	8.3			27.4		100.1	174.2	182.6	164.5	142.8	144.5	176.0	204.5	11.58		0.57	20.48	843
NE163	65	R1		9.1			47.2		102.2	153.7	204.2	197.8	248.5	242.9	283.0	328.9			0.36	16.52	819
NE163	66	R2		19.0	3.6	10.5	49.1		145.6	191.7	254.9	408.8	508.3	517.8	653.7	714.6	33.73		0.22	17.74	827
NE163	76	R2	5.9	29.3	14.4	18.0	34.0	29.7	77.7	119.1	121.3	133.0	154.9	136.0	168.0	183.7	297.94	0.04	0.46	11.59	782
NE163	89	RC		13.1		9.5	54.6	32.7	331.8	593.4	1077.7	1828.0	2738.2	3317.0	4229.1	5382.9		0.01	0.08	47.23	1012
NE163	90	R1		11.9					65.1	74.2	105.2	177.7	208.9	221.1	301.2	380.9			0.22	25.77	869
NE163	96	RC		15.8			17.2		31.9	83.1	124.1	271.6	491.1	702.0	1206.5	1769.1			0.03	16.05	869
NE163	97	R0		11.1			19.9		40.2	100.6	151.7	167.6	206.3	215.0	307.5	350.8			0.13	9.77	813
NE163	98	RC		19.2	4.5				85.6	170.4	231.4	432.2	572.8	838.1	1173.7	1458.1	43.49		0.07	11.27	828
NE163	99	R0		20.0					63.5	159.6	263.9	448.5	676.9	989.5	1400.1	1767.1			0.05	15.33	863
NE163	101	R0		15.2				28.1	69.2	140.4	193.1	398.5	503.7	716.6	973.3	1352.0			0.07	11.58	831

[a]Temperature calculated with Ferry & Watson (2007) calibration with *a* SiO2 = 1 and *a* TiO2 = 0.8. Empty values indicates that analysis was below detection limits of LA-ICP-MS.